Contribution to the study of ejector expansion heat pump cycle : Modeling and experimental approach

Cong You

N°d'ordre NNT: 2024ISAL0029

THESE de DOCTORAT DE L'INSA LYON, membre de l'Université de Lyon

Ecole Doctorale N° 162
Mécanique, Energétique, Génie civil, Acoustique

Spécialité/ discipline de doctorat :
Thermique Energétique

Soutenue publiquement le 04/04/2024, par :
Cong YOU

Contribution to the study of ejector expansion heat pump cycle: modeling and experimental approach

---

Devant le jury composé de :

COLIN, Catherine	Professeur des Universités, IMFT Toulouse	Examinatrice
PHAN, Hai trieu	Docteur HDR, CEA Grenoble	Rapporteur
TREMEAC, Brice	Professeur des Universités, CNAM Paris	Rapporteur
REVELLIN, Rémi	Professeur des Universités, INSA Lyon	Directeur de thèse
MICHEL, Benoit	Maître de Conférences, INSA Lyon	Co-encadrant

Département FEDORA – INSA Lyon - Ecoles Doctorales

SIGLE	ECOLE DOCTORALE	NOM ET COORDONNEES DU RESPONSABLE
ED 206 CHIMIE	**CHIMIE DE LYON** https://www.edchimie-lyon.fr Sec. : Renée EL MELHEM Bât. Blaise PASCAL, 3e étage secretariat@edchimie-lyon.fr	**M. Stéphane DANIELE** C2P2-CPE LYON-UMR 5265 Bâtiment F308, BP 2077 43 Boulevard du 11 novembre 1918 69616 Villeurbanne directeur@edchimie-lyon.fr
ED 341 E2M2	**ÉVOLUTION, ÉCOSYSTÈME, MICROBIOLOGIE, MODÉLISATION** http://e2m2.universite-lyon.fr Sec. : Bénédicte LANZA Bât. Atrium, UCB Lyon 1 Tél : 04.72.44.83.62 secretariat.e2m2@univ-lyon1.fr	**Mme Sandrine CHARLES** Université Claude Bernard Lyon 1 UFR Biosciences Bâtiment Mendel 43, boulevard du 11 Novembre 1918 69622 Villeurbanne CEDEX e2m2.codir@listes.univ-lyon1.fr
ED 205 EDISS	**INTERDISCIPLINAIRE SCIENCES-SANTÉ** http://ediss.universite-lyon.fr Sec. : Bénédicte LANZA Bât. Atrium, UCB Lyon 1 Tél : 04.72.44.83.62 secretariat.ediss@univ-lyon1.fr	**Mme Sylvie RICARD-BLUM** Laboratoire ICBMS - UMR 5246 CNRS - Université Lyon 1 Bâtiment Raulin - 2ème étage Nord 43 Boulevard du 11 novembre 1918 69622 Villeurbanne Cedex Tél : +33(0)4 72 44 82 32 sylvie.ricard-blum@univ-lyon1.fr
ED 34 EDML	**MATÉRIAUX DE LYON** http://ed34.universite-lyon.fr Sec. : Yann DE ORDENANA Tél : 04.72.18.62.44 yann.de-ordenana@ec-lyon.fr	**M. Stéphane BENAYOUN** Ecole Centrale de Lyon Laboratoire LTDS 36 avenue Guy de Collongue 69134 Ecully CEDEX Tél : 04.72.18.64.37 stephane.benayoun@ec-lyon.fr
ED 160 EEA	**ÉLECTRONIQUE, ÉLECTROTECHNIQUE, AUTOMATIQUE** https://edeea.universite-lyon.fr Sec. : Philomène TRECOURT Bâtiment Direction INSA Lyon Tél : 04.72.43.71.70 secretariat.edeea@insa-lyon.fr	**M. Philippe DELACHARTRE** INSA LYON Laboratoire CREATIS Bâtiment Blaise Pascal, 7 avenue Jean Capelle 69621 Villeurbanne CEDEX Tél : 04.72.43.88.63 philippe.delachartre@insa-lyon.fr
ED 512 INFOMATHS	**INFORMATIQUE ET MATHÉMATIQUES** http://edinfomaths.universite-lyon.fr Sec. : Renée EL MELHEM Bât. Blaise PASCAL, 3e étage Tél : 04.72.43.80.46 infomaths@univ-lyon1.fr	**M. Hamamache KHEDDOUCI** Université Claude Bernard Lyon 1 Bât. Nautibus 43, Boulevard du 11 novembre 1918 69 622 Villeurbanne Cedex France Tél : 04.72.44.83.69 direction.infomaths@listes.univ-lyon1.fr
ED 162 MEGA	**MÉCANIQUE, ÉNERGÉTIQUE, GÉNIE CIVIL, ACOUSTIQUE** http://edmega.universite-lyon.fr Sec. : Philomène TRECOURT Tél : 04.72.43.71.70 Bâtiment Direction INSA Lyon mega@insa-lyon.fr	**M. Etienne PARIZET** INSA Lyon Laboratoire LVA Bâtiment St. Exupéry 25 bis av. Jean Capelle 69621 Villeurbanne CEDEX etienne.parizet@insa-lyon.fr
ED 483 ScSo	**ScSo**[1] https://edsciencessociales.universite-lyon.fr Sec. : Mélina FAVETON Tél : 04.78.69.77.79 melina.faveton@univ-lyon2.fr	**M. Bruno MILLY** (INSA : J.Y. TOUSSAINT) Univ. Lyon 2 Campus Berges du Rhône 18, quai Claude Bernard 69365 LYON CEDEX 07 Bureau BEL 319 bruno.milly@univ-lyon2.fr

[1] ScSo : Histoire, Géographie, Aménagement, Urbanisme, Archéologie, Science politique, Sociologie, Anthropologie

"All those had passed will turned into beautiful memories and deposit"

Aleksandr Sergeyevich Pushkin

Abstract

The Heating, Ventilation, Air Conditioning, and Refrigeration (HVAC&R) industry is a notable contributor to both global warming and ozone depletion. To address these environmental concerns, there is a growing inclination toward adopting carbon dioxide (CO_2) as refrigerant fluid because it is an eco-friendly alternative. However, the inherent challenges of low critical temperature and high critical pressure of CO_2 lead to predominant operation in transcritical mode, characterized by a high pressure ratio in traditional expansion valves. This elevated pressure ratio results in significant irreversibility during the expansion process.

The introduction of an ejector as a substitute for conventional expansion valves in the transcritical CO_2 heat pump cycle involves the acceleration of high-pressure fluid through a converging-diverging nozzle. This process enables the entrainment and mixing of low-pressure vapor from the evaporator, leading to substantial improvements in pressure recovery. The resultant reduction in compression work has been scientifically validated, establishing this ejector-based configuration as an effective alternative with superior system efficiency compared to conventional expansion valve cycles.

Despite their potential advantages, ejectors introduce complexities related to two-phase flow and sonic shock waves. Consequently, understanding the intricate flow field within the ejector is crucial for enhancing performance in heat pump cycles. Therefore, simulation and experimental studies are deemed necessary.

This thesis comprehensively investigates the ejector expansion CO_2 heat pump cycle across different scales. It commences with a detailed review of state-of-the-art technology and historical trends in refrigerants. A systematic comparison of ejector technology with alternative enhancement methods is presented, followed by the introduction and validation of thermodynamic models. Key aspects such as isentropic efficiency are addressed, and novel data post-processing techniques are proposed.

In the realm of theoretical exploration, this study delves into the cycle scale, where various 0-D thermodynamic models of the ejector expansion heat pump cycle are comparatively examined and validated using independent data. Specifically, a 1-D homogeneous equilibrium model for the ejector region is introduced, validated, and applied for parametric analysis and geometry design. This 1-D model is further compared with 0-D thermodynamic models of the ejector. Finally, a dedicated experimental test facility is established, providing valuable insights into ejector performance and working modes across varying evaporation pressures.

In essence, this research significantly contributes to the understanding of CO_2 heat pump cycles, with a specific focus on ejector technology. The integration of theoretical models and experimental studies provides essential insights for optimizing ejector design and cycle operation parameters, addressing the evolving needs of the HVAC&R industry and promoting sustainable refrigeration applications.

Keywords: Heat pump cycle, Carbon dioxide, Ejector, Thermodynamic, Modeling, Experimental validation

Résumé

L'industrie du chauffage, de la ventilation, de la climatisation et de la réfrigération (CVC&R) est une contributrice notable au réchauffement climatique et à la destruction de la couche d'ozone. Pour faire face à ces préoccupations environnementales, le dioxyde de carbone (CO_2) est de plus en plus utilisé comme fluide frigorigène car il représente une alternative plus respectueuse de l'environnement. Cependant, sa basse température critique et à sa haute pression critique du CO_2 conduisent à une utilisation prédominante de ces cycles en mode transcritique, caractérisée par un rapport de pression élevé dans le détendeur. Ce rapport de pression élevé entraîne une irréversibilité significative lors du processus de détente.

L'utilisation d'un éjecteur en remplacement des détenteurs conventionnels dans le cycle frigorifique au CO_2 transcritique implique l'accélération du fluide à haute pression à travers une tuyère convergente-divergente. Ce processus permet l'entraînement et le mélange de la vapeur basse pression provenant de l'évaporateur, conduisant à des améliorations substantielles de la récupération de pression. La diminution du travail de compression a été scientifiquement validée, conduisant à une meilleure efficacité de ces systèmes à éjection par rapport aux cycles conventionnels.

Malgré leurs avantages potentiels, les éjecteurs introduisent des complexités liées à l'écoulement diphasique et aux ondes de choc soniques. Par conséquent, la compréhension du champ d'écoulement complexe à l'intérieur de l'éjecteur est cruciale afin d'améliorer les performances des cycles frigorifiques. Des études de simulation et une étude expérimentale sont donc jugées nécessaires.

Cette thèse entreprend une investigation approfondie du cycle frigorifique avec éjecteur au CO_2 à différentes échelles. Un état de l'art en matière de frigorigènes est tout d'abord présenté. Une comparaison systématique de la technologie de l'éjecteur avec d'autres méthodes d'amélioration des performances des systèmes frigorifiques est ensuite présentée, suivie de l'introduction et de la validation de modèles thermodynamiques. Des aspects clés tels que les rendements isentropiques sont abordés, et des techniques novatrices de post-traitement des données sont proposées.

Dans le domaine de l'exploration théorique, cette étude se plonge à l'échelle du cycle, où divers modèles thermodynamiques à zéro dimension du cycle frigorifique à éjection sont examinés et validés de manière comparative à l'aide de données indépendantes. Plus précisément, un modèle d'équilibre homogène monodimensionnel pour la région de l'éjecteur est introduit, conduisant à sa conception géométrique. Ce modèle est ensuite comparé avec des modèles thermodynamiques à zéro dimension. Finalement, un banc d'essai dédié à l'étude de l'éjecteur a été developpé, fournissant des perspectives précieuses sur les performances de l'éjecteur et les modes de fonctionnement à travers des pressions d'évaporation variables.

En résumé, ce travail de recherche contribue de manière significative à la compréhension des cycles frigorifiques au CO_2, avec un accent spécifique sur la technologie de l'éjecteur. L'intégration de modèles théoriques et d'études expérimentales offre des perspectives essentielles pour optimiser la conception de l'éjecteur et les paramètres opérationnels du cycle, répondant aux besoins évolutifs de l'industrie CVC&R et promouvant des applications de réfrigération durables.

Mots-clés : Cycle frigorifique, Dioxyde de carbone, Éjecteur, Thermodynamique, Modélisation, Validation expérimentale

Acknowledgements

I would like to express my sincere gratitude to the individuals who have been instrumental in helping me complete this thesis. Without the kindness and support of everyone mentioned here, I would not have persevered until today.

First and foremost, I extend my deepest thanks to my supervisor, Rémi Revellin, and my co-supervisor, Benoit Michel. Throughout the thesis period, you provided invaluable suggestions and inspiration for the research. Rémi, acting as the captain of our thesis ship, consistently steered it in the right direction and taught me how to be a qualified researcher. The skills and research mindset I acquired from him will continue to guide me in my research career. Benoit, akin to an experienced sailor, guided me through the challenges encountered during the thesis. Building a test facility from scratch, especially amid the obstacles posed by COVID, presented numerous detailed and intricate problems. Yet, with Benoit's guidance, we found solutions to every challenge. I am deeply grateful for your mentorship over the years; you both have been inspirational teachers on my research journey.

I also want to express my gratitude to my friends at CETHIL. Special thanks to the wonderful colleagues from the workshop, Christophe, Nicolas, Xavier, and Antoine. Your support was crucial for the establishment of the test facility, and I appreciate your patience in guiding me like an ignorant child. I will cherish the memories of our collaborative work on the test facility and the enduring friendships among us. Thanks also to our engineers, Loic, Bertrand, Anthony, Serge, and Pierrick, for their assistance in constructing the test facility. Heartfelt thanks to Marc, Romuald, Mériem, and Marilyne, considering the numerous 'bon de commande' I made during the thesis.

My appreciation extends to the Ph.D. students at CETHIL. Thank you for the companionship over the past four years. We shared memorable moments, and the friendships forged during this time will remain etched in my mind and heart forever. A special mention to my office mate, Antoine; our office was always filled with a cheerful atmosphere, and the camaraderie we built in that small room was truly amazing. You are always welcome, and I will reserve a chair for you in my future office, maybe even in my place in China.

I am also grateful for the friendships formed with the Chinese groups here in Lyon. Whether on the basketball court, during traditional Chinese festivals, or on European trips, we shared great times. Despite hailing from different parts of China and possibly being scattered worldwide, the memories created here are permanent and will be cherished forever.

Lastly, my heartfelt thanks to my family, including my girlfriend Xiaorui, and our 'kids' (dog Yixiu, cats Yingmu, and Huadao). They also go by their French names: Nature, Science, and Nano. Xiaorui, you are an amazing girl, and I consider myself fortunate to have met and fallen in love with you. Life with you is a new beginning, and I look forward to continuing this journey together. To my parents and grandma

in China, though you cannot be here physically, your unwavering and selfless support is always with me. I am proud to be your son and aspire to make you proud.

Thank you once again to everyone mentioned here and those not explicitly named. Life may be filled with challenges, but the journey becomes wonderful and radiant with the presence of each one of you.

Contents

List of Figures

List of Tables

Introduction

Climate change is a global concern with the potential to threaten human survival, and its two main causes are the greenhouse effect and the depletion of the ozone layer. Fig. 1 and Fig. 2 depict the trends in global warming effects and ozone layer destruction, respectively. In 2022, annual global CO_2 emissions surpassed 35 billion tons, a staggering increase from the pre-1950 levels of less than 5 billion tons. Despite efforts to phase out ozone-depleting substances, the area of the Antarctic ozone hole remains at a high level compared to the early 1980s.

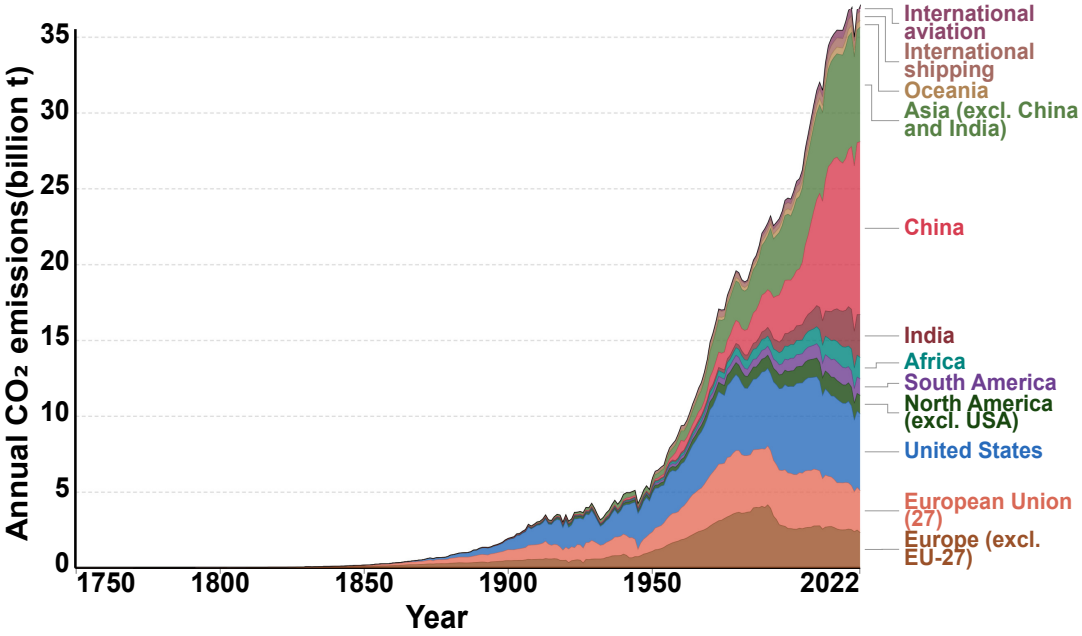

FIGURE 1: Annual CO_2 emissions by world region, emissions from fossil fuels and industry are included. Source: Global Carbon Budget (2023)

In the Heating, Ventilation, Air Conditioning, and Refrigeration (HVAC&R) industry, a major source of CO_2 emissions and ozone-depleting substances, the use of CO_2 to replace traditional refrigerants can effectively mitigate the impact on the climate. As a natural refrigerant, CO_2 is environmentally friendly with 0 ODP (Ozone Depletion Potential) and 1 GWP (Global Warming Potential).

Within the normal temperature range for the condensation of heat pump or refrigeration cycles (30 to 60 °C), CO_2 will reject heat in a supercritical state (the critical temperature of CO_2 is 31 °C). Considering the high critical pressure of CO_2 (approximately 7.4 MPa), the pressure ratio for the expansion process in the transcritical

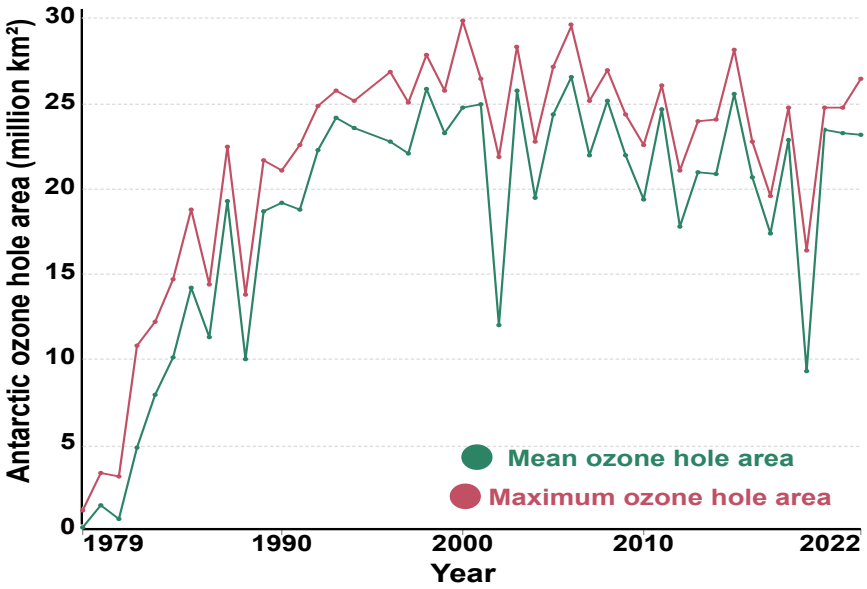

FIGURE 2: Annual maximum and mean Antarctic stratospheric ozone hole area, resultant from the emission of ozone-depleting substances. Source: NASA Ozone Watch (2023)

CO_2 heat pump or refrigeration cycle is very high, causing a significant amount of irreversibility.

To recover the expansion losses in the transcritical CO_2 heat pump and refrigeration cycle, using an ejector to replace the traditional expansion valve has proven to be a promising method.

In 1858, the French inventor Henry Giffard patented a condensing ejector designed to pump liquid water into a tank within a steam engine boiler [1]. In 1910, Leblanc proposed the first ejector jet refrigeration system, utilizing an ejector to create a low-pressure vessel where water vaporized, producing a cooling effect by harnessing low-grade energy sources. This system found initial success in ships due to the availability of cool seawater, its simplicity, and ruggedness. It was widely adopted for air conditioning in factories, large buildings, and trains during the early 1930s [2].

However, ejectors involve the complex merging of two separate flows, a common feature in most heat pump and refrigeration applications where two-phase flow phenomena are prevalent. Moreover, the flow velocity routinely surpasses the local speed of sound, leading to the development of shock waves throughout the flow path. Due to the intricate nature of the flow field within the ejector, our contemporary understanding of the complex flow dynamics, optimization strategies for ejector design, and the nuanced configuration of boundary conditions for the ejector remains, as of now, incomplete.

On the other hand, for the actual operation of the ejector expansion heat pump cycle, modeling of the cycle is necessary to predict key performance indices and adjust the operational conditions based on the working modes of the ejector. Balancing the accuracy and time consumption of the cycle modeling is essential for practical

implementation in industrial systems.

Motivated by the promising prospects and numerous challenges associated with ejector expansion heat pump cycles, as well as the complex flow field of the ejector, this thesis is dedicated to conducting comprehensive numerical and experimental investigations into the ejector expansion transcritical CO_2 heat pump and refrigeration cycles. The overarching objective is to enhance our understanding of the fundamental working principles and intricate flow dynamics governing the ejector system. Additionally, at the cycle scale, the aim is to optimize the modeling, finding a balance between complexity and accuracy.

The thesis is divided into four chapters. It is organized as follows:

Chapter 1: Overview and Introduction

In this chapter, we present a thorough review of the state-of-the-art ejector expansion transcritical CO_2 heat pump cycle. We briefly examine the historical evolution of refrigerants used in heat pump and refrigeration cycles, followed by a comparative analysis of the advantages of ejector technology in contrast to other performance enhancement methods. The introduction delves into the intricacies of ejector composition and classification, elucidating working modes and simulation methods. Furthermore, we delve into experimental research on the ejector expansion cycle, providing a comprehensive exploration that includes the depiction of novel ejector expansion cycles.

Chapter 2: Thermodynamic Modeling and Validation

This chapter introduces three 0-D thermodynamic models and conducts a comparative validation using two sets of independent data. A sensitivity analysis is performed to study the influence of input isentropic efficiency for both the ejector components and the compressor. A novel method for data post-processing is proposed to eliminate the liquid mass imbalance issue during actual cycle operation, a key factor contributing to simulation deviations in 0-D thermodynamic models.

Chapter 3: 1-D Homogeneous Equilibrium Modeling

A 1-D homogeneous equilibrium model for the ejector region is proposed based on the Finite Volume Method. The model is validated with experimental data and used for parametric analysis of ejector operation. Additionally, the proposed model is employed for geometry design and comparison with various 0-D thermodynamic models introduced in Chapter 2.

Chapter 4: Design and Prototype of Test Facility

To investigate ejector performance and working modes, a test facility for the ejector expansion heat pump cycle is established. System configuration and parameter regulation enable control over both ejector inlet and outlet pressures, providing flexibility for ejector studies. The test facility is designed to operate across a wide

range of evaporation pressures, ensuring a comprehensive understanding of ejector expansion cycle performance for various applications.

Chapter 1

State of the art review

This chapter presents a state-of-the-art review of ejector enhanced transcritical CO_2 heat pump cycle. The initial focus is on introducing the heat pump cycle, highlighting its advantages over other systems, and providing a basic schematic. Following this, a historical retrospective on refrigerants utilized in the heat pump cycle is subsequently presented, tracing their evolutionary trajectory and driving motivations behind. The analysis then turns to comparing common refrigerants in the market, including the fourth generation and natural refrigerants like CO_2, with a particular emphasis on their environmental impact.

Then the basic working principle of an ejector enhanced transcritical CO_2 heat pump cycle will be explained. More details about the ejector will be presented, such as its classification, modeling method, and a comparison with traditional expansion valve heat pump cycles.

Finally, some novel configuration of ejector expansion heat pump cycle will be presented, aiming at providing an optimization orientation of the ejector expansion heat pump cycle.

1.1 Introduction of heat pump system using CO_2 as refrigerant

Heat pumps stand out as the most efficient alternative to fuel combustion and electric systems within the realm of heating, ventilation, air conditioning, and refrigeration (HVAC&R). In contrast to systems relying on combustion processes, heat pumps are not only more cost-effective but also boast enhanced safety during operation. Moreover, their extended life-span, averaging at 15 years, underscores their exceptional reliability as a heating and cooling source, requiring comparatively less maintenance [3]. The concept of a heat pump is often credited to Lord Kelvin, but he did not demonstrate the concept. The first commercial heat pump installation was in the Equitable Building of Portland, Oregon in 1948 [4].

Various types of heat pumps exist, with some requiring external mechanical work and others relying on external thermal energy. Commercially, heat pumps based on the vapor compression or absorption cycle are prevalent in different industries [5]. In Fig. 1.1, the schematic and corresponding *P-h* diagram of a typical

heat pump cycle is illustrated, featuring a mechanical vapor compressor. This cycle facilitates the transfer of heat from a low-temperature heat source in the evaporator to a high-temperature heat sink in the condenser. The heat source can encompass air, water, ground, waste heat, and more. A power supply is essential for the compressor to execute the heat transfer.

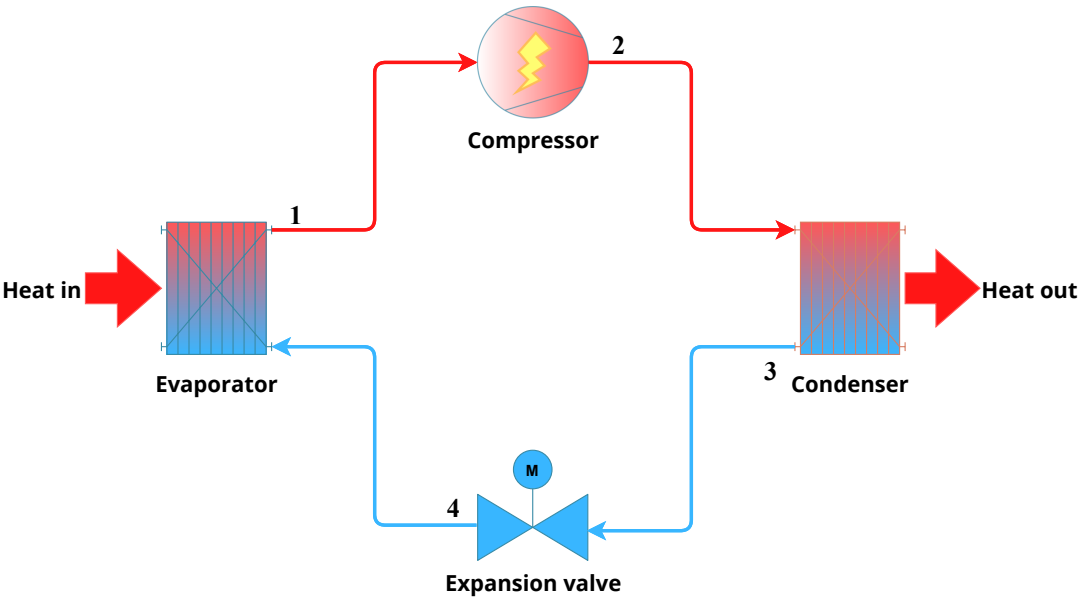

(A) Schematic of heat pump cycle

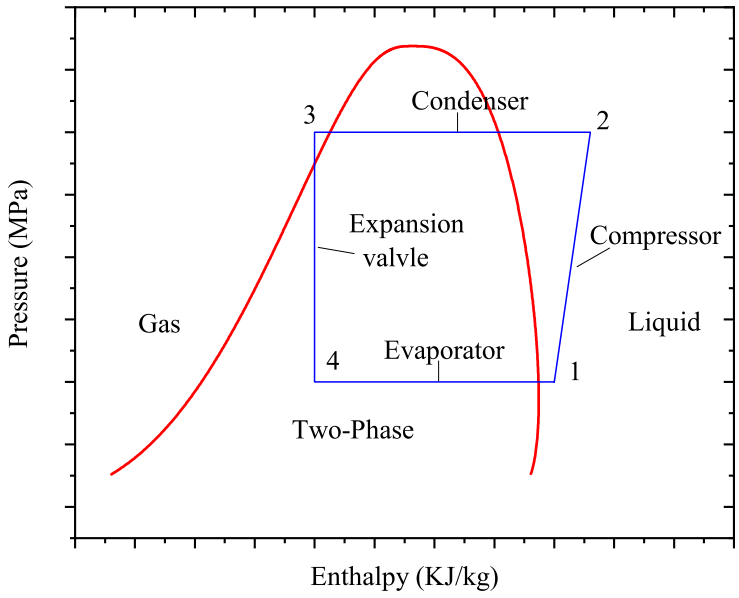

(B) *P-h* diagram

FIGURE 1.1: Schematic and *P-h* diagram of a typical heat pump cycle

The operational mode of a heat pump is contingent upon its intended purpose, functioning either in heating or refrigeration mode. In the mode of heating, the heat

is absorbed to the cycle in the evaporator from the environment, and the refrigerant will evaporate into saturated vapor (or super heated vapor). The absorbed heat will be discharged into the space where there is demand by the condensing of the refrigerant in the condenser. The condensing temperature is higher than the evaporation temperature, and the corresponding pressure is also higher than the evaporation pressure. Therefore, the compressor will play the role of raising the pressure of the refrigerant from evaporation pressure into condensing pressure. After condensing in the condenser, the refrigerant will pass through an expansion valve and the pressure will decrease to the evaporation pressure. The heat pump will sustain this cycle, ensuring a consistent and reliable delivery of heat. For the mode of refrigeration, the working principle is similar to the heating mode but the circulating direction of the refrigerant is reversed, which means the heat will be absorbed in the space where there is a demand of refrigeration and discharged into the environment with higher temperature. Therefore, a heat pump cycle can work at two different modes, just the location of the evaporator and condenser will be opposite for different modes.

1.1.1 Traditional refrigerant used in heat pump cycle

Since the inception of the heat pump cycle, the refrigerants employed have undergone a discernible evolution, progressing from the first generation to the early stages of the fourth generation. The progression in the refrigerants over time is shown in Fig. 1.2. The history of refrigerants begins with the use of natural refrigerants (1800s) and, in 1930, they were replaced by synthetic refrigerants, considering the performance, safety and durability as major indicators [6]. After that the evolution is markedly influenced by international protocols addressing climate change as follow:

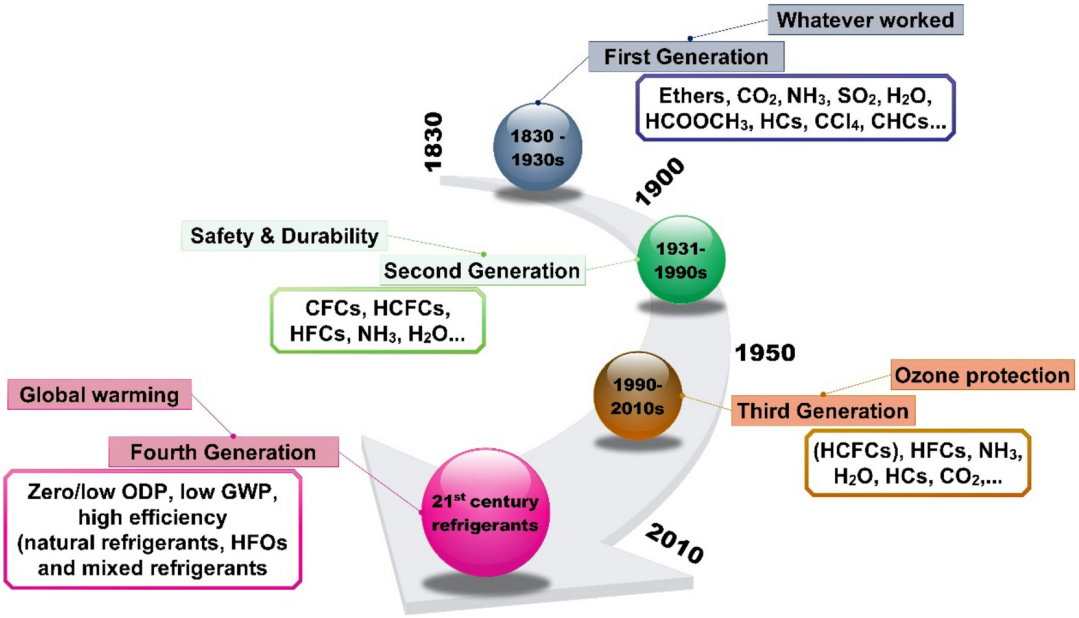

FIGURE 1.2: Progression in the refrigerants over time [7]

- Montreal Protocols: Adopted on 16 September 1987, the landmark multilateral environmental agreement that regulates the production and consumption of nearly 100 man-made chemicals referred to as ozone depleting substances (ODS).
- Kyoto Protocol: Adopted on 11 December 1997, committing industrialized countries and economies in transition to limit and reduce greenhouse gases (GHG) emissions in accordance with agreed individual targets.
- Kigali amendments: Reached on 15 October 2016, an amendment to the Montreal Protocol, agreed to add hydrofluorocarbons (HFCs) to the list of controlled substances and approved a timeline for their gradual reduction by 80-85 % by the late 2040s.

Concurrently, governmental initiatives aimed at mitigating environmental concerns, such as the depletion of the stratospheric ozone layer (ozone depletion potential, ODP) and global warming (global warming potential, GWP), have played a vital role in steering this trajectory [8].

Historically, chlorofluorocarbons (CFCs) and hydrochlorofluorocarbons (HCFCs) dominated the landscape as primary refrigerants for an extended period. Currently, the market features a diverse array of heat pumps employing various refrigerants. Notable among these are R410A, R134A, R32, R404A, R407C, and R22 [9, 10]. Detailed information on these common refrigerants used in heat pump cycles is provided in Table. 1.1, with emphasis on their ODP and GWP values. It is essential to note that GWP values are referenced to CO_2 and represent a 100-year impact on the environment.

TABLE 1.1: Summary of common refrigerants used in heat pump cycle

Refrigerant	Composition	Chemical formula	T_{crit} (°C)	P_{crit} (MPa)	ODP	GWP
R410A	HFC	CH_2F_2	72.13	4.93	0	2100
R134A	HFC	CH_2FCF_3	101.08	4.06	0	1430
R32	HFC	CH_2F_2	78.35	5.82	0	675
R404A	HFC	$C_2HF_5/CH_2FCF_3/C_2H_3F_3$	72.07	3.73	0	3800
R407C	HFC	$CH_2F_2/CHF_2CF_3/CF_3CH_2F$	86.74	4.62	0	1610
R22	HCFC	$CHClF_2$	96.15	4.99	0.05	1700

Analysis of Table. 1.1 reveals that the commonly used refrigerants in contemporary heat pump cycles predominantly belong to the third or second generation, characterized by negligible ODP. However, it is crucial to address the substantial GWP associated with these refrigerants.

Among them, R410A and R404A exhibit the most significant GWP effects. Despite this, they are extensively employed as medium-low temperature refrigerants in

various applications, including domestic air conditioners, small and medium-sized commercial air conditioners (such as unitary and house-type central air conditioners, multi-connected units), mobile air conditioners, dehumidifiers, refrigerated dryers, marine refrigeration equipment, and industrial refrigeration. These applications have a direct impact on our daily lives and are in high demand.

The environmental implications arising from the use of traditional refrigerants have become a focal point in both the industrial and research sectors. This growing concern underscores the need for sustainable alternatives and environmentally friendly practices in the field of refrigeration.

1.1.2 CO_2 as refrigerant in heat pump cycle

To mitigate the environmental impact of traditional refrigerants in heat pump cycles, there is an urgent demand for environmentally friendly alternatives. In order to respond to this need, after 2010 the fourth generation refrigerants were introduced with the prime motive to focus on low GWP, 0 ODP and short lifetime [7]. The fourth generation refrigerants are often referred to the re-enablement of natural refrigerants, the hydrofluoro-olefins (HFOs) and mixed refrigerants [7, 11]. Table. 1.2 listed the main fourth generation refrigerants used in the heat pump cycle. Among which R600A and R290 are hydrocarbon (HC) refrigerant, they are one of the most climate-friendly and cost-effective refrigerants used in the heat pump cycle, but all hydrocarbon refrigerants are classified as highly flammable.

TABLE 1.2: Summary of main fourth generation refrigerants used in heat pump cycle

Refrigerant	Composition	Chemical formula	T_{crit} (°C)	P_{crit} (MPa)	ODP	GWP
R1234ze	HFO	$C_3F_4H_2$	109.4	3.64	0	< 1
R1234yf	HFO	$C_3H_2F_4$	94.7	3.38	0	< 1
R600A	HC	C_4H_{10}	135	3.65	0	3
R290	HC	C_3H_8	96.7	4.25	0	3.3
R744	Natural	CO_2	30.98	7.38	0	1
R717	Natural	Ammonia	132.4	11.42	0	0
R718	Natural	Water	374.15	22.1	0	0

Table. 1.2 illustrates that fourth-generation refrigerants exhibit significantly lower GWP values compared to second and third-generation options, especially R1234ze and R1234yf, with a GWP lower than 1.

In recent years, there has been a resurgence of interest in natural refrigerants, such as ammonia, water, and carbon dioxide, driven by environmental concerns. Ideally, a refrigerant should possess attributes like low GWP, non-toxicity, non-flammability, and zero ODP. While ammonia and water both have a GWP and ODP of 0,

ammonia raises toxicity concerns, and water exhibits thermophysical disadvantages in heat pump cycles.

As a natural fluid, CO_2 emerges as a promising alternative to traditional refrigerants. It offers the advantage of minimal impact on climate change, with zero ODP and a GWP of 1. Additionally, it is non-toxic, non-flammable, and non-corrosive [12].

Thermodynamic properties of CO_2

Despite the environmental advantages of using CO_2 as a refrigerant in the heat pump cycle, its exceptional thermodynamic performance have also contributed to the widespread use.

Fig. 1.3 illustrates the phase distribution of CO_2. It is evident that within the traditional temperature range for cooling (-25 to 5 °C) or heating (usually above 20 °C) applications, the corresponding pressures for the vapor and liquid states are high.

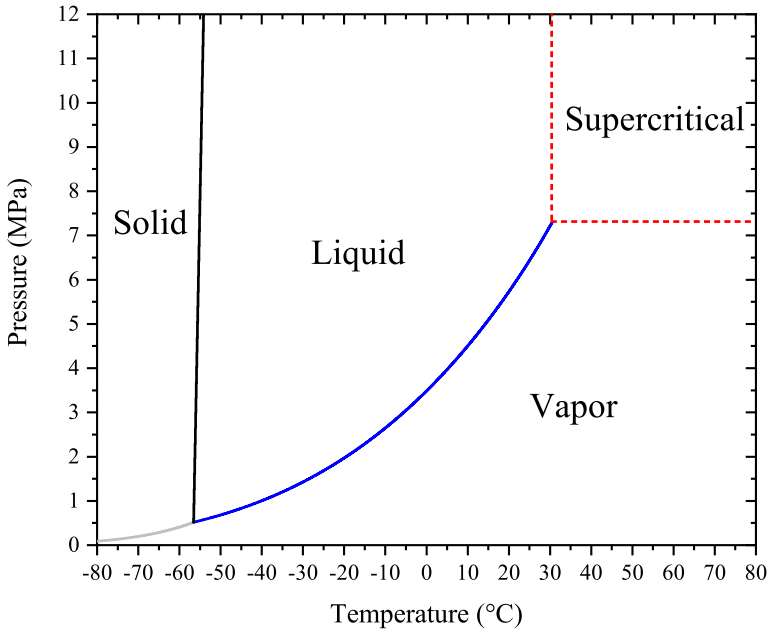

FIGURE 1.3: Phase diagram of CO_2

Fig. 1.4 presents the thermodynamic properties of CO_2 as a function of temperature at different pressures. Among which Fig. 1.4a shows the specific heat capacity distribution in the temperature range between -30 and 120 °C, within the pressure range between 3 to 13 MPa. The specific heat capacity indicates the ability of an object to absorb or dissipate heat. At each pressure level, the peak value occurs at the phase change point (liquid and vapor). When comparing the specific heat capacity at the same temperature but different pressures, it is observed that, for the vapor state,

higher pressure generally results in higher specific heat capacity values. Fig. 1.4b, Fig. 1.4c and Fig. 1.4d shows the distribution of the density, viscosity and thermodynamic conductivity of CO_2. All these properties have the similar distribution. For lower temperature and higher pressure, the value is higher.

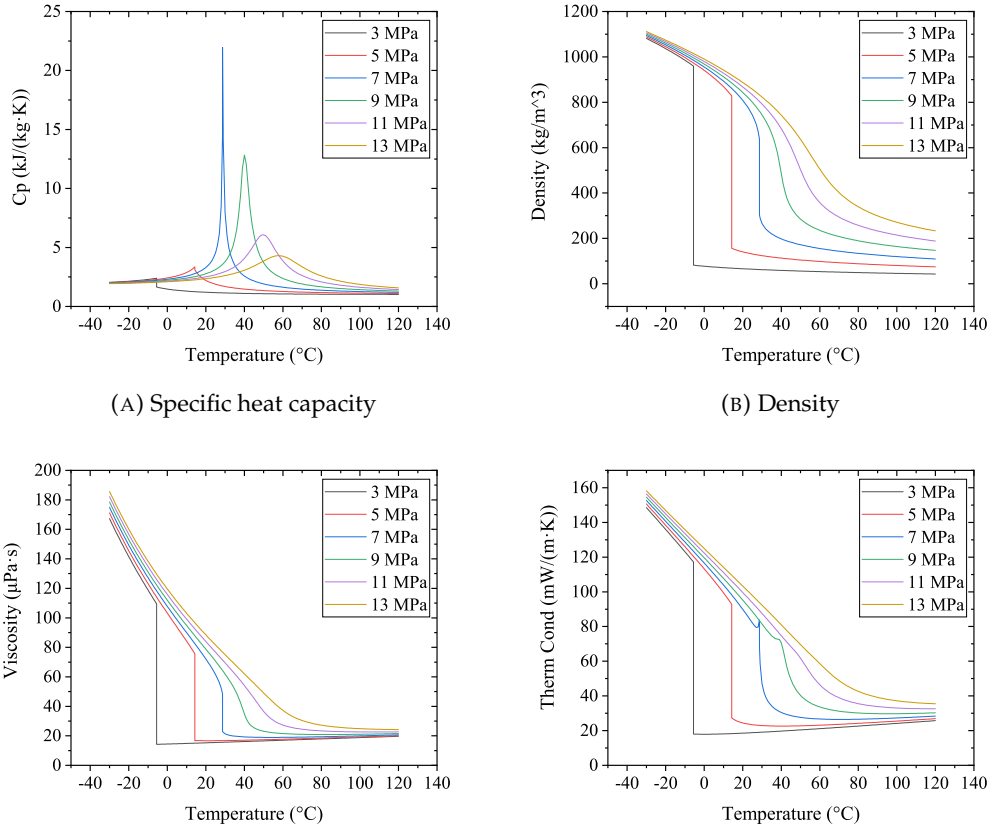

(A) Specific heat capacity

(B) Density

(C) Viscosity

(D) Thermodynamic conductivity

FIGURE 1.4: Thermodynamic properties of CO_2 as a function of temperature at different pressures

To make a comparison between CO_2 and other refrigerants, Table. 1.3 to Table. 1.5 present the thermodynamic properties of major environmentally friendly refrigerants at the temperature of -20 °C, 0 °C and 20 °C. At the temperature of -20 °C, the saturated pressure of R1234ze and R600A is below the atmosphere pressure, while R1234yf is just above. In this case, when using these refrigerants in the heat pump cycle for heating or refrigeration application, there will be a challenging problem of maintaining a vacuum for the system. However, in the higher temperature case, for example at 20 °C, the saturated pressure of CO_2 is around 5.7 MPa, which is a relative high pressure and may bring higher requirements for the pressure resistance of pipelines.

Table. 1.3 to Table. 1.5 also present the other thermodynamic parameters such as density, specific heat capacity, thermal conductivity and viscosity. With higher specific heat capacity and thermal conductivity, the refrigerant has better heat transfer

performance. With lower viscosity, the refrigerant has better transportation property. Comparing all the listed refrigerants, for the saturated liquid state, CO_2 has the best thermal conductivity at 0 °C and 20 °C, the best specific heat capacity at 0 °C and 20 °C. For saturated vapor state, CO_2 has the best specific heat capacity at 0 °C and 20 °C, and best thermal conductivity for all the temperature range. At the same time, the viscosity of CO_2 is better for saturated liquid state at -20 °C and 20 °C.

As to the latent heat of all the refrigerants, even compared to R600A and R290, the latent heat at all the temperature range is lower. However, consider the difference of density, for the volume limited heat exchanger, the latent heat per unit volume of CO_2 is still general higher than other refrigerants at both saturated liquid and saturated vapor state. This advantage has practical implications: in systems with the same geometric size, the refrigeration or heating capacity is significantly higher for CO_2 compared to other environmentally friendly refrigerants. Conversely, for the same capacity, the required volumetric size of CO_2 is much lower. Owing to this characteristic and the environment-friendly as well as the inflammable property, CO_2 is particularly suitable for heating and cooling heat pump systems with space limitations. An example application is the refrigeration and heating system designed for electric vehicles [13].

TABLE 1.3: Summary of thermodynamic properties of main refrigerants at the temperature of -20 °C

Refrigerant	Pressure	Saturated liquid				Saturated vapor				Latent heat
	MPa	Density kg/m^3	Cp kJ/(kg · K)	Therm Cond mW/(m· K)	Viscosity μPa· s	Density kg/m^3	Cp kJ/(kg · K)	Therm Cond mW/(m· K)	Viscosity μPa· s	KJ/kg
R1234ze	0.097	1296.40	1.28	90.57	347.64	5.47	0.83	10.04	10.39	196.21
R1234yf	0.151	1236.30	1.22	78.22	268.94	8.71	0.85	10.02	9.34	175.18
R600A	0.072	602.88	2.18	106.65	251.90	2.07	1.50	12.45	6.38	372.31
R290	0.245	554.45	2.36	116.62	154.73	5.50	1.58	13.63	6.89	400.77
R744	1.970	1031.70	2.17	134.64	139.33	51.70	1.29	15.09	13.12	282.44

TABLE 1.4: Summary of thermodynamic properties of main refrigerants at the temperature of 0 °C

Refrigerant	Pressure	Saturated liquid				Saturated vapor				Latent heat
	MPa	Density kg/m^3	Cp kJ/(kg · K)	Therm Cond mW/(m· K)	Viscosity μPa· s	Density kg/m^3	Cp kJ/(kg · K)	Therm Cond mW/(m· K)	Viscosity μPa· s	KJ/kg
R1234ze	0.217	1240.10	1.32	83.06	268.95	11.71	0.88	11.58	11.20	184.18
R1234yf	0.316	1176.30	1.29	71.47	208.33	17.67	0.93	11.63	10.07	163.29
R600A	0.157	580.58	2.28	98.63	198.56	4.26	1.62	14.30	6.86	354.34
R290	0.474	528.59	2.49	105.97	125.59	10.35	1.74	15.74	7.45	374.87
R744	3.485	1031.70	2.54	134.64	139.33	97.67	1.86	19.67	14.79	230.89

TABLE 1.5: Summary of thermodynamic properties of main refrigerants at the temperature of 20 °C

Refrigerant	Pressure MPa	Saturated liquid				Saturated vapor				Latent heat KJ/kg
		Density kg/m^3	Cp kJ/(kg · K)	Therm Cond mW/(m· K)	Viscosity μPa· s	Density kg/m^3	Cp kJ/(kg · K)	Therm Cond mW/(m· K)	Viscosity μPa· s	
R1234ze	0.427	1179.30	1.37	75.93	211.49	22.61	0.95	13.17	12.02	170.63
R1234yf	0.592	1109.90	1.37	65.08	163.73	32.80	1.02	13.39	10.87	149.29
R600A	0.302	556.86	2.40	91.07	159.34	7.91	1.76	16.29	7.37	334.33
R290	0.836	500.06	2.67	96.07	102.29	18.08	1.95	18.24	8.09	344.31
R744	5.729	773.39	4.26	85.68	66.15	194.20	4.56	33.94	18.19	152.00

1.2 Transcritical heat pump cycle using CO_2 as refrigerant

As a natural fluid, refrigerant R744 (CO_2) stands out as an excellent alternative to HFCs, owing to its ODP and minimal GWP, and favorable fluidity under low temperatures. However, the critical temperature of CO_2 is 30.98 °C. This implies that sub-critical operation, as known from common refrigeration technology, is only possible when the average heat sink temperature is rather low. On the other hand, when CO_2 is used in a conventional sub-critical cycle, the efficiencies are extremely low and are not cost effective [14].

At higher average heat sink temperatures and for better cycle efficiency, transcritical operation is necessary. Transcritical CO_2 technology, operating as a highly efficient thermodynamic cycle with a pure natural fluid and utilizing aerothermal energy, offers substantial advantages in terms of energy consumption, equivalent carbon content, and environmental benefits. It emerges as a crucial technological solution for global carbon neutrality and the transformation of the renewable energy structure. Notably, CO_2 has been introduced into high-temperature heating applications with requirements ranging from 80 to 120 °C, demonstrating enhanced cooling and heating performances with the transcritical operating mode [14].

A typical transcritical heat pump cycle using CO_2 as a refrigerant, along with the corresponding *P-h* diagram, is illustrated in Fig. 1.5. The cycle involves compressing the saturated or superheated CO_2 from the evaporator into a high-pressure and high-temperature supercritical state in the compressor. Subsequently, it moves to the heat sink (gas cooler) for heat rejection. After this step, the high-pressure and low-temperature CO_2, still in a supercritical state, passes through the expansion valve, transitioning into a two-phase flow. The low-pressure and low-temperature CO_2 then travels through the heat source, evaporating in the evaporator, completing the loop.

In contrast to conventional heat pump cycles where both high-pressure heat rejection and low-pressure heat absorption processes occur in the subcritical region, the transcritical CO_2 cycle encompasses both supercritical heat rejection and subcritical heat absorption processes. When the CO_2 vapor is compressed beyond the critical pressure, it can deliver higher heat rejection enthalpy through sensible cooling.

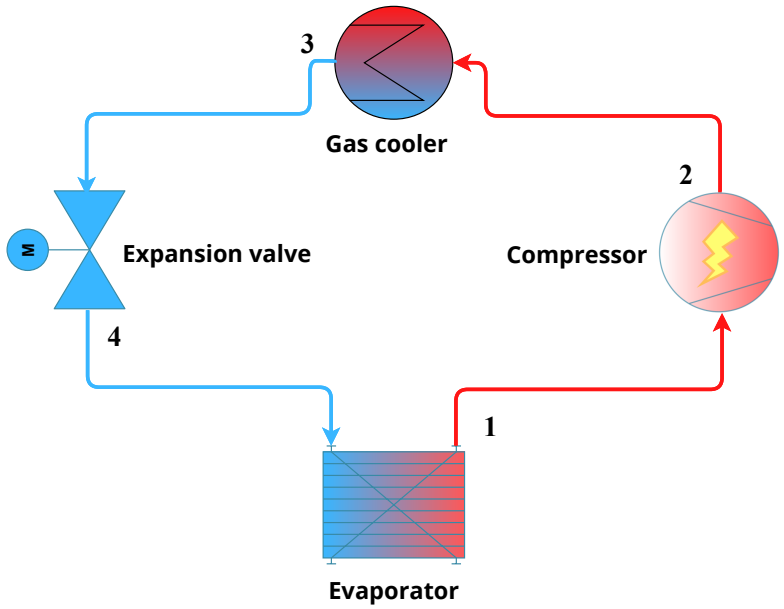

(A) Schematic of transcritical heat pump cycle

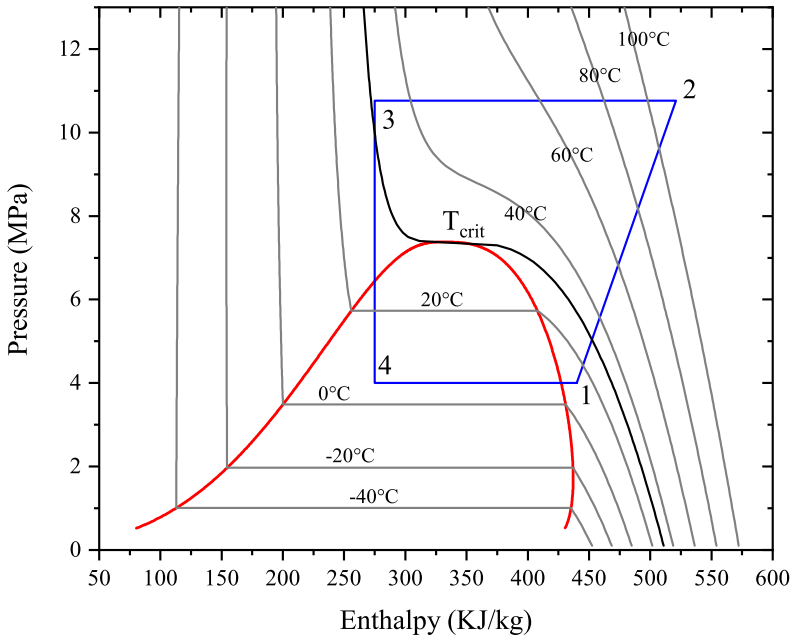

(B) *P-h* diagram

FIGURE 1.5: Schematic and *P-h* diagram of transcritical CO_2 heat pump cycle

On the other hand, in traditional subcritical cycle, the enthalpy value of condenser outlet is just the function of temperature (or pressure), without the case of subcooling. That is to say, as long as evaporation temperature and condensing temperature are determined, the performance of this cycle can be basically defined. However, in supercritical region of CO_2 transcritical cycle, temperature and pressure are two independent variables. When the outlet temperature of gas cooler is constant, the high pressure of the system also affects fluid enthalpy. Therefore, when the outlet temperature of the gas cooler is fixed, the cycle can be optimized based on the heat rejection pressure [15].

Numerous studies have delved into the transcritical heat pump cycle utilizing CO_2 as a refrigerant. Among which, few scholars conducted a general review on the advanced transcritical CO_2 heat pump system [4, 14, 16–19].

Concluded from the reviews, the research into the performance and benefits of a transcritical heat pump cycle using carbon dioxide began in the early 1990s [19]. The operating pressure of the transcritical CO_2 heat pump is so high that the security cannot be guaranteed in the early devices. Thus, the transcritical CO_2 heat pump are not promoted extensively until the sharp deterioration of environmental issues occurred around the world [14]. Followed by Japan, which is one of the first countries where the policies are pushed to promote the employment of transcritical CO_2 heat pump. Europe, USA and China pushed similar policies and standards to cater the introduction of transcritical CO_2 heat pump as a new and promising technology on traditional application fields [17].

Nowadays, plenty theoretical and experimental research, as well as commercial system development, has improved transcritical system performance to a level similar to that of conventional heat pump systems [4]. The transcritical CO_2 heat pumps have found worldwide applied because of the environmental friendliness and other thermodynamic advantages, however, the inefficiency of the CO_2 cycle has been the most issue blocking its popularization [16–18].

1.3 Performance enhancement of transcrtical CO_2 heat pump cycle

The heat pump cycle utilizing CO_2 as the refrigerant demonstrates clear advantages in terms of environmental considerations and efficiency improvements when compared to other fuel combustion and electric systems in the heating, ventilation, air conditioning, and refrigeration field. However, in the traditional CO_2 heat pump cycle employing a throttling valve as an expansion device, a significant amount of irreversibilities occurs during the expansion process, leading to a decrease in cycle COP. These irreversibilities become even more pronounced in the transcritical CO_2 cycle, given the higher pressure ratio during expansion compared to other fluids such as R134a, R245fa, or R1233zd. Currently, an emerging research topic focuses on

enhancing the performance of refrigeration and heat pump systems through cycle modifications.

The improvement of overall cycle performance in a transcrtical CO_2 heat pump cycle generally requires consideration of the system as a whole. The interactions between the components do not always allow for isolated improvements to a single component. Still, each component or process in the cycle plays a role in dictating the overall performance of the system [4].

1.3.1 Internal heat exchanger modifications

An internal heat exchanger (IHX) is a heat exchanger introduced to utilise the heat available from the outlet of the CO_2 gas cooler to superheat the gas in the compressor suction line. A typical transcrtical CO_2 heat pump cycle with internal heat exhcnager along with the corresponding *P-h* diagram, is illustrated in Fig. 1.6. Compared to the basic transcritical cycle, the IHX enhances subcooling at the entrance of the expansion device, reducing the amount of flash gas production. Simultaneously, the IHX increases superheating at the compressor inlet, thereby decreasing the compressor's work consumption.

The installation of an IHX is normally aimed to increase the system cooling capacity and improve the COP. The IHX typically increases the system efficiency. However, the benefit of installing an IHX to improve the system performance is affected by the system operating conditions.

The ambient temperature of the working system has an great influence on the benefit of the internal heat exchanger. Rigola et al. [20] present the influence of using an internal heat exchanger (IHX) in order to improve the cycle performance under real working conditions by both numerical and experimental comparative study. It was found that for ambient temperature of 35 °C, the COP increase adding IHX is around 20 % on both numerical results and experimental data.

The disacharge pressure is another parameter which influence the performance of the internal heat exchanger. Cao et al. [21] experimentally investigated a transcritical CO_2 heat pump water heater prototype with IHX. The results showed that the optimal discharge pressure reduced with the application of IHX, and this reduction could be amplified by the decrease of the ambient temperature, the increase of the water inlet temperature and the increase of the water outlet temperature. From the energy point of view, under the optimal discharge pressure, the coefficient of performance (COP) increased by up to 6.65 % and the total power consumption decreased by up to 6.22 % via using IHX.

The trend was validated by more research. Qin et al. [22] investigated the effect of internal heat exchanger based on a novel evaluation method in the transcritical CO_2 heat pump system. The results show that the internal heat exchanger greatly reduces the exergy efficiency under the discharge pressure of 7.31 MPa and the ambient temperature of 15 °C, and the difference value between the system with and

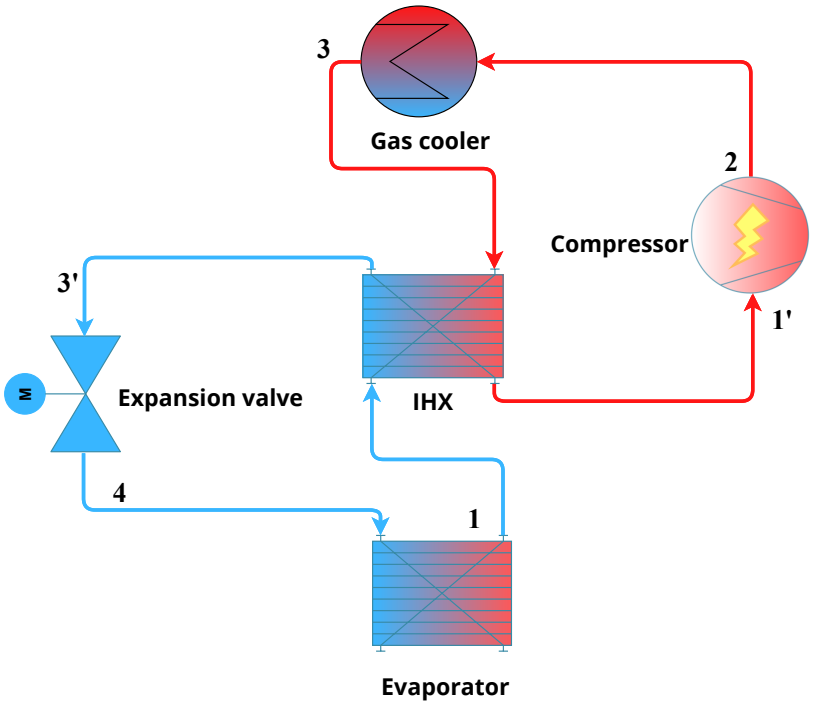

(A) Schematic of transcritical heat pump cycle with internal heat exchanger

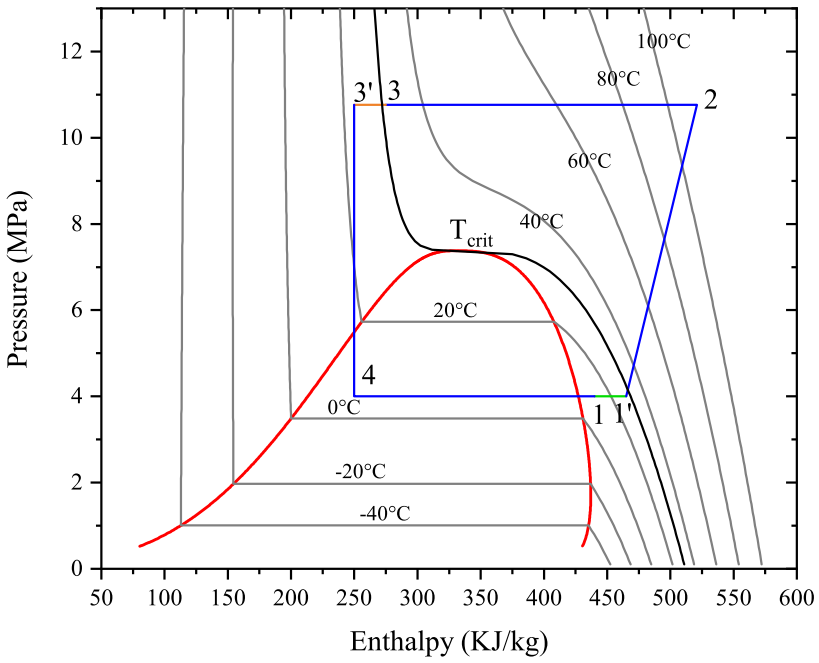

(B) *P-h* diagram

FIGURE 1.6: Schematic and *P-h* diagram of transcritical CO_2 heat pump cycle with internal heat exchanger

without internal heat exchanger reaches 39 %. However, the influence of the internal heat exchanger on exergy efficiency decreases with the increase of discharge pressure and ambient temperature, the minimum difference value is only 0.1 % at 11 MPa and 30 °C.

1.3.2 Compression process modifications

Efficiency of a transcritical CO_2 heat pump cycle can be improved by various modifications of the compression process. The most basic compressor modification is two-stage compression. By separating compression into two stages, each compressor will have a lower pressure ratio which in turn improves the isentropic efficiency. Further improvements in cycle efficiency can be obtained by cooling the refrigerant between the compression stages.

Cecchinato et al. [23] conducted thermodynamic evaluation and optimisation of different two stage transcritical carbon dioxide cycles. Five different two stage cycles (shown in Fig. 1.7) are studied:

- Basic single stage cycle: : the basic cycle with a single-throttling valve and a single compressor
- Single-Throttling, Double-Compression (STDC): the cycle with a single-throttling valve and two-stage compression with inter-cooling of the vapour at the intermediate pressure
- Double-Throttling, Double-Compression, Split Cycle (DTDC_SC): The high pressure fluid after the gas cooler is split into two streams; one of them is throttled down to the intermediate pressure and is used to cool the residual stream of high pressure gas, before the throttling valve that feeds the evaporator
- Double-Throttling, Double-Compression, Open Flash Tank (DTDC_OFT): the high pressure gas after the gas cooler is throttled down to the intermediate pressure and enters a vessel from which the vapour is sucked by the high pressure compressor; the stream of the vapour produced by flashing is used to cool the high pressure gas exiting from the gas cooler. The liquid collected inside the open flash tank is throttled down to the evaporation pressure
- Double-Throttling, Auxiliary Compressor Cycle (DTAC): after the gas cooler, the gas undergoes a further cooling process, provided by an auxiliary circuit, using an Internal Secondary Heat exchanger (ISHX). The gas is then throttled down to the evaporation pressure

Each basic cycle is analysed for the effect of internal heat transfer between different streams of refrigerants. In the case of two-stage compression, intermediate cooling between the compressor stages is present. Each cycle is optimised with regards to energy performance, calculating the optimal values of both the upper and the intermediate pressures.

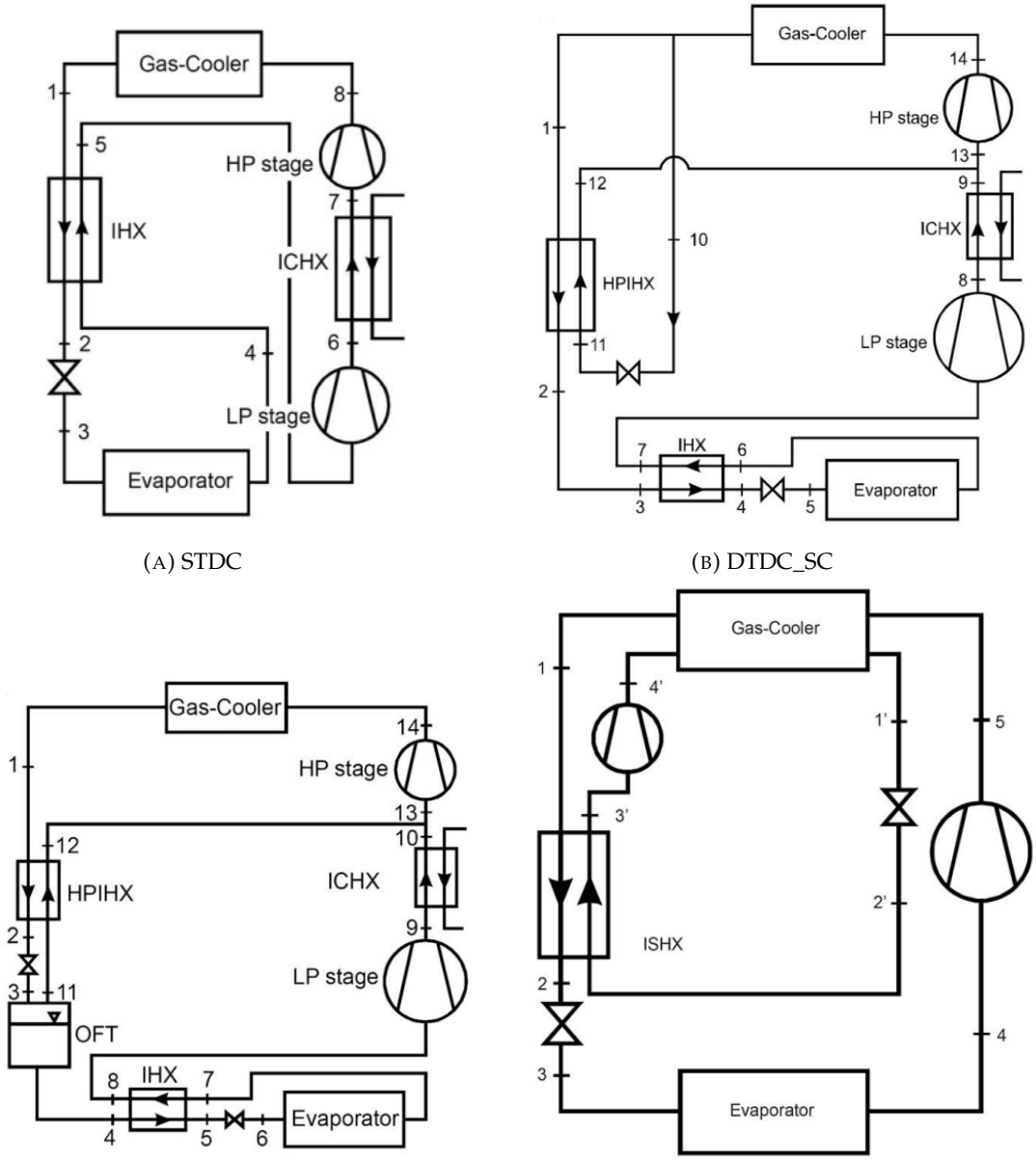

(A) STDC

(B) DTDC_SC

(C) DTDC_OFT

(D) DTAC

FIGURE 1.7: Schematic of two stages transcritical carbon dioxide cycles [23]

The analysis has shown that, unlike traditional cycle, staged compression with inter-cooling carried out with an external fluid for the heat rejection plays a major role in improving energy efficiency. Since this heat rejection depends heavily on the value of the intermediate pressure, the optimal value of this parameter is a crucial choice; for the same reason, an effective heat exchanger between the suction line and the line before the throttling valve often allows a significant benefit in energy efficiency.

The most elaborate cycles (DTDC_SC and DTDC_OFT) present the greatest improvement, especially for the heaviest operating conditions (the lowest evaporating temperature and the highest external temperature); for -30/+35 °C (evaporation temperature/external temperature) both cycles behave similarly and give rise to 70 % increase in energy efficiency against the simplest solution (Single-Throttling, Single-Compression). Being the double-compression mandatory for limiting the temperature at the compressor outlet in such conditions, the only alternative is Single-Throttling, Double-Compression (roughly 50 % increase in energy efficiency). The final choice therefore results from the best trade-off between increased installation costs and decreased operating costs, taking into account also the reliability and the safety characteristics of the system.

For less severe operating conditions, probably a cheaper system design can be preferable; for example at +4/+30 °C operations, the best cycles (again DTDC_OFT and DTDC_SC) improve energy efficiency by 16 % against the cheapest solution (single throtting, single compression), while the system with an auxiliary compressor (DTAC) is quoted for 12 % improvement. Since the last system is rather simple, reliable and cost effective, this solution is worth considering.

As follows from the results of the present analysis, it is not always easy to choose the best system for a definite application and this problem is often complicated by the need of finding the optimal values for one or two independent operating variables.

Cho et al. [24] experimentally investigated the performance and operating characteristics of a two-stage CO_2 cycle with gas injection, as shown in Fig. 1.8. The discharged refrigerant from the first-stage compressor flows into the mixing box, and mixes with the cold vapor refrigerant from the flash tank, and then the cooled refrigerant from the mixing box enters the second stage compressor. However, when the pressure at the exit of the first-stage compressor is higher than that at the flash tank, it is not possible to inject the gas refrigerant into the mixing box, resulting in reverse flow from the mixing box to the flash tank. Therefore, a check valve was installed between the mixing box and the flash tank to prevent the reverse flow. The pressure at the flash tank was controlled by adjusting the electrical expansion valve (EEV) openings. Based on the measured data, the cooling COP of the two-stage gas injection cycle was maximally enhanced by 16.5 % over that of the two stages non-injection cycle in the experiments. In addition, the discharge temperature of the second-stage compressor in the two-stage gas injection cycle decreased by 5 °C to 7

°C from that in the two-stage non-injection cycle due to inter cooling effects.

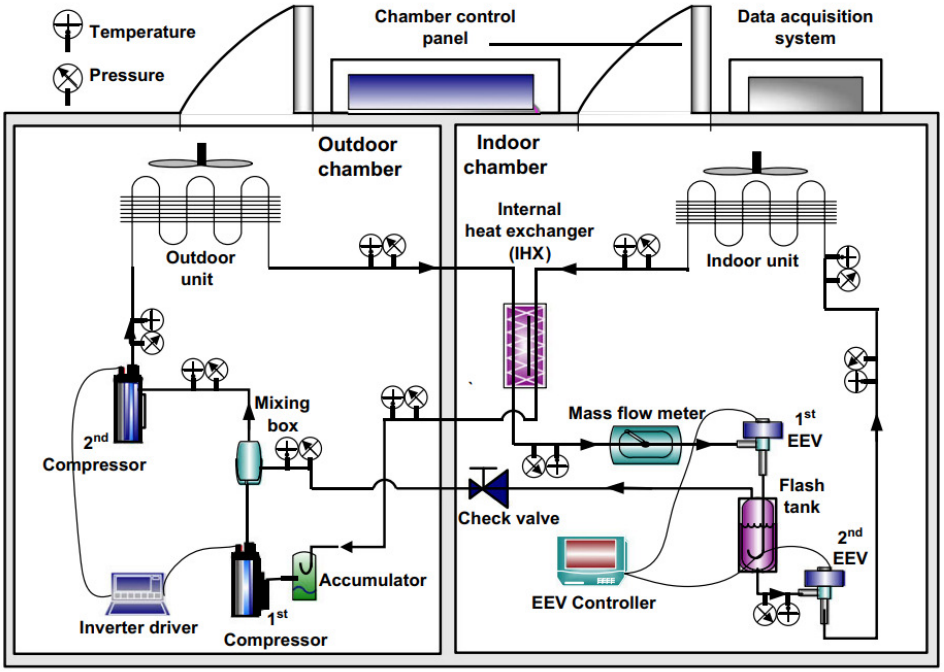

FIGURE 1.8: Schematic of two-stage CO_2 cycle with gas injection [24]

1.3.3 Expansion process modifications

In the traditional transcritical CO_2 heat pump cycle, the expansion device serves two primary functions: maintaining the pressure difference between the gas cooler and the evaporator and ensuring proper flow distribution to the evaporator. Achieving optimum system performance relies on maintaining the ideal pressure in the gas cooler, underscoring the pivotal role of the expansion device in efficient system operation [25]. However, due to the large pressure difference between high and low pressures of CO_2 cycle, the recovery of expansion work has always been one of the most problems for a long time. According to the current researches, the most promising ways to achieve the industrialization of expansion work recovery included the following four methods: vortex tube, capillary tube, expander and ejector [4, 14].

The vortex tube technology

Vortex tube was a throttling device to recover the pressure energy of high-pressure fluid. The schematic diagram of vortex is illustrated in Fig. 1.10. It can convert high-pressure fluid into two low-pressure fluids by utilizing the complicated heat and mass transfer between the internal bidirectional vortexes, one of which was a stream with high-temperature (high enthalpy) and the other was that with low-temperature (low enthalpy), and those two streams flowed out from the two outlets, respectively [26]. It should be noted that, if the fluid state at the cold outlet happened to be in the

two-phase region, the saturated vapor and saturated liquid would flow out from the near wall region and the central region respectively under the centrifugal action of high-speed vortex.

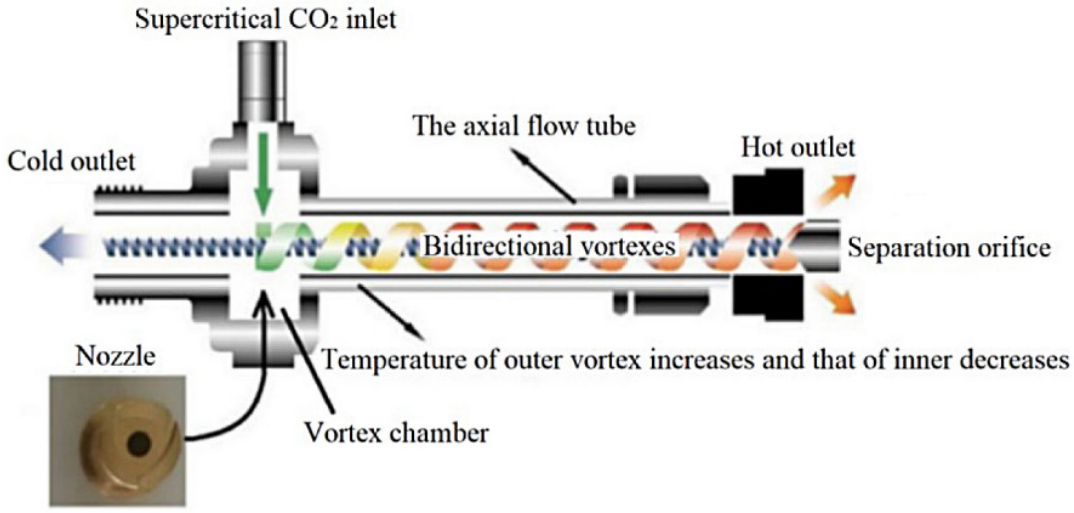

FIGURE 1.9: The schematic diagram of the standard CO_2 vortex tube [14]

The vortex tube technology has been developed in the field of compressed air throttling and has been introduced into the vapor compression cooling cycles with conventional refrigerants for years. According to study, the employment of vortex tube in the CO_2 cycle always performed better among different fluid types, due to not only the large pressure difference potential but also its high molecular weight and low specific heat ratio. Relevant theoretical research results indicated that the system COP of the transcritical CO_2 cycle can be improved by about 10 % for refrigeration and 5.8 % to 13.9 % for heat pump in varying conditions under the premise of proper vortex tube design. The gas-cooler outlet temperature has a great impact on the system performance, there is a higher COP improvement when the cycle at lower evaporation temperature or higher gas-cooler outlet temperature [14, 27].

Luo et al. [28] proposed a general parameter matching method for transcritical CO_2 cycles with vortex tube by using the self-defined functional blocks that can easily and quickly realize the parameter matching of components in refrigeration cycles with diverse architectures. Based on this new method, simulation and optimization of existing transcritical CO_2 systems with or without vortex tube are implemented. A two-stage compression transcritical CO_2 system with serial vortex tubes is proposed and proven to have a high cooling performance and less exergy loss in comparison with existing transcritical CO_2 systems.

Aghagoli et al. [29] conducted thermodynamics analysis of a novel transcritical CO_2 vortex tube heat pump cycle. The results show that by partially replacing the

vortex tube, the coefficient of the performance is improved by 8 % and with increasing the gas cooler pressure, COP decreases for the vortex tube heat pump system. In addition, employing vortex tube produces greater gas cooler and evaporator heat load than conventional heat pump cycle. Similar thermodynamic analysis was also conducted by Mansour et al. [30]. It was found that the heating coefficient of performance of the vortex tube heat pump is improved by a maximum of 43.7 % when compared to that of the conventional heat pump.

Although the feasibility of using vortex tube in the transcritical CO_2 cycle has been widely accepted, considering that the idea has not been put forward for a long time, there was still no relevant detailed experimental verification can be found, and the actual effect of the CO_2 vortex tube sample was also unknown, which needed to be further studied [14].

The capillary tube technology

The capillary tube stands out as the most preferred expansion device in small vapor compression refrigerating and air conditioning systems due to its simplicity, low initial cost, and the ability to minimize the starting torque of the compressor. The commonly favored configuration involves a non-adiabatic capillary tube, as illustrated in Fig. 1.10, where the capillary tube is soldered to the outer surface of the suction line, forming a counter-flow heat exchanger known as a capillary tube-suction line heat exchanger between the evaporator outlet and the compressor inlet. This provides superheated vapor to the compressor.

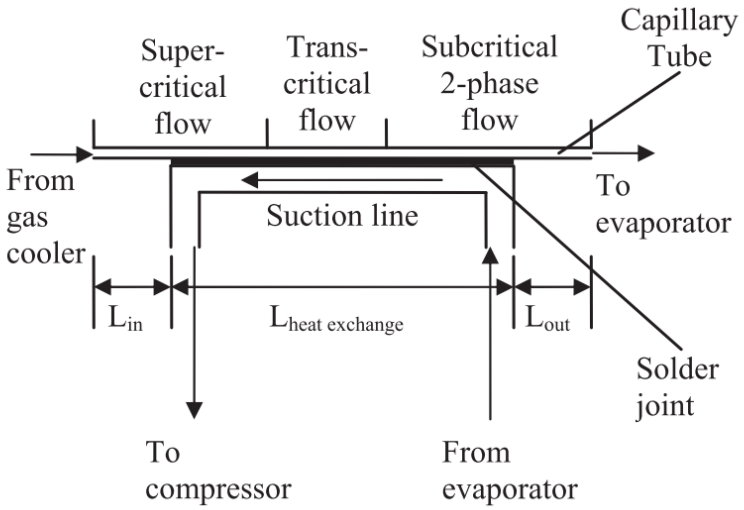

FIGURE 1.10: Section of a non-adiabatic capillary tube heat exchanger [31]

Small refrigeration and heat pump units using conventional refrigerants commonly incorporate capillary tubes for expansion control, but there has been uncertainty about the effectiveness of capillary tubes in transcritical CO_2 systems. In order to ensure that a capillary tube can maintain the optimum gas cooler pressure

and achieve optimal overall system performance theoretical studies have been conducted [4].

In a transcritical CO_2 heat pump cycle, the capillary tube is typically positioned between the gas cooler and evaporator, traversing three distinct regions: supercritical, transcritical, and subcritical two-phase. The optimal location of thermal contact between the capillary tube and the suction line plays a crucial role in ensuring optimum system performance. Non-adiabatic capillary tubes contribute to enhancing system performance by increasing refrigeration capacity and preventing liquid entry into the compressor through the superheating of suction vapor.

Madsen et al. [32] carried out the first theoretical and experimental studies to investigate the effects of using adiabatic capillary tube as an expansion device in a transcritical CO_2 refrigeration system. Various configurations of capillary tubes having length of 0.5 to 4 m and diameter of 1 to 2 mm were tested and employing a static model, it was indicated that the COP of a system with capillary tubes generally is better than that using fixed high pressure but is not as good when variable optimal high pressure is used. Capillary tubes are especially interesting in applications where the evaporation pressure is constant and the temperature out of the gas cooler varies no more than ± 10 K from the design condition. The reduction in COP is more significant at low temperatures out of the gas cooler.

Agrawal and Bhattacharyya [33] developed a steady state simulation model to evaluate the performance of a capillary tube based transcritical CO_2 heat pump system for simultaneous heating and cooling at 73 °C and 4 °C, respectively against optimized expansion valve systems. Capillary tubes of various configurations having diameters of 1.4, 1.5 and 1.6 mm along with internal surface roughness of 1–3 μm have been tested to obtain the optimum design and operating conditions. It is observed that the capillary tube system is quite flexible in response to changes in ambient temperature, almost behaving to offer an optimal pressure control. System performance is marginally better with a capillary tube at higher gas cooler exit temperature. Capillary tube length turns out to be the critical parameter that influences system optimum conditions.

Song et al. [34] experimentally investigated a transcritical CO_2 heat pump system using a capillary tube as an expansion device. The comparison with the transcritical CO_2 heat pump using an electronic expansion valve at different gas cooler outlet temperatures showed that the transcritical CO_2 heat pump using the capillary tube is promising and could achieve performance close to the heat pump using electronic expansion valve. Over the entire experimental gas-cooler outlet temperature range, the capillary tube based heat pump achieved a COP higher than 80 % of the COP of the system using electronic expansion valve. At the gas-cooler outlet temperature above 42 °C , the capillary tube based transcritical heat pump has almost the same performance as the expansion valve cycle. Experimental study was also conducted under different outdoor and indoor temperatures. The results showed that the system cooling capacity and coefficient of performance (COP) dropped by 22 % and 24

%, respectively as the outdoor air temperature increased from 30 to 40 °C and increased by 12 % and 15 %, respectively as the indoor air temperature increased from 22 to 32 °C.

The expander technology

Using an expansion valve, vortex tube or capillary tube results in energy losses as no useful work is done during the expansion process. While these losses are generally small in heat pumps using conventional refrigerants, they become more significant in transcritical CO_2 cycles due to the greater pressure difference. This increased pressure difference makes work recovery more feasible and beneficial.

The expander can recover the pressure of the high pressure fluid at the expander inlet and convert it into shaft work with a certain isentropic efficiency, replacing part of the compressor power consumption, so as to improve the overall efficiency of the cycle, as shown in Fig. 1.11.

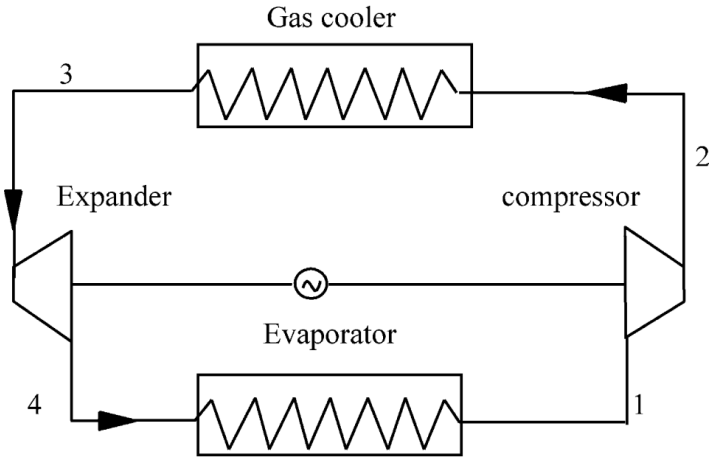

FIGURE 1.11: Schematic of transcritical CO_2 cycle with an expander [35]

Yang et al. [35] conducted a comparative study on transcritical carbon dioxide refrigeration cycles with a throttling valve and with an expander, considering the first and second laws of thermodynamics. The study revealed that in the throttling valve cycle, the largest exergy loss occurs in the throttling valve, accounting for approximately 38 % of the total cycle irreversibility. In the expander cycle, irreversibility mainly stems from the gas cooler (about 38 %) and the compressor (about 35 %). The Coefficient of Performance and exergy efficiency of the expander cycle are, on average, 33 % and 30 % higher than those of the throttling valve cycle, respectively.

Hua et al. [36] designed an expander to recover expansion power in CO_2 transcritical cycle. A test facility is used to test the designed expander. The theoretical analysis and calculation show that 14–23 % of input power of compressor can be recovered. The experimental results show that the recovery ratio and expander efficiency are affected by rotational speed, inlet temperature and mass flow of expander.

The highest recovery ratio can reach up to 0.145, which means 14.5 % of input power of compressor can be recovered. The expander efficiency can reach to 45 %.

There exist numerous devices that can potentially serve as expanders for work recovery in a transcritical CO_2 heat pump cycle. Apart from turbines, various expander types include rotary, reciprocating, scroll, screw, and vane. Each design comes with its own set of advantages and limitations. Both experimental and theoretical research has been conducted on a wide variety of systems, as documented in studies [37–41].

The ejector technology

Due to no moving parts, low cost, simple structure and low maintenance requirements, two-phase ejectors have emerged as a promising cycle modification for expansion recovery for trancrtical CO_2 heat pump cycle in recent years [25, 42].

The application of ejectors as an alternative to classic expansion devices has been considered for several decades.The steam jet refrigeration systems were initially developed in the early 1900s, and the use of ejectors in vapor compression systems for performance improvement gained attention in the next years. Kornhauser [43] first proposed the use of ejectors in the expansion refrigeration cycle, analyzing the thermodynamic performance with R12 as a refrigerant.

Incorporating a two-phase ejector in the heat pump cycle to replace the traditional expansion valve offers a significant advantage by recovering the expansion work typically wasted in throttling processes. This approach proves to be an efficient means of reducing throttling losses or expansion irreversibility in refrigeration/heat pump cycles. A typical schematic of the CO_2 ejector expansion heat pump cycle, along with the corresponding pressure-enthalpy diagram, is depicted in Fig. 1.12. The main components in the cycle include the compressor, gas cooler, ejector, vapor-liquid separator, expansion valve, and evaporator. Auxiliary pipes and valves are not presented in the diagram. In comparison to traditional heat pump cycles, the ejector replaces the expansion valve to recover expansion energy.

As depicted in Fig. 1.12b, the refrigerant at state 1 is compressed into a supercritical fluid (state 2) in the compressor, then cooled down in the gas cooler (state 3). Following expansion in the ejector, the main flow is divided into saturated vapor and saturated liquid in the separator (states 1 and 7). The saturated liquid then passes through the expansion valve (state 8) and enters the evaporator. After evaporation (state 9), the vapor from the evaporator is entrained at the ejector's inlet, completing the cycle.

In the ejector expansion transcritical CO_2 heat pump cycle, the high-pressure motive flow operates in a supercritical state, characterized by pressures and temperatures exceeding the refrigerant's critical point. Conversely, the low-pressure suction flow consists of either saturated or superheated vapor from the evaporator. These two distinct flows are then combined within the ejector, where they mix and exit as a two-phase flow. The mixed flow is subsequently separated in the separator,

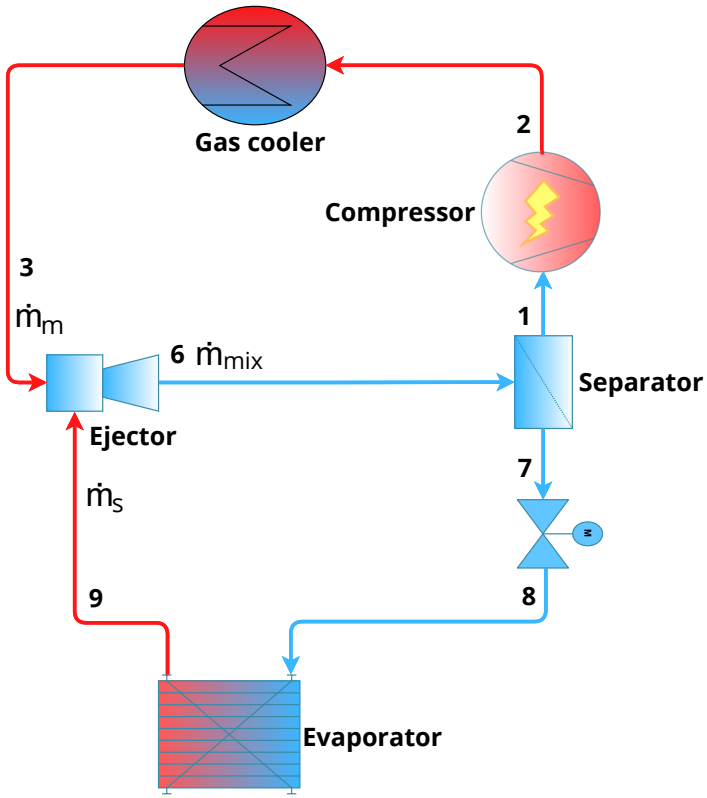

(A) Schematic of traditional ejector expansion heat pump cycle

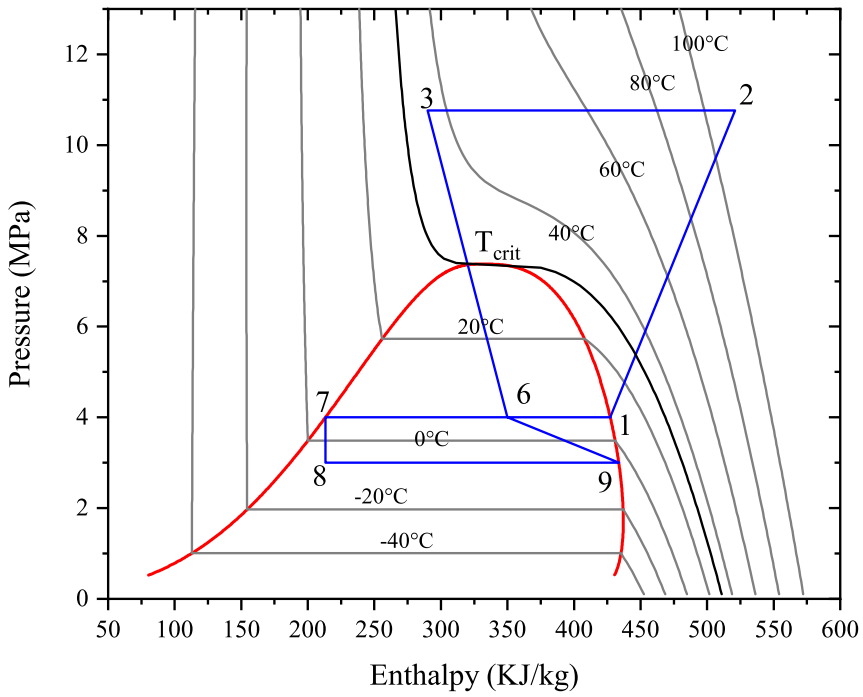

(B) *P-h* diagram

FIGURE 1.12: Schematic and *P-h* diagram of ejector expansion transcritical CO_2 heat pump cycle

with each component directed separately into the compressor and the evaporator, respectively.

Comparing the ejector expansion cycle to the traditional valve expansion heat pump cycle depicted in Fig. 1.5a, both operating at the same evaporation temperature or pressure, reveals key advantages for ejector cycle. In the ejector expansion cycle, the inlet pressure of the compressor (pressure at state 6 and 1) is higher than that in the traditional heat pump cycle (pressure at state 9) when both cycles share identical heat sink temperature and pressure conditions. As a result, the pressure ratio in the compressor is smaller in the ejector expansion cycle, leading to lower power consumption.

The entrainment effect of the high-pressure flow in the motive nozzle of the ejector plays a crucial role in recovering entropy loss in the expansion valve of the traditional heat pump cycle. This pressure recovery contributes to an improved COP for the cycle. Literature studies indicate that the COP improvement for refrigeration applications in the ejector expansion cycle can reach up to 22 % compared to the traditional valve expansion heat pump cycle [42].

Experimental studies conducted by Lee et al. [44] further support these findings, revealing that the coefficient of performance of the system using an ejector was approximately 15 % higher than that of the conventional system.

1.3.4 Conclusion

In the traditional CO_2 heat pump cycle with a throttling valve as the expansion device, significant irreversibilities occur during the expansion process, leading to a decrease in cycle coefficient of performance. This issue becomes more pronounced in transcritical CO_2 cycles, where the pressure ratio of the expansion is higher than that of other fluids.

Several methods have been explored to mitigate expansion losses and reduce irreversibilities in the expansion valve of the traditional transcritical CO_2 heat pump cycle. These methods include vortex tube and capillary tube expansion, replacing the expansion valve with an expander, or utilizing a two-phase ejector. Among these options, the use of a two-phase ejector stands out due to its lack of moving parts, low cost, simple structure, and low maintenance requirements. Recently, it has become a promising cycle modification. The theoretical and experimental evidence supports the improvement of COP for the ejector expansion cycle compared to the traditional valve expansion heat pump cycle.

1.4 Detailed introduction of ejector

The ejector stands out as the most crucial component in the ejector expansion heat pump cycle. Fig. 1.13 offers a detailed view of a typical ejector used in the heat pump cycle, segmented into distinct sections: the motive nozzle, suction nozzle, a

pre-mixing section, a constant-area mixing section, and a diffuser. The ejector's operation involves the blending of two distinct flows, with the two-phase flow typically originating from the throat of the motive nozzle.

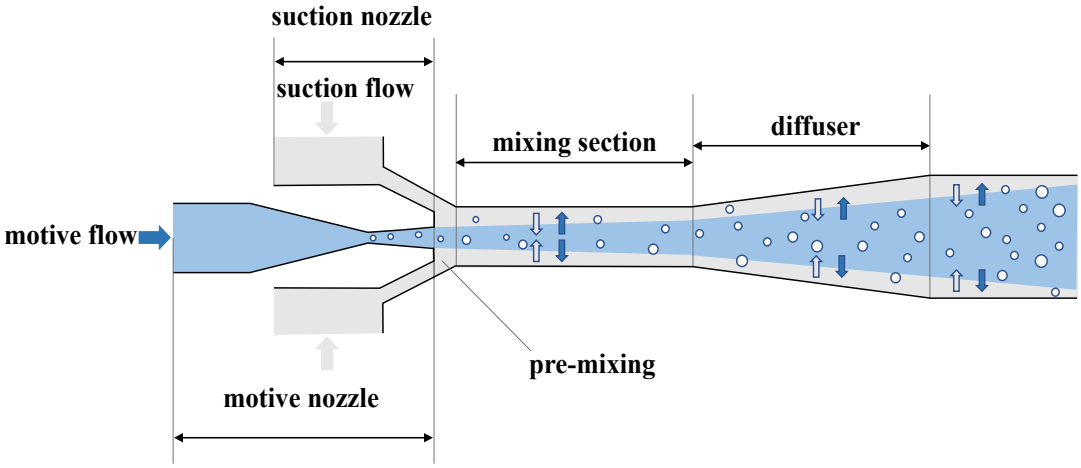

FIGURE 1.13: Structure of a typical ejector

1.4.1 Classification of ejector

In addition to the typical structure of the ejector shown in Fig. 1.13, various ejector configurations exist. Motivated by the design of the motive nozzle, ejectors can be classified into two main groups: those equipped with a convergent-divergent (C-D) type motive nozzle, as depicted in Fig. 1.13 [45–47], and those with a convergent (C) type motive nozzle, shown in Fig. 1.14 [48–50]. In the motive nozzle, the high-pressure flow enters the convergent part, where the section area decreases, causing the velocity to increase. During actual operation of the ejector cycle, the flow typically reaches local sound speed, with Mach number (Ma) equals 1 at the throat section of the nozzle. Subsequently, for C-D type nozzles, the flow continues to accelerate in the divergent part, and the pressure continues to decrease until the exit of the nozzle, reaching a supersonic state. However, for C type nozzles, due to geometric limitations, the exit velocity can only reach local sound speed ($Ma = 1$) or remain in a subsonic state ($Ma < 1$). In most cases, ejectors with C-D type motive nozzles achieve higher exit speeds and lower pressures, benefiting the entrainment effect.

On the other hand, depending on the exit position of the motive nozzle, ejectors can be categorized into two groups: constant area mixing ejectors (CAM) and constant pressure mixing ejectors (CPM), as illustrated in Fig. 1.15. In the former, the exits of the motive nozzle and suction nozzle are positioned exactly at the inlet of the constant-area mixing section, eliminating the need for a separate pre-mixing section. The mixing of the motive and suction flows occurs within the constant-area mixing section. Conversely, in the latter, the exit of the nozzle is located before the inlet of the constant-area mixing section, incorporating a pre-mixing section. Here,

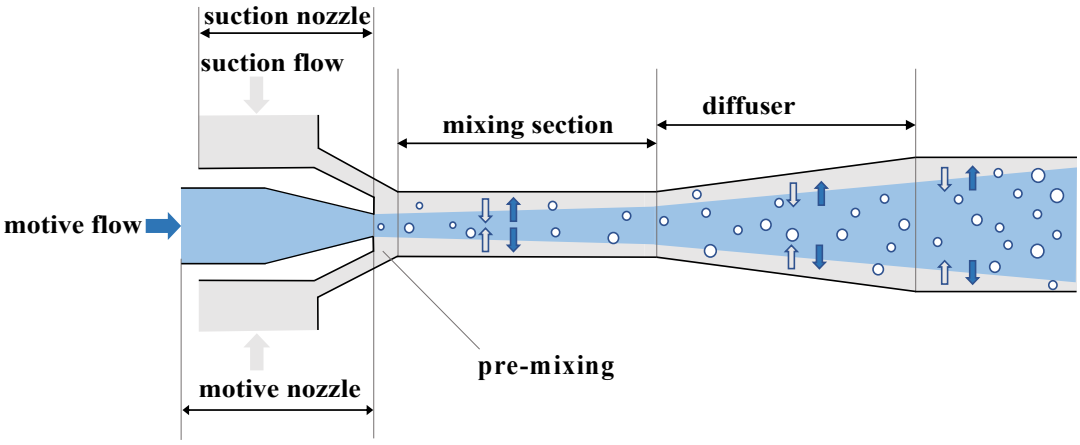

FIGURE 1.14: Ejector with convergent nozzle

the mixing of the motive and suction flows commences. Both types of ejectors are present in current studies and actual ejector expansion cycles.

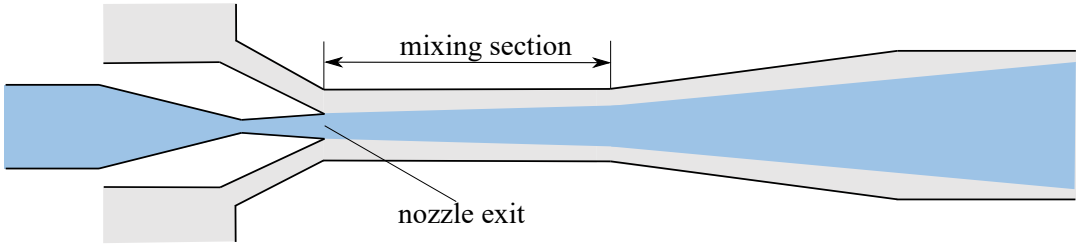

(A) constant-area mixing ejector

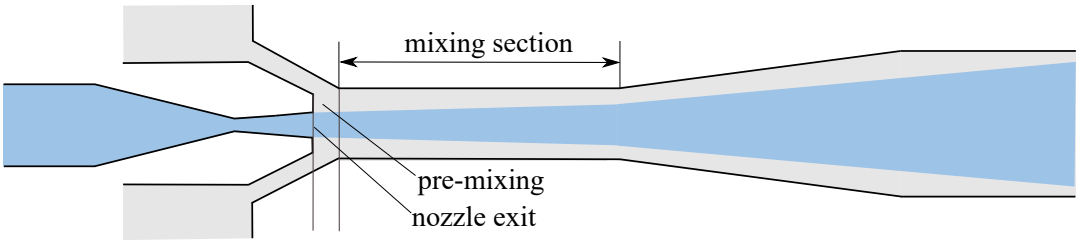

(B) constant-pressure mixing ejector

FIGURE 1.15: Schematic view of an ejector

Investigations into the performance disparity between CAM and CPM ejectors have yielded valuable insights. Kumar et al. [51] conducted a comprehensive review on constant area mixing (CAM) and constant pressure mixing (CPM) ejectors. This review examines ejector development freezing systems using a combination ejector with constant pressure and constant area mixing as an expansion mechanism. It was summarized that constant pressure mixing improves the cooling effect, overall efficiency, and coefficient of performance and reduces power consumption.

Other research also suggest that the constant pressure mixing ejector is more widely utilized due to its superior performance compared to the constant area mixing ejector [42, 52]. However, it's noteworthy that the theory of constant area mixing is better understood, and its performance can be predicted with a higher degree of accuracy [53].

Interestingly, contrary to prevailing conclusions, Atmaca [54] theoretically investigated the ejector expansion refrigeration cycle to compare the constant pressure mixing and constant area mixing ejector theories making use of thermodynamic models. The findings reveal that at higher condenser temperatures and lower evaporator temperatures, similar performance improvement ratios are observed for both mixing assumptions. And when optimum performance values under both of the mixing assumptions were compared, CAM assumption offers slightly higher performance results for the ejector expansion refrigeration cycle.

1.4.2 Working modes of ejector

For a fixed geometry and constant ejector input conditions, the working modes of the ejector can be categorized into three types based on the ejector outlet pressure [55, 56], as illustrated in Fig. 1.16. The entrainment ratio of the ejector, denoted as w, is defined as the ratio between the mass flow rate of the suction flow ($\dot{m}_s$) and the mass flow rate of the motive flow ($\dot{m}_m$), as given by Eq. (1.1). The critical pressure and breakdown pressure of the ejector are associated with both the ejector geometry and the ejector input conditions. Correlations for the critical pressure and breakdown pressure have been investigated both theoretically and experimentally [55–60].

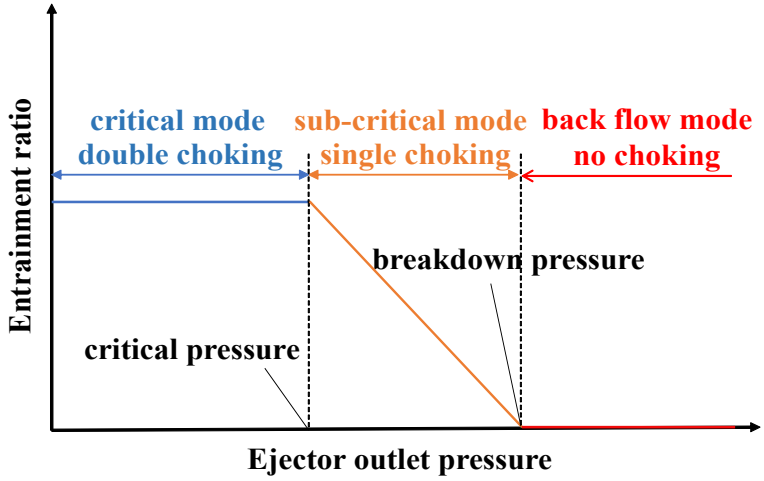

FIGURE 1.16: Working modes of the ejector

$$w = \frac{\dot{m}_s}{\dot{m}_m} \tag{1.1}$$

The choking state of the motive flow occurs when the flow attains the speed of sound at the throat of the motive nozzle. With a fixed ejector geometry, the mass flow rate of the motive flow reaches its maximum value under this condition. As the back pressure (ejector outlet pressure) continues to decrease, the mass flow rate remains constant. In the case of the suction flow, choking typically occurs in the premixing or mixing section, and the underlying principle is analogous to that of the motive flow.

Critical mode

When the ejector back pressure is below the critical pressure, the ejector operates in the critical mode. In this mode, both the motive flow and suction flow are in a choking state, wherein their mass flow rates reach their maximum values. Consequently, the entrainment ratio of the ejector also attains its maximum value.

Sub-critical mode

When the ejector back pressure falls within the range of the critical pressure and breakdown pressure, the ejector operates in the sub-critical mode. In this mode, only the motive flow is in a choking state, while the mass flow rate of the suction flow decreases as the back pressure increases. Consequently, the entrainment ratio decreases with the back pressure in this operational regime.

Back flow mode

When the ejector back pressure surpasses the breakdown pressure, the ejector operates in the backflow mode, where choking does not occur within the ejector, and the working fluid flows back towards the suction flow inlet. In this state, the ejector cannot operate normally.

In general, the ejector achieves optimal performance when operating at critical back pressure. Therefore, it is crucial to control the ejector to operate in the critical mode, near the critical point. This ensures both steady operation and high-efficiency performance, as emphasized in the experimental work by Wang et al. [56].

1.4.3 Simulation of ejector

The ejector is a complex device in which the flow involves the mixing of two distinct flows: high-pressure motive flow and low-pressure suction flow. The flow pattern in the ejector is complicated because it involves two-phase flow as well as trans-sonic issues. As discussed in the section above, the phase change starts from the throat of the motive nozzle, and the flow velocity also reaches the critical state (Ma=1). Then, the flow becomes two-phase flow and supersonic along the motive nozzle. In the mixing section, after the mixing with the low-speed suction flow, the supersonic flow will be slowed down and turn into subsonic. So, the trans-sonic flow will cause shock waves inside the ejector, increasing the complexity of the flow pattern.

To have a better and more detailed understanding of the flow pattern inside the ejector, simulation of the ejector is necessary. Based on the dimensionality and complexity, the modeling of the ejector can be classified as:

- 0-D/ pseudo 1-D thermodynamic models
- 1-D models based on the Finite Volume Method (FVM)
- 2-D / 3-D CFD simulations

Classification of the modeling assumptions of two-phase flow

Since the ejector involves two-phase flow, the modeling can be classified into several groups based on the assumptions used for two-phase flow, as shown in Fig. 1.17.

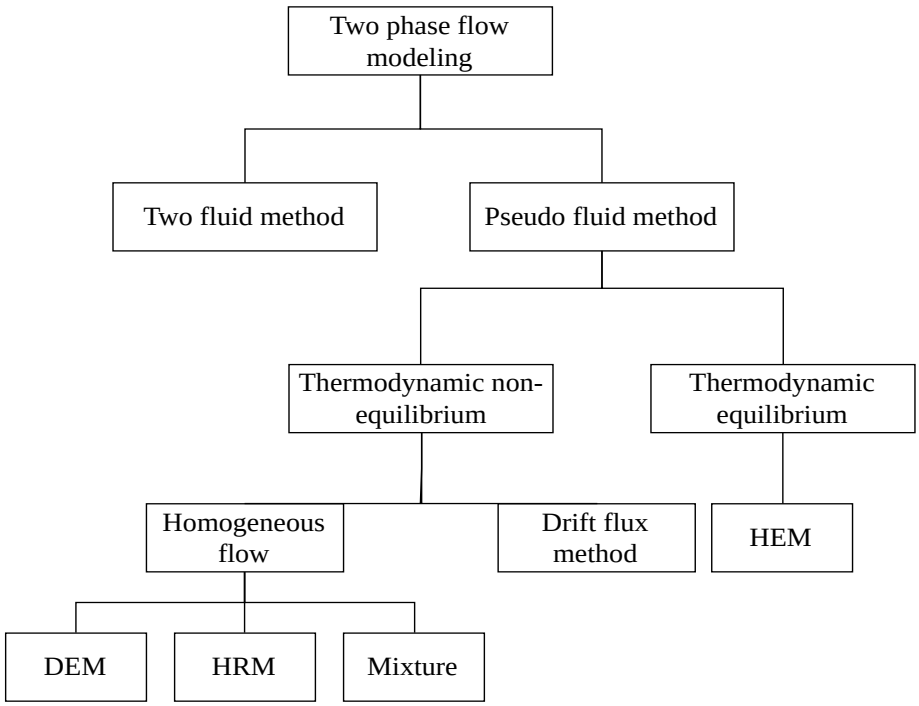

FIGURE 1.17: Classification of typical modeling methods of two-phase ejector

Firstly, the models are classified based on the fluid numbers assumption during modeling. For the two-fluid method, each phase has a set of equations. In the pseudo-fluid method, both phases are averaged based on mass or volume fraction, and a single set of equations is used to describe the two-phase flow.

Moreover, in a two-phase flow, non-equilibrium states exist between vapor and liquid phases. This non-equilibrium can be divided into thermodynamic and transport (or mechanical) non-equilibriums. Thermodynamic non-equilibrium is related to the superheated or subcooled state of a liquid or vapor, respectively. Transport non-equilibrium is related to differing temperatures, pressures, or velocities of the phases.

In multi-phase flow modeling, a commonly used assumption is homogeneous flow. This approach assumes the phases to be at mechanical equilibrium, meaning both phases are described with a single velocity and pressure field to reduce the complexity of the model by neglecting the modeling of the slip velocity. Essentially, the two phases can then be treated as a single pseudo-fluid with transport properties derived according to an averaging procedure [61]. The Homogeneous Equilibrium Model (HEM) assumes thermodynamic equilibrium of the phases at all points in the flow. Consequently, the temperatures and pressures of both phases are equal. It also

assumes that phases are uniformly distributed (perfectly mixed), resulting in equal velocities and mechanical equilibrium.

Different from HEM, Delayed Equilibrium Model (DEM) assumes the existence of three fractions: the meta-stable liquid phase, the saturated liquid phase, and the saturated vapor phase. The meta-stable fraction is assumed to have the same pressure as the saturated phases but a higher temperature. Therefore, DEM takes into account thermal non-equilibrium effects but does not include mechanical non-equilibrium effects. An index is used to denote the fraction of vaporization, which is the sum of the mass fraction of saturated liquid and saturated vapor.

Similar to HEM, Homogeneous Relaxation Model (HRM) assumes homogeneous multi-phase flow. However, HRM treats the phase change as a relaxation process toward equilibrium. A relaxation factor is used to denote the delay of the equilibrium. In relation to the previously established notation, this yields a more accurate description of the phase fraction. This improvement is based on an appropriate estimate of the relaxation time scale.

A modeling approach that has recently garnered attention from the research community is the mixture model. These 4-equation models aim to model the phase change mechanisms in the flow. Here, the transport equation for the volume fraction is solved with the mass transfer terms for evaporation and condensation explicitly. Such an improved estimation of the phase composition allows for a more accurate estimate of the mixture properties. The properties are calculated based on a mass-weighted average for the thermodynamic variables, e.g., enthalpy or total energy, or a volume-weighted average for the variables mixture density, molecular viscosity, or thermal conductivity [61].

Notably, all 0-D or pseudo 1-D models rely on the assumption that two-phase flow is based on HEM. The listed different assumptions are only applicable in 1-D modeling and CFD modeling.

0-D / pseudo 1-D modeling of ejector

0-D/pseudo 1-D models are employed for simulating ejectors in refrigeration systems. These models focus on thermodynamic simulations at critical sections along the flow path, including the inlet and outlet of the motive and suction nozzles, the throat of the motive nozzle, and the inlets and outlets of the mixing section and diffuser. The 0-D/pseudo 1-D models assume that the two-phase flow is in a homogeneous equilibrium state, where the saturated vapor and saturated liquid share the same pressure, temperature, and velocity. Thermodynamic parameters, such as specific enthalpy and density, are determined based on mass fraction averages and void fraction averages, respectively.

The development of these models began with Kornhauser in 1999 [43] and has since been advanced by numerous researchers.

Li and Groll [62] established a similar pseudo 1-D model based on constant pressure mixing method. The effect of the entrainment ratio and the pressure drop in

the suction nozzle of the ejector on the relative performance of the ejector expansion transcritical CO_2 cycle was investigated for typical air conditioning operation conditions. It was found that the COP of the ejector expansion transcritical CO_2 cycle can be improved by more than 16 % over the basic transcritical CO_2 cycle.

Deng et al. [63] developed a similar pseudo 1-D model but it was assumed there was no pressure drop in the suction nozzle and the mixing pressure is identical to the inlet pressure of suction flow, which was assumed as evaporation pressure. It was concluded that for the working conditions studied, the ejector expansion system maximum cooling COP is up to 18.6 % better than the internal heat exchanger cycle cooling COP and 22.0 % better than the conventional vapor compression refrigeration cycle cooling COP.

A more intricate pseudo 1-D model was proposed by Atmaca et al. [54]. In this model, the outlet pressure of suction nozzle, the pressure at the inlet and outlet of the mixing section are unknown values to be calculated by iteration. Among which the outlet pressure of the suction nozzle is obtained with an iteration loop until the ejector outlet pressure reaches the peak value, which means the ejector has the optimum performance under the working condition.

Another typical pseudo 1-D model was presented by Ameur et al. [64]. This model emphasizes that the design of primary and secondary nozzles is performed by maximising the mass flow rate at their respective throats, thus circumventing the approximate determination of the velocity of sound and the Mach number in a two-phase flow environment. In the mixing chamber, the flow is handled in such a way as to account for the wall friction in the momentum balance equation. The result of computations by the present model agrees fairly well with experimental data from a dedicated test bench as well as with those found in the available literature.

More 0-D / pseudo 1-D thermodynamic models of ejector applied in the transcritical CO_2 heat pump cycle and the main remarks are listed in Table. 1.6.

1-D modeling of ejector

0-D or pseudo 1-D models offer advantages such as rapid results generation, compatibility with cycle models, and widespread use among researchers. However, they come with limitations, including inaccuracies in simulating ejector performance and dependence on adiabatic efficiency input.

To obtain a more precise understanding of the flow patterns inside the ejector, a 1-D model is developed to capture complete flow profiles along the flow path. Unlike 0-D models, a 1-D model allows for tracking the evolution of flow patterns, including phase transitions and crossing the critical point (where $Ma = 1$). However, this model requires a detailed definition of two-phase flow and how two distinct flows interact in the mixing process. To simplify the simulation, various assumptions are applied in the modeling process. Two-phase flow models can be classified based on different simplifications and assumptions.

TABLE 1.6: Summary of 0-D / pseudo 1-D thermodynamic ejector models applied in trancrtical CO_2 heat pump cycles

Author	Year	Remarks
Zeng et al. [65]	2022	Expansion in the suction nozzle is included; The efficiency of the mixing section is defined; Shock wave is predicted in the constant area mixing section.
Purjam et al. [66]	2021	The discharge pressure of the primary nozzle is set to 95 % suction pressure of the secondary nozzle; Shock wave is predicted in the constant area mixing section.
Liu et al.[67]	2019	Expansion in the suction nozzle is neglected; Constant pressure mixing is assumed, and the pressure is equal to the evaporation pressure.
Taleghani et al. [68]	2019	A friction factor is calculated for constant area duct; Mass flux maximization criterion is used for both nozzles; A shock wave is assumed to take place at the inlet of constant area mixing section.
Sarkar [69]	2008	Expansion in the suction nozzle is included; The outlet pressure of motive and suction nozzle is defined by iteration based on mass balance.
Bai et al. [70]	2015	The pressure drop of the suction flow is neglected; The efficiency of the constant mixing section is a fixed given value.
Al-Tameemia et al. [71]	2017	A thermodynamic approach for designing the two-phase motive nozzle of the ejector for transcritical CO_2 heat pump system is proposed; Two thermodynamic approaches (ideal and non-ideal) are adapted to model the expansion processes for comparison.
Zheng et al. [72]	2016	The mixing process begins after the chocking of the suction flow, where motive and suction flows share the same pressure; Constant area mixing theory is used and the flow pressure lift in the mixing section is calculated; Speed of sound of two-phase fluid is calculated during the modeling.
Ahammed et al. [73]	2014	The secondary nozzle pressure drop is assumed to be 0.3 bar; Only the motive nozzle reach the choke condition with the maximum mass flux.

The 1-D Homogeneous Equilibrium Model has been widely used in the literature to model CO_2 ejector flow structure and characteristics [74–76]. Palacz et al. [77] investigated the application range of the HEM approach within typical supermarket refrigeration conditions. The results showed that for operating conditions close to or above the critical point of CO_2, the HEM is accurate (within 5 % error of mass flow rate prediction). However, as the temperature and pressure are reduced below the critical point, to off-critical expansion, the deviation of the prediction on the mass flow rate of motive flow reaches up to 50 %. The significant errors were attributed to the non-equilibrium effects that are neglected by HEM.

In addition to the HEM, the Homogeneous Relaxation Model (HRM) and Delayed Equilibrium Model (DEM) have also been studied in the 1-D modeling of ejectors by scholars [75, 78–81]. Both models account for non-equilibrium effects during phase transition. However, the accuracy of each model is closely tied to the correlation of the additional introduced index quantifying non-equilibrium—specifically, the vaporization index for DEM and the relaxation factor for HRM.

A more detailed summary of the existing 1-D models will be presented in the third chapter.

CFD modeling of ejector

Compared to 1-D modeling of ejectors, Computational Fluid Dynamics (CFD) is a robust and powerful tool for their modeling. CFD is a branch of fluid mechanics that employs numerical methods and algorithms to solve and analyze problems related to the behavior of fluids, encompassing both liquids and gases. It involves the use of computer simulations to explore fluid flow and associated physical phenomena, such as heat transfer, chemical reactions, and turbulence.

In CFD, the mathematical equations governing fluid flow, known as the Navier-Stokes equations, are discretized and solved using computational methods. Different CFD models can also be classified based on the two-phase flow modeling method (HEM, DEM, and HRM). A summarized table is provided in Table. 1.7, focusing specifically on the ejector expansion cycle using CO_2 as the refrigerant.

From Table. 1.7, it is evident that CFD studies are predominantly carried out using the commercial software ANSYS FLUENT, a widely adopted platform for CFD simulations. Additionally, some scholars utilize the open-source platform OpenFOAM.

Except for the difference of simulation tools, there is significant variability in the applied multiphase modeling methods, and researchers have undertaken comparisons between different methods.

For instance, Palacz et al. [88] conducted a comparative analysis of the accuracies of the Homogeneous Equilibrium Model (HEM) and Homogeneous Relaxation Model (HRM). Their study focused on simulating carbon dioxide flow in ejectors designed for supermarket refrigeration systems. The observed discrepancies for selected operating regimes ranged from 0.3 % to 43.3 % for HEM and 0.7 % to 42.0

TABLE 1.7: Summary of CFD modeling of ejector expansion cycle

Author	Method & tools	Remarks
Lucas et al. [82]	HEM & OpenFOAM	The pressure recovery of the ejector operated without a suction flow is determined with an error of 10 %. This error increases to 20 % when the ejector is operated with a suction flow.
Ringstad et al. [83]	HEM & Fluent	The Gaussian process regression (GPR) machine learning tool for R744 two-phase ejector design has been trained using large databases of CFD data. A performance map of an ejector at various pressure and temperature operating conditions was presented. Based on this prediction tool, the optimal combination of mixing chamber length and diameter was analyzed. And the final ejector design was found to have an ejector efficiency of 43 %.
Palacz et al.[84]	HEM & Fluent	The geometry of a CO_2 ejector mixing section was optimised. The optimisation results showed a very strong relation between ejector performance and the mixer diameter and the ejector efficiency of the optimised design was as much as 2 % higher than that of the baseline design.
Li and Deng [85]	Non-equilibrium model & FLUENT	The novel model was experimental verified with various nozzle diverging angles. The results suggested that prediction errors of secondary flow mass flow rate using the proposed model were less than 9 %, and the maximum error of primary flow mass flow rate was within the range of 15 %, which was much smaller than that of 34.55 % predicted by HEM modeling.
Haida et al. [86]	HRM & Fluent	An ejector equipped with thermocouple channels was designed and manufactured to investigate temperature distribution in the inner walls. The proposed CFD model predicted the wall temperatures with $\pm 5K$ accuracy for most of the validated points.
Zhang et al. [87]	Mixture Model & Fluent	A numerical model was validated by experimental data and void fraction correlation. It was found that Low temperature on the wall will exacerbate the non-equilibrium phase transition, leading to an increase in the critical mass flow rate of the nozzle. At this time, high thermal conductivity walls will also exacerbate exergy losses, by using low thermal conductivity walls can improve the consequences.

% for HRM. Notably, HRM exhibited higher accuracy than HEM at lower pressures and temperatures, with errors approximately 5 % lower.

In another study, Angielczyk et al. [89] compared the prediction accuracy of critical mass rate and pressure distribution for flashing carbon dioxide flow in a convergent-divergent nozzle using HEM and Delayed Equilibrium Model (DEM) approaches. The results indicated that, without an appropriate correlation for the DEM approach, the prediction accuracy of critical mass flow rate and pressure distribution was even worse than the HEM approach. However, the performance of the DEM approach improved with a better definition of the mass fraction evolution of the metastable flow, and traditional correlations for water did not apply to CO_2.

1.4.4 Conclusion

In conclusion, the traditional CO_2 heat pump cycle utilizing a throttling valve as an expansion device suffers from significant irreversibilities during the expansion process, leading to a decrease in cycle COP. The replacement and cycle modification with an ejector can substantially reduce expansion losses.

The ejector is a complex device involving the mixing of two flows, especially considering the inclusion of two-phase flow. 0-D / pseudo 1-D modeling based on thermodynamics remains the primary approach for ejector simulation due to its simplicity and high computational efficiency. However, 1-D modeling based on Finite Volume Method and CFD simulations can provide a more detailed flow pattern along the ejector's flow path. The 1-D and CFD models also vary depending on assumptions about two-phase flow, with thermodynamic equilibrium being a crucial consideration during modeling. Noting that the CFD simulation is more intensive in terms of computational resources, therefore 1-D modeling based on Finite Volume Method is a compromised choice between simulation efficiency and accuracy.

1.5 Experimental study on transcritical ejector expansion heat pump cycle using CO_2 as refrigerant

In addition to numerical analyses of ejectors and heat pump cycles using ejectors as expansion devices, numerous scholars have conducted experimental studies. Table. 1.8 listed the experimental study on the system performance and Table. 1.9 listed the study on the geometric parameters of the ejector and visualization study of ejector.

From Table. 1.8, it can be concluded that the main studied parameters influencing the performance of the ejector expansion transcritical CO_2 heat pump cycle include the pressure of the gas cooler and evaporator, the back pressure of the ejector and the compressor rotating speed. The effect of the internal heat exchanger is also a focus for the performance improvement of the cycle.

TABLE 1.8: Summary of experimental study on the parametric analysis of transcrtical CO_2 ejector expansion heat pump cycle

Author	Key words	Remarks
Xu et al. [90]	Adjustable ejector	The effects of the high-side pressure on the system performance are analyzed. A control strategy for maximum COP is developed by correlating the CO_2 pressure and temperature at the gas cooler exit.
Zhu et al. [91]	High COP (4.6)	The effects of hot-water outlet temperature, compressor discharge pressure, compressor rotation speed, and expansion valve opening on the ejector and overall system performance were investigated for tap water outlet temperatures ranging from 50 to 90 °C.
Zhang et al.[92]	Dual heat sources	Experimentally investigates the feasibility and performance of a novel compression/ejection transcritical CO_2 heat pump system with dual heat sources.
Guangming et al. [93]	Characteristic-curve equations	This work accounts for the effects of primary flow pressure, entrained flow pressure and back pressure on the entrainment ratio in off-design conditions. Using ejector characteristic-curve equations, the predictions are in good agreement with the experimental data.
Zou et al. [94]	Electric vehicle application	A transcritical CO_2 refrigeration cycle with dual ejectors in parallel (DEP) for electric vehicle heat pump system is established and its operation condition weight statistics method in all climate is proposed.
Taleghani et al. [68]	Model validation	The effects of gas cooler and evaporator pressures on system performance are investigated. A 0-D thermodynamic model is validated.
Nakagawa et al. [95]	Internal heat exchanger	The effect of internal heat exchanger in the performance of ejector refrigeration system was analyzed experimentally and compared with conventional expansion refrigeration system.
Boccardi et al. [96]	Multi-Ejector	A complete heat pump system with multi ejector pack and internal heat exchanger for production of hot water for sanitary use and for space heating have been established.
Lucas et al. [97]	Ejector efficiency correlation	An ejector operation characteristic for a CO_2 ejector based on experimental data is presented and correlations for the ejector efficiency and the motive mass flow rate are accomplished.

TABLE 1.9: Summary of experimental study on the geometric analysis of transcrtical CO_2 ejector expansion heat pump cycle

Author	Key words	Remarks
Liu et al. [98]	Motive nozzle throat	Experimental results show that the total capacity and the total COP of an ejector CO_2 system reach their maxima at the ejector throat diameter of 2.0 mm under extreme operating conditions.
Banasiak et al. [99]	Optimum geometry	Different ejector configurations were examined, including various lengths and diameters of the mixer and various angles of divergence for the diffuser, an optimal configuration was found.
Elbel and Hrnjak [100]	Motive nozzle and diffuser sizing	The COP increased when using the integrated needle to reduce the motive nozzle throat area in the ejector. Highest ejector efficiencies were achieved when the smallest diffuser angle of 5 was used.
Bouzrara [101]	Optimum geometry	A comprehensive geometry study of the ejector was carried out. The studied parameters included the position of the motive nozzle, the divergent angle of the motive nozzle, diameter of the motive nozzle throat, diameter and length of the constant mixing section.
Zheng and Deng [102]	Ejector component efficiencies	Combine the experimental measurement data and the theoretical model of ejector to determine CO_2 ejector component efficiencies including the motive nozzle, suction chamber, mixing section, diffuser as well as the total ejector efficiency.
Zhu et al. [103]	Visualization	The flow fields in the suction chamber and the mixing chamber of the ejector were visualized by direct photography for various operating conditions.
Palacz et al. [104]	Visualization	A high-speed camera and additional light sources were used to capture the flow inside the mixing section.The collected results showed that the expansion angle increased with increasing mass flow rate in the motive nozzle.
Li et al. [105]	Visualization	The two-phase flow in the primary converging-diverging nozzle of a transcritical CO_2 ejector was investigated by a visualization measurement. The transition of the phase change position in the primary nozzle was discovered experimentally.

From Table. 1.9, to achieve the optimal performance, the ejector need to be well designed. Efforts have been contributed to the ejector geometric design, the main geometric parameters include the position and angle of the motive nozzle, the diameter and length of the constant area mixing section, the length and angle of the diffuser. Substantial efforts have been devoted to visualizing the flow patterns within ejectors.

The experimental test facilities vary in terms of system schematics, size, and refrigeration capacity. Scholars have examined different types of ejectors, with the convergent-divergent nozzle ejector emerging as the primary choice. This type of ejector, capable of reaching supersonic states, exhibits superior pressure recovery potential. Nevertheless, some researchers have also opted for ejectors with converging nozzles in their investigations.

1.5.1 Conclusion

In conclusion, ongoing experimental research on the ejector-enhanced transcritical CO_2 heat pump cycle remains crucial. Despite the commercial validation of this technology, the intricate flow patterns within the ejector underscore the need for additional laboratory validation. This is imperative not only for enhancing system performance but also for delving into additional possibilities for cycle configurations.

1.6 Novel system of transcritical ejector expansion CO_2 heat pump cycle configuration

The conventional configuration of an ejector expansion heat pump cycle is illustrated in Fig. 1.12a. In addition to this typical system arrangement, researchers have proposed numerous novel configurations aimed at enhancing cycle performance, including improvements in COP, exergy efficiency, and ejector efficiency. While some of these innovative systems have undergone experimental validation, a significant portion remains in the theoretical design and analysis stage.

1.6.1 two-stages evaporation cycle

In the realm of actual vapor-compression refrigeration or heat pump systems with variable-temperature heat reservoirs, a two-stage evaporation cycle stands out as an effective method to enhance the coefficient of performance. However, its application is constrained by the requirement for two separate suction pressures, necessitating two cylinders or compressors.

To address this limitation, Cao et al. [106] propose a two-stage evaporation cycle with a shared single-stage compressor. An ejector is employed to elevate the lower evaporation pressure to the higher evaporation pressure or the compressor suction pressure, as depicted in Fig. 1.18. A thermodynamic model is developed to analyze

the performance of this innovative system. Numerical results reveal that the COP of the novel cycle surpasses the one-stage ejector cycle by 12.1 %, outperforms the two-stage evaporation cycle by 6.9 %, and exceeds the basic refrigeration cycle by 22.0 % under underrated operating conditions. The exergy analysis further indicates that the novel cycle can reduce exergy loss in the expansion process by 49.6 % and in the heat transfer process in evaporators by 21.5 % compared to the basic refrigeration cycle.

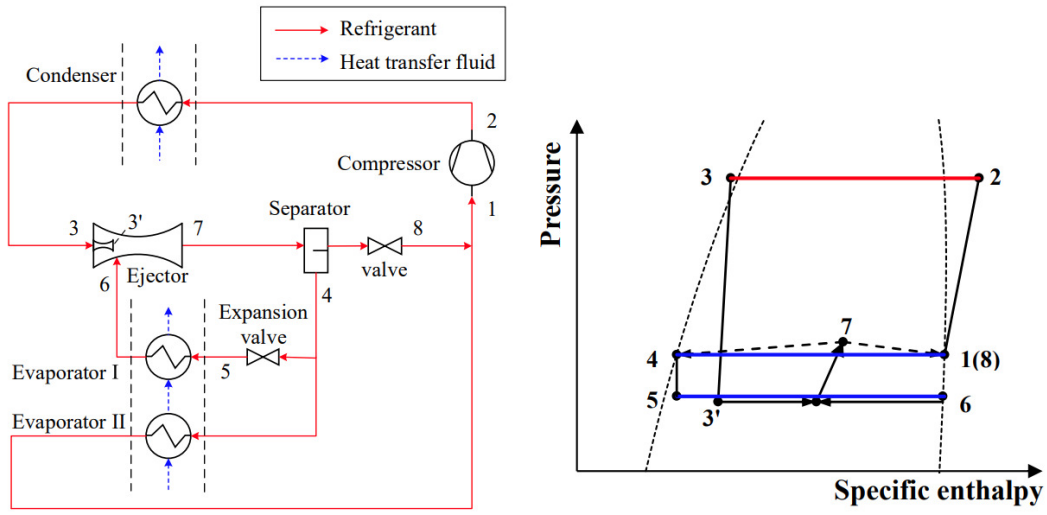

FIGURE 1.18: Schematic and *P-h* diagram of the ejector-assisted two-stage evaporation single-stage vapor-compression cycle [106]

A new two-stage configuration of an ejector-expansion transcritical CO_2 refrigeration cycle is introduced by Yari et al. [107], shown in Fig. 1.19. This configuration incorporates an internal heat exchanger and an inter-cooler to enhance the cycle's performance. The theoretical analysis of the performance characteristics was conducted based on the first and second laws of thermodynamics. Simulation results reveal that, in comparison to the conventional two-stage transcritical CO_2 cycle, the new two-stage cycle exhibits approximately 12.5 % to 21 % higher values for both COP and second law efficiency. The study concludes that the performance of this innovative two-stage transcritical CO_2 refrigeration cycle can be significantly improved, making it a promising refrigeration cycle from both thermodynamic and technical perspectives.

1.6.2 Traditional CO_2 ejector cycle with an additional feed back loop

For the traditional ejector expansion cycle, the primary flow from the gas cooler and the secondary flow from the evaporator pass through the nozzle, mixing, and diffuser sections of the ejector. They then separate into vapor and liquid, and this ratio should match the inlet ratio of primary and secondary flows. This regulation limits the operation of the cycle. To mitigate this limitation, Li and Groll [62] proposed a modified cycle with an additional feedback loop, as shown in Fig. 2.25. The main

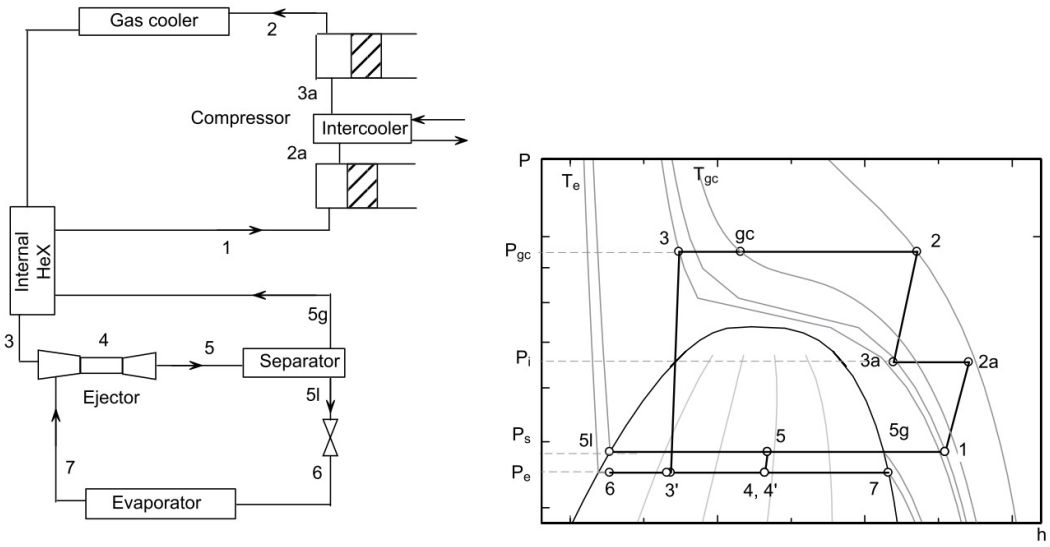

FIGURE 1.19: Schematic and *P-h* diagram of the two-stage evaporation single-stage vapor-compression cycle [107]

difference from the conventional ejector cycle is that some part of the vapor from the separator is fed back to the evaporator through a throttle valve to regulate the vapor quality of the evaporator inlet. This modification allows the ejector cycle to operate over a wider range of working conditions.

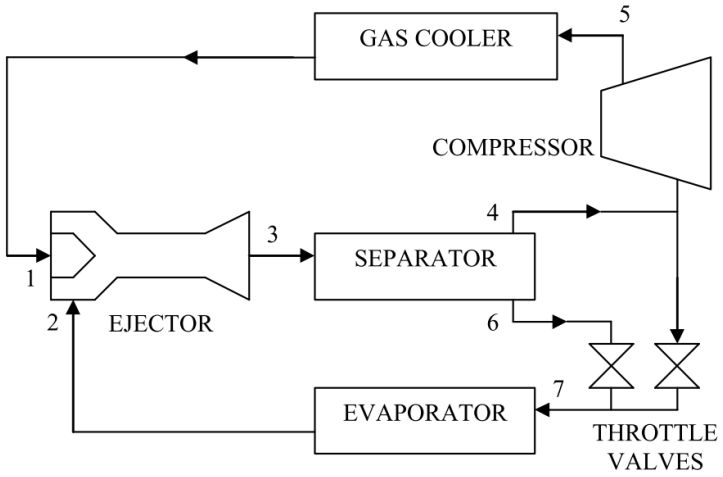

FIGURE 1.20: Modified cycle with an additional feed back loop [62]

1.6.3 Transcritical CO_2 refrigeration cycle with an adjustable ejector

The fixed ejector has to work under a restricted operating condition to keep its positive effectiveness on the transcritical CO_2 refrigeration cycle, and a controllable ejector will be helpful. A schematic diagram of an adjustable ejector is shown in Fig. 1.21. A needle is installed in the motive nozzle to control the throat diameter. The control of the needle can be manual or by a step motor as shown in Fig. 1.21.

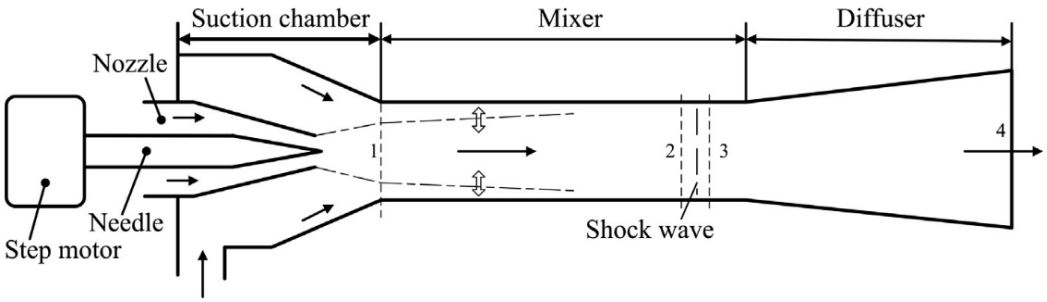

FIGURE 1.21: A schematic diagram of an adjustable ejector [108]

In the study by Smolka et al. [109], the performances of fixed-geometry ejectors of various sizes were simulated and compared with the corresponding performances of controllable-geometry ejectors at several needle positions. For both types of ejectors, the global efficiency as a function of the mass flow rate is presented and discussed. The results indicate that each fixed-geometry ejector configuration exhibits high efficiency over the entire range of operating conditions. In the case of controllable-geometry ejectors, the efficiency was, in most cases, 25 % higher than that in the fixed-geometry case when the motive nozzle throat was reduced by approximately 35 %. Similarly, Liu et al. [110] found through experimental validation that the ejection ratio and coefficient of performance can significantly increase as the ejector motive nozzle throat diameter decreases. It was also concluded that the ejection ratio, suction pressure ratio, cooling capacity, and COP reached their maximum levels when the distance between the ejector motive nozzle exit and mixing section constant-area entry was equal to 3 times the mixing section diameter.

However, some researchers have reached a different conclusion regarding the comparison. He et al. [111] compared the performance of adjustable and fixed ejectors with the same key structural sizes using exergy flux distribution analysis. The results revealed that the main exergy transfer (interaction between the primary and secondary flows) occurs in the suction chamber. Furthermore, higher exergy loss was observed in the suction chamber of the adjustable ejector due to flow separation along the needle and higher viscous dissipation of oblique shock waves, resulting in a 5 % to 11 % lower entrainment ratio than that of the fixed ejector. On the other hand, the higher velocity in the fixed ejector led to increased friction on the wall and more intense flow separation in the diffuser, causing higher exergy loss in the mixer and diffuser. Consequently, the exergy efficiency of the adjustable ejector is only 0.5 % lower than that of the fixed ejector.

1.6.4 Conclusion

In the realm of transcritical ejector expansion CO_2 heat pump cycles, a departure from traditional configurations has given rise to innovative cycle designs with the overarching goals of enhancing efficiency and adaptability to varying operational

conditions. Diverse cycle modifications have been introduced, each tailored to specific application conditions. While both numerical simulations and experimental investigations have been undertaken to validate the efficacy of these modifications, a crucial aspect yet to be addressed comprehensively is their economic viability for real-world commercial operations. A more holistic analysis, grounded in economic considerations, is imperative to gauge the practical feasibility and financial implications of implementing these advancements in the field.

1.7 Conclusions of the State-of-the-Art Review

In this chapter, a comprehensive state-of-the-art review of the ejector enhanced transcritical CO_2 heat pump cycle has been conducted. The working principle of the cycle, the rationale behind the evolution of refrigerants, and system configurations have been elucidated. Key achievements in this research domain have been succinctly presented. In summary, further research is warranted in the following areas:

- Despite being the primary modeling method identified in the literature review, there is a scarcity of comparisons between different 0-D/pseudo 1-D models of ejectors. Detailed analyses are required to understand the impact of simplifications and assumptions in different models on modeling accuracy.
- 1-D modeling based on Finite Volume Method is relatively uncommon compared to the abundance of CFD modeling. Considering the computational cost of CFD modeling, 1-D modeling offers a compromise solution between modeling accuracy and efficiency.
- Although the CO_2 ejector expansion system has been commercialized, its pioneering nature necessitates more laboratory experimental validation. This is crucial for gaining a comprehensive understanding of the complex flow patterns within the ejector.

Chapter 2

Thermodynamic-based simulation of transcritical CO_2 ejector expansion heat pump cycle

Despite being the primary modeling method identified in the literature review, there is a scarcity of comparisons between different 0-D/pseudo 1-D models of ejectors. Detailed analyses are required to understand the impact of simplifications and assumptions in different models on modeling accuracy.

In this chapter, we will replicate three zero-dimensional thermodynamic models of the ejector, increasing in complexity based on existing literature [54, 62, 63]. These models will then be integrated into a transcritical CO_2 heat pump cycle.

Following this, a sensitivity analysis will be performed for the input isentropic efficiencies of the ejector components. The effect on the cycle COP, ejector outlet pressure and ejector efficiency will be quantitatively analyzed.

Subsequently, the experimental validation of the three zero-dimensional thermodynamic models will be conducted using two independent sets of data from the literature [112, 113]. The simulation accuracy concerning the ejector outlet pressure, entrainment ratio, and the cycle COP will be compared.

Finally, we will identify the source of simulation deviation and introduce a data processing method aimed at eliminating the primary deviation arising from the liquid imbalance issue in the cycle. The simulation accuracy will then be compared for the cycle before and after implementing the modification.

2.1 Key definitions of 0-D/pseudo 1-D thermodynamic models of ejector

The ejector consists of five main parts: the motive and suction nozzle, the pre-mixing section, the constant-area mixing section, and the diffuser, as shown in Fig. 2.1. The motive flow, entering at high pressure and in a supercritical state from the gas cooler outlet, passes through the motive nozzle. The suction nozzle inlet typically receives saturated or superheated vapor from the evaporator outlet. The motive flow expands in the nozzle and entrains the low-pressure suction flow. These two flows

mix in the pre-mixing and constant-area mixing sections before passing through the diffuser. Due to the combination of the two flows and geometric design, the outlet pressure exceeds the evaporation pressure, providing a pressure boost to the suction flow. The brief pressure and velocity profiles along the flow path of the ejector are also presented in Fig. 2.1. The shock wave occurs when the flow velocity surpasses the local sound speed from the supersonic state, resulting in a steep pressure increase and velocity drop. Noting that this pressure and velocity curves are just a typical abbreviated schematic, the actual pressure and velocity curves will vary depending on the modeling assumptions.

The pressure lift P_{lift} of an ejector is defined as the pressure difference between the ejector outlet and suction flow. The entrainment ratio of the ejector is defined as the ratio between the mass flow rate of the suction flow and the motive flow, as introduced in the first chapter (Eq. (1.1)).

In 0-D/pseudo 1-D thermodynamic models, the focus of modeling is directed towards the inlets and the outlet of these distinct sections. Notably, the geometric parameters such as diameter, convergent and divergent angles, etc., are not included as input parameters for the modeling of each section. Instead, isentropic efficiency of the motive nozzle, the suction nozzle and the diffuser, defined by Eq. (2.1) to Eq. (2.3), are utilized as inputs to assess the performance and optimize the geometric design and operation of these sections.

$$\eta_m = \frac{h_{am} - h_{am,is}}{h_m - h_{am}} \tag{2.1}$$

$$\eta_s = \frac{h_{as} - h_{as,is}}{h_s - h_{as}} \tag{2.2}$$

$$\eta_d = \frac{h_{d,is} - h_c}{h_d - h_c} \tag{2.3}$$

Here, h_{am}, h_{as}, h_c, and h_d denote the specific enthalpy at the outlet of the motive nozzle, suction nozzle, mixing section, and diffuser. $h_{am,is}$, $h_{as,is}$, and $h_{d,is}$ represent the specific enthalpy for an isentropic process at the outlet of the motive nozzle, suction nozzle, and diffuser sections. h_m and h_s represent the inlet specific enthalpy of the motive and suction nozzle. In an isentropic process, the entropy gain is zero, indicating no irreversibility loss. The isentropic efficiencies, expressed by equations Eq. (2.1) to Eq. (2.3), serve as a measure of proximity to the ideal isentropic process.

Ejector efficiency η_{eje}, a crucial performance metric, is defined as the ratio of the amount of expansion work recovered by the ejector to the maximum possible expansion work rate recovery potential (Eq. (2.4)). The specific enthalpy $h_{s,is}$ for an assumed isentropic change of state from the suction flow inlet condition to the ejector outlet pressure is vital for this calculation. Likewise, $h_{m,is}$ represents the specific enthalpy for an assumed isentropic change of state from the motive flow inlet condition to the ejector outlet pressure [100, 113, 114]. Ejector efficiency is influenced

not only by the geometric design of the ejector but also by operational conditions, making it a key metric for evaluating ejector performance.

$$\eta_{eje} = \frac{\dot{m}_s}{\dot{m}_m} \cdot \frac{h_{s,is} - h_s}{h_m - h_{m,is}} \tag{2.4}$$

Fig. 2.2 presents the ejector expansion process on the *P-h* diagram of CO_2. The points m, s, and d represent the inlet of motive flow, suction flow, and the ejector outlet flow. $\delta h = 0$ and $\delta s = 0$ represent the isenthalpic and isentropic processes, respectively. One of the advantages of using ejector efficiency as a performance index for the ejector is that, in this situation, the ejector can be assumed as a black box. The efficiency can be calculated based only on the inlet and outlet parameters without knowing the detailed process happening inside the ejector.

2.2 Modeling methodology

Based on current literature, it is evident that zero-dimensional (0-D) and pseudo one-dimensional (pseudo 1-D) models, relying on thermodynamic equilibrium states, have been extensively studied. However, the accuracy of these models in predicting various parameters, such as ejector outlet pressure and entrainment ratio, across diverse operating conditions requires validation through additional experimental data.

The impact of simplifications made during the 0-D modeling process remains unclear. Furthermore, there is a notable scarcity of studies dedicated to the comparative analysis of different 0-D models. In this section, we present three representative 0-D thermodynamic models of ejectors, each characterized by increasing complexity (Deng et al. [63], Li et al. [62], Atmaca et al. [54]).

The 0-D thermodynamic models are classified into two categories based on the variation of pressure before and after the mixing process inside the ejector: the first group neglects the pressure variation during the mixing process and for the second group the pressure variation is considered. In this section, the two groups of models are named as constant pressure mixing model [63] and variable pressure mixing model [54, 62]. Noting that this classification is based on the assumptions during the modeling, distinguished from the constant area mixing (CAM) ejector and constant pressure mixing (CPM) ejector discussed in the first chapter which is based on the geometry character of the ejector.

Some common assumptions are applied to simplify the simulation for all the 0-D thermodynamic models [54, 62, 63]:

(1) Pressure drop along the pipe and in the main components is neglected.

(2) The system is adiabatic except for heat exchange with the environment in the gas cooler and evaporator.

(3) Kinetic energies of the refrigerant at the ejector inlet and outlet are negligible.

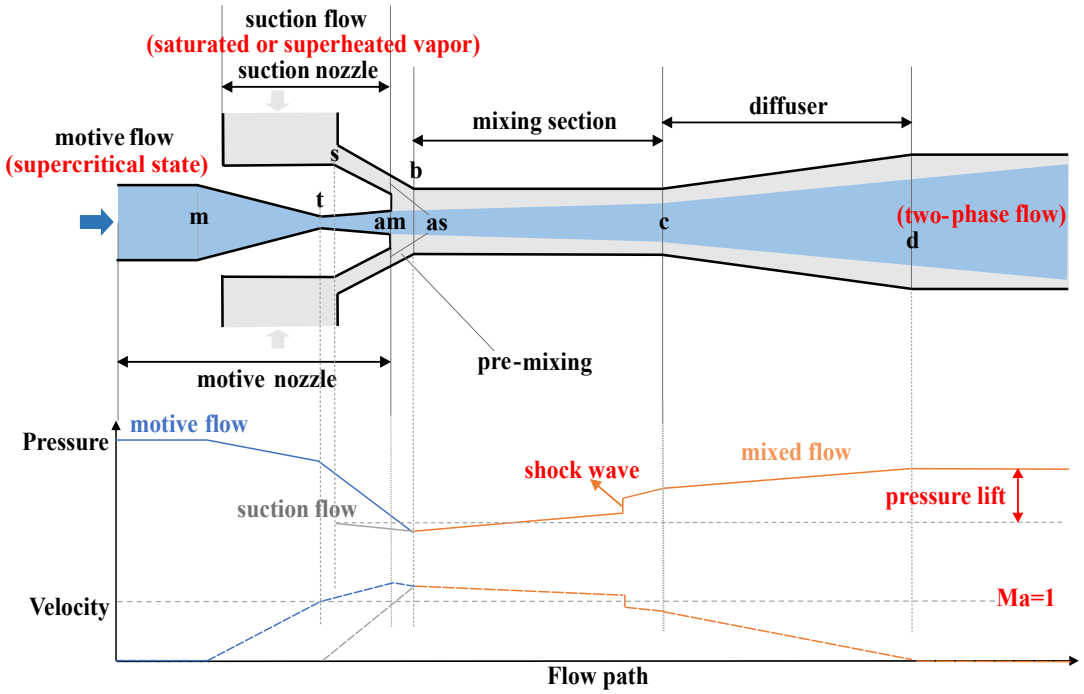

FIGURE 2.1: Structure of the ejector and a brief pressure profile along the flow path

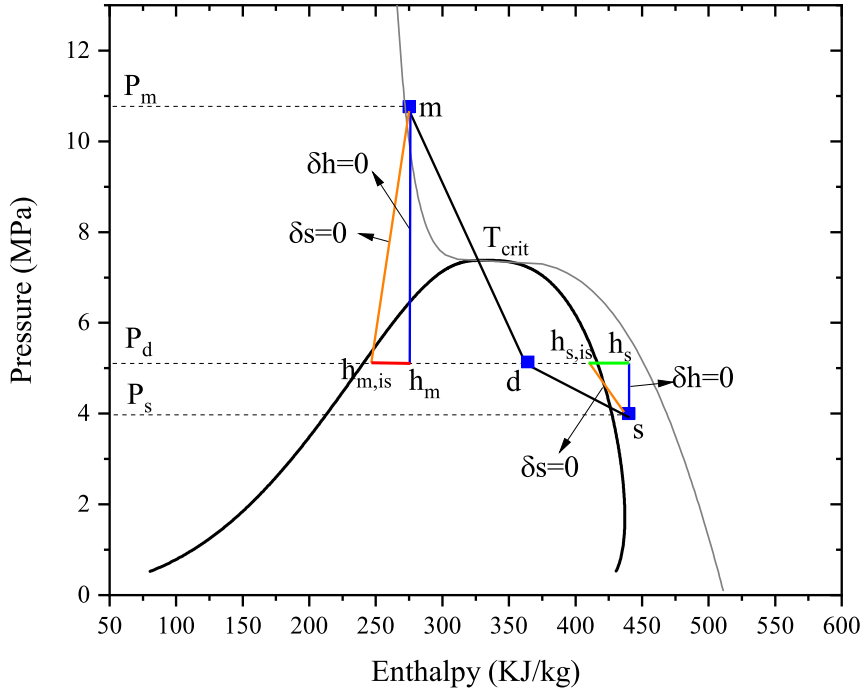

FIGURE 2.2: *P-h* diagram of the ejector expansion process

(4) The flow through the throttle valve is isenthalpic.

(5) The friction losses in the mixing section is neglected.

2.2.1 Constant pressure mixing model of ejector [63]

The constant pressure mixing model of ejector is referred to Deng et al. [63]. For the constant pressure mixing model, the pressure variation in the mixing section is neglected. The motive flow expands to the evaporation pressure at the motive nozzle outlet and the pressure keeps unchanged until the inlet of the diffuser.

Modeling of motive nozzle

Within the ejector, the motive flow undergoes acceleration with a pressure drop from P_m to P_a before mixing. Here, P_a is assumed to be the suction nozzle outlet pressure and equals to the inlet pressure of the suction nozzle P_s in the model of Deng [63]. The specific enthalpy of the motive flow at the nozzle outlet is determined by Eq. (2.5), where η_m represents the isentropic efficiency of the motive nozzle, and $h_{am,is}$ is the ideal specific enthalpy for an isentropic expansion.

The flow velocity of the motive flow (u_{am}) at the nozzle outlet is determined through an energy balance between motive nozzle inlet and outlet, utilizing Eq. (2.6), where h_{am} represents the specific enthalpy of the motive flow at the nozzle outlet. It is important to note that, in this analysis, the inlet velocity of the motive nozzle is neglected and assumed to be zero.

Furthermore, the density of the motive flow at the nozzle outlet is determined using the equation of state available in REFPROP, as outlined by Eq. (2.7).

$$h_{am} = h_m - \eta_m \cdot (h_m - h_{am,is}) \tag{2.5}$$

$$\frac{1}{2} \cdot {u_{am}}^2 = h_m - h_{am} \tag{2.6}$$

$$\rho_{am} = f(h_{am}, P_a) \tag{2.7}$$

Applying the conservation of mass, the area occupied by the motive flow at the nozzle outlet per unit total ejector flow rate (a_{am}) is determined by Eq. (2.8), where w represents the entrainment ratio of the ejector as defined by Eq. (1.1) in the first chapter.

$$a_{am} = \frac{1}{(1+w) \cdot \rho_{am} \cdot u_{am}} \tag{2.8}$$

Modeling of suction nozzle

In Deng's model [63], there is no expansion in the suction nozzle. The outlet parameters of the suction nozzle (Eq. (2.9) to Eq. (2.11)) remain identical to the inlet, representing the flow from the outlet of the evaporator.

$$h_{as} = h_s \tag{2.9}$$

$$u_{as} = u_s = 0 \tag{2.10}$$

$$\rho_{as} = \rho_s \tag{2.11}$$

Modeling of pre-mixing section and constant area mixing section

The motive flow and suction flow then mix in the pre-mixing section and constant area mixing section. In the mode of Deng [63], it is assumed that the mixture pressure in the ejector equals the evaporator pressure, as the small pressure difference can be neglected in the transcritical CO_2 cycle.

Furthermore, the analysis assumes the conservation of fluid momentum in the mixing section and the velocity of the mixed flow u_c can be obtained by Eq. (2.12).

$$u_c = u_{am}/(1+w) \tag{2.12}$$

The specific enthalpy of the mixed flow h_c can be calculated by the overall energy balance equation by Eq. (2.13):

$$h_c = h_m/(1+w) + h_s \cdot w/(1+w) - \frac{1}{2} \cdot u_c^2 \tag{2.13}$$

Note that all calculations are based on the assumption that the total mass flow rate of the ejector is normalized to unity.

Modeling of diffuser

An isentropic efficiency η_d is assumed to determine the isentropic outlet specific enthalpy of the ejector (Eq. (2.14)). The ejector outlet specific enthalpy h_d is obtained through the energy balance between the inlet and the outlet of the ejector (Eq. (2.15)). Subsequently, the outlet pressure is determined using equation of state with the known outlet specific enthalpy and entropy for an isentropic process.

$$h_{d,is} = \eta_d \cdot h_d + (1-\eta_d) \cdot h_c \tag{2.14}$$

$$h_d = 1/(1+w) \cdot h_m + w/(1+w) \cdot h_s \tag{2.15}$$

After obtaining the ejector outlet pressure, along with the calculated actual specific enthalpy at the outlet, more thermodynamic parameters, such as entropy and vapor quality, can be acquired through the equations of state.

2.2.2 Variable pressure mixing models of ejector [54, 62]

For the variable pressure mixing models of ejector, the pressure variation during the mixing section is considered. An extra unknown pressure P_c is introduced and an additional loop is used to obtain the pressure after mixing process. The other main assumptions regarding pressure drop in the pipe, friction losses, etc., are the same as those in the constant pressure mixing model. Two variable pressure mixing models of ejector are introduced [54, 62].

Variable pressure mixing model proposed by Li and Groll [62]

The modeling of Li's ejector [62] is fundamentally consistent with Deng's model [63]. However, being a more complex model, Li's approach introduces some distinguishing features.

In Li's model, a slight expansion is assumed in the suction nozzle. The calculation of the outlet specific enthalpy and flow velocity in the suction nozzle is analogous to that of the motive flow, as given by Eq. (2.16) to Eq. (2.19).

$$h_{as} = h_s - \eta_s \cdot (h_s - h_{as,is}) \tag{2.16}$$

$$\frac{1}{2} \cdot {u_{as}}^2 = h_s - h_{as} \tag{2.17}$$

$$\rho_{as} = f(h_{as}, P_a) \tag{2.18}$$

$$a_{as} = \frac{w}{(1+w) \cdot \rho_{as} \cdot u_{as}} \tag{2.19}$$

Here, P_a is slightly lower than the inlet pressure of the suction nozzle P_s. The pressure difference between the inlet and outlet of the suction nozzle is expected to vary with the operating parameters. Li and Groll [62] investigated the effect of various pressure differences (0.01 MPa, 0.03 MPa, and 0.05 MPa) on the ejector entrainment ratio and system COP, but they did not provide a correlation. Additionally, there is no available methodology in the open literature to calculate the pressure difference. Therefore, we set 0.03 MPa as the default value in this section.

Another difference in the model of Li [62] is the mixing section. For the mixing process, an unknown pressure P_c is introduced. According to the conservation of momentum before and after the mixing of the motive and suction flows, Eq. (2.20) is

obtained, where u_c is the flow velocity of the mixed flow. According to the conservation of energy, the specific enthalpy of the fluid after the mixing can be determined by Eq. (2.21).

$$P_a \cdot (a_{am} + a_{as}) + 1/(1+w) \cdot u_{am} + w/(1+w) \cdot u_{as} = P_c \cdot (a_{am} + a_{as}) + u_c \quad (2.20)$$

$$(1+w) \cdot (h_c + \frac{1}{2} \cdot {u_c}^2) = h_{am} + w \cdot h_{as} \quad (2.21)$$

Besides the features mentioned above, the rest of the ejector modeling remains identical to Deng's model [63].

Variable pressure mixing model proposed by Atmaca et al. [54]

As the most complex 0-D thermodynamic model studied in this chapter, Atmaca's model [54] determines the value of P_a iteratively. The iterative loop continues until the outlet pressure of the ejector reaches its peak value, signifying that the ejector has achieved optimal performance.

Apart from the difference mentioned above, the rest of the ejector modeling in the model of Atmaca [54] is identical to the model of Li [62].

2.2.3 Modeling of other components

After expansion in the ejector, the mixed flow proceeds through the separator. Here, the saturated vapor undergoes compression in the compressor, while the saturated liquid expands through the valve and enters the evaporator. In this section, the modeling of different components in the system is introduced sequentially, drawing references from the literature by [54, 62, 63].

A brief cycle schematic of the ejector expansion heat pump cycle is presented in Fig. 2.3. It is important to note that, due to the absence of pressure drop along the pipe and the adiabatic nature of the ejector, the pressure, enthalpy, and other properties at the inlet of the motive nozzle (state m) are identical to those at the outlet of the gas cooler (state 3). Similarly, the same principle applies to the suction nozzle, where the properties at the inlet (state s) are identical to those at the outlet of the evaporator (state 9). Considering the end part of the ejector after the diffuser as a constant area tube, the properties at the outlet of the diffuser (state d) are identical to the outlet of the ejector (state 6).

For the modeling of the compressor, compression is assumed to be adiabatic, and an isentropic efficiency η_{comp} is introduced to characterize the performance of the compressor. With the isentropic efficiency and a fixed outlet pressure of the compressor, the outlet specific enthalpy can be calculated using Eq. (2.22), where h_1 and $h_{2,\text{is}}$ represent the inlet specific enthalpy and outlet specific enthalpy of an isentropic

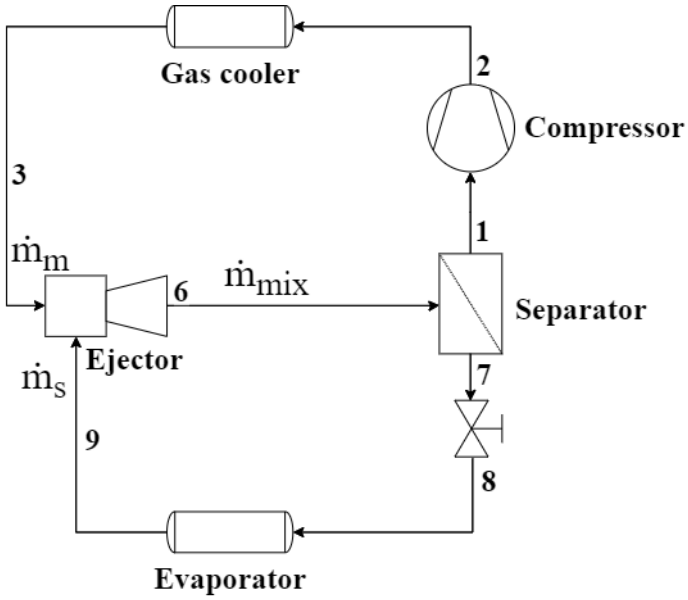

FIGURE 2.3: Schematic of an ejector expansion heat pump

process for the compressor. The model of Deng [63] incorporates an empirical correlation expressed by Eq. (2.23) [115], where P_1 and P_2 are the inlet and outlet pressures of the compressor. In Li's model [62] and Atmaca's model [54], the isentropic efficiency of the compressor is a fixed value of 0.75.

$$\eta_{comp} = \frac{h_{2,is} - h_1}{h_2 - h_1} \tag{2.22}$$

$$\eta_{comp} = 1.003 - 0.121 \cdot (P_2/P_1) \tag{2.23}$$

The remaining thermodynamic parameters can be determined using equations of state. The power consumed by the compressor is expressed by Eq. (2.24).

$$\dot{W}_{comp} = \dot{m}_m \cdot (h_2 - h_1) \tag{2.24}$$

After compression in the compressor, the motive flow undergoes cooling in the gas cooler. The outlet pressure and temperature are known during modeling, and the outlet specific enthalpy can be determined using state equations. Using the inlet and outlet enthalpies, the gas cooler capacity is calculated using Eq. (2.25).

$$\dot{Q}_{heating} = \dot{m}_m \cdot (h_2 - h_3) \tag{2.25}$$

After exiting the separator, the saturated liquid flows through a throttle valve and is then heated to the saturated or superheated vapor in the evaporator. The expansion through the valve is considered isenthalpic in the modeling ($h_8 = h_7$). The cooling capacity of the evaporator is then expressed by Eq. (2.26), where h_9 is known from input values of temperature and pressure.

$$\dot{Q}_{cooling} = \dot{m}_s \cdot (h_9 - h_8) \tag{2.26}$$

In the referenced literature [54, 62, 63], the heat pump is employed for cooling applications. Therefore, the COP of cooling is chosen as the system evaluation indicator and is calculated using Eq. (2.27).

$$COP_{cooling} = \frac{\dot{Q}_{cooling}}{\dot{W}_{comp}} \tag{2.27}$$

2.3 Resolution of the 0-D thermodynamic models

To solve the 0-D thermodynamic models presented in this chapter, coding in Matlab involves various iteration loops. The properties of CO_2 are obtained using equations of state from the NIST REFPROP database, version 9.1. The flow charts illustrating the modeling sequence of the ejector models are shown from Fig. 2.4 to Fig. 2.6.

The closure of the simulation is based on the tolerated deviation (ϵ) of the iterated parameters. In the constant pressure mixing model, there is only one unknown parameter: entrainment ratio w which needs to be found by an iteration based on the mass balance of the vapor between the inlet and the outlet of the ejector, as depicted by Eq. (2.28), where x_6 is the vapor quality at the ejector outlet, which is acquired by the equation of state.

$$x_6 = 1/(1+w) \tag{2.28}$$

In the variable pressure mixing models, besides entrainment ratio, the pressure value after the mixing of the motive and suction flows is also unknown and needs to be found by an iteration. The closure criteria is the mass conservation of the mixed flow (Eq. (2.29)), where ρ_c is the density of the mixed flow.

$$\rho_c \cdot (a_{am} + a_{as}) \cdot u_c = 1 \tag{2.29}$$

In the model proposed by Atmaca et al. [54], it is assumed that the ejector operates under optimal conditions. This implies that the outlet pressure of the ejector reaches its peak value based on the iteration of the nozzle outlet pressure. The initial value of P_{check} will be set to the value of the ejector outlet pressure P_6 for the first iteration of the suction nozzle outlet pressure (P_a).

The output parameters of the ejector model include pressure and specific enthalpy values at the entrance and exit of each section, the outlet vapor quality, the entrainment ratio of the ejector and the ejector efficiency. After obtaining these parameters and running the models for the remaining components, as described in the above section, the modeling of the ejector expansion heat pump cycle is terminated.

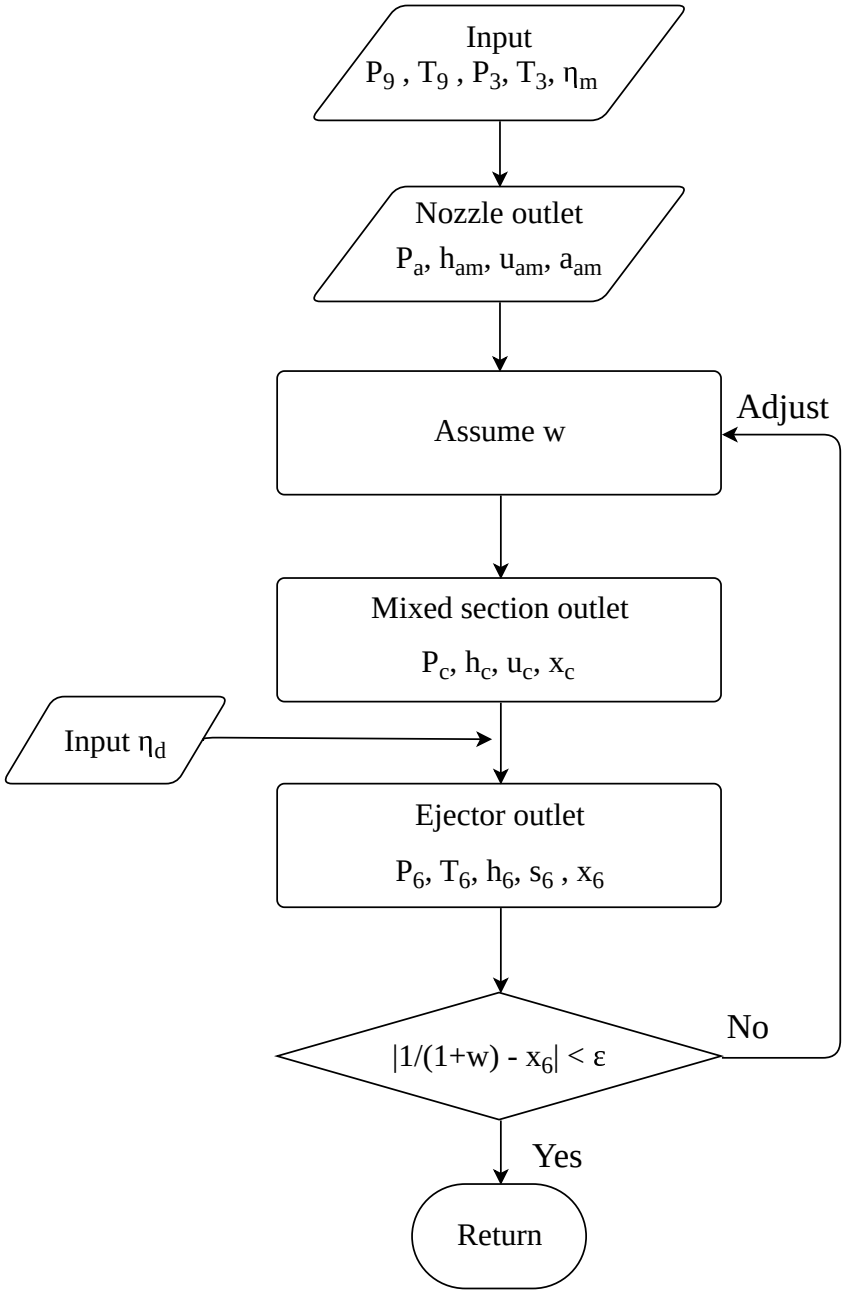

FIGURE 2.4: Flow chart of modeling sequence for the ejector model of Deng [63]

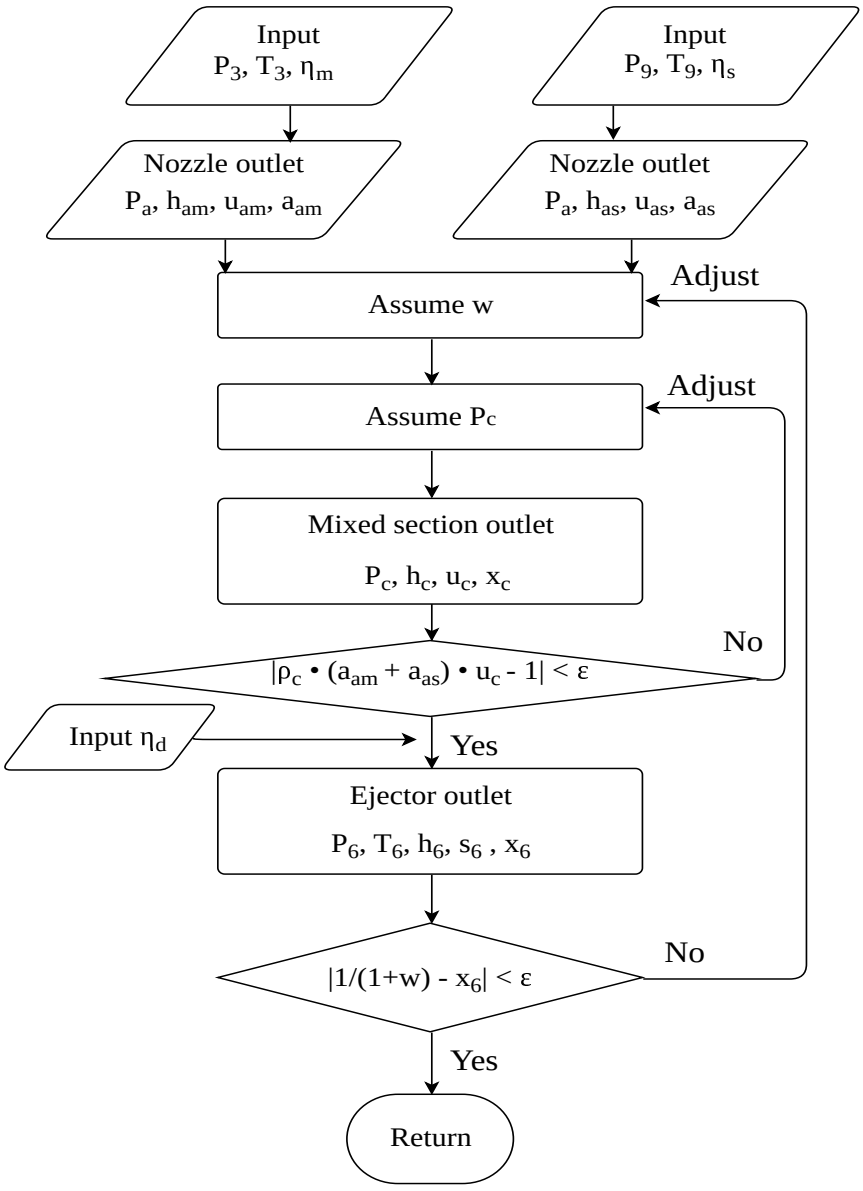

FIGURE 2.5: Flow chart of modeling sequence for the ejector model of Li [62]

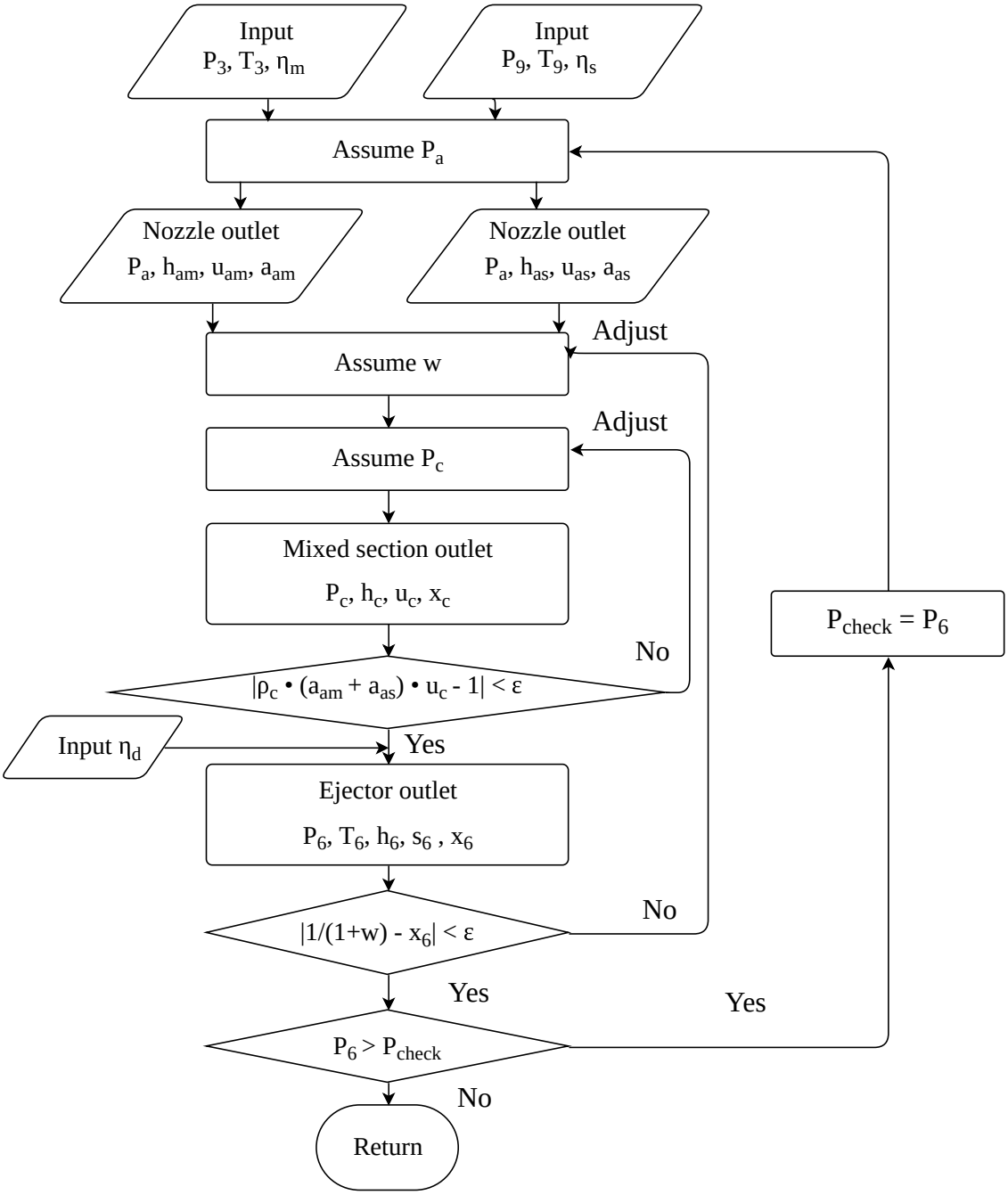

FIGURE 2.6: Flow chart of modeling sequence for the ejector model of Atmaca [54]

Upon reproducing the three models based on the original works [54, 62, 63], the simulated entrainment ratio, ejector outlet vapor quality, and cycle COP are compared with the original simulation values from the respective articles [54, 62, 63]. The comparison shows good agreement, as depicted in the Appendix.A. As a result, the models are validated and can be used to compare with each other using independent experimental data, a comparison that has never been done in the literature before.

2.4 Sensitivity analysis of isentropic efficiencies in ejector components and compressor

After reproducing the three 0-D thermodynamic models, the influence of the input isentropic efficiencies of ejector components and the compressor can be numerically analyzed.

2.4.1 Boundary conditions for sensitivity analysis

The efficiencies of the ejector components depend on various factors, including the ejector geometry, flow path design, working fluid, as well as pressure and temperature values. The choice of isentropic efficiency for each section lacks a universal standard. In most of the literature studied, individual ejector component isentropic efficiencies are assumed to range from 0.5 to 0.95 [54, 62–73]. To investigate the impact of these efficiencies on the ejector and system performance, this section presents a sensitivity analysis of the isentropic efficiencies of the ejector components and the compressor using the reproduced models. Throughout the sensitivity analysis, all models operate under identical working conditions, as shown in Table. 2.1. The default efficiencies for the nozzle, diffuser, and compressor are 0.8, 0.8, and 0.75, respectively.

TABLE 2.1: Input parameters for sensitivity analysis

Gas cooling pressure	Evaporation pressure	Gas cooler outlet temperature	Evaporation temperature
101.3 bar	25.4 bar	48.1 °C	0.3 °C

The results of the sensitivity analysis of the 0-D thermodynamic models are presented in Fig. 2.7 through Fig. 2.9. For each model, the influence of the isentropic efficiencies of ejector components on the ejector outlet pressure and the cycle COP is examined. Additionally, the impact of the compressor efficiency on the cycle COP is also investigated.

2.4.2 Results of sensitivity analysis for model of Deng [63]

For Deng's model [63], where there is no expansion in the suction nozzle, only the efficiencies of the motive nozzle, diffuser, and compressor are studied. As depicted

in Fig. 2.7a, the ejector outlet pressure increases with the efficiencies of the ejector components. Specifically, the outlet pressure rises from 29.8 bars to 42.3 bars (approximately a 42 % increase) when the motive nozzle efficiency increases from 0.3 to 0.9. Similarly, for the diffuser, the trend is the same, and the outlet pressure increases from 30.0 bars to 42.1 bars (about a 40 % increase). The impact of the motive nozzle and diffuser efficiencies is nearly identical, with the ejector outlet pressure being slightly more sensitive to changes in motive nozzle efficiency.

As shown in Fig. 2.7b, the cycle COP increases as the efficiency of the components improves, and the correlation is nearly linear. Among the three component efficiencies, the COP is most sensitive to the efficiency of the compressor. When the isentropic efficiency of the compressor increases from 0.3 to 0.9, the COP rises from 0.50 to 1.49, resulting in a relative change in COP of around 200 %. For the motive nozzle and the diffuser, the two curves almost overlap, indicating that the isentropic efficiency of the motive nozzle and the diffuser has nearly the same effect on the system COP in this model. The sensitivity related to the motive nozzle and the diffuser is much lower than for the compressor, with the relative change in COP being nearly 37 %.

2.4.3 Results of sensitivity analysis for the model of Li [62]

For Li's model [62], as the model considers that the suction flow also slightly expands in the nozzle, an extra efficiency is added to the analysis. As illustrated in Fig. 2.8a, the ejector outlet pressure also increases with the efficiencies of the ejector components. The outlet pressure is most sensitive to the motive nozzle efficiency, increasing from 29.6 bars to 35.9 bars (a 21.4 % augmentation) in the interval from 0.3 to 0.9. The second most sensitive component is the suction nozzle efficiency, resulting in a pressure lift from 32.0 bars to 35.4 bars (a 10.4 % augmentation). The least sensitive component is the diffuser, with a pressure lift from 34.0 bars to 35.2 bars (a 3.5 % augmentation).

As observed in Fig. 2.8b, the isentropic efficiency of the compressor also has the most significant impact on the system COP for Li's model [62], compared to the individual components of the ejector. Among the ejector components, the system COP is more sensitive to the motive nozzle efficiency, followed by the suction nozzle, and lastly, the isentropic efficiency of the diffuser. Specifically, when the isentropic efficiency of each component increases from 0.3 to 0.9, the corresponding relative changes in COP are 200 %, 17 %, 10 %, and 3 %, respectively.

2.4.4 Results of sensitivity analysis for model of Atmaca [54]

For Atmaca's model [54], the trend is generally similar to the two models above. As shown in Fig. 2.9a, the correlation is generally linear, except in the range of high isentropic efficiency of the motive nozzle. Quantitatively analyzed, the relative increase in ejector outlet pressure when component efficiencies rise from 0.3 to 0.9 is 49

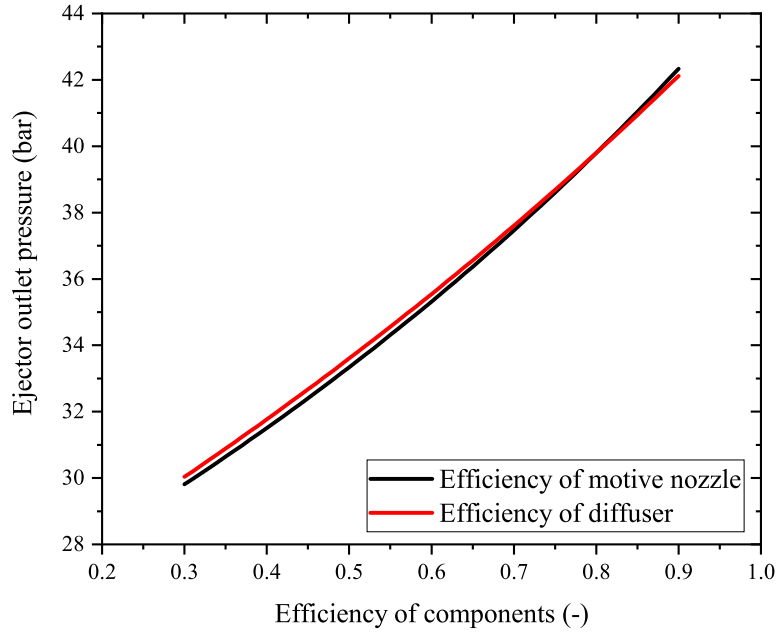

(A) Ejector outlet pressure as a function of components efficiency

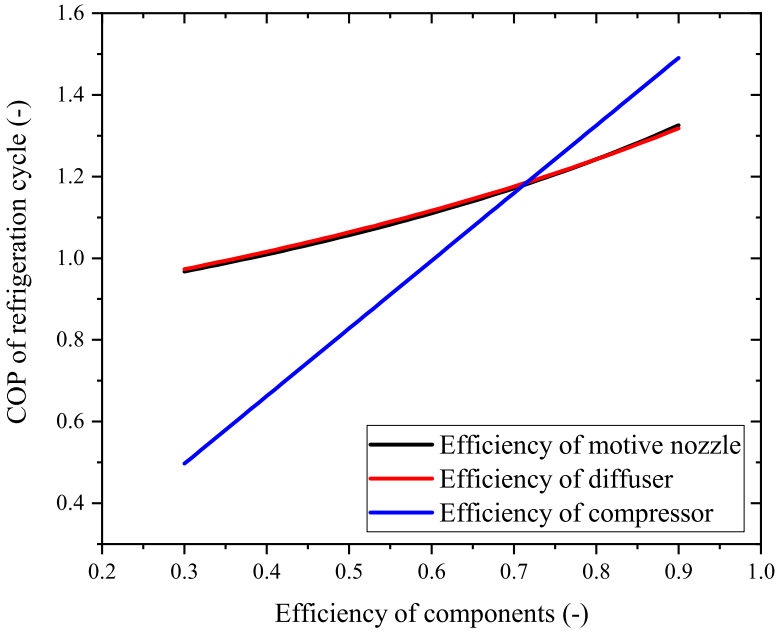

(B) Cycle COP as a function of components efficiency

FIGURE 2.7: Sensitivity analysis for the ejector components and compressor efficiencies, model of Deng [63]

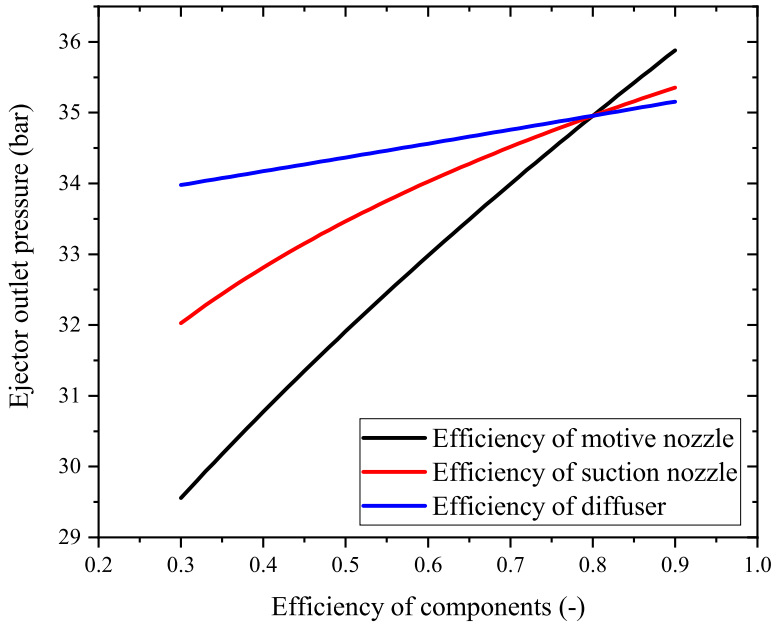

(A) Ejector outlet pressure as a function of components efficiency

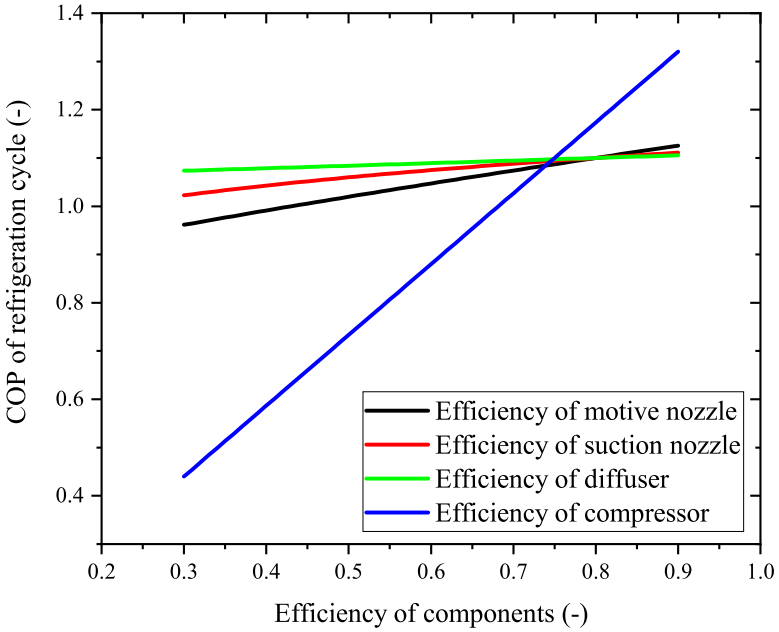

(B) Cycle COP as a function of components efficiency

FIGURE 2.8: Sensitivity analysis for the ejector components and compressor efficiencies, model of Li [62]

%, 14 %, and 13 % for the motive nozzle, suction nozzle, and diffuser, respectively. The ejector outlet pressure is most sensitive to the motive nozzle efficiency, followed by the suction nozzle and diffuser, with almost the same effect.

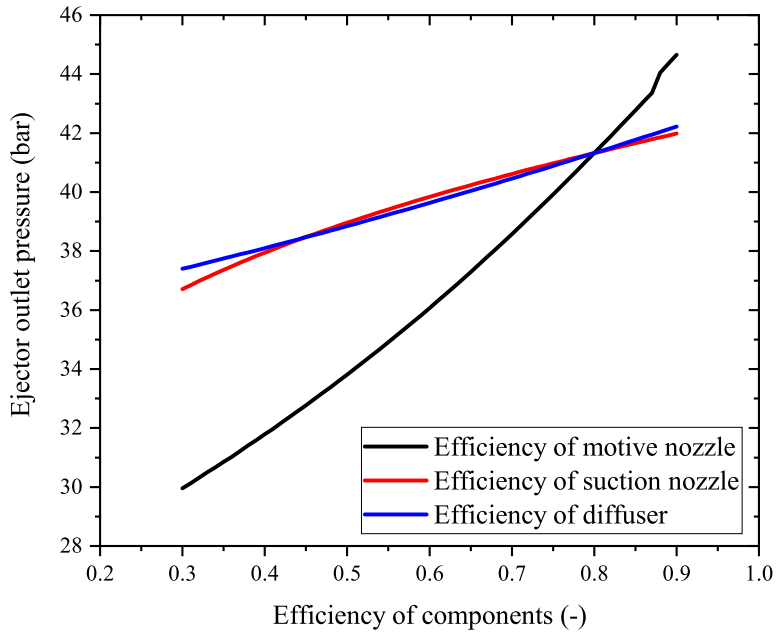

(A) Ejector outlet pressure as a function of components efficiency

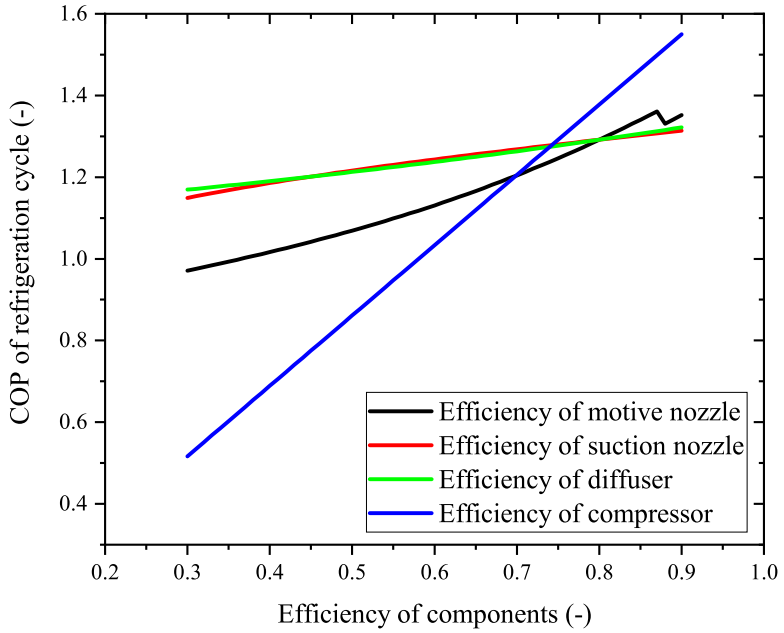

(B) Cycle COP as a function of components eefficiency

FIGURE 2.9: Sensitivity analysis for the ejector components and compressor efficiencies, model of Atmaca [54]

In Fig. 2.9b, it can be concluded that the isentropic efficiency of the compressor also has the most significant impact on the system COP for Atmaca's model [54], followed by the motive nozzle, suction nozzle, and diffuser. The relative increase in COP is 200 %, 39 %, 14 %, and 13 %, respectively.

It's noteworthy that when the motive nozzle increases from 0.87 to 0.88, the ejector outlet pressure increases, but the cycle COP decreases. This decrease is attributed to the change in entrainment ratio, dropping from 0.25 to 0.24 (while the entrainment ratio remains the same at 0.25 for the rest of the simulation). Therefore, even though the compression work in the compressor per unit mass flow decreases, the cycle COP decreases due to the worsened entrainment effect of the ejector.

2.4.5 Conclusion

In the above analysis, it is observed that for the ejector, the performance is most sensitive to the motive nozzle efficiency in Li's model [62] and Atmaca's model [54], compared to the suction nozzle and diffuser. However, for Deng's model [63], the effects of the motive nozzle and diffuser are nearly identical. Additionally, the COP of the system is much more sensitive to the isentropic efficiency of the compressor than to that of the individual components of the ejector for all three models [54, 62, 63]. Therefore, when conducting 0-D simulations of the ejector expansion cycle, it is crucial to verify the accuracy of the input efficiency of the compressor to avoid simulation failure. While approximate performance curves provided by manufacturers often serve as a reference for compressors during simulations, there is no accurate calculation formula in the available literature that is universally applicable for all operating conditions for the ejector components. Hence, deviations in the efficiencies of ejector components during the modeling process can lead to significant cumulative simulation errors.

2.5 Experimental validation of 0-D thermodynamic models

Two sets of independent experimental data, compiled from current literature sources [112, 113], are employed to compare and validate the models. The accuracy of the two models can be analyzed and compared by comparing the simulation results with the experimental data under the same operating parameters.

2.5.1 Experimental setup from Haberschill et al. [112]

The first set of experimental data is derived from a prototype of an air/water refrigeration machine that employs CO_2 as a refrigerant [112]. The simplified cycle schematic is depicted in Fig. 2.10. The system consists of three independent circuits. The first circuit is dedicated to CO_2, the second is an auxiliary water circuit with controlled temperature and flow rate to simulate variations in the hot source, and the third is an air circuit with regulated temperature and humidity to simulate changes

in climatic conditions. A Bock RKX26/31-4 brand 6-cylinder semi-hermetic radial piston compressor, powered by a Danfoss variable-speed driver operating from 0 to 1450 rpm, is employed. Additionally, a coaxial high-pressure water exchanger is installed to cool the vapor.

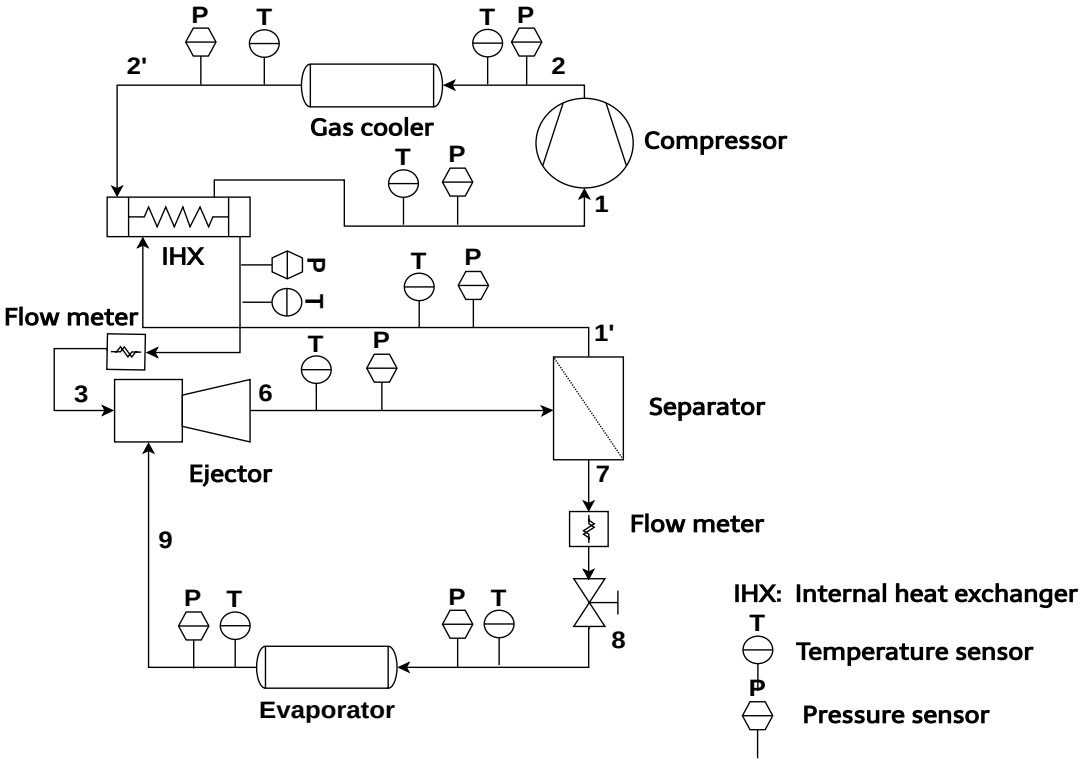

FIGURE 2.10: Schematic of the test bench from Haberschill et al. [112]

In Fig. 2.10, an internal heat exchanger is integrated into the system, allowing the supercritical flow at high temperatures from the gas cooler to preheat the saturated vapor exiting from the separator. As an adjustment to the model, the temperature of the heated vapor is considered an additional input, and the outlet parameters of the cooled fluid are calculated based on energy balance. The input pressure and temperature values, along with the mass flow rates for the motive and suction flows, fall within the ranges specified in Table. 2.2.

TABLE 2.2: Range and measurement accuracy of the input parameters, data from Haberschill et al. [112]

	Mass flow rate ($\dot{m}_m / \dot{m}_s$)	Input pressures (P_m / P_s)	Input temperatures (T_m / T_s)
Range	139.7 to 185.3 kg/h 36.4 to 62.8 kg/h	7.8 to 10.3 MPa 2.2 to 3.0 MPa	33.5 to 52.1 °C -9.5 to 4.3 °C
Accuracy	0.5 %	± 0.25 %	± 0.5 °C

2.5.2 Experimental setup from Zhu et al. [113]

To further validate the accuracy of the models, an additional set of experimental data, obtained from Zhu et al. [113], is briefly outlined here. The experimental rig schematic is depicted in Fig. 2.11. In the ejector expansion refrigeration cycle, the compressor used is a DORIN CD180H equipped with a 7.5 kW inverter for compressor speed control. The gas cooler is a counter-flow plate heat exchanger rated at 7.5 kW, using water as the coolant. The evaporator features a parallel flow microchannel heat exchanger with a variable-speed fan to control the super heat of the evaporator outflow, and its capacity is 5 kW. Additionally, a fan heater with a maximum capacity of 3 kW is positioned near the evaporator to maintain room temperature.

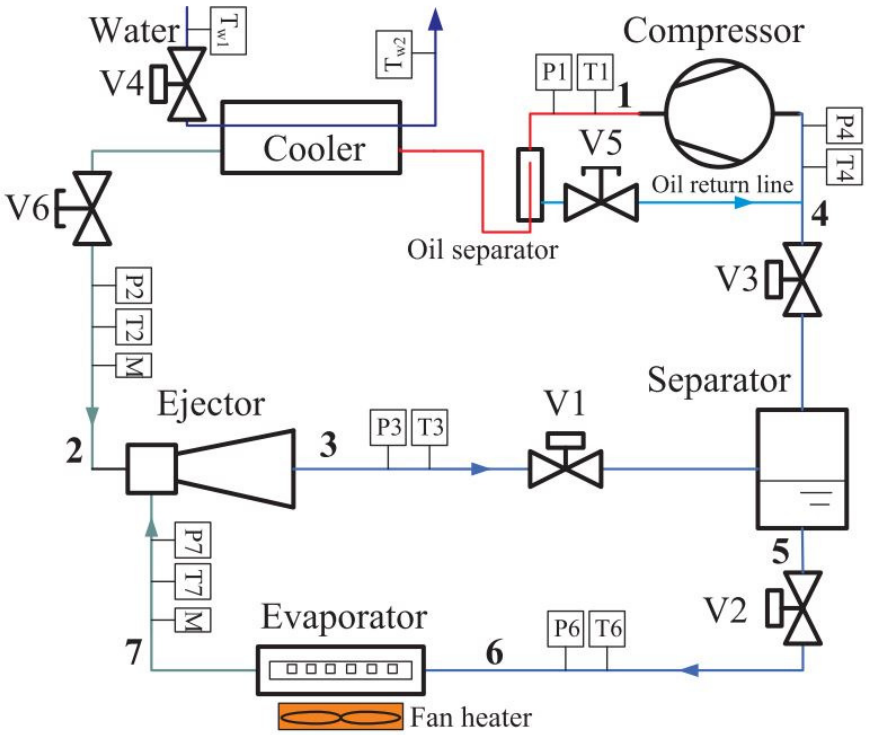

FIGURE 2.11: Schematic of the test bench from Zhu et al. [113]

The input pressure and temperature values, along with the mass flow rates for the motive and suction flows, are within the ranges specified in Table. 2.3.

TABLE 2.3: Range and measurement accuracy of the input parameters, data from Zhu et al. [113]

	Mass flow rate ($\dot{m}_m / \dot{m}_s$)	Input pressures (P_m / P_s)	Input temperatures (T_m / T_s)
Range	60.0 to 109.5 kg/h 13.3 to 65.1 kg/h	8.1 to 9.9 MPa 3.0 to 3.7 MPa	34.9 to 35.8 °C 20.5 to 24 °C
Accuracy	± 0.1 %	± 0.1 %	± 0.2 °C

2.5.3 Results and analysis of the comparatively experimental validation of 0-D thermodynamic models

To validate the 0-D thermodynamic models presented in this paper, the required input parameters include the temperatures and pressures of the motive and suction flows. When utilizing the dataset from Haberschill et al. [112], the outlet temperature of the internal heat exchanger for the heated flow is considered an additional input parameter. Considering its significant impact on system performance, the compressor efficiencies for both test units are extracted from the corresponding experimental data to prevent substantial deviations.

The input isentropic efficiency of the motive nozzle, suction nozzle, and diffuser is set at 0.6 for the ejector of Haberschill et al. [112] due to the low COP and entrainment ratio concluded from the experimental data. For the ejector of Zhu et al. [113], the isentropic efficiencies are set at 0.8. In the model of Li [62], the fixed pressure drop in the suction nozzle is set as 0.03 MPa.

The three 0-D models undergo verification using the two chosen sets of independent experimental data, focusing on key performance indicators such as ejector outlet pressure and COP for refrigeration applications. For each model, the simulated entrainment ratio of the ejector is compared to the value derived from the measured flow rates of the primary and suction flows. Additionally, other parameters, including vapor quality at the ejector outlet, are cross-verified with the experimental data.

Validation results based on the experimental data of Haberschill et al. [112]

Fig. 2.12 to Fig. 2.15 show the comparison between the simulated parameters by three 0-D thermodynamic models with the measured values or calculated values based on measured data from Haberschill et al. [112]. These parameters include the outlet pressure, entrainment ratio, outlet vapor quality of the ejector, as well as the cycle COP for the refrigeration application.

From Fig. 2.12, all three models [54, 62, 63] predict the ejector outlet pressure with satisfactory accuracy; the absolute relative deviation is mostly below 10 % for all three models [54, 62, 63]. However, for the models of Li and Atmaca, the deviation can reach up to 20 % in some cases. In general comparison, the model of Deng [63] has the most accurate prediction for the ejector outlet pressure.

Moving to Fig. 2.13, the simulation values show a large deviation from the measured data. The models of Deng and Li demonstrate similar accuracy, with deviations generally below 30 %, though in some cases, it can reach close to 50 %. For the model of Atmaca [54], the deviation is much larger, exceeding 50 % for high entrainment ratio cases.

The prediction accuracy for the ejector outlet vapor quality is similar for all three models [54, 62, 63], with simulated values agreeing well with the experimental data, showing an absolute relative deviation below 5 %. It is worth noting that for the

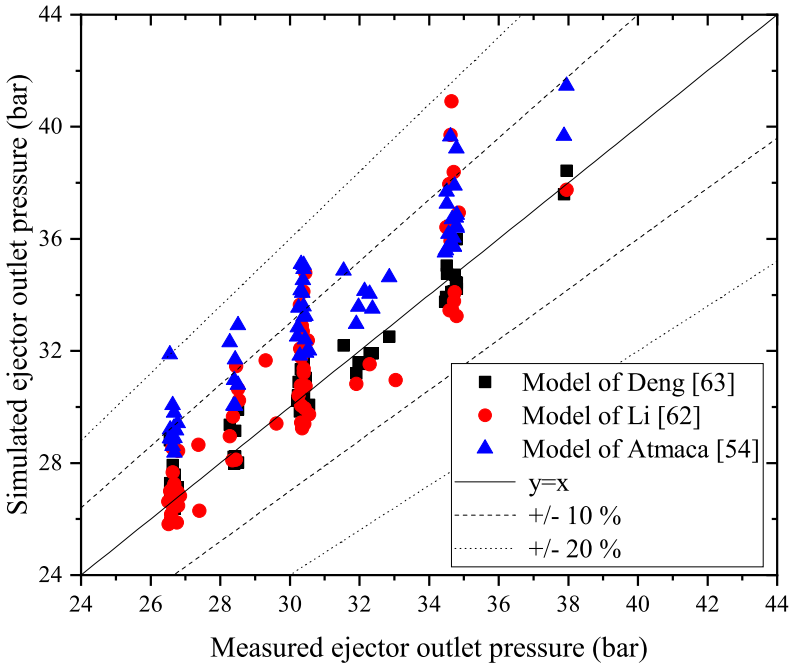

FIGURE 2.12: Simulated ejector outlet pressure versus measured data from Haberschill et al. [112]

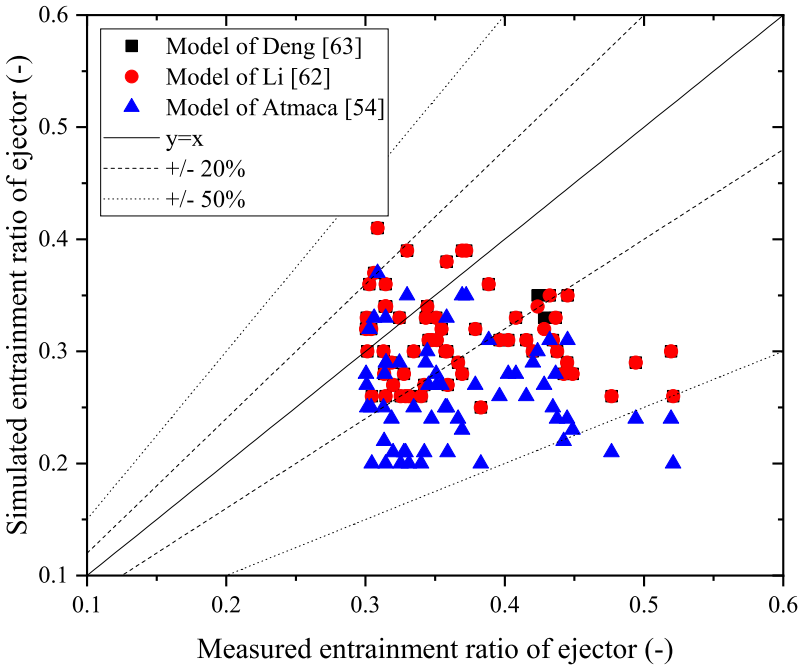

FIGURE 2.13: Simulated ejector entrainment ratio versus measured data from Haberschill et al. [112]

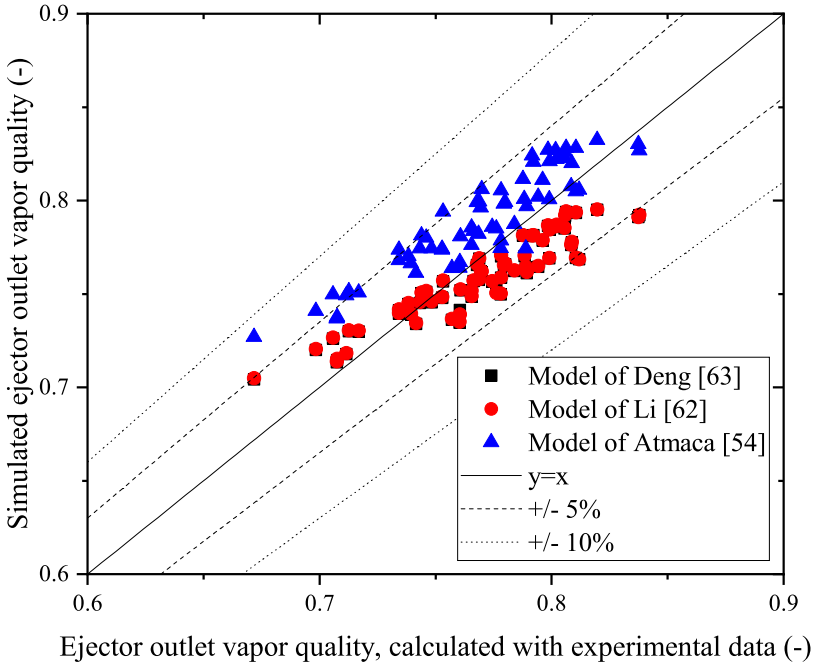

FIGURE 2.14: Simulated outlet vapor quality as a function of the vapor quality calculated with experimental data from Haberschill et al. [112]

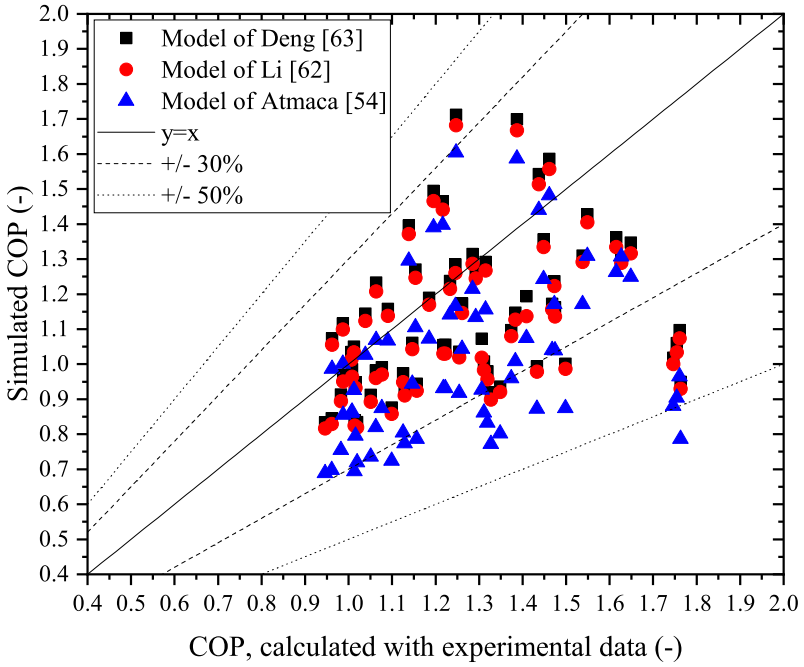

FIGURE 2.15: Simulated cycle COP as a function of the COP calculated with experimental data from Haberschill et al. [112]

model of Atmaca, the simulated vapor quality is higher than the value calculated with experimental data, as concluded from Fig. 2.14.

Regarding the cycle COP, the results mirror those of the entrainment ratio. For the models of Deng and Li, the absolute relative deviation is generally below 30 %, while for the model of Atmaca [54], in some cases, the deviation can exceed 50 %.

Validation results based on the experimental data of Zhu et al. [113]

Fig. 2.16 to Fig. 2.19 shows the comparison between the simulated parameters by three 0-D thermodynamic models with the measured values or calculated values based on measured data from Haberschill et al. [113].

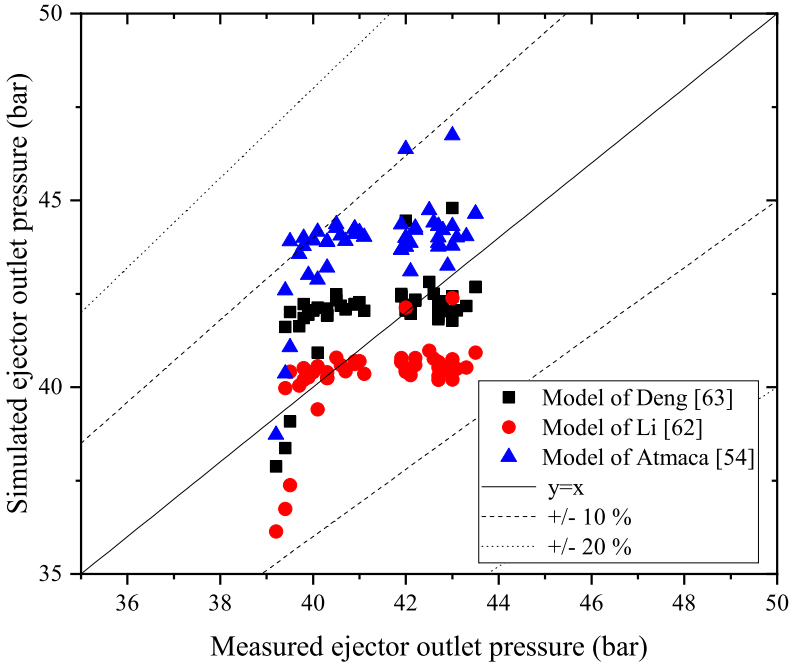

FIGURE 2.16: Simulated ejector outlet pressure versus measured data from Zhu et al. [113]

From Fig. 2.16, the model of Atmaca [54] shows a less accurate prediction of the ejector outlet pressure compared to the models of Li and Deng. However, the absolute relative deviation is mostly below 10 % for all three models [54, 62, 63]. Therefore, the 0-D thermodynamic models predict the ejector outlet pressure well.

When validating the three 0-D models using the dataset from Zhu et al. [113], all three models [54, 62, 63] show similar accuracy in predicting the ejector entrainment ratio, vapor quality, and cycle COP, as concluded from Fig. 2.17 to Fig. 2.19. In more detail, the simulated outlet vapor quality agrees well with the value calculated from

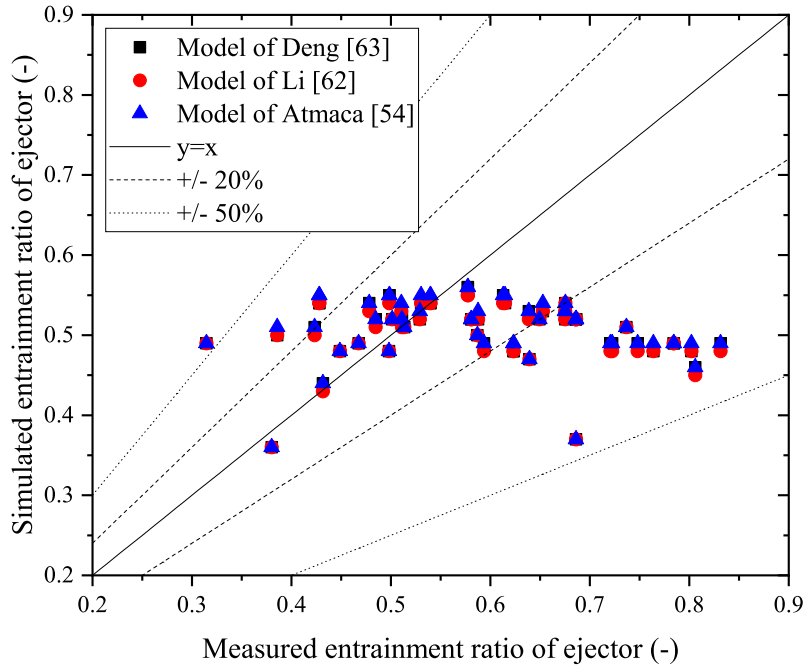

FIGURE 2.17: Simulated ejector entrainment ratio versus measured data from Zhu et al. [113]

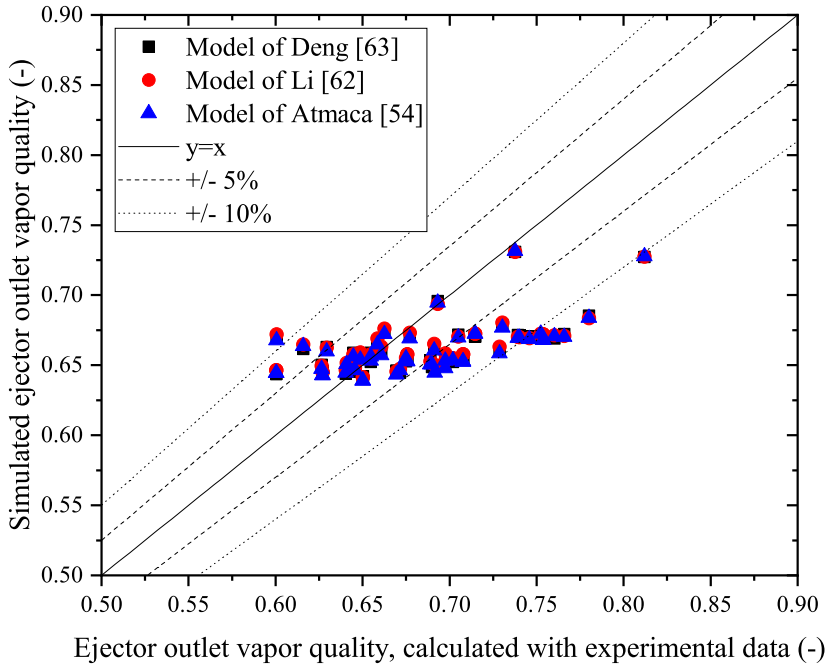

FIGURE 2.18: Simulated outlet vapor quality as a function of the vapor quality calculated with experimental data from Zhu et al. [113]

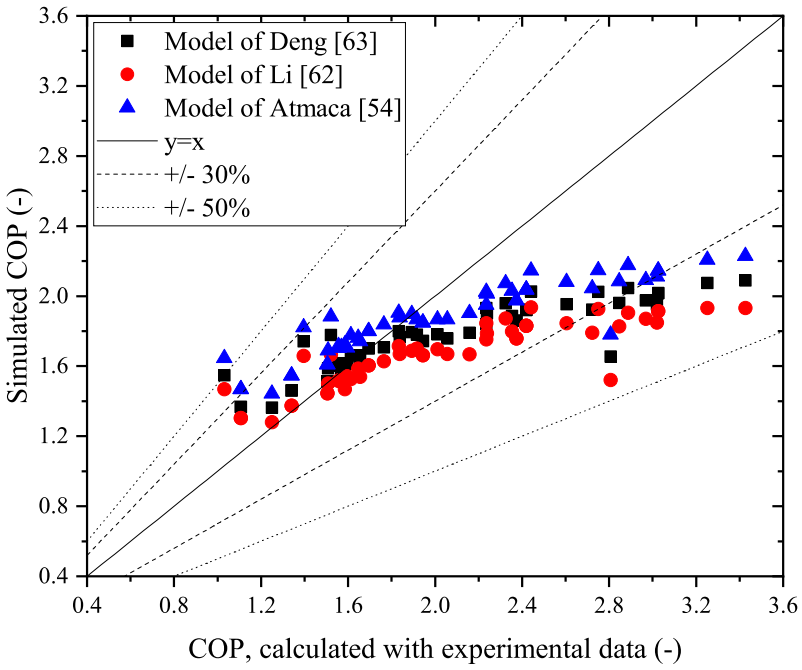

FIGURE 2.19: Simulated cycle COP as a function of the COP calculated with experimental data from Zhu et al. [113]

measured experimental data, with an absolute relative deviation below 10 %. However, the deviation between the simulated entrainment ratio and cycle COP is much larger, exceeding 50 % in some cases.

Ejector efficiency analysis

Ejector efficiency is a crucial performance metric defined as the ratio of the amount of expansion work recovered by the ejector to the maximum possible expansion work rate recovery potential (Eq. (2.4)). Fig. 2.20 and Fig. 2.21 show the calculated ejector efficiency change based on the results simulated by three thermodynamic models with the measured entrainment ratio by Haberschill et al. [112] and Zhu et al. [113].

Concluding from Fig. 2.20 and Fig. 2.21, for all three 0-D thermodynamic models and both datasets, the ejector efficiency is nearly linearly correlated to the entrainment ratio. The ejector efficiency shows a higher value based on the simulation results of the model of Atmaca [54], followed by the model of Deng [63], and then the model of Li [62]. Moreover, by comparing Fig. 2.20 and Fig. 2.21, it can be observed that the ejector of the test facility from Zhu et al. [113] has a higher value of ejector efficiency than the ejector of the test facility from Haberschill et al. [112], indicating that the ejector performs better with the geometry configuration of the ejector and operational conditions of Zhu et al. [113]

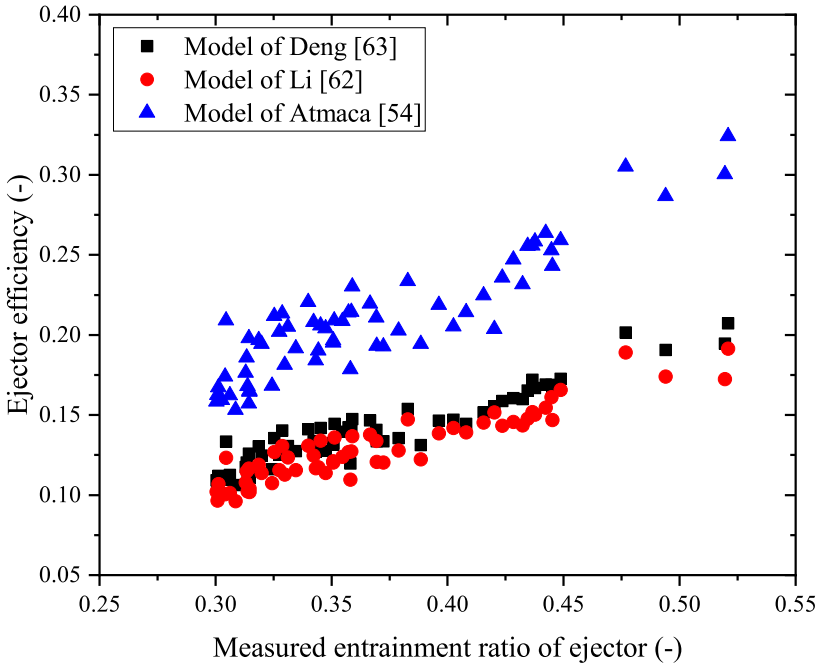

FIGURE 2.20: Simulated ejector efficiency as a function of the measured entrainment ratio of ejector from Haberschill et al. [113]

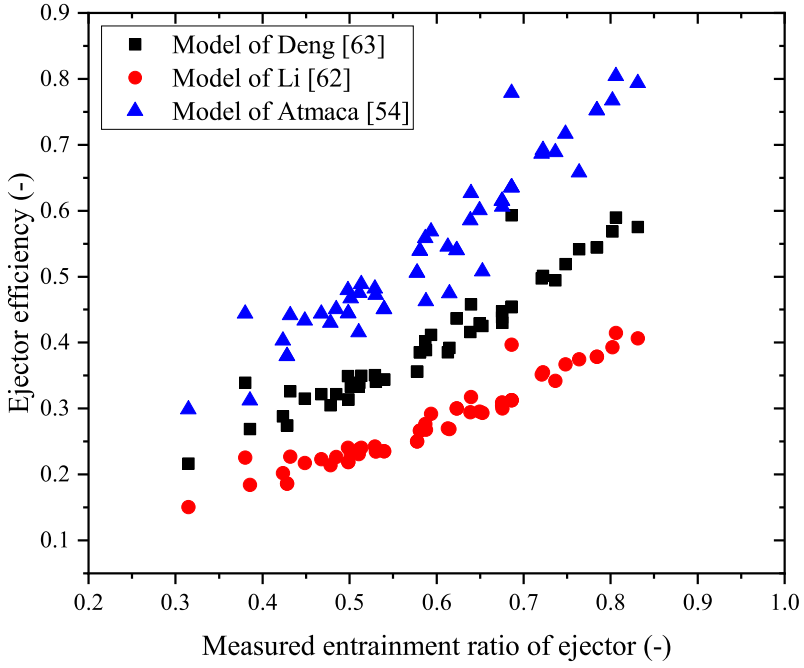

FIGURE 2.21: Simulated ejector efficiency as a function of the measured entrainment ratio of ejector from Zhu et al. [113]

2.5.4 Conclusion

Concluding from the above validation and analysis of the three 0-D thermodynamic models, it can be inferred that these models offer satisfactory predictions for the outlet pressure and vapor quality of the ejector (absolute relative deviation below 10 %). However, for the entrainment ratio and cycle COP, the simulation deviation is substantial (absolute relative deviation as high as 50 %). In a general evaluation, the model of Deng [63] shows better performance, indicating that the simplification of the pressure variation during the mixing section has no significant effect on simulation accuracy.

Ejector efficiency is a crucial index for evaluating ejector performance. It is linearly correlated with the ejector entrainment ratio and varies significantly between different ejectors.

2.6 Liquid mass balance in the separator

In the ejector expansion cycle, the motive flow mixes with the suction flow, exiting the ejector as a two-phase flow. Subsequently, in the separator, the liquid at the ejector outlet is separated and directed to the evaporator. Conversely, the vapor emerging from the ejector outlet is divided, with a portion entering the compressor, as illustrated in Fig. 2.22.

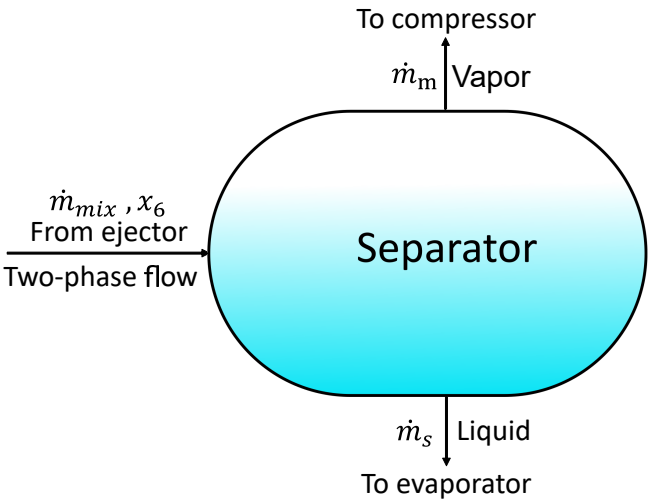

FIGURE 2.22: Liquid mass balance before and after the separator

During steady-state operation of the system, there is a general mass balance for the separator, as defined by Eq. (2.30), which is maintained. In addition, the liquid mass balance is defined by Eq. (2.31). Under this equilibrium, the mass flow of liquid entering the separator precisely matches the mass flow exiting the separator, resulting in a constant liquid level within the separator. The liquid portion at the ejector outlet flow is entirely separated by the separator and directed towards the evaporator. All three 0-D models under study are based on such a liquid balance state.

$$\dot{m}_{mix} = \dot{m}_m + \dot{m}_s \tag{2.30}$$

$$\dot{m}_{mix} \cdot (1 - x_6) = \dot{m}_s \tag{2.31}$$

2.6.1 Definition of liquid imbalance

It is evident from the analysis based on two sets of experimental data [112, 113] that maintaining liquid balance in the actual system operation is challenging in most cases. In actual system operation under steady-state conditions, considering mass balance, momentum conservation, and energy conservation, it is observed that the liquid level in the separator continually changes—either rising or falling. This operating state of the actual system is termed pseudo-steady state to differentiate it from the steady state with liquid balance in the 0-D models.

Although the general mass balance for the separator remains valid under pseudo-steady state, the liquid balance (Eq. (2.31)) before and after the separator is disrupted, and the liquid level undergoes constant changes during operation. In practice, experimental test facilities often use larger separator volumes to prevent complete filling with vapor or liquid and ensure a stable operation period [112, 113].

The liquid imbalance primarily arises due to discrepancies between the entrainment ratio of the ejector and the vapor quality at the ejector outlet. In actual operation, for a chosen ejector, the entrainment ratio w and vapor quality x_6 satisfy Eq. (2.28) (equivalent to Eq. (2.31)) only under specific operating conditions, which are difficult to maintain and predict. However, in the actual operating system, Eq. (2.28) does not consistently hold because operating parameters, such as pressures and temperatures, deviate from specific values for steady state, and the system lacks self-regulation. As a result, the liquid level in the separator dynamically changes. This is why some researchers have proposed improved ejector refrigeration systems to control the liquid level of the separator [62, 69, 116].

A new expression for the coefficient of liquid mass imbalance [113] for the vapor-liquid separator, denoted as β, is defined by Eq. (2.32). β can be used to quantify the deviation of the separator from pseudo-steady state during actual operation compared to the ideal steady state in 0-D models.

$$\beta = (\dot{m}_{mix} \cdot (1 - x_6) - \dot{m}_s)/\dot{m}_s \tag{2.32}$$

The liquid imbalance coefficient signifies the presence of excess vapor or liquid at the separator outlet, resulting from the disparity between the ejector inlet entrainment ratio and the ejector outlet vapor quality. A negative value of β indicates a surplus of liquid at the separator outlet, while a positive value suggests an excess of vapor at the outlet.

Fig. 2.23 and Fig. 2.24 show the correlation between the relative deviation of the simulated cycle COP and the coefficient of liquid imbalance based on both datasets.

It can be concluded that the simulation deviation of the cycle COP is linearly correlated with the coefficient of liquid mass imbalance. This implies that the liquid mass imbalance occurring in the actual operation of the cycle is the main source of the simulation deviation of the cycle COP.

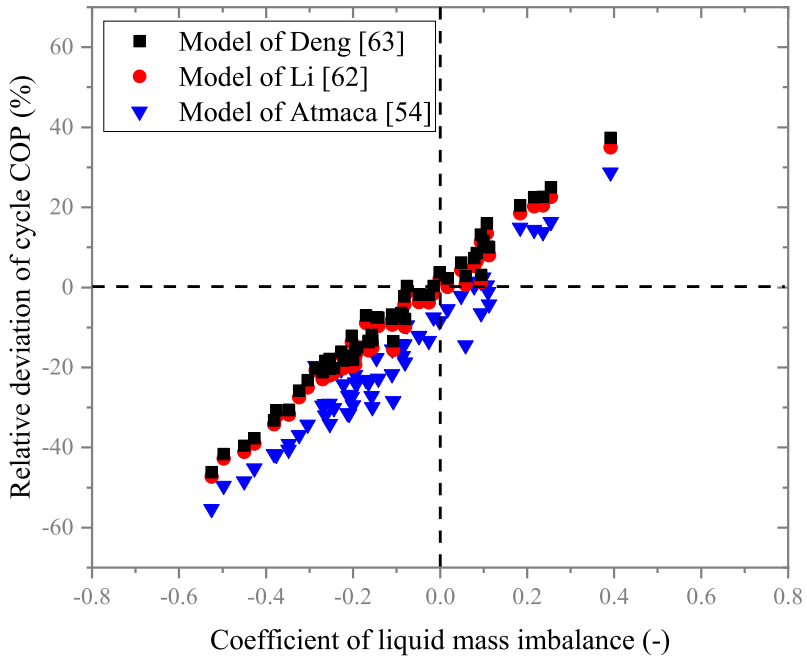

FIGURE 2.23: The relative deviation of simulated cycle COP as a function of coefficient of liquid imbalance based on data from Haberschill et al. [112]

2.6.2 Elimination of liquid imbalances through data post-processing

For all the 0-D models available in the literature, the liquid balance (Eq. (2.31)) is one of the core criteria for loop iteration to obtain the entrainment ratio of the ejector [54, 62–73], which means during the 0-D modeling, the cycle works at a steady state and the liquid level in the separator will keep constant. However, for real operation system, the liquid imbalance is a common issue and hard to eliminate. There are currently no scholars who have built an actual experimental system with liquid level regulation control device [113].

In order to validate the 0-D models using the available experimental data [112, 113] based on steady state (without liquid imbalance), a data post-processing method based on a hypothetical system is introduced (inspired by the new theoretical configuration of the ejector expansion refrigeration system from He et al. [116]). The schematic of the hypothetical corrected system is depicted as Fig. 2.25. The method is not a restructuring of the actual operating system but rather an extrapolation of the system's performances if it operated without liquid imbalance. Then, the processed

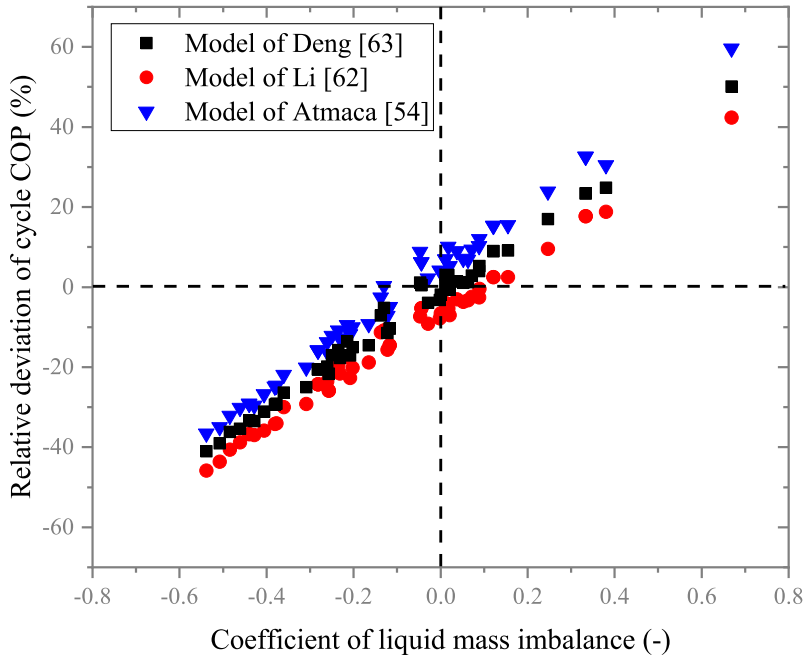

FIGURE 2.24: The relative deviation of simulated cycle COP as a function of coefficient of liquid imbalance based on data from Zhu et al. [113]

experimental data can be used to validate the three 0-D thermodynamic models that operate at steady state without liquid imbalance, as described in the modeling.

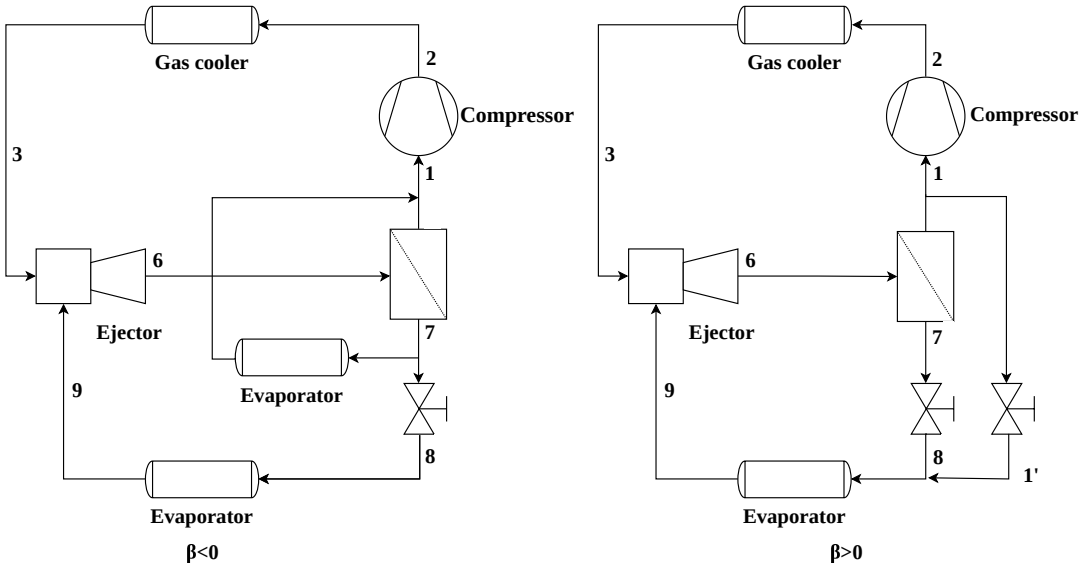

FIGURE 2.25: Schematic of the hypothetical optimized system for the data post-processing. β is the coefficient of liquid mass balance (Eq. (2.32))

From Fig. 2.25, there are two cases for data processing based on the value of β.

To offset the excess liquid (β is negative), it can be assumed that an additional evaporator is installed to evaporates the liquid into saturated vapor. The saturated vapor mixes with the vapor from the separator outlet and then flows into the compressor. For the case of excess vapor at the outlet (β is positive). It can be assumed that there is a bypass loop to mix the excess vapor at the outlet of the separator with the two-phase flow exiting after the expansion valve. The mixture then enters into the evaporator.

The mass flow rates of the motive and suction flows after data post-processing are determined by the vapor quality at the ejector outlet. The unit mass flow rate of motive and suction flows ($\dot{m}_{m,unit}$,$\dot{m}_{s,unit}$) can be expressed by Eq. (2.33) and Eq. (2.34), where w_{new} is the new entrainment ratio after data post-processing. The unit mass flow rate is based on the basis that the total flow rate is 1.

$$\dot{m}_{m,unit} = 1/(1 + w_{new}) = x_6 \tag{2.33}$$

$$\dot{m}_{s,unit} = w_{new}/(1 + w_{new}) = 1 - x_6 \tag{2.34}$$

After data post-processing, for the compressor, the inlet and outlet temperatures and pressures are unchanged, so the variation of compression work is only related to the correction of the mass flow rate.

The capacity of the evaporator will change accordingly to the value of β. When β is negative, besides the change due to the mass flow rate correction, the capacity of the extra evaporator has to be considered. The modified capacity of the evaporator for unit total mass flow rate is calculated using Eq. (2.35) and Eq. (2.36). Where $\dot{m}_{s,unit} \cdot \beta$ is the mass flow rate in the extra evaporator, $h_1 - h_7$ is the specific enthalpy change in the extra evaporator and $h_9 - h_8$ is the specific enthalpy change in the main evaporator.

$$\dot{Q}_{cool,extra,unit} = \dot{m}_{s,unit} \cdot \beta \cdot (h_1 - h_7) \tag{2.35}$$

$$\dot{Q}_{cool,unit} = \dot{m}_{s,unit} \cdot (h_9 - h_8) + \dot{Q}_{cool,extra,unit} \tag{2.36}$$

When β is positive, in addition to the correction of the flow rate, the specific enthalpy of the evaporator inlet also changes due to the mixing of the two fluids (fluid from the outlet of the separator and the exceed vapor from the bypass loop of compressor inlet). The new capacity of the evaporator for unit total mass flow rate is calculated by Eq. (2.37) and Eq. (2.38), where $h_{8,new}$ is specific enthalpy value of mixed fluid at state 8.

$$h_{8,new} = (\dot{m}_s \cdot h_8 + \dot{m}_s \cdot \beta \cdot h_1)/((\dot{m}_m + \dot{m}_s) \cdot (1 - x_6)) \tag{2.37}$$

$$\dot{Q}_{cool,unit} = \dot{m}_{s,unit} \cdot (h_9 - h_{8,new}) \tag{2.38}$$

With such recalculation applied to the obtained experimental data, the liquid imbalance during the operation of the actual system can be theoretically eliminated, then the corrected experimental data allows to validate the models under a steady state (without liquid imbalance), which is consistent to the state in all the 0-D thermodynamic models.

2.6.3 Validation of 0-D models with post-processed data

After the post-processing of the obtained experimental data, the liquid imbalance during the operation of the actual system can be theoretically eliminated. The simulated entrainment ratio of the ejector and cycle COP are then validated again with the modified entrainment ratio and cycle COP.

Fig. 2.26 and Fig. 2.27 display the simulated ejector entrainment ratio as a function of entrainment ratio with post-processed data from both datasets. It is concluded that after the post-processing of the obtained experimental data to eliminate the liquid imbalance during the actual operation of the test facility, all three 0-D thermodynamic models demonstrate good accuracy on the prediction of the ejector entrainment ratio. The relative deviation of the entrainment ratio is generally below 10 % for the dataset of Haberschill et al. [112], and is below 5 % for the dataset of Zhu et al. [113].

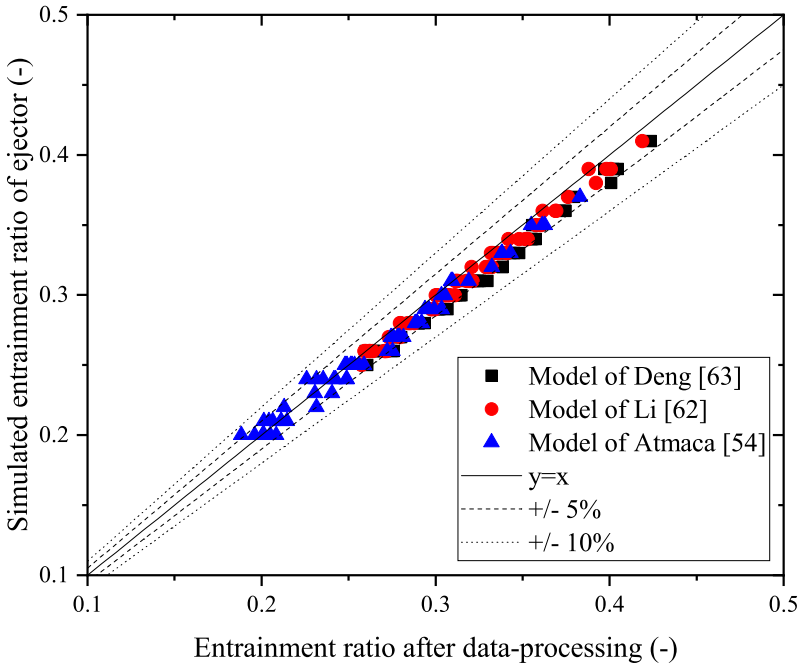

FIGURE 2.26: Simulated ejector entrainment ratio as a function of entrainment ratio with post-processed data from Haberschill et al. [112]

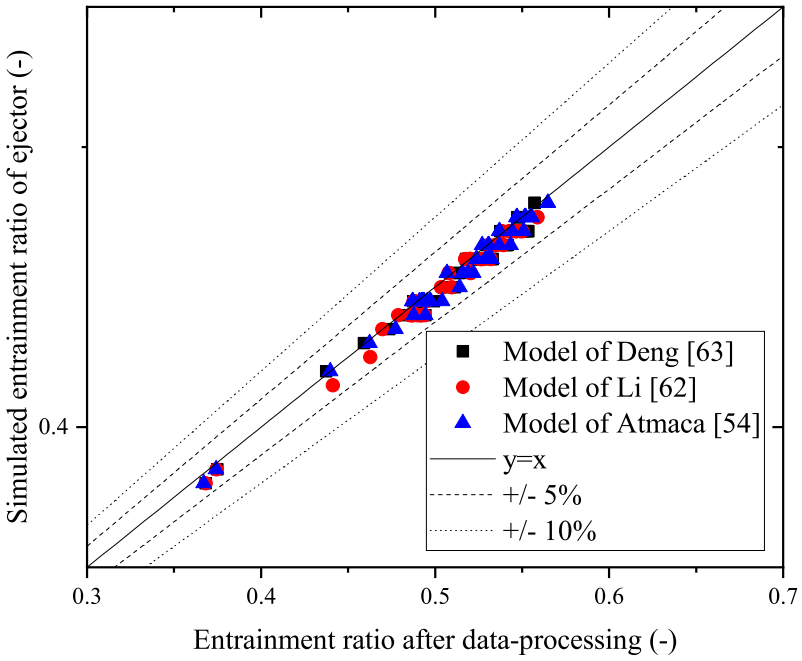

FIGURE 2.27: Simulated ejector entrainment ratio as a function of entrainment ratio with post-processed data from Zhu et al. [113]

Fig. 2.28 and Fig. 2.29 depict the simulated cycle COP as a function of the COP with post-processed data from both datasets. Upon comparing the relative deviation before and after data processing, we conclude that by eliminating the liquid imbalance, all three 0-D thermodynamic models can predict the cycle COP with satisfactory accuracy. The relative deviation of COP generally remains below 10 % for all the 0-D models in both datasets. In a few instances, the relative deviation reaches around 30 %.

2.6.4 Conclusion

Liquid mass imbalance in the separator is a common phenomenon that occurs during the actual operation of the test facility. The liquid mass imbalance does not conflict with the overall conservation of mass, momentum, and energy for the ejector. The cause of the imbalance is due to the mismatch between the liquid mass fraction at the ejector outlet and the entrainment ratio of the ejector. However, for all the 0-D thermodynamic models, the link between the liquid mass fraction (vapor quality) at the ejector outlet and the entrainment ratio is a core closure equation for the modeling.

The relative simulation deviation of the cycle COP exhibits a linear correlation with the coefficient of liquid imbalance. Introducing a novel approach to data post-processing, the relative deviation of the ejector entrainment ratio remains below 10 %

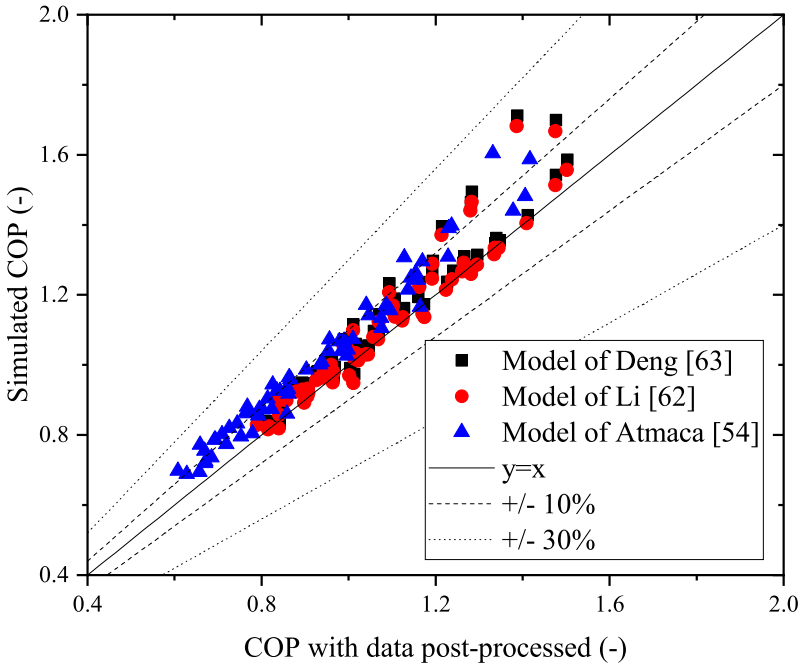

FIGURE 2.28: Simulated cycle COP as a function of COP with post-processed data from Haberschill et al. [112]

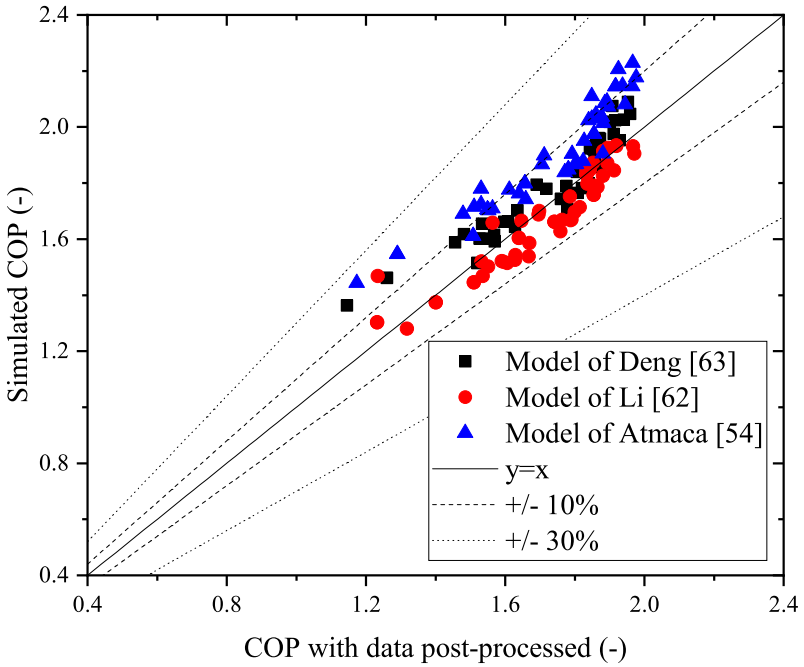

FIGURE 2.29: Simulated cycle COP as a function of COP with post-processed data from Zhu et al. [113]

with the post-processed experimental data. Additionally, the simulated cycle COP aligns well with the new COP value after data post-processing, with the general relative deviation decreasing from 30 % to 10 %.

2.7 Conclusion of the thermodynamic-based simulation

In this chapter, three 0-D thermodynamic models (one constant pressure mixing model and two variable pressure mixing models) with an increasing complexity of the ejector are studied. Two independent datasets are used for the validation of the 0-D models. Sensitivity analysis is conducted to study the influence of the input isentropic efficiency of the ejector components and also the compressor on the ejector outlet pressure, ejector efficiency, and cycle COP. A novel method of data post-processing is introduced to eliminate the liquid mass imbalance in the separator. The main conclusions are:

- The ejector performance is most sensitive to the motive nozzle efficiency, compared to the suction nozzle and diffuser. Additionally, the COP of the system is much more sensitive to the isentropic efficiency of the compressor than to that of the individual components of the ejector for all three models [54, 62, 63].
- The simplification of neglecting the pressure variation during the mixing section has no obvious effect on the modeling accuracy. Under specific conditions, the simpler model even shows better accuracy.
- All the 0-D thermodynamic models predict well on the ejector outlet pressure and vapor quality; however, the prediction on the ejector entrainment ratio and cycle COP is not satisfactory.
- Liquid imbalance is a common phenomenon during the actual operation of the ejector expansion heat pump cycle and is the main cause of the simulation deviation of the cycle COP.
- Through a novel data post-processing method, the liquid imbalance effect can be eliminated, and the simulation deviation of the ejector entrainment ratio and cycle COP can be reduced remarkably.

Chapter 3

1-D modeling of transcritical two-phase CO_2 ejector

While 1-D modeling using the Finite Volume Method is less common compared to the widespread use of CFD modeling, it emerges as a viable compromise between modeling precision and computational time when considering the computational expenses associated with CFD modeling and the limited informativeness of 0-D modeling.

In this chapter, a 1-D homogeneous equilibrium model (HEM) for the ejector is presented. The model is partitioned into various sections based on the geometric configuration, each employing distinct assumption and modeling method.

Firstly, a comprehensive summary of existing one-dimensional ejector models available in the literature is provided. Building upon this review, a 1-D HEM for the ejector is established.

Next, the 1-D ejector model is experimentally validated using data from the literature. The modeling accuracy is quantitatively analyzed.

Subsequently, the 1-D ejector model is applied for parametric analysis, ejector geometry design and comparison analysis with 0-D models.

3.1 Summary of 1-D models of two-phase ejector

The 0-D or pseudo 1-D model proves to be a valuable tool for swiftly predicting crucial parameters such as pressure, temperature, and velocity at key cross-sections within the ejector. When integrated into a simplified system model, it facilitates rapid predictions of system performance indices, including COP, pressure lift ratio, and others.

However, it is essential to acknowledge the limitations of the 0-D model. Specifically, its simulation of the ejector may lack the necessary accuracy and specificity. Additionally, its dependence on the predefined isentropic efficiencies of ejector components as input parameters means the model has a large degree of randomness.

To address this limitation of 0-D modeling and provide more detailed information about the flow field inside the ejector, 1-D modeling of two-phase ejector is proposed. As introduced in the Chapter 1, the 1-D modeling can be divided into three groups based on the assumptions of the two-phase flow: HEM, DEM and HRM.

Fig. 3.1 depicts an abbreviated *P-h* plot illustrating the saturation and homogeneous nucleation lines of CO_2. Observing Fig. 3.1, we can determine when CO_2 begins to evaporate from the saturated liquid state or condense from the saturated vapor state. Notably, homogeneous nucleation does not occur immediately. For evaporation, bubbles appear after a certain degree of superheating for the liquid. Prior to the formation of bubbles, the liquid exists in a meta-stable state. Similarly, in the condensation process, before homogeneous nucleation occurs, the vapor is in a meta-stable state. Only after reaching a certain degree of subcooling do droplets appear in the vapor phase.

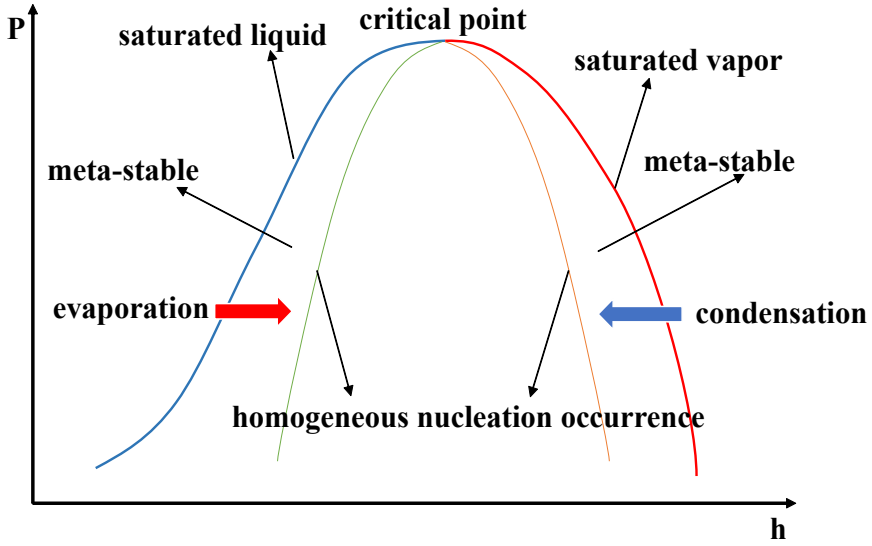

FIGURE 3.1: *P-h* plot of the saturation and homogeneous nucleation lines

Considering the 1-D modeling of ejector, for Homogeneous Equilibrium Model (HEM), the meta-stable state is neglected. When the evaporation happens around the throat of the motive nozzle, the two-phase flow is considered as the mix of saturated liquid and saturated vapor. Both phases share the same pressure, temperature and velocity, all the thermodynamic properties are calculated based on the mass fraction average or void fraction average.

For the Delayed Equilibrium Model (DEM) of an ejector, it permits the existence of meta-stable and saturated states of liquid. The assumption is that only a fraction of the liquid is maintained at a superheated temperature, while the other fraction is at saturation temperature. This model recognizes three states for the two-phase flow: the meta-stable liquid, saturated liquid, and saturated vapor.

In the case of the Homogeneous Relaxation Model (HRM), akin to the HEM, it assumes that two-phase flow is a mixture of saturated liquid and saturated vapor. However, HRM treats the phase change as a relaxation process towards equilibrium vapor quality. During the modeling, two vapor qualities are considered: one is the instantaneous vapor quality, and the other is the time-averaged equilibrium vapor quality. The relaxation introduces a delay to the onset of phase change with a relaxation time.

Banasiak and Hafner [75] devised a one-dimensional model for a two-phase flow ejector. Notably, the motive nozzle segment is modeled using the DEM, adding complexity compared to the HEM. The suction nozzle and pre-mixing portion employ a 0-D model based on thermodynamics. For the constant-area mixing section and the diffuser, the model adopts HEM with the mixing of two flows.

Subsequently, the DEM for the motive nozzle underwent enhancement by incorporating two distinct nucleation approaches: solely homogeneous nucleation and a superposition of homogeneous and heterogeneous nucleation [80]. Homogeneous nucleation is determined solely by fluid properties and actual superheat or subcooling. On the other hand, the heterogeneous nucleation mechanism involves two additional effects: the influence of the walls' structure, typically expressed by surface roughness, and the molecular interaction between solid and liquid, characterized by a parameter known as the contact angle. The homogeneous equilibrium model served as a reference case in this study. A correlation for the reduction factor in heterogeneous nucleation work was developed and validated across a typical range of operating conditions. The simulation results demonstrated good consistency with experimental findings, particularly for the critical mass flux.

Accordingly, Angielczyk et al. [78] developed a homogeneous relaxation model (HRM) for the CO_2 supersonic two-phase flow through the ejector motive nozzle. This model demonstrates greater consistency than the HEM concerning propagation velocity and, consequently, the prediction of speed of sound. Pressure distributions, derived from this model, were compared with experimental data. The results exhibit reasonable agreement with measurements downstream of the throat.

Nevertheless, it was identified that a more comprehensive assessment of the model requires additional experimental data. Specifically, having pressure taps along the entire length of the nozzle (including convergent and divergent sections), along with supplementary information such as temperature profiles, quality profiles, and critical flow rate, is crucial to properly evaluate the model and propose a suitable correlation for the relaxation time.

In recent years, Angielczyk et al. [79] also introduced a 1-D DEM for CO_2 convergent-divergent nozzle transonic flashing flow. The study highlighted that the direct application of DEM, equipped with the original saturation index evolution law and Lockhart-Martinelli approach, is insufficient for accurately predicting CO_2 transonic

flow. Additionally, it was observed that the Darcy friction factor approach significantly influences simulation results. In this work, these challenges have been addressed by presenting a new law for the evolution of the saturation index and a novel approach to frictional pressure gradient for CO_2 transonic two-phase flows. The proposed models were subjected to experimental validation, and the obtained data were discussed in detail.

To compare the different 1-D modeling method, Wilhelmsen et al. [76] developed a new HRM to describe the two-phase transition in the motive nozzle. And a new 1-D HEM for the entire ejector region based on the work of Banasiak [75]. The performance of HRM was compared to the HEM, which assumes full equilibrium at all times. For experiments where evaporation in the throat of the motive nozzle limits the critical mass flow rate, HRM gave an average deviation of 2.6 %. This was significantly more accurate than HEM, which gave an average deviation of 8.4 % for the experiments considered. They also presented new experimental data where the critical mass flow rate in the ejector was governed by condensation in the throat of the motive nozzle. In this case both HRM and HEM were in excellent agreement with the experimental data, with average deviations below 0.9 %. The reason for this is that the limit of metastability in the liquid-phase is much closer to the coexistence curve than the corresponding limit in the vapor-phase, which leads to very similar results for HRM and HEM.

Rather than simulating the whole ejector region, Atmaca et al. [74] focused on the motive nozzle part of the ejector and developed a simplified one-dimensional HEM for converging-diverging motive nozzle. This model aims to compute pressure, temperature, velocity, and Mach number distributions. The 1-D nozzle model is established by employing the conservation equations of mass, momentum, and energy, along with the equation of state. The model operates under steady, frictional, and adiabatic flow assumptions, maintaining the homogeneous equilibrium condition.

From the literature review, it is evident that one-dimensional modeling of ejectors or motive nozzles is still relatively scarce, especially when considering the modeling of the entire ejector domain rather than focusing solely on the trans-sonic motive nozzle zone.

In comparison to DEM and HRM, the HEM involves the fewest equations for describing the flow inside the ejector. Notably, DEM heavily relies on the evolution of the saturation index, which can vary significantly among different DEM. Similarly, HRM introduces complexity with the correlation of relaxation time. In cases where these parameters are not precisely defined, the modeling accuracy can be compromised, and in some instances, it may be less accurate than the HEM approach. Therefore, HEM stands out as a balanced choice, taking into account the trade-off between modeling complexity and accuracy.

Furthermore, HEM is commonly considered as a pragmatic choice, particularly

for supercritical conditions. This is attributed to the minimal thermodynamic non-equilibrium expected during near-critical expansion, leading to rapid phase change. The simplicity of the HEM contributes to the stability of the model, a crucial aspect for its application in optimization algorithms [61].

In conclusion, there is a scarcity of studies on the 1-D modeling of the entire ejector region, especially with the HEM approach, in comparison to DEM and HRM. In this section we introduce a novel 1-D ejector model using the HEM approach to investigate the flow field inside the ejector. We validate the model experimentally and conduct a parametric analysis of the boundary conditions and ejector design using the established 1-D HEM of the ejector.

3.2 A novel 1-D homogeneous equilibrium model of two-phase ejector

In the 1-D HEM of the ejector, the two-phase flow comprises only two elements: saturated vapor and saturated liquid. Unlike the DEM, there is no thermal non-equilibrium, eliminating the presence of a meta-stable state. Furthermore, the HEM approach assumes that both phases can be described with a single velocity and pressure field, simplifying the model by neglecting the modeling of slip velocity. This simplification allows treating the two phases as a single pseudo-fluid, with transport properties derived through an averaging procedure.

3.2.1 Computational zones division of the ejector

The ejector is a sophisticated and complex device, as previously described, consisting of multiple components. Consequently, the 1-D modeling of the ejector is conducted in discrete sections. The simulation strategies applied differ across these sections, guided by factors such as the presence of phase transition and the combination of motive and action flows. The classification into distinct regions is shown in Fig. 3.2.

(1) Motive nozzle : 1-D HEM, phase transition, single flow

(2) Suction nozzle : 0-D modeling, single phase, single flow

(3) Pre-mixing section : 0-D modeling, two-phase flow, double flows

(4) Constant-area mixing section and diffuser : 1-D HEM, two-phase flow, double flows

For a well-geometrically designed suction nozzle, one-dimensional modeling may be suitable. However, in the case of most ejectors employed in the heat pump cycle, the flow path and geometric design of the suction nozzle are not one-dimensional and cannot be numerically defined in a 1-D simulation. Consequently, a 0-D modeling approach is employed for this zone.

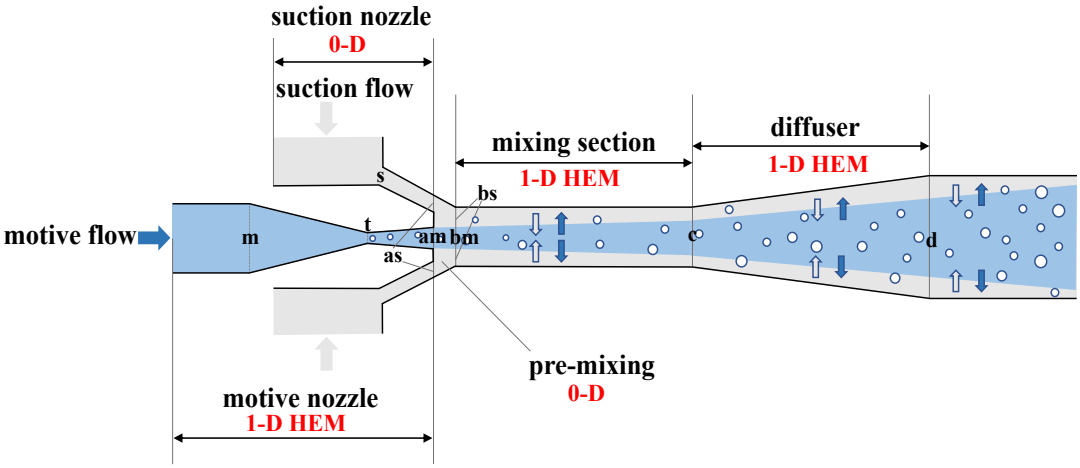

FIGURE 3.2: Simulation zones division of ejector

In the pre-mixing section, a 0-D modeling method is selected because it entails the transient mixing of two distinct flows (motive and suction flow). The mixing process is transient, and currently, there is no mature 1-D modeling method available to describe the intricacies of this transient process.

As for the motive nozzle, constant-area mixing section, and diffuser, a 1-D HEM approach is employed for modeling. The specifics of this modeling approach will be presented in detail in subsequent sections.

3.2.2 Modeling of motive nozzle

The 1-D homogeneous equilibrium model for the motive nozzle is defined based on the conservation of mass, momentum, and energy. In this study, given the small size and high velocity of the fluid within the motive nozzle, it is assumed that the wall is adiabatic. Additionally, since the motive nozzle is positioned horizontally, the influence of gravity is negligible. The fluid is considered viscous, and shear stress is taken into account between the tube wall and the fluid. In summary, the mathematical equations governing the 1-D HEM for the motive nozzle can be outlined as follows respectively for the conservation of mass, momentum, and energy:

$$\frac{\mathrm{d}(A_{cs} \cdot \rho \cdot u)}{\mathrm{d}z} = 0 \tag{3.1}$$

$$\frac{\mathrm{d}(A_{cs} \cdot \rho \cdot u^2)}{\mathrm{d}z} + A_{cs} \cdot \frac{\mathrm{d}p}{\mathrm{d}z} = \tau_{lt} \cdot C_{lt} \tag{3.2}$$

$$\frac{\mathrm{d}(A_{cs} \cdot \rho \cdot u \cdot (h + \frac{1}{2} \cdot u^2))}{\mathrm{d}z} = 0 \tag{3.3}$$

In the above equations, ρ and h represent the volume fraction averaged density and mass fraction averaged specific enthalpy, while u and p denote the velocity and pressure of the flow. A_{cs}, C_{lt}, and τ_{lt} represent the cross-sectional area, lateral section

area, and shear stress coefficient, respectively. The variable z denotes the flow path direction.

The independent variables chosen for the simulation include pressure, velocity, and specific enthalpy. Density can be expressed as a function of pressure and specific enthalpy based on the equations of state. The simulation is conducted using Matlab, and the thermodynamic parameters of CO_2 are obtained from the NIST REFPROP database, version 9.1. After transformation, the equations (Eq. (3.1) to Eq. (3.3)) and the equation of state are expressed as follows:

$$\frac{1}{u}\cdot\frac{\mathrm{d}u}{\mathrm{d}z}+\frac{1}{A_{cs}}\cdot\frac{\mathrm{d}A_{cs}}{\mathrm{d}z}+\frac{1}{\rho}\cdot\frac{\mathrm{d}\rho}{\mathrm{d}z}=0 \tag{3.4}$$

$$A_{cs}\cdot\frac{\mathrm{d}p}{\mathrm{d}z}+A_{cs}\cdot u\cdot\rho\cdot\frac{\mathrm{d}u}{\mathrm{d}z}+f\cdot\frac{u^2}{2}\cdot\frac{\mathrm{d}A_{lt}}{\mathrm{d}z}=0 \tag{3.5}$$

$$\frac{\mathrm{d}h}{\mathrm{d}z}+u\cdot\frac{\mathrm{d}u}{\mathrm{d}z}=0 \tag{3.6}$$

$$\frac{\partial\rho}{\partial p}\cdot\frac{\mathrm{d}p}{\mathrm{d}z}+\frac{\partial\rho}{\partial h}\cdot\frac{\mathrm{d}h}{\mathrm{d}z}-\frac{\mathrm{d}\rho}{\mathrm{d}z}=0 \tag{3.7}$$

In the equation, f represents the friction factor used to calculate the friction loss of the flow.

The aforementioned equations can be formulated as a system of nonlinear first-order ordinary differential equations, as shown in Eq. (3.8). Here, X is the vector of independent variables for the system (ordered as u, p, h), encompassing velocity, pressure, and specific enthalpy. The vector A (Eq. (3.9)) comprises system variables that are solely functions of the independent variables, while B (Eq. (3.10)) is additionally correlated to the spatial coordinate.

$$A(X)\cdot\frac{\mathrm{d}X}{\mathrm{d}z}=B(z,X) \tag{3.8}$$

$$\begin{bmatrix} 1/u & 1/(\rho\cdot\frac{\partial\rho}{\partial p}) & 1/(\rho\cdot\frac{\partial\rho}{\partial h}) \\ \rho\cdot u\cdot A_{cs} & A_{cs} & 0 \\ u & 0 & 1 \end{bmatrix} \tag{3.9}$$

$$\begin{bmatrix} -\frac{1}{A_{cs}}\cdot\frac{\mathrm{d}A_{cs}}{\mathrm{d}z} \\ -\frac{1}{2}\cdot f\cdot\rho\cdot u^2\cdot\frac{\mathrm{d}A_{lt}}{\mathrm{d}z} \\ 0 \end{bmatrix} \tag{3.10}$$

The derivatives $\frac{\partial\rho}{\partial p}$ and $\frac{\partial\rho}{\partial h}$ are numerically evaluated to account for density

changes corresponding to infinitesimal pressure variations at constant specific enthalpy and density changes resulting from infinitesimal specific enthalpy changes at constant pressure, respectively.

The friction factor f is estimated using the model developed by Churchill [117], a model validated for all fluid-flow regimes.

$$f = 8 \cdot \left[\frac{8}{Re} + \frac{1}{(A_f + B_f)^{3/2}} \right]^{1/12} \tag{3.11}$$

$$A_f = \left[2.457 \cdot ln \cdot \frac{1}{(\frac{7}{Re})^{0.9} + \frac{0.27 \cdot \varepsilon_w}{D_C}} \right]^{16} \tag{3.12}$$

$$B_f = \left[\frac{37530}{Re} \right]^{16} \tag{3.13}$$

Here, Re denotes the Reynolds number, calculated as given in Eq. (3.14). The parameters A_f and B_f are defined parameters utilized in the calculation of the friction factor. Additionally, ε_w and D_c represent the surface roughness and diameter of the flow path of the motive nozzle.

$$Re = \frac{\rho \cdot u \cdot D_c}{\mu} \tag{3.14}$$

Here, μ stands for the coefficient of dynamic viscosity, and it is defined according to Eq. (3.15) for the case of homogeneous equilibrium two-phase flow, as per the model developed by Awad and Muzychka [118].

$$\begin{aligned} \mu =& 0.25 \cdot ((3 \cdot x - 1) \cdot \mu_v + (3 \cdot (1 - x) - 1) \cdot \mu_l + \\ & \sqrt{((3 \cdot x - 1) \cdot \mu_v + (3 \cdot (1 - x) - 1) \cdot \mu_l)^2 + 8 \cdot \mu_v \cdot \mu_l)} \end{aligned} \tag{3.15}$$

In this context, x represents the vapor quality for two-phase flow, while μ_v and μ_l denote the dynamic viscosity of saturated vapor and saturated liquid, respectively. These values can be obtained through the equations of state in REFPROP.

To solve the one-dimensional partial differential equations, the motive nozzle undergoes discretization along the flow direction, dividing it into sufficiently small meshes. The boundary conditions encompass the temperature, pressure, and mass flow rate at the inlet of the motive nozzle. Additionally, geometrical parameters serve as input data for solving the motive nozzle model.

Prediction of critical mass flow rate of motive nozzle

In the motive nozzle, the fluid at the inlet is typically in a supercritical state. It undergoes acceleration at the convergent part and reaches the critical state at the throat, where the flow velocity equals the local speed of sound (Mach number, $Ma = 1$, assumption). Subsequently, it continues to accelerate at the divergent part and exits the motive nozzle at supersonic speed. For a motive nozzle with a defined geometry

and specified inlet pressure and temperature, there exists a corresponding critical mass flow rate, ensuring that the motive flow reaches the critical state precisely at the nozzle throat.

To predict the critical mass flow rate of the motive nozzle and verify the input mass flow rate, this section introduces a solution algorithm that incorporates the Possible-Impossible Flow (PIF) algorithm and Cramer's rule.

Cramer's rule

Cramer's rule is a fundamental method utilized in the solution of systems of equations. This method involves the calculation of variable values through the determinants of matrices, earning it the designation of the determinant method.

Considering a system of n linear equations, each with n unknowns, represented in matrix multiplication form as follows:

$$A_n X_n = B_n \tag{3.16}$$

In the context where the $n \times n$ matrix A_n possesses a nonzero determinant, the system admits a unique solution, and the values of the unknowns can be determined by:

$$x_i = \frac{det(A_i)}{det(A)} \qquad i = 1, ..., n \tag{3.17}$$

In this context, A_i is the matrix obtained by substituting the i-th column of A_n with the column vector of B_n.

Possible-Impossible flow algorithm (PIF)

The system of ordinary differential equations represented by Eq. (3.8) constitutes an initial-value problem. A solution to these equations is a trajectory denoted as $X(z)$ within the 4-dimensional phase space. At each point along this trajectory, the vector $[dz, dp, du, dh]$ is tangent to $X(z)$. Consequently, vector X is defined as per Eq. (3.18) by applying Cramer's rule.

$$\left[\frac{\mathrm{d}z}{\mathrm{d}t}, \frac{\mathrm{d}u}{\mathrm{d}t}, \frac{\mathrm{d}p}{\mathrm{d}t}, \frac{\mathrm{d}h}{\mathrm{d}t}\right] = [D, A_1, A_2, A_3] \tag{3.18}$$

In this context, D denotes the determinant of the matrix A, and A_i represents the determinants of matrices created by replacing the corresponding columns of A_n with the column vector of B_n. The parameter t serves as a dummy parameter, facilitating the transition from Eq. (3.17) to Eq. (3.18).

By definition, the speed of sound c is the speed of propagation of an infinitesimal disturbance in a continuous medium. A comprehensive definition of the speed of sound is provided by Eq. (3.19) in scenarios where the disturbance is infinitesimal and the process is isentropic.

$$c^2 = \frac{\partial p}{\partial \rho} \tag{3.19}$$

In the HEM approach, the density of the fluid, whether single-phase or two-phase, can be determined using the equations of state in REFPROP, employing pressure and specific enthalpy values. When the fluid reaches the local speed of sound ($Ma = 1$) in the motive nozzle, the flow velocity can be obtained from Eq. (3.19) using pressure and density values. Consequently, the velocity can be expressed as a function of pressure and specific enthalpy values. In such a case (critical state, $Ma = 1$), the velocity is no longer an independent variable in the system of ordinary differential equations in Eq. (3.16) but is associated with the other two independent variables (pressure and specific enthalpy). In matrix terms, the determinant of the matrix A_n becomes zero, i.e., the value of D in Eq. (3.18) is zero.

When the pressure and temperature at the inlet of the motive nozzle remain constant, altering the mass flow rate of the fluid only changes the velocity at the inlet. Fig. 3.3 illustrates the projection of trajectories corresponding to flows through a converging-diverging nozzle on the pressure-spatial coordinate plane. The inlet conditions related to these flows differ only in the velocities.

If the flow in the motive nozzle is subsonic in the entire region, its trajectory is represented by the green curve in Fig. 3.3. Such a curve is termed a possible flow (PF) as it can be solved using Cramer's rule and has real physical meaning. For the red curves in Fig. 3.3, the trajectories pass through the points where $D = 0$. The flow velocity reaches the local sound speed, and after these points, $D < 0$, then $dz = dt \cdot D < 0$. The imaginary flow will move back to the inlet of the motive nozzle. These red curves are termed impossible flow (IF) because they can be solved with Cramer's rule as Eq. (3.18), but they hold no physical meaning. For the transonic flow aimed at, it will pass through the point S, where $D = 0$, and also A_u, A_p, A_h are zero. At this point, the ordinary differential equations have no solution, regardless of the iterative algorithm used. Therefore, the point and this trajectory can never be computationally found, but a value close enough to be within an acceptable error can be obtained by PIF iteration.

The core of PIF is based on the understanding that the transonic trajectory is located between PF and IF trajectories, as shown in Fig. 3.3. PF and IF are solvable numerically with Cramer's rule. Therefore, after a certain number of iterations, we can obtain a trajectory that is sufficiently close to the transonic one. The iteration proceeds as follows:

(1) Set the initial mass flow rate $\dot{m}_{PF}$ and $\dot{m}_{IF}$ for PF and IF.

(2) The initial input mass flow rate will be $\dot{m} = (\dot{m}_{PF} + \dot{m}_{IF})/2$.

(3) Solve the initial problems of the ordinary differential equations with Cramer's rule and check the value and sign of D.

(4) If D changed the sigh before the end of the motive nozzle, then assign the value of $\dot{m}$ to $\dot{m}_{IF}$.

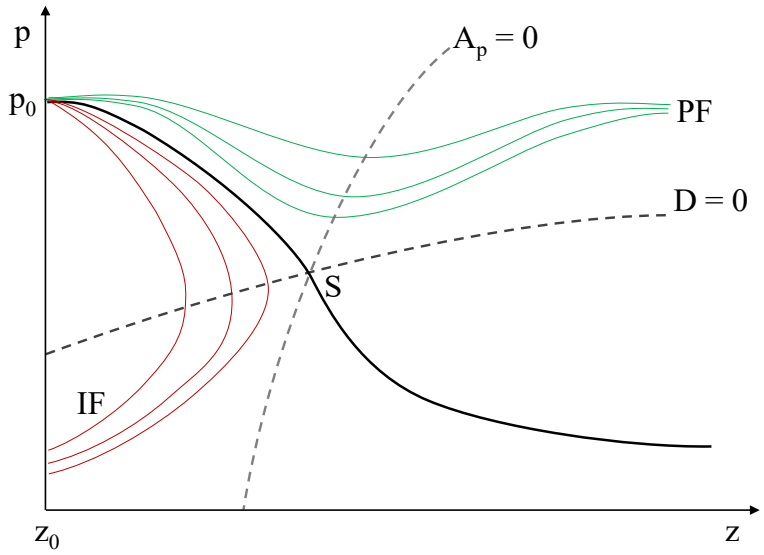

FIGURE 3.3: Projection of solutions to the initial-value problems on $p - z$ plane, S is critical point, D is the determinant of matrix A, Ap is the determinant of the matrix of A but replace the second column by the matrix of B

(5) If D deoes't change the sigh before the end of the motive nozzle, then assign the value of $\dot{m}$ to $\dot{m}_{PF}$.

(6) Check the gap between $\dot{m}_{PF}$ and $\dot{m}_{IF}$, if the absolute difference is lower than the tolerant error, stop the iteration, otherwise start from the step 1.

After a certain number of iterations following steps 1 to 6, a reasonable mass flow rate for the motive nozzle can be obtained within the tolerated deviation. At this mass flow rate, the motive flow reaches the critical state ($Ma = 1$) at the throat of the motive nozzle. In well-designed ejectors, the motive nozzle typically operates at the critical state, and the mass flow rate of the motive flow can be numerically simulated.

After determining the critical mass flow rate of the motive nozzle, other properties such as pressure, specific enthalpy, and velocity can be obtained based on Finite Volume Method. The boundary conditions include the inlet temperature and pressure of the motive flow, as well as the geometric parameters of the motive nozzle.

In comparison to other solving methods, such as the fourth-order Runge-Kutta method applied by Banasiak and Hafner [75], where the calculation step is fixed at a given value, the Cramer's rule is applied in the solution algorithm for the ordinary differential equation system. As a result, the calculation step along the flow direction is variable. During the simulation, an initial step will be provided, and then the calculation step depends on the determinants of D. Considering that D is smaller when it's close to the throat, meaning around the position of the motive nozzle throat, the calculation step is smaller. Taking into account the critical change in this position, the self-adjustable calculation step method can improve the accuracy and efficiency of the modeling.

By solving the ordinary differential equations along the flow path, the profiles of pressure, specific enthalpy, and velocity can be obtained, and the density will be given by the equations of state in REFPROP with pressure and specific enthalpy values. At this point, the simulation of the motive nozzle is considered complete.

3.2.3 Modeling of suction nozzle

For the suction nozzle, the flow path is typically not one-dimensional, and the geometric configuration is much more complex than that of the motive nozzle. Therefore, utilizing a similar 1-D flow modeling method as the motive nozzle and defining the flow as one-dimensional is challenging. Banasiak and Hafner [75] define it as 1-D flow like the motive nozzle, but there is a simplification of the geometric configuration of the suction nozzle. Moreover, this 1-D modeling cannot apply to every ejector due to the variations in the geometric configuration of the suction nozzle among ejectors.

To enhance the model's adaptability for most ejectors, a 0-D modeling method is employed for the suction nozzle in this section. The inlet parameters of the suction nozzle, such as specific enthalpy, entropy, vapor quality, and density, can be calculated based on input parameters (temperature and pressure of the flow out of the evaporator) using equations of states with REFPROP. The input velocity can be obtained with the known mass flow rate of the suction flow, the input diameter of the suction nozzle, and the calculated density. The suction nozzle is assumed to be adiabatic to the environment, meaning there is no heat loss in the suction nozzle. Additionally, friction loss is neglected for the suction nozzle.

An iteration on the outlet pressure will be conducted for the simulation of the suction nozzle. The modeling process is depicted in the flow chart in Fig. 3.4.

The outlet velocity of the suction nozzle is determined through the application of momentum conservation, as expressed by Eq. (3.20) with an initial value of P_{as}. Here, a_s represents the inlet cross-sectional area of the suction nozzle, and a_{as} signifies the cross-sectional area at the outlet of the suction nozzle. Both of these parameters are known and defined by the ejector's geometry.

Subsequently, the density at the outlet of the suction nozzle is calculated with mass conservation by Eq. (3.21). And the outlet specific enthalpy at the suction nozzle outlet is calculated with energy conservation by Eq. (3.22). Here the u_s can be calculated by the mass balance at the inlet of the suction nozzle (Eq. (3.23)).

After obtaining the specific enthalpy and density, the outlet pressure can be obtained using the equation of state in REFPROP.

Finally, the obtained pressure value ($P_{as,cal}$) is compared with the iteration value (P_{as}) until the error falls within a tolerated range ϵ.

$$P_s \cdot a_s = P_{as} \cdot a_{as} + \dot{m}_s \cdot u_{as} \tag{3.20}$$

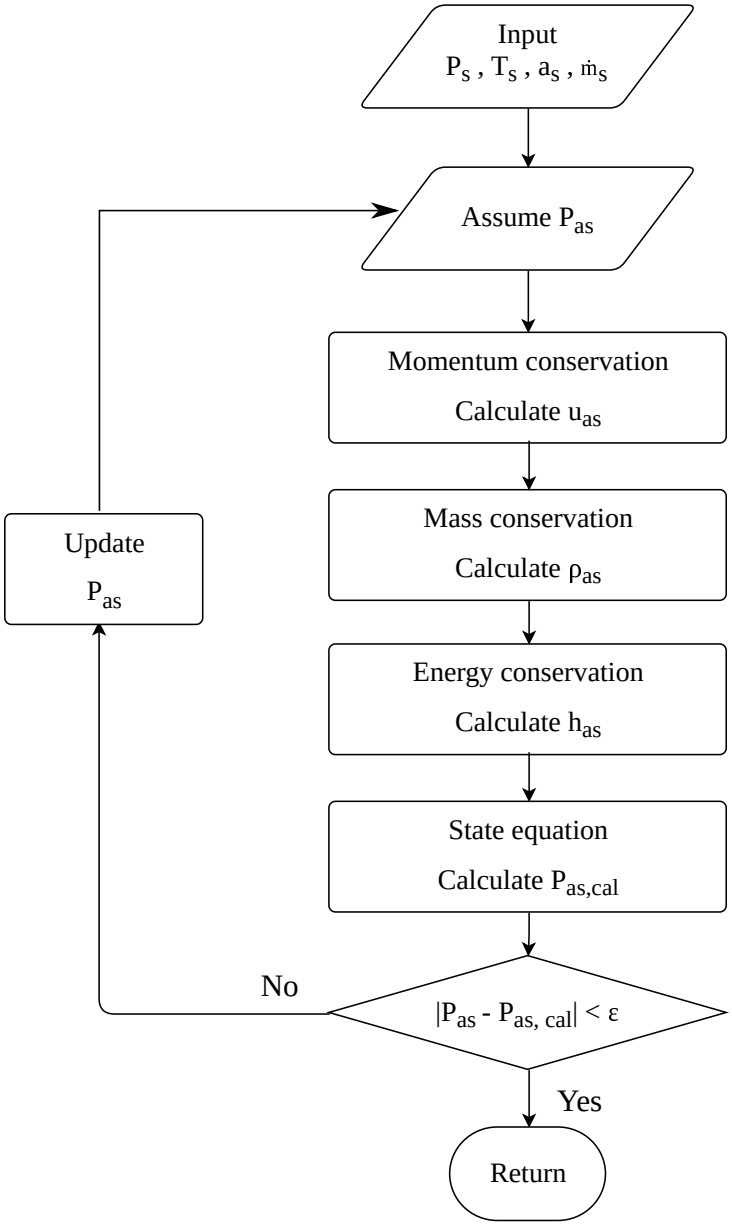

FIGURE 3.4: Flow chart of suction nozzle simulation

$$\rho_{as} \cdot u_{as} \cdot a_{as} = \dot{m}_s \tag{3.21}$$

$$h_s + \frac{1}{2} \cdot \mathrm{u_s}^2 = h_{as} + \tfrac{1}{2} \cdot \mathrm{u_{as}}^2 \tag{3.22}$$

$$\rho_s \cdot u_s \cdot a_s = \dot{m}_s \tag{3.23}$$

3.2.4 Modeling of pre-mixing section

For the pre-mixing section, it involves both motive and suction flows, and the flow is multidimensional because the flow direction of the motive flow and suction flow is not identical. To simplify the simulation, a 0-D approach based on the work of Banasiak and Hafner [75] is utilized in this zone.

The key assumptions for pre-mixing section modeling are as follows:

(1) Both flows have the same static pressure at the outlet of the pre-mixing section.

(2) Both flows form a perfectly coaxial double-fluid flow at the outlet of the pre-mixing section, where the motive flow is in the center and is annularly surrounded by suction flow.

(3) The motive and suction flows do not mix together inside the pre-mixing section, meaning the modeling is separately conducted for the two flows, but the control volume is represented by the whole volume of the pre-mixing section.

(4) In the pre-mixing section, an isentropic expansion/compression is assumed, meaning the outlet entropy of both flows is identical to their respective input entropy.

The flow chart of the simulation of the pre-mixing section is shown in Fig. 3.5.

An iteration on the outlet pressure P_b will be conducted for the simulation of the pre-mixing section. With the known pressure and entropy, the outlet specific enthalpy (h_{bm}, h_{bs}) and density (ρ_{bm}, ρ_{bs}) of motive flow and suction flow will be calculated separately using equations of state in REFPROP. The input parameters of the motive nozzle exit (P_{am} and T_{am}) are acquired from the 1-D simulation of the motive nozzle. Furthermore, a_{am} and a_{as} denote the cross-sectional areas, both of which are determined by the geometric parameters. The values for P_{as} and T_{as} are calculated in the subsequent section.

Then the velocities of motive and suction flow can be calculated based on energy conservation by Eq. (3.24) and Eq. (3.25), respectively. Where the specific enthalpy (h_{am}, h_{as}) and velocity (u_{am}, u_{as}) of both flows at the nozzle exist are already calculated in the sections before.

$$h_{am} + \frac{1}{2} \cdot \mathrm{u_{am}}^2 = h_{bm} + \tfrac{1}{2} \cdot \mathrm{u_{bm}}^2 \tag{3.24}$$

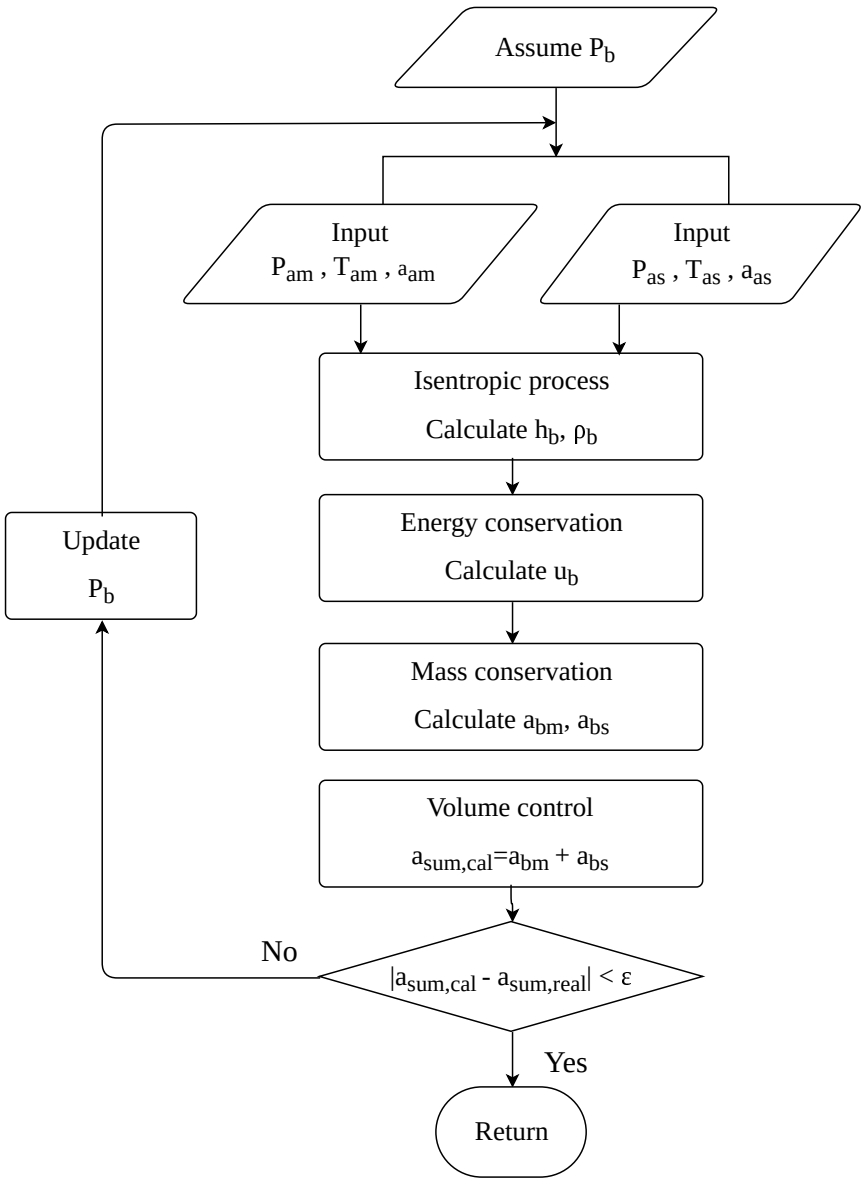

FIGURE 3.5: Flow chart of pre-mixing section simulation

$$h_{as} + \frac{1}{2} \cdot \mathrm{u}_{as}{}^2 = h_{bs} + \tfrac{1}{2} \cdot \mathrm{u}_{bs}{}^2 \tag{3.25}$$

The occupied section area will be calculated with mass conservation for both flows by Eq. (3.26) and Eq. (3.27). Where the mass flow rate of the motive flow ($\dot{m}_m$ is calculated by the 1-D modeling of motive nozzle.

$$\rho_{bm} \cdot u_{bm} \cdot a_{bm} = \dot{m}_m \tag{3.26}$$

$$\rho_{bs} \cdot u_{bs} \cdot a_{bs} = \dot{m}_s \tag{3.27}$$

Finally, the sum of the occupied section area for both flows ($a_{sum,cal}$) will be compared with the input geometric parameter ($a_{sum,real}$), and then the outlet pressure will be updated based on the deviation until it falls within a tolerated range.

3.2.5 Modeling of mixing section and diffuser

For the mixing section and diffuser, it involves the mixing of motive flow and suction flow, as well as two-phase flow, making it another challenging part of the simulation. The 1-D HEM approach is utilized in this section, and the modeling is referenced to the work of Banasiak and Hafner [75].

The key assumptions for this part of the simulation are introduced as follows:

(1) The motive flow and suction flow are perfectly coaxial double-fluid flow throughout the passage of the mixing section and diffuser, where the motive flow is in the center, and the suction flow circulates the motive flow annually.

(2) There is mass, momentum, and energy transfer between the motive and suction flow.

(3) The static pressure for motive and suction flow is identical.

(4) Mass transfer in this system can be attributed to three distinct mechanisms: condensation, entrainment of the suction flow by the motive flow, and deposition of the motive flow onto the suction flow.

(5) Momentum transfer may be described by the drag forces exerted at the interface between the two flows and momentum gains/losses due to the transferred mass.

(6) Energy transfer may be accounted for with the enthalpy and kinetic energy gains/losses due to the transferred mass.

(7) Friction pressure drop may be accounted for not only at the wall boundary layer but also for an imaginary, infinitely thin 'mixing layer' separating both streams. The computational approach applied is identical to that used for the wall friction factor case.

(8) Metastability effects were neglected due to the presence of a fully-developed two-phase area.

(9) The two phase flow is assumed to be in a homogeneous equilibrium state where the properties of the flow is determined by a mass or volume fraction average.

Mass transfer between motive and suction flows

The mass transfer from suction flow to motive flow by the entrainment effect is given by the following correlation, as referred to [119]:

$$\frac{\mathrm{d}\dot{M}_{s\to m}}{\mathrm{d}z} = \begin{cases} 1.175\cdot 10^{-4}\cdot u_m\sqrt{\rho_m\cdot\rho_s}\cdot\eta_s\cdot(Re_s - Re_m)\cdot\dfrac{\mathrm{d}A_{int}}{\mathrm{d}z} & (Re_s \geq Re_{s,\infty}) \\ 0 & (Re_s \leq Re_{s,\infty}) \end{cases} \tag{3.28}$$

Where u, ρ, η and A_{int} are the velocity, density, kinematic viscosity and area of the interface between two flows (the inner surface of the annular region of the suction flow), respectively. The index m and s denote the motive flow and suction flow. $Re_{s,\infty}$ is the local equilibrium film Reynolds number, which is calculated as given by Eq. (3.29), also referred to [119]:

$$Re_{s,\infty} = exp(5.8504 + 0.4249\cdot\frac{\eta_m}{\eta_s}\cdot\sqrt{\frac{\rho_s}{\rho_m}}) \tag{3.29}$$

The condensation mass transfer at the interface is given by Eq. (3.30):

$$\frac{\mathrm{d}\dot{M}_{cond}}{\mathrm{d}z} = \frac{\alpha_{int}\cdot(T_m - T_s)}{h_{int} - h_{l,sat}}\cdot\frac{\mathrm{d}A_{int}}{\mathrm{d}z} \tag{3.30}$$

Where α_{int} represents the heat transfer coefficient at the interface.

For the interface between the motive and suction flows, the definition of velocity and specific enthalpy is contingent upon the temperature difference between the two flows, specifically, on the direction of condensation.

$$\begin{cases} u_{int} = u_m, \quad h_{int} = h_m & (T_m > T_s) \\ u_{int} = u_s, \quad h_{int} = h_s & (T_s > T_m) \end{cases} \tag{3.31}$$

Mass transfer via the deposition mechanism is considered negligible in this section.

$$\frac{\mathrm{d}\dot{M}_{m\to s}}{\mathrm{d}z} = 0 \tag{3.32}$$

Momentum transfer between motive and suction flows

The momentum transfer between the motive and suction flows involves the formulation of friction forces for both interfaces: the passage walls and the imaginary interface between the two flows.

$$\frac{dW_{f,int}}{dz} = 0.5 \cdot f_{int} \cdot \rho_m \cdot (u_m - u_s)^2 \cdot \frac{dA_{int}}{dz} \tag{3.33}$$

$$\frac{dW_{f,wall}}{dz} = 0.5 \cdot f_{wall} \cdot \rho_s \cdot u_s^2 \cdot \frac{dA_{wall}}{dz} \tag{3.34}$$

Where A_{wall} is the contact surface between the suction flow and the tube wall, and f is the friction factor determined as described in the motive nozzle section. An equivalent roughness of the mixing layer between the two flows is introduced in this study. The roughness of the mixing layer is considered a parameter adjusted individually for each two-stream computational zone (mixer and diffuser) based on experimental results.

The momentum transfer at the interface is expressed as:

$$\frac{dT_{mom}}{dz} = 0.5 \cdot \rho_m \cdot C_{m\to s} \cdot |u_m - u_s| \cdot (u_m - u_s) \cdot \frac{dA_{wall}}{dz} \tag{3.35}$$

Where $C_{m\to s}$ is the interface drag coefficient describing mechanical interactions between the two coaxial flows. A correlation referred to [120] is adopted:

$$C_{m\to s} = a_{eje} \cdot Re_{m\to s}^{-0.25} \tag{3.36}$$

where

$$Re_{m\to s} = \frac{\rho_s}{\eta_s} \cdot (u_m - u_s) \cdot D_c \cdot \sqrt{\frac{A_m}{A_m + A_s}} \tag{3.37}$$

The coefficient of scale a_{eje} is experimentally determined for each double flow zone, namely, the mixing section and diffuser. Here, D represents the diameter of the passage, while A_m and A_s denote the occupied section areas by the motive and suction flows along the flow path.

Conservation equations

After the definition of the mass and momentum transfer between motive and suction flow, the conservation equations of each flow can be obtained.

The conservation of mass for the motive flow and suction flow is expressed by Eq. (3.38) and Eq. (3.39):

$$\begin{aligned} &\frac{1}{u_m} \cdot \frac{du_m}{dz} + \frac{1}{A_m} \cdot \frac{dA_m}{dz} + \frac{1}{\rho_m} \cdot \frac{d\rho_m}{dz} = \\ &- \frac{1}{A_m \cdot u_m \cdot \rho_m} \cdot \left(\frac{d\dot{M}_c}{dz} + \frac{d\dot{M}_{m\to s}}{dz} - \frac{d\dot{M}_{s\to m}}{dz}\right) \end{aligned} \tag{3.38}$$

$$\frac{1}{u_s} \cdot \frac{du_s}{dz} + \frac{1}{A_s} \cdot \frac{dA_s}{dz} + \frac{1}{\rho_s} \cdot \frac{d\rho_s}{dz} = \frac{1}{A_s \cdot u_s \cdot \rho_s} \cdot \left(\frac{d\dot{M}_c}{dz} + \frac{d\dot{M}_{m\to s}}{dz} - \frac{d\dot{M}_{s\to m}}{dz}\right) \tag{3.39}$$

The conservation of momentum for the motive flow and suction flow is expressed as Eq. (3.40) and Eq. (3.41):

$$\begin{aligned} &A_m \cdot \frac{\mathrm{d}P}{\mathrm{d}z} + A_m \cdot u_m \cdot \rho_m \cdot \frac{\mathrm{d}u_m}{\mathrm{d}z} = \\ &-(u_{int} - u_m) \cdot \frac{\mathrm{d}\dot{M}_c}{\mathrm{d}z} + (u_s - u_m) \cdot \frac{\mathrm{d}\dot{M}_{s\to m}}{\mathrm{d}z} - \frac{\mathrm{d}T_{mom}}{\mathrm{d}z} - \frac{\mathrm{d}W_{f,int}}{\mathrm{d}z} \end{aligned} \tag{3.40}$$

$$\begin{aligned} &A_s \cdot \frac{\mathrm{d}P}{\mathrm{d}z} + A_s \cdot u_s \cdot \rho_s \cdot \frac{\mathrm{d}u_s}{\mathrm{d}z} = \\ &-(u_s - u_{int}) \cdot \frac{\mathrm{d}\dot{M}_c}{\mathrm{d}z} - (u_s - u_m) \cdot \frac{\mathrm{d}\dot{M}_{m\to s}}{\mathrm{d}z} + \frac{\mathrm{d}T_{mom}}{\mathrm{d}z} - \frac{\mathrm{d}W_{f,wall}}{\mathrm{d}z} \end{aligned} \tag{3.41}$$

The conservation of energy for the motive flow and suction flow is expressed as Eq. (3.42) and Eq. (3.43):

$$\begin{aligned} &A_m \cdot u_m^2 \cdot \rho_m \cdot \frac{\mathrm{d}u_m}{\mathrm{d}z} + A_m \cdot u_m \cdot \rho_m \cdot \frac{\mathrm{d}h_m}{\mathrm{d}z} = \\ &(h_m - h_{int} + 0.5 \cdot (u_m^2 - u_{int}^2)) \cdot \frac{\mathrm{d}\dot{M}_c}{\mathrm{d}z} + (h_s - h_m + 0.5 \cdot (u_s^2 - u_m^2)) \cdot \frac{\mathrm{d}\dot{M}_{s\to m}}{\mathrm{d}z} \end{aligned} \tag{3.42}$$

$$\begin{aligned} &A_s \cdot u_s^2 \cdot \rho_s \cdot \frac{\mathrm{d}u_s}{\mathrm{d}z} + A_s \cdot u_s \cdot \rho_s \cdot \frac{\mathrm{d}h_s}{\mathrm{d}z} = \\ &(h_{int} - h_s + 0.5 \cdot (u_{int}^2 - u_s^2)) \cdot \frac{\mathrm{d}\dot{M}_c}{\mathrm{d}z} - (h_s - h_m + 0.5 \cdot (u_s^2 - u_m^2)) \cdot \frac{\mathrm{d}\dot{M}_{m\to s}}{\mathrm{d}z} \end{aligned} \tag{3.43}$$

Solving method

For the mixing section and diffuser, the solving method is akin to the motive nozzle; however, the corresponding set of ordinary differential equations will have more unknown variables due to the mixing of motive and suction flow in these two zones.

In this section, there are seven independent variables in the two zones, namely, pressure (same for the motive flow and suction flow), velocity, specific enthalpy, and the cross-sectional area of motive and suction flows.

Similar to the modeling in the motive nozzle simulation, the differential of density is expressed as a function of pressure and specific enthalpy.

The cross-sectional area occupied by the motive flow and suction flow is related to the total cross-sectional area of the flow channel as follows:

$$\frac{\mathrm{d}A_m}{\mathrm{d}z} + \frac{\mathrm{d}A_s}{\mathrm{d}z} = \frac{\mathrm{d}A_{cs}}{\mathrm{d}z} \tag{3.44}$$

Where A_{cs} is the section area of the flow path. For constant mixing section, the area remains constant, and for the diffuser, it varies along the flow direction. The definition of the change is inputted with the known angle, length, and diameter information of the ejector.

After converting the above expressions into matrix form, the system of equations can be solved using Cramer's rule with a variable-step algorithm. A grid independent analysis is conducted to eliminate the effect of the mesh refinements on the results, as presented in Appendix B. All the coefficients used during the modeling are listed in Appendix C.

Based on the presented model, profiles of pressure, temperature, and velocity for both motive and suction flows can be obtained. Additionally, thermodynamic parameters such as vapor quality, specific enthalpy, and entropy can be derived. Distinguished from the 0-D model, the 1-D homogeneous equilibrium model provides a continuous change curve for all these parameters along the flow direction, except in the suction nozzle and pre-mixing sections. This feature allows for a more detailed understanding of the flow pattern inside the ejector.

3.3 Experimental validation of the 1-D HEM

In this section, the established 1-D ejector model is validated by using the experimental data from Zhu et al. [113]. Other experimental data from the open literature are also available; however, due to the lack of complete geometric information on the ejector, they cannot be used for the 1-D model validation.

3.3.1 Introduction of studied ejector

The schematic of the tested ejector is shown in Fig. 3.6, and the geometric parameters of the ejector are depicted in Table. 3.1.

The ejector studied in Fig. 3.6 features a convergent motive nozzle, which sets it apart from the more commonly used convergent-divergent nozzle. The throat of the nozzle is not simply a single point but rather a passage with a certain length. With a convergent nozzle, the maximum velocity of the flow at the outlet is limited to the local speed of sound, while a convergent-divergent nozzle can achieve supersonic velocities.

TABLE 3.1: Geometric parameters of the tested ejector from Zhu et al. [113]

D_t (mm)	D_m (mm)	NXP (mm)	L_m (mm)	θ_d (°)	θ_m (°)	D_P (mm)	D_S (mm)	D_B (mm)
0.8	2	3.4	18	7	40	8	8	7

3.3.2 Experimental validation of 1-D HEM for single case

To validate the 1-D HEM, the input parameters include the pressure and temperature values at the ejector inlets, as well as the mass flow rate of suction flow. The validated parameters are the ejector outlet pressure. Meanwhile, the 1-D HEM can also predict the mass flow rate of the motive flow and obtain the isentropic efficiency

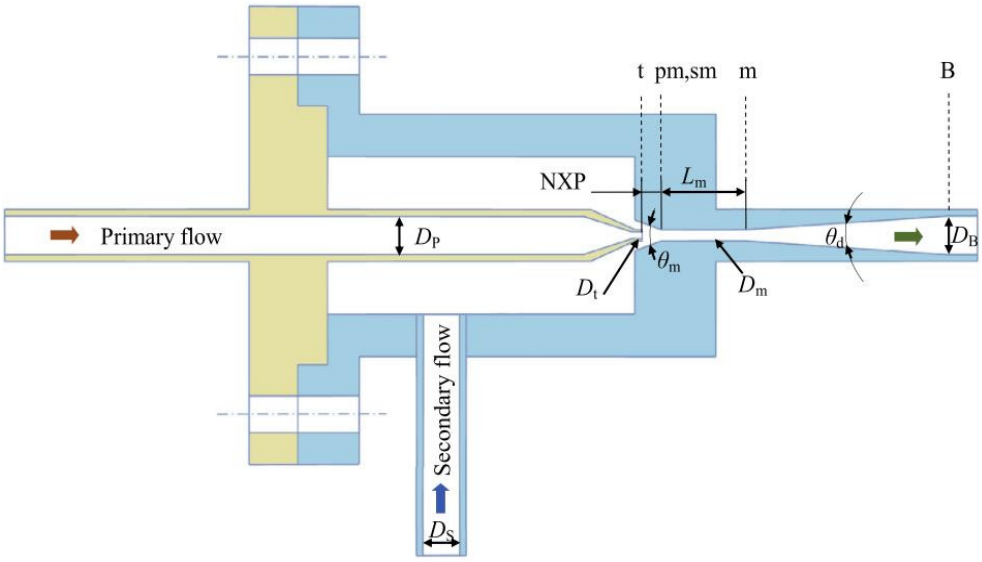

FIGURE 3.6: Schematic of the tested ejector from Zhu et al. [113]

of the motive nozzle. After simulating with the 1-D HEM, profiles of pressure, temperature, velocity, and various thermodynamic parameters along the flow path are obtained.

Fig. 3.7 illustrates the pressure curves for both the motive flow and the suction flow as well as the measured pressure for ejector inlet and outlet ports. The input parameters for the studied case are listed in Table. 3.2.

TABLE 3.2: Boundary conditions of ejector [113]

P_m (MPa)	P_s (MPa)	T_m (°C)	T_s (°C)	$\dot{m}_s$ (kg/h)
8.4	3.6	35.2	22.8	57.5

The 1-D model furnishes a comprehensive pressure curve for both flows throughout the entire flow path, demonstrating a close correlation between the measured ejector outlet pressure and the simulated values. It's noteworthy that, in the case of the motive nozzle, a constant area section follows the throat of the convergent part, contributing to the sustained pressure drop as illustrated in Fig. 3.7. As the motive flow approaches the critical state ($Ma = 1$), small variations lead to significant changes in the thermodynamic properties of CO_2. Consequently, the pressure curve for the motive flow exhibits distinct fluctuations near the throat position.

For the studied case presented in Table. 3.2, the sum of the mass flow rates of the motive and suction flows is 134.1 kg/h. The outlet value from the 1-D HEM is 133.3 kg/h, resulting in a relative error of 0.60 %. Additionally, the relative error of the energy balance is 0.61 %. The small relative errors in mass and energy balance indicate that the 1-D HEM is convergent, with a very small margin of error.

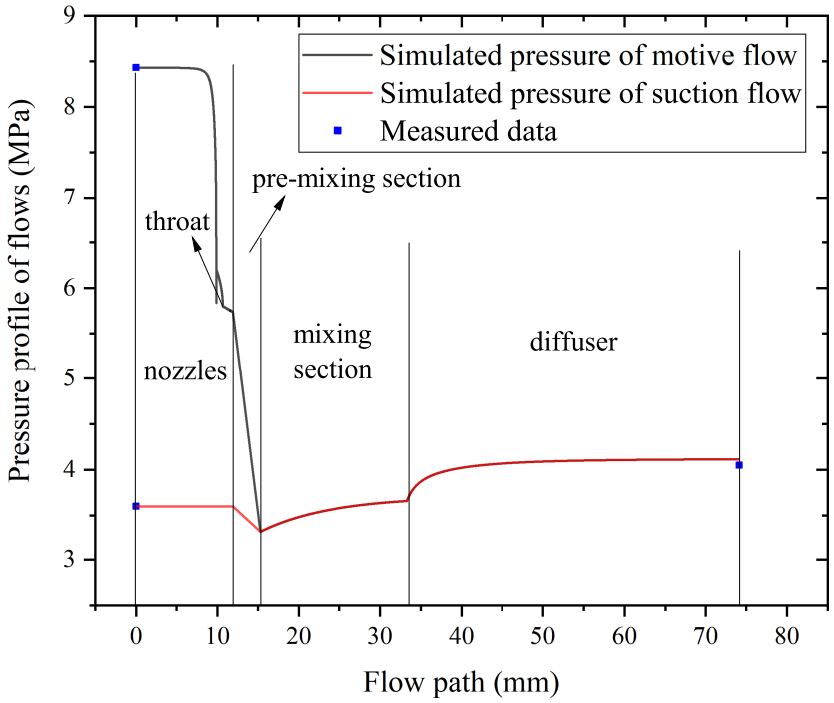

FIGURE 3.7: Pressure profile of ejector simulated by 1-D HEM based on ejector experimental results of Zhu et al. [113]

3.3.3 Validation of 1-D HEM with groups of data

Based on additional experimental data from Zhu et al. [113], the 1-D HEM is further validated. The simulated values of ejector outlet pressure and the mass flow rate of the motive flow are compared with the measured data.

Ejector outlet pressure validation

The simulated ejector outlet pressure is compared with the experimentally measured pressure, as shown in Fig. 3.8.

From Fig. 3.8, the simulated data and experimental data agree well, with absolute relative deviations generally within 5 %, except for rare cases where deviations exceed 5 %. It can also be observed from the figure that the simulated ejector outlet pressure is, in general, higher than the experimentally measured pressure.

Mass flow rate of motive flow validation

When the input pressure and temperature of the motive nozzle are set in accordance with a well-designed ejector, the motive nozzle operates under choked conditions, maximizing the mass flow rate of the motive flow. In this state, the motive flow attains the local speed of sound at the nozzle throat, resulting in the peak mass flow rate. Even though the exit pressure of the ejector continues to decrease, the mass flow

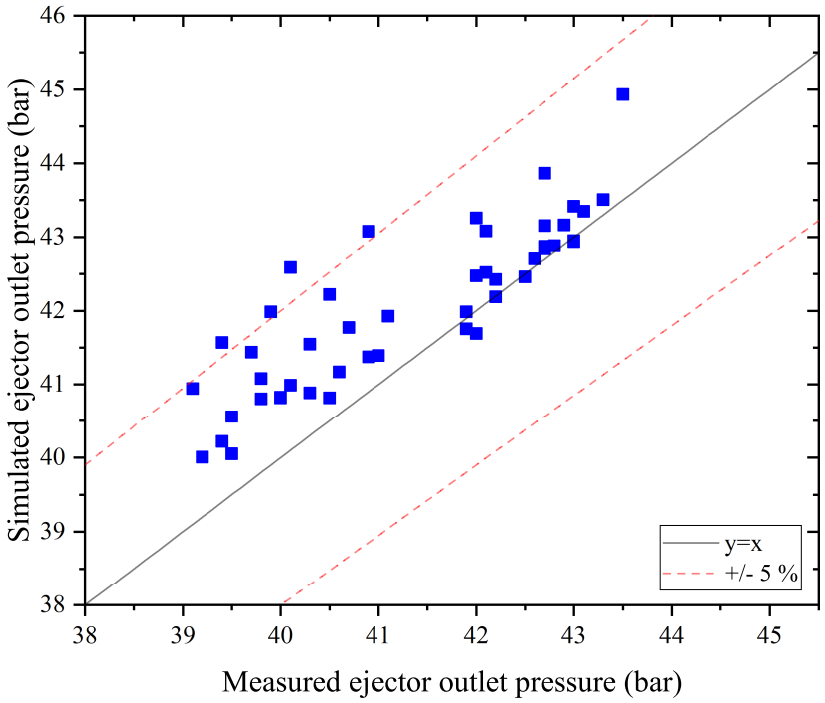

FIGURE 3.8: Simulated ejector outlet pressure as a function of measured outlet pressure from Zhu et al. [113]

rate remains constant, reaching a value known as the critical mass flow rate of the motive nozzle. This phenomenon is supported by the findings of the experimental data source [113].

With 1-D HEM, a prediction of the critical mass flow rate of the motive nozzle was conducted. This prediction is based on input pressure and temperature values of the motive flow and geometric parameters of the ejector, using data provided by [113]. The deviation between the actual mass flow rate and the predicted critical mass flow rate was plotted in Fig. 3.9. Analysis of the figure reveals that, in general, the actual mass flow rate is below the critical value, with a relative deviation of less than 15 %.

After validating the 1-D homogeneous equilibrium model with experimental data from the literature, it was observed that the 1-D HEM, based on Finite Volume Method, exhibits good agreement with the experimental results. The predictions of the ejector outlet pressure and critical mass flow rate of the motive nozzle are generally accurate, with deviations less than 5 % and 15 %, respectively.

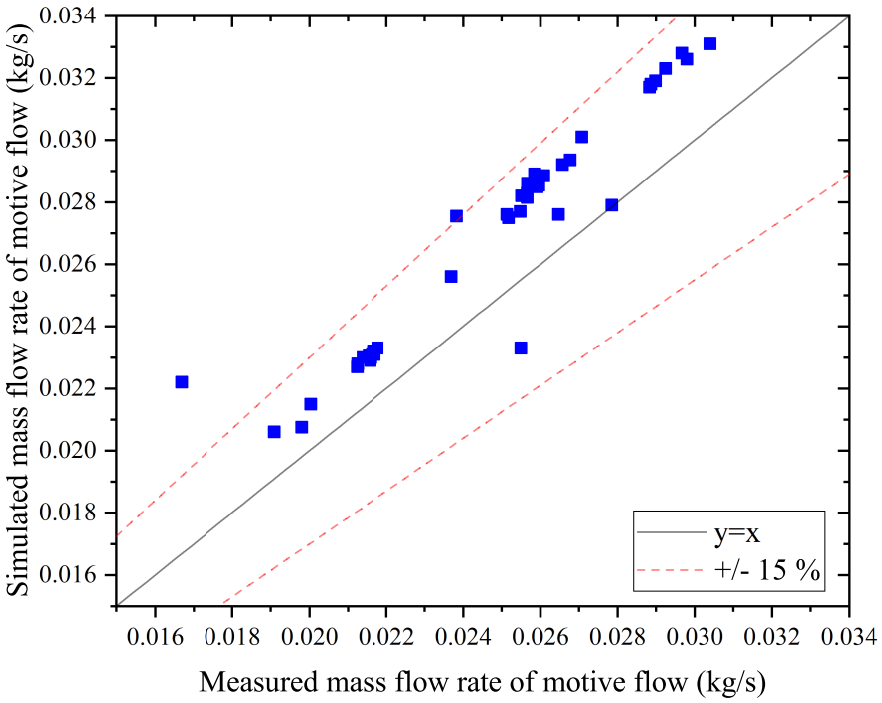

FIGURE 3.9: Calculated mass flow rate as a function of measured mass flow rate of motive flow from Zhu et al. [113]

3.3.4 Comprehensive analysis of thermodynamic parameters by 1-D HEM

Beyond experimentally validated parameters like the ejector outlet pressure and motive flow mass flow rate, the 1-D HEM furnishes an extended array of thermodynamic parameters, enriching the analysis of the internal flow field within the ejector.

Profiles of velocity of motive and suction flows

In Fig. 3.10, simulated velocity profiles for both the motive and suction flows along the ejector's flow path are presented. It is crucial to acknowledge that, given the intricate geometric configuration of the suction nozzle, the expansion of the suction flow is disregarded in the studied case. This assumption implies a constancy of thermodynamic parameters until the pre-mixing section, where the suction flow undergoes expansion, resulting in an increase in velocity.

In the case of the motive nozzle, the velocity undergoes a continuous increase until reaching the outlet of the pre-mixing section, exhibiting slight fluctuations around the nozzle throat. Subsequently, within the constant area mixing section and diffuser, the motive flow velocity steadily decreases.

Conversely, for the suction nozzle, there is a minor fluctuation in velocity within the mixing section, followed by a significant drop in the diffuser. This decrease in

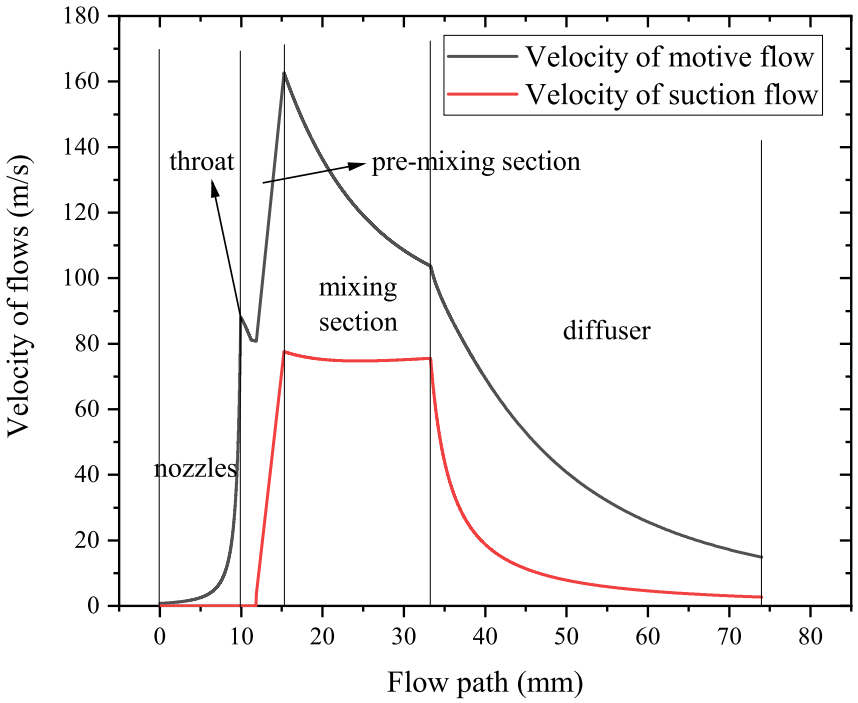

FIGURE 3.10: Velocity profile of ejector, with input parameters listed in Table. 3.2

kinetic energy elucidates the pressure recovery observed in the diffuser for both the motive and suction flows.

In the 1-D HEM, the motive flow and suction flow are simulated separately, and their interaction is governed by equations. As a result, the velocities of the motive and suction flows do not reach the same value at the diffuser outlet. However, in the final part of the diffuser, as it extends in length, the gap between the two velocities decreases. When the diffuser is sufficiently long, the two velocities will eventually merge and approach zero.

Calculation of isentropic efficiency of motive nozzle

In Fig. 3.11, the calculated values of the isentropic efficiency for the motive nozzle, as expressed in Eq. (3.45), are presented. Here, h_m and h_a represent the calculated specific enthalpy of the flow at the inlet and outlet of the motive nozzle, respectively, and $h_{a,is}$ is the outlet specific enthalpy for an ideal isentropic expansion process, which is obtained by state of equation with known specific entropy and pressure values.

$$\eta_m = \frac{h_{a,is} - h_m}{h_a - h_m} \tag{3.45}$$

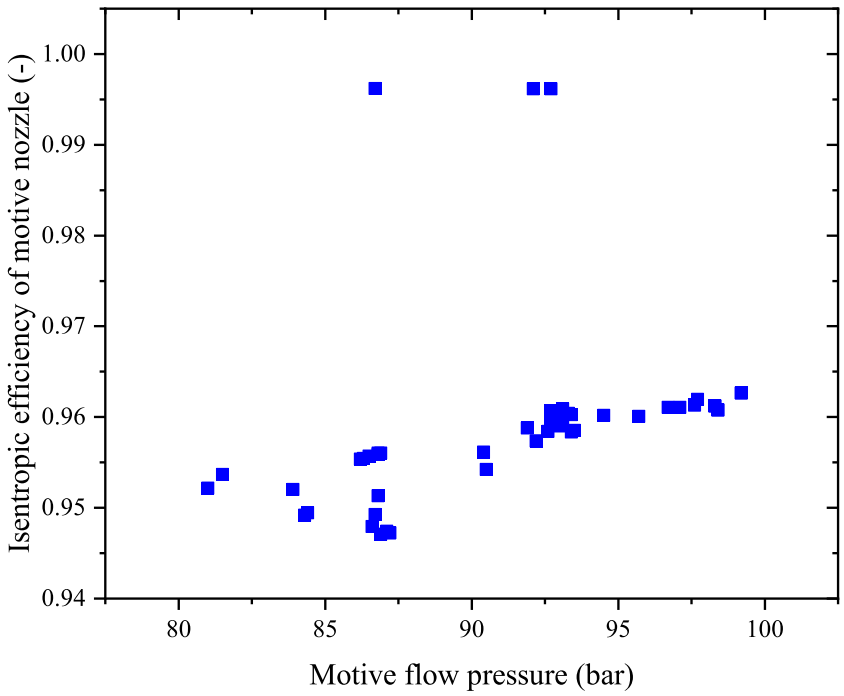

FIGURE 3.11: Calculated isentropic efficiency as a function of motive pressure [113]

The isentropic efficiency of motive nozzle serves as an input parameter for the 0-D thermodynamic models. In the cases examined, the motive nozzle efficiency generally ranges between 0.94 and 0.96, with only a few exceptions where the value exceeds 0.99. This discrepancy could be attributed to measurement deviations or fluctuations in the operation of the ejector.

3.3.5 Conclusion

The simulated ejector outlet pressure and motive flow mass flow rate align well with the measured data obtained from the literature [113]. The absolute relative deviation of the ejector outlet pressure remains consistently below 5 %, while for the mass flow rate of the motive flow, it stays within the range of 15 %. Furthermore, the 1-D HEM exhibits its capability to furnish a comprehensive profile of the pressure and various thermodynamic parameters along the entire flow path. This represents a significant advantage over 0-D models, which are limited to provide data at only a few points in the flow direction.

3.4 Parametric analysis of ejector operation conditions

After experimental validation of the 1-D HEM, the model becomes a valuable tool for the parametric analysis of ejector operating conditions. The examined parameters encompass the inlet temperature and pressure of both motive and suction nozzles, along with the mass flow rate of the suction flow. Key indices of the ejector include the ejector outlet pressure, ejector efficiency (Eq. (2.4)), and the mass flow rate of the motive flow. The parametric study is based on the ejector geometry outlined by Zhu et al. [113], with default input parameters detailed in Table. 3.3.

TABLE 3.3: Boundary conditions of ejector for parametric analysis of ejector operation conditions [113]

P_m (MPa)	P_s (MPa)	T_m (°C)	T_s (°C)	$\dot{m}_s$ (kg/h)
9.6	3.6	35.4	21.2	48.0

3.4.1 Analysis of the inlet pressure of suction flow

The study focuses on the inlet pressure of the suction flow, with the pressure range set between 3 and 5 MPa. It's important to note that, within this range, the default temperature for the boundary conditions in Table. 3.3 remains in a super-heated state.

Since the suction nozzle pressure does not affect the mass flow rate of the motive flow, and the mass flow rate of the suction nozzle is held constant at the default value provided in Table. 3.3, the entrainment ratio of the ejector remains constant throughout the analysis. The simulation results are illustrated in Fig. 3.12.

Analysis of Fig. 3.12 reveals a nearly linear correlation between the increase in the inlet pressure of the suction flow and the subsequent rise in ejector outlet pressure. Since the mass flow rate and inlet pressure of the motive flow are held constant, the compression capacity remains almost uniform across all cases. As the inlet pressure of the suction flow increases, with a constant mass flow rate, the suction flow undergoes compression to a higher pressure, resulting in a corresponding elevation in the ejector outlet flow, which is a mixture of the motive flow and suction flow.

Examining ejector efficiency, it exhibits an initial fluctuation followed by a decrease with the rise in the inlet pressure of the suction flow. Notably, an optimal ejector efficiency of 0.415 is observed at an inlet pressure of 33 bar within the studied range.

3.4.2 Analysis of the inlet temperature of suction flow

The study focuses on the inlet temperature of the suction flow, with the temperature range set between 2 and 30 °C. Other inputs remain consistent with those listed in

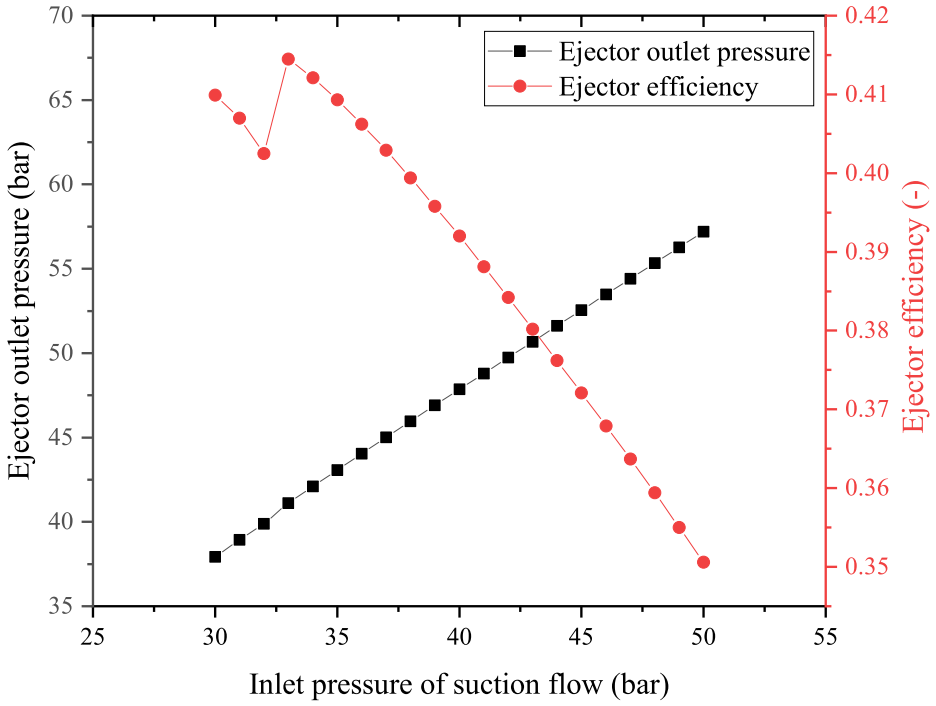

FIGURE 3.12: Ejector outlet pressure and ejector effiency as a function of inlet pressure of suction flow

Table. 3.3. Throughout the entire temperature range under consideration, the suction flow remains in a super-heated state, albeit with varying degrees of super heat. The simulation results are depicted in Fig. 3.13.

Examining Fig. 3.13, initial fluctuations are observed for both the ejector outlet pressure and ejector efficiency. Within the temperature range of 7 °C to 18 °C, the ejector outlet pressure exhibits a consistent decline with increasing temperature. Notably, the ejector efficiency reaches an optimal value of 0.392 at an inlet temperature of 13 °C. Beyond this range, a linear decrease in ejector outlet pressure with increasing inlet temperature is observed, accompanied by a linear increase in ejector efficiency.

In practical operation, the degree of super heat depends on the evaporator design. The stable range of inlet temperatures identified by the 1-D HEM can serve as a valuable reference for defining rated operational conditions.

3.4.3 Analysis of the mass flow rate of suction flow

For the analysis of the mass flow rate of the suction flow, the inlet pressure and temperature values of both motive and suction flows are set to the default values listed in Table. 3.3. The mass flow rate of the motive flow is also kept constant, calculated by the 1-D HEM. The examined range for the mass flow rate of the suction flow

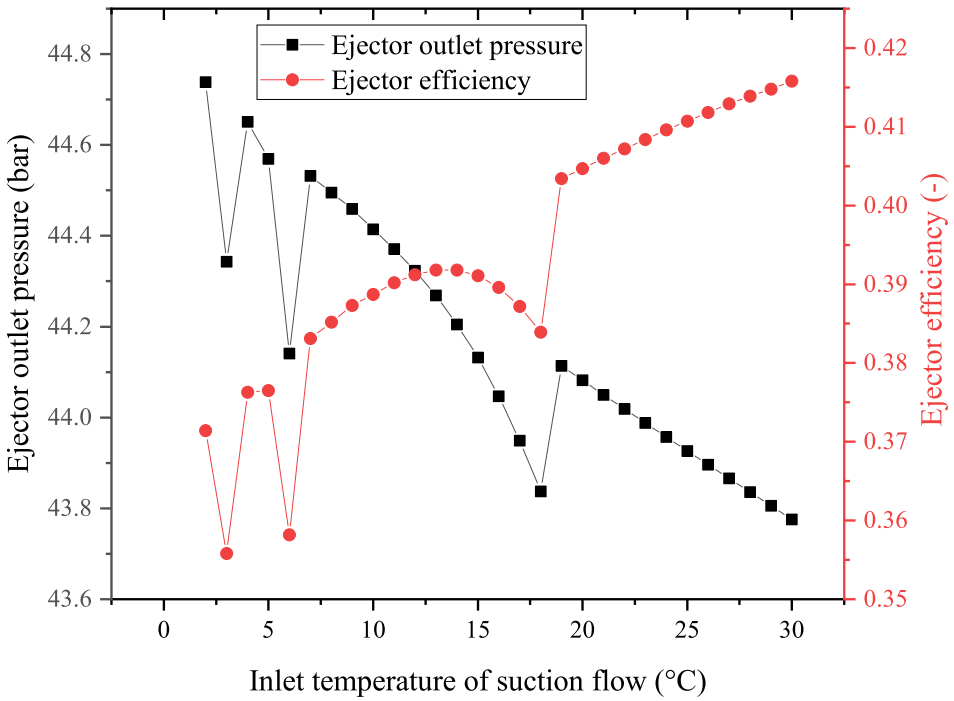

FIGURE 3.13: Ejector outlet pressure and ejector efficiency as a function of inlet temperature of suction flow

spans from 15 kg/h to 100 kg/h, considering that the mass flow rate of the motive flow is approximately 110 kg/h. The simulation results are depicted in Fig. 3.14.

Analyzing Fig. 3.14, it is observed that the ejector outlet pressure decreases with the increasing mass flow rate due to the fixed compression capacity of the motive flow. The ejector efficiency exhibits a rapid rise from 0.2 to 0.4 as the mass flow rate changes from 15 kg/h to 45 kg/h. Subsequently, the ejector efficiency continues to increase with the mass flow rate, but the margins become minimal, showing only an 8 % relative increase when the mass flow rate is 100 kg/h compared to 45 kg/h. Given the constant value of the mass flow rate of the motive flow, an increase in the mass flow rate of the suction flow results in a higher entrainment ratio of the ejector. These results underscore the existence of an optimal entrainment ratio range for the actual operation of the ejector, considering the tradeoffs between ejector efficiency and pressure boosts.

3.4.4 Analysis of inlet pressure of motive flow

For the analysis of the inlet pressure of motive flow, the inlet pressure and temperature values of suction flows as well as the mass flow rate of suction flow and inlet temperature of the motive flow, are set to the default values listed in Table. 3.3. The mass flow rate of the motive flow is calculated by the 1-D HEM and various with the

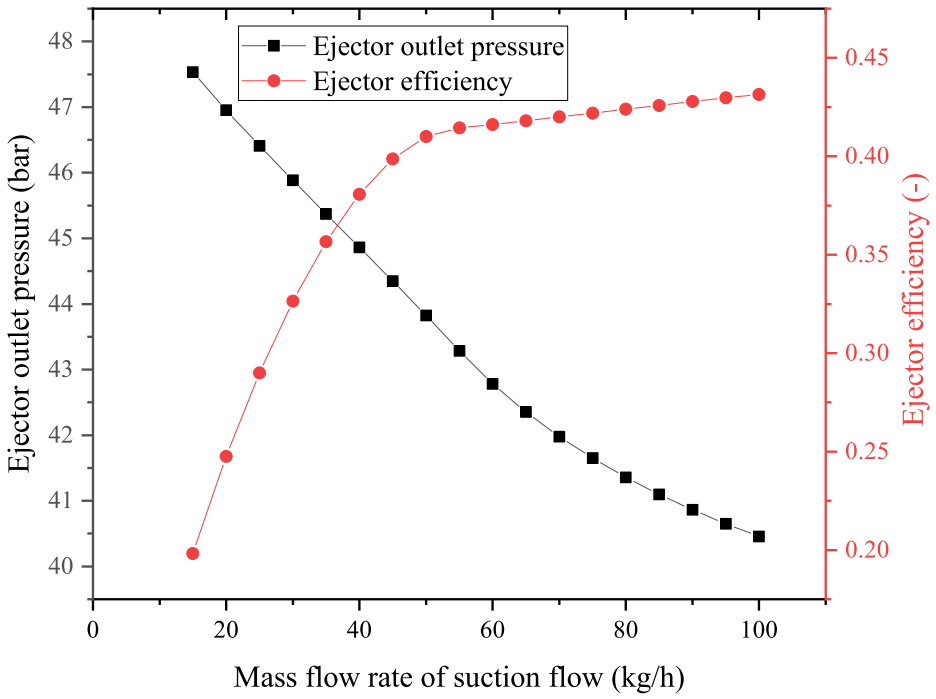

FIGURE 3.14: Ejector outlet pressure and ejector efficiency as a function of mass flow rate of suction flow

inlet pressure of motive flow. The examined range for the inlet pressure of motive flow is between 84 bar to 130 bar. The simulation results are depicted in Fig. 3.14.

Analyzing Fig. 3.15, it is observed that in general, the ejector outlet pressure and mass flow rate of motive flow increase with the inlet pressure of motive flow except few cases with small fluctuation. The ejector outlet pressure increases from 40.9 bar to 50.8 bar (24.3 %), and the mass flow rate increase from 56.2 kg/h to 176.0 kg/h (213.5 %). The trend of the mass flow rate is identical to the experimental data from Zhu et al. [113], as shown in Fig. 3.16.

For the ejector efficiency, when the inlet pressure of motive flow changes, the ejector efficiency varies in a small range (0.39 to 0.41), and no clear trend is concluded, which means the ejector efficiency is an index influenced by multiple factors and is not strongly affected to the inlet pressure of motive flow.

3.4.5 Analysis of inlet temperature of motive flow

For the analysis of the inlet temperature of motive flow, the inlet pressure and temperature values of suction flows as well as the mass flow rate of suction flow and inlet pressure of motive flow are set to the default values listed in Table. 3.3. The mass flow rate of the motive flow is calculated by the 1-D HEM and various with

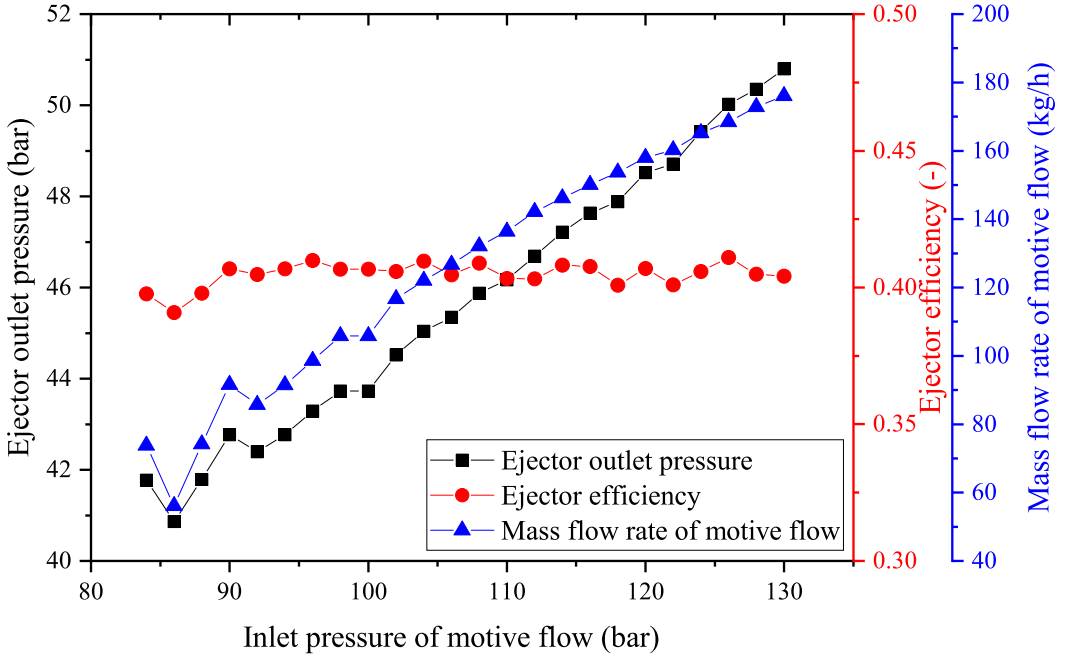

FIGURE 3.15: Ejector outlet pressure, ejector efficiency and mass flow rate of motive flow as a function of inlet pressure of motive flow

the inlet pressure of motive flow. Considering the cycle should work in a transcritical mode and when the inlet temperature of motive flow is too high, the flow will be in superheated state after the expansion in the motive nozzle, the examined range for the inlet temperature of motive flow is between 35 °C to 42 °C. The simulation results are depicted in Fig. 3.17.

Analyzing Fig. 3.17, it is observed that in general, the ejector efficiency and mass flow rate of motive flow decrease with the inlet temperature of motive flow. The relative change of ejector efficiency and mass flow rate of motive flow is -8.7 % and -32.4 %, respectively. For the ejector outlet pressure, in general the ejector outlet pressure decreases with the inlet temperature, but when the temperature is 36 and 39 °C, there is an increase steeply, probably due to the shock wave in the mixing section or pre-mixing section.

3.4.6 Conclusion

Five boundary conditions for the ejector operation are analyzed: the inlet temperature and pressure of motive and suction flows, the mass flow rate of the suction flow. The change of ejector outlet pressure, ejector efficiency and mass flow rate of the motive flow are tracked for the parametric analysis. It is concluded that in general, the ejector efficiency increases with a higher inlet temperature of suction flow,

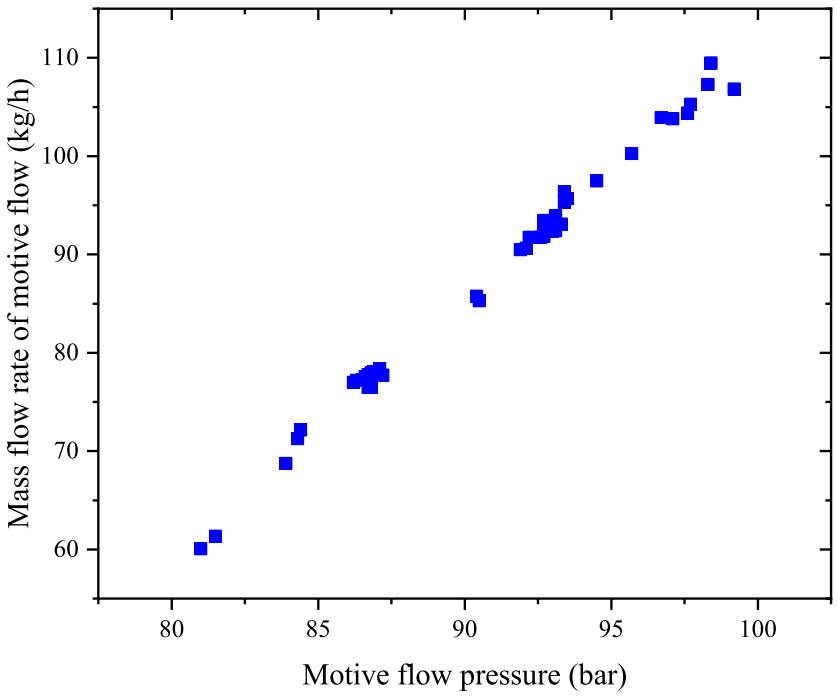

FIGURE 3.16: The measured mass flow rate of motive flow as a function of inlet pressure of motive flow, data from Zhu et al. [113]

and higher mass flow rate of suction flow. The ejector efficiency decreases with the inlet temperature of motive flow and inlet pressure of suction flow. And no clear correlation is found between ejector efficiency and inlet pressure of motive flow.

The ejector outlet pressure increases with the inlet pressure of motive and suction flow. On the contrary, the ejector outlet pressure decreases with the inlet temperature of suction flow, the mass flow rate of the suction nozzle and the inlet temperature of motive flow.

When changing the inlet pressure and temperature of the motive flow, the mass flow rate of motive flow will also change. It increases with the inlet pressure and decreases with the temperature.

The trends above are in general for the studied range, however, major fluctuation happens in some points, the most possible reason is due to the change of the numbers of the shock wave inside the ejector. With shock wave, the flow velocity will have a steep decrease and the pressure will have a steep increase.

3.5 Ejector design with 1-D HEM

The established 1-D homogeneous equilibrium model of the entire ejector region proves versatile for ejector design applications. Fig. 3.18 illustrates the detailed geometric configuration and main parameters of a typical constant-pressure mixing

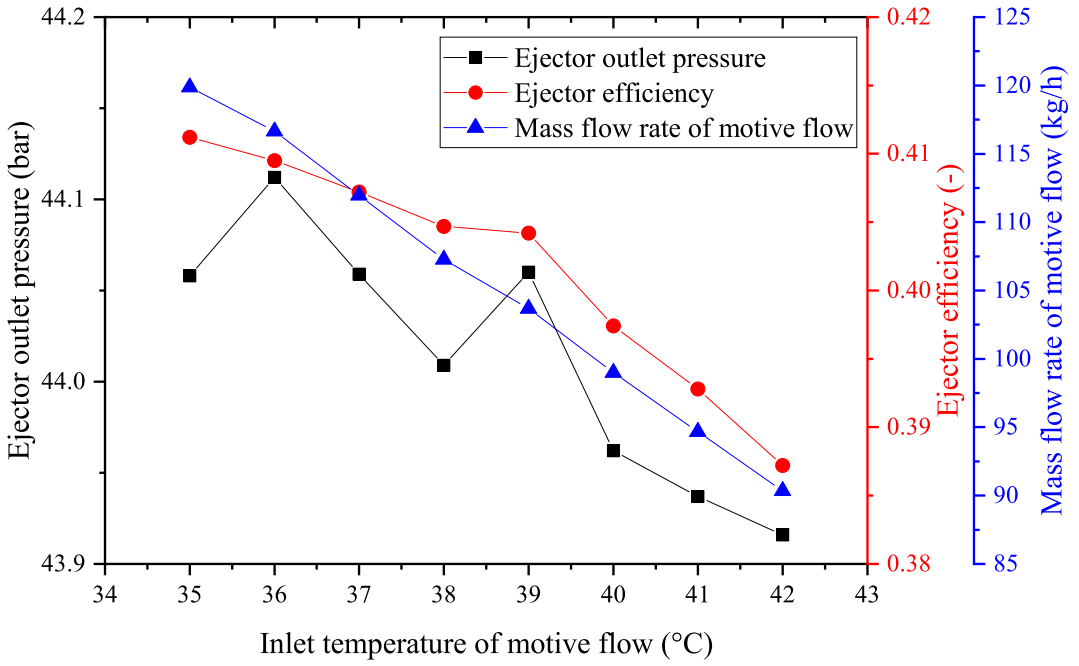

FIGURE 3.17: Mass flow rate of motive flow, ejector outlet pressure and ejector efficiency as a function of inlet temperature of motive flow

ejector with a convergent-divergent motive nozzle.

In this section, the analysis focuses on five parameters: the length of the constant area mixing section (L_{mix}), the length of the diffuser (L_{dif}), the diameter of the mixing section (D_{mix}), the diffuser angle (γ_{dif}) and the roughness of the wall. Given that the primary function of the ejector in the heat pump cycle is the compression of the suction flow through the expansion of the motive flow, key parameters during the design process include the ejector outlet pressure and entrainment ratio.

However, it's worth noting that the geometric parameters of the nozzle part are not under consideration in this analysis. Additionally, with given inlet pressures and temperatures, as well as the mass flow rate of the suction flow, the entrainment ratio remains constant irrespective of variations in the mentioned geometric parameters. Therefore, this section delves into studying the impact of the five geometric parameters on the ejector outlet pressure and ejector efficiency. The objective is to optimize the design of the ejector using the 1-D HEM as a valuable auxiliary tool.

For all geometric studies, the reference ejector is chosen as the ejector from Zhu et al. [113], and the boundary parameters are chosen as the configuration listed in Table. 3.4.

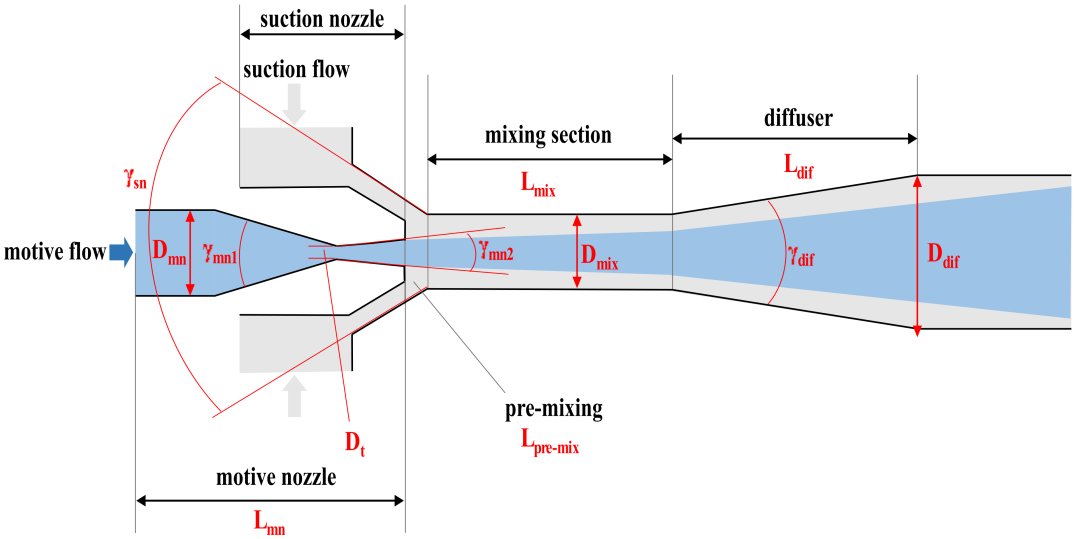

FIGURE 3.18: Geometric parameters of the ejector

TABLE 3.4: Boundary conditions used for ejector design based on ejector from Zhu et al. [113]

P_m (MPa)	P_s (MPa)	T_m (°C)	T_s (°C)	$\dot{m}_s$ (kg/h)
9.3	3.6	35.5	22.8	46.9

3.5.1 The length of the constant area mixing section

The relationship between the ejector outlet pressure and ejector efficiency in response to variations in the length of the constant-area mixing section is illustrated in Fig. 3.19.

As the mixing section length changes from 6 mm to 44 mm, the ejector outlet pressure demonstrates an increase from 41.5 bars to 43.4 bars, reflecting a relative change of 4.5 %. Simultaneously, the ejector efficiency undergoes a noticeable improvement, rising from 0.31 to 0.44, indicating a relative change of 40.7 %.

Analysis of Fig. 3.19 suggests that increasing the length of the mixing section in an ejector can enhance the outlet pressure and ejector efficiency, up to a certain threshold. This phenomenon arises from the mixing section, where the high-pressure, high-velocity motive fluid interacts with and blends into the low-pressure, low-velocity suction fluid. The extended mixing section allows for more efficient mixing and momentum transfer, resulting in a higher outlet pressure and higher ejector efficiency.

However, there are limitations to this benefiting. An excessively long mixing section may experience restricted pressure recovery due to friction losses or other inefficiencies, hindering further increases in the outlet pressure[121]. Additionally, the impact of mixing section length on the ejector outlet pressure is constrained by the magnitude of the increase.

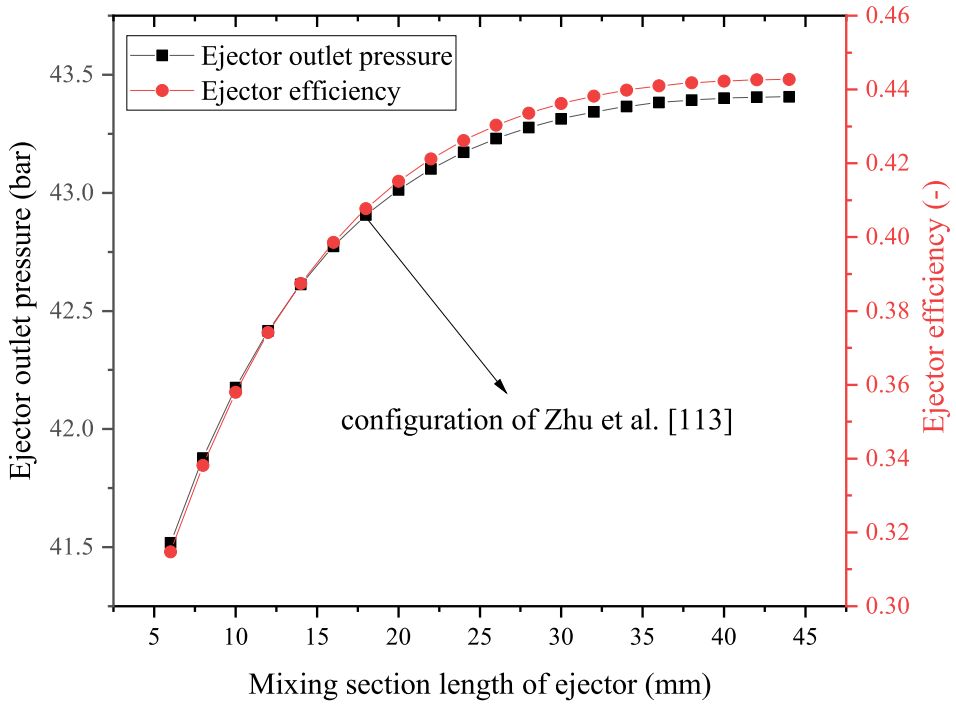

FIGURE 3.19: Ejector outlet pressure and ejector efficiency as a function of the mixing section length

Similar findings were reported by Varga et al. [122]. They observed that the length of the constant area section did not significantly influence the entrainment ratio of the ejector within the studied range. Nevertheless, the critical back pressure increased with the length, reaching an optimum at 155 mm. This allowed the ejector to operate in double choking mode for higher condenser pressure (temperature). Further lengthening did not improve the critical back pressure, making 155 mm the optimal length. The increase in critical back pressure implies that, when the input parameters of the ejector are fixed, the ejector outlet pressure will rise.

Contrastingly, Nakagawa et al. [123] investigated the effect of mixing length on ejector system performance. Using mixing lengths of 5 mm, 15 mm, and 25 mm with a constant rectangular cross-section, they found that mixing length significantly influenced entrainment ratio, pressure recovery magnitude, and profile. The 5 mm and 15 mm types yielded the lowest and highest ejector efficiency and COP in all conditions, respectively. The 15 mm type also provided the highest pressure recovery.

Moreover, the optimum length of the mixing section depended on the inlet pressure to the motive nozzle and ranged between 20 mm and 25 mm in the study by Banasiak et al. [124].

3.5.2 The length of the diffuser

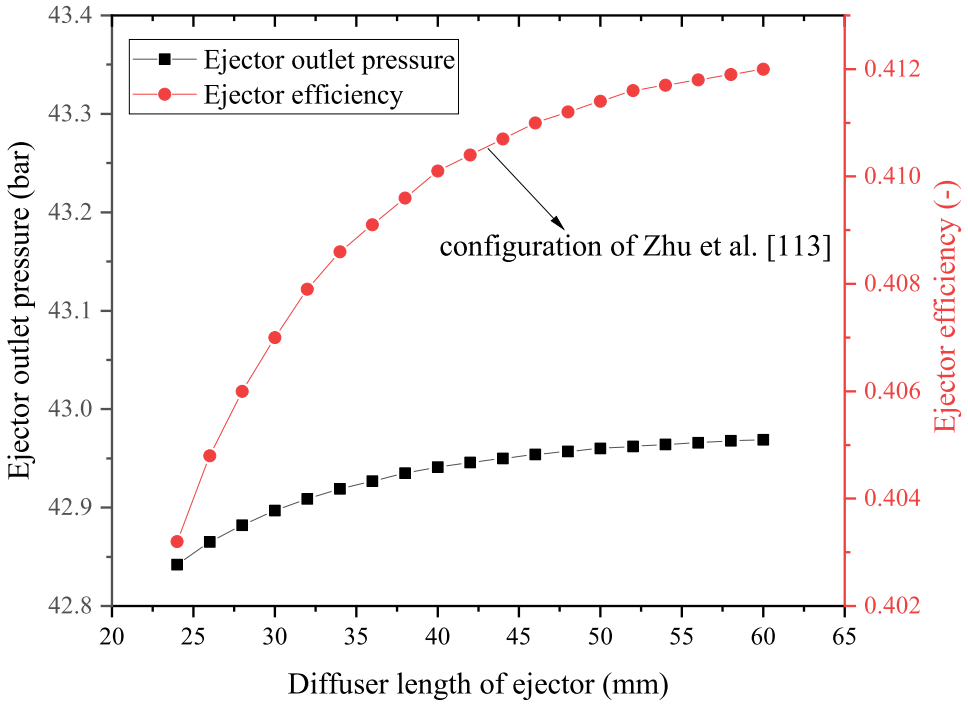

FIGURE 3.20: Ejector outlet pressure and ejector efficiency as a function of the diffuser length

Testing the ejector under the conditions specified in Table. 3.4 while varying diffuser lengths provided results showcased in Fig. 3.20. The ejector outlet pressure ranges from 42.8 bars to 43.0 bars, reflecting a minimal relative change of 0.3 %. Simultaneously, the ejector efficiency experiences a slight increase from 0.40 to 0.41, indicating a relative change of 2 %, as the diffuser length varies from 24 mm to 60 mm.

While varying the length of the diffuser, it is important to note that the diffuser angle (7°) remains constant, leading to changes in the outlet diameter of the diffuser with variations in length.

Analyzing the results presented in Fig. 3.20, it can be concluded that the length of the diffuser has a limited impact. Although both the ejector outlet pressure and ejector efficiency show increases with the diffuser length, the gains are relatively modest. Consequently, the clear benefit of a longer diffuser length in the process of ejector design remains uncertain. These findings align with the trend identified by Wu et al. [125].

3.5.3 The diameter of the constant area mixing section

Under the conditions specified in Table. 3.4, the ejector was tested with various diameters of the constant area mixing section, and the results are illustrated in Fig. 3.21. The ejector outlet pressure exhibits a range from 39 bars to 44 bars as the diameter of the constant mixing section changes from 1 mm to 6 mm.

When altering the diameter of the constant area mixing section while maintaining a constant length, the outlet diameter of the diffuser and the divergent angle of the diffuser remain unchanged. However, the length of the diffuser varies with the different diameters of the mixing section. Nevertheless, considering the analysis of the effect of the diffuser length, the impact of the change in diffuser length during the alteration of the diameter of the constant area mixing section can be considered negligible.

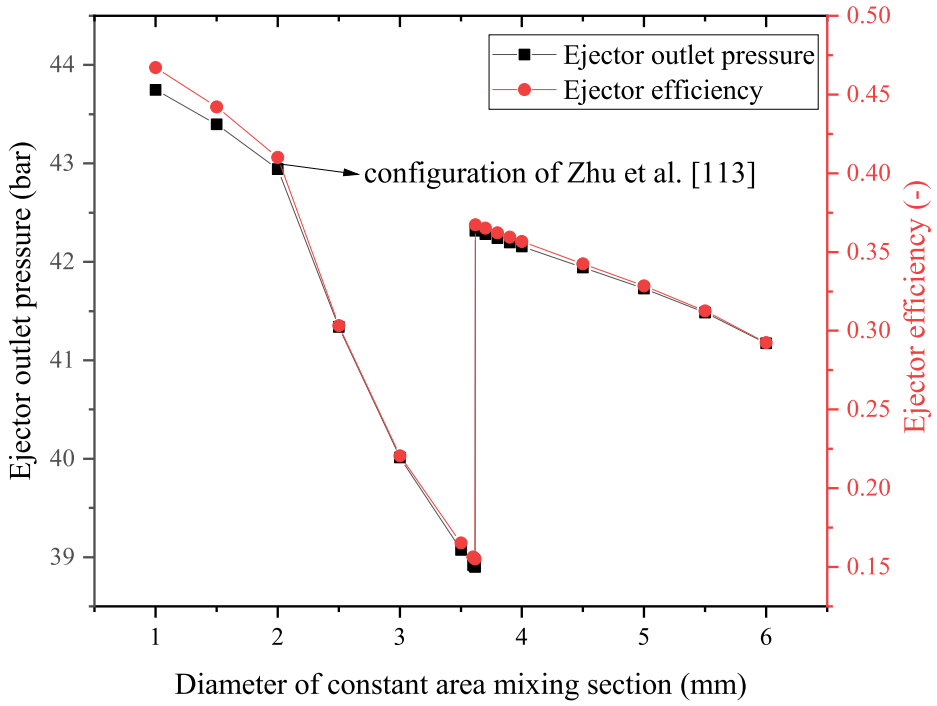

FIGURE 3.21: Ejector outlet pressure and ejector efficiency as a function of the mixing section diameter

Banasiak et al. [124] experimentally demonstrated that the best performance was achieved with a 3 mm diameter (ranging from 2 mm to 5 mm with a step of 1 mm). For smaller diameters, the ejector was unable to entrain the appropriate amount of super-heated vapor from the evaporator at higher pressure values. This phenomenon was likely caused by throttling of the secondary flow in the mixer and a consecutive oblique-shock wave flow pattern. For larger diameters, the ejector was

unable to achieve high values of either pressure lift or efficiency due to poorer momentum exchange, possibly as a result of intensified recirculation.

Analyzing Fig. 3.21, a general trend emerges where the outlet pressure of the ejector and ejector efficiency tend to decrease with the increasing diameter of the mixing section. This observation aligns with the findings from the experimental analysis conducted by Banasiak et al. [124]. However, it's important to note that this trend is not entirely monotonic. At a diameter of 3.6 mm, there is a notable and steep rise, followed by a subsequent decrease in the ejector outlet pressure with further increases in the diameter of the constant mixing section. This trend is mirrored in the ejector efficiency. An explanation for this abrupt pressure rise is attributed to the presence of a shock wave in the mixing section, a phenomenon experimentally observed by researchers [126, 127].

3.5.4 The angle of the diffuser

The diffuser angle stands as a pivotal parameter in ejector design, extensively scrutinized by researchers. Banasiak et al. [124] conducted experiments to explore optimum ejector geometry for a small-capacity R744 heat pump. Their findings indicated that a diffuser angle of 5° yielded the best ejector performance among alternative options examined (7.5° and 10°). Similar results were reported by Elbel and Hrnjak [100], where small angles of 5° produced superior static pressure recovery compared to angles of 10° and 15°.

Numerical investigations further supported these findings. Levy et al. [128], using their developed model, explored various design parameters of the ejector as functions of the diffuser angle, concluding that better pressure recovery was achieved with smaller diffuser angles (1°, 3°, 5°, and 7° were studied).

Fig. 3.22 visually represents the ejector outlet pressure and ejector efficiency as functions of the diffuser angle, ranging from 1° to 11°. The results show a decrease in the ejector outlet pressure from 44.5 bars to 42.4 bars (relative change of -4.8 %), and a drop in ejector efficiency from 0.53 to 0.37 (relative change of -28.7 %), consistent with findings from the literature cited above.

However, based on the findings in the literature, there appears to be a limit to how small the diffuser angle can be made. Angles that are too small result in an extended section of small cross-sectional flow areas at the inlet of the diffuser. The increased frictional pressure drop, which is proportional to the flow velocity squared, reduces performance. On the other hand, if the angle is too large, boundary layer-induced flow separation causes the formation of turbulent vortices, which lower the static pressure recovery characteristics of the diffuser. This demonstrates the trade-off between kinetic energy losses due to vortex formation and losses caused by frictional pressure drop [129].

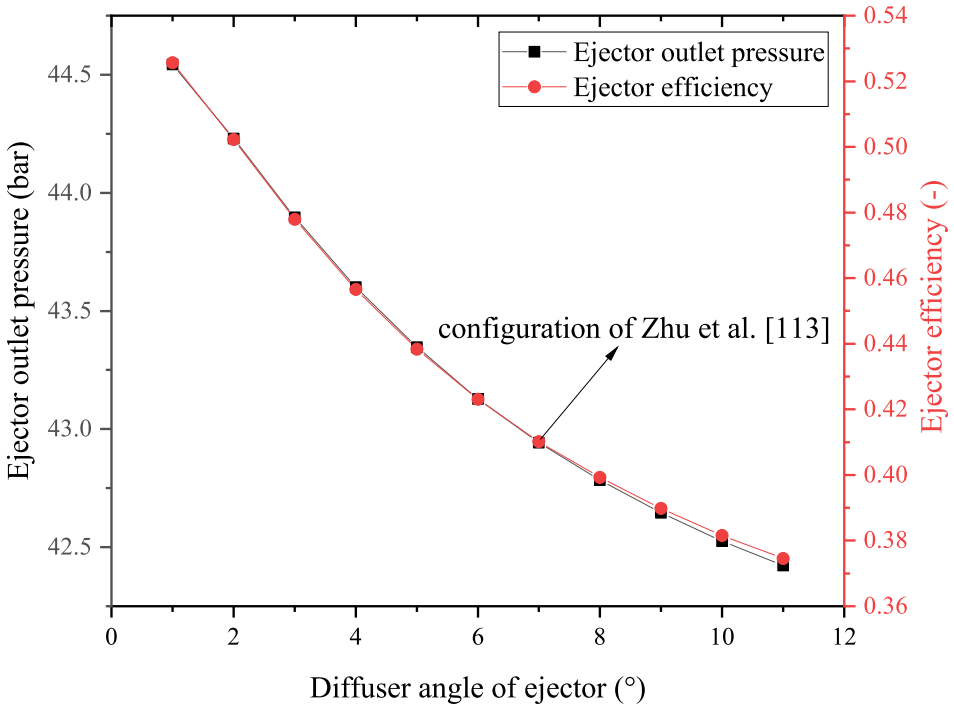

FIGURE 3.22: Ejector outlet pressure and ejector efficiency as a function of the diffuser angle

This trend is not explicitly evident from the simulation results in this section, possibly due to the simplifications in the modeling. Therefore, more detailed simulation and experimental studies need to be conducted to verify this trade-off and understand the optimal range for the diffuser angle.

3.5.5 The roughness of the wall

Under the conditions specified in Table. 3.4, the ejector was tested with various roughness of the wall (ϵ_{wall}), and the results are illustrated in Fig. 3.23.

From Fig. 3.23, it is evident that both the ejector outlet pressure and efficiency decrease with an increase in wall roughness due to higher friction losses between the fluid and the wall. However, given the small size of the ejector (less than 8 cm along the flow direction), the impact of roughness is quite limited. Specifically, when the wall roughness increases from 1 μm to 10 μm, the ejector outlet pressure drop is less than 0.3 bar, resulting in a relative change of around 0.49 %.

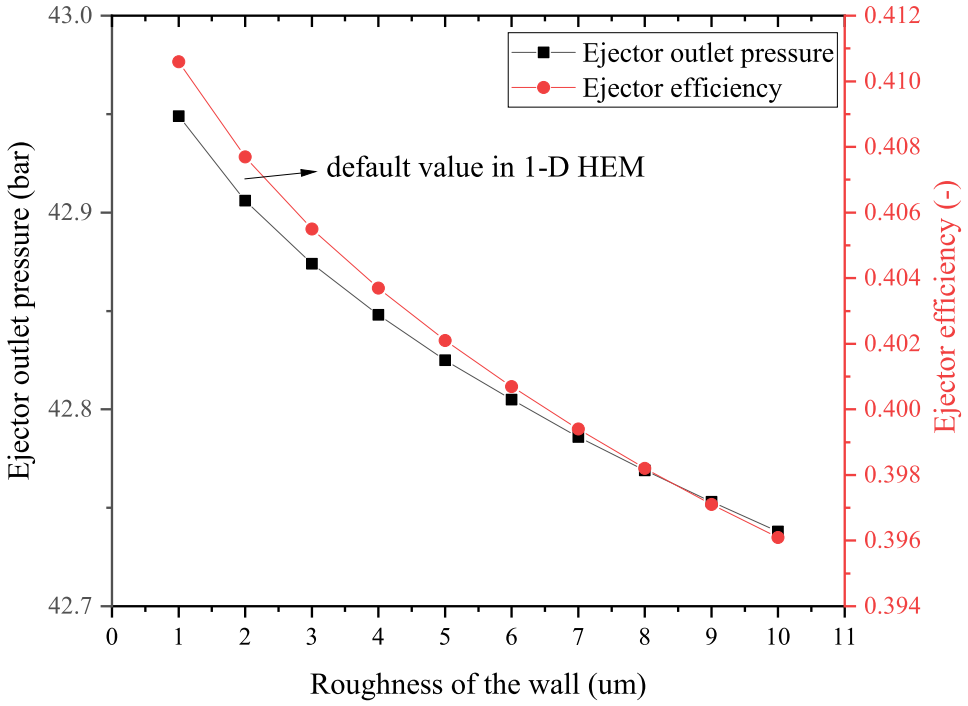

FIGURE 3.23: Ejector outlet pressure and ejector efficiency as a function of the roughness of the wall

3.5.6 Conclusion

In this section, five fundamental geometry parameters of the ejector (L_{mix}, L_{dif}, D_{mix}, γ_{dif}, ϵ_{wall}) were systematically analyzed using the 1-D HEM. The quantitative impact of these parameters on ejector performance, specifically the ejector outlet pressure and ejector efficiency, is presented. Among these parameters, the diffuser angle and the diameter of the constant area mixing section exhibit significant effects on ejector performance, followed by the length of the mixing section. Both the diffuser length and the roughness of the wall have an impact on the ejector performance, albeit within limited extents. Achieving the optimal design of the ejector requires a comprehensive analysis and valuation of these parameters.

3.6 Comparison with 0-D thermodynamic models

Fig. 3.24 presents simulation results of three 0-D thermodynamic models, along with the results of the 1-D HEM, for comparison. The analysis utilizes the same ejector studied by Zhu et al. [113], and the experimental data used in the validation section of the 1-D HEM. For the three 0-D thermodynamic models, the input isentropic efficiency of motive nozzle, suction nozzle, diffuser is 0.85, 0.85 and 0.8, respectively. The fixed pressure drop for the model of Li [62] is assumed to be 0.05 MPa.

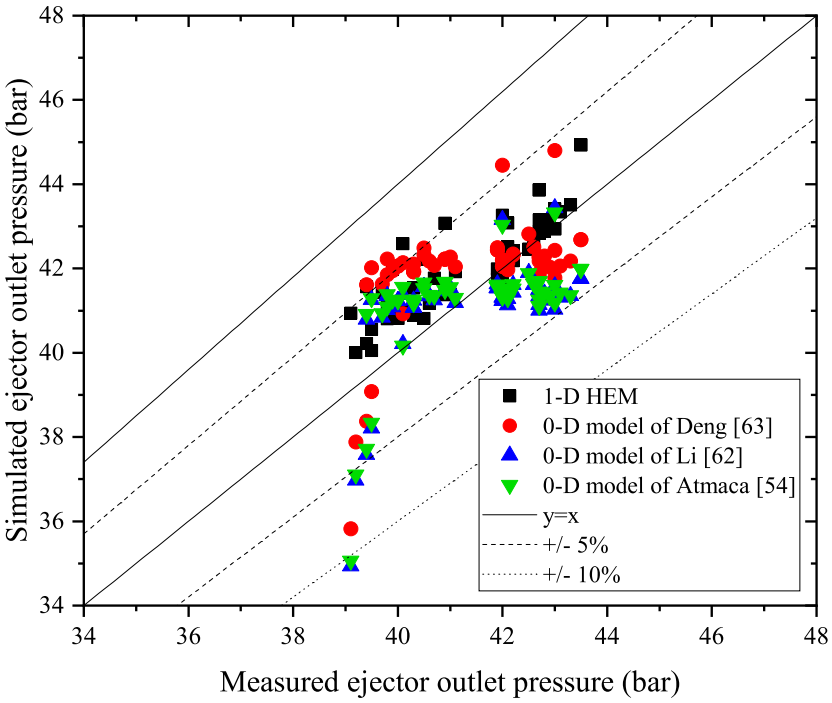

FIGURE 3.24: Comparison of 0-D thermodynamic models with 1-D HEM in simulating ejector outlet pressure

From Fig. 3.24, it is evident that the 1-D HEM demonstrates better agreement with the experimental data. The 0-D models exhibit cases where the relative error can reach more than 10 %. Additionally, it is observed that, compared to the models proposed by Deng and Li [62, 63], the model from Atmaca [54] performs better. However, the extent of this improvement is not substantial. Considering the increasing complexity of the three models (Deng, Li, and Atmaca) in ascending order, the benefit gained does not seem justified.

It is important to note that the input isentropic efficiencies of ejector components differ from those discussed in Chapter 2 when validating all the 0-D models using the same experimental data from Zhu et al. [113]. In contrast to the findings presented in Chapter 2, which focused on comparing various 0-D models and concluded that the model proposed by Deng [63] exhibited the best performance, there is a discrepancy in the conclusion drawn from Fig. 3.24. This observation leads to the inference that the accuracy of 0-D thermodynamic models is significantly influenced by the efficiencies of the input ejector components.

Fig. 3.25 illustrates the simulated ejector efficiency as a function of the measured entrainment ratio for both 0-D thermodynamic models and the 1-D HEM. Analyzing the figure, it is evident that, for 0-D thermodynamic models, the ejector efficiency demonstrates a nearly linear correlation with the measured entrainment ratio, consistent with the results presented in Chapter 2. On the other hand, for the 1-D HEM,

the ejector efficiency increases with the entrainment ratio up to a certain point, after which it remains constant. This disparity suggests that the 1-D HEM, with its increased complexity and incorporation of additional factors affecting ejector efficiency—such as friction loss along the wall and the friction arising from the mixing of two flows—produces a trend closer to reality compared to the simpler 0-D thermodynamic models.

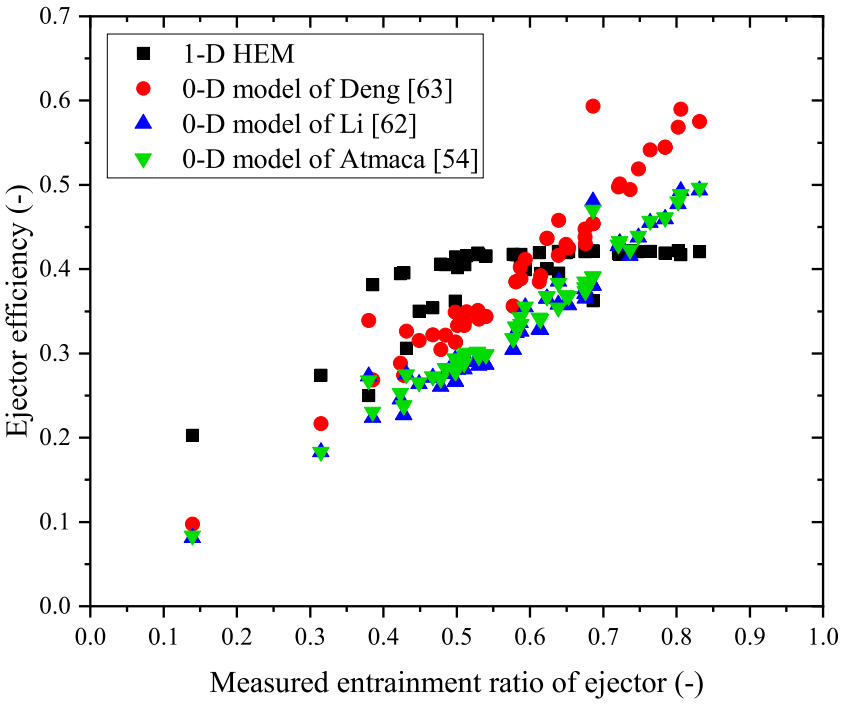

FIGURE 3.25: Comparison of 0-D thermodynamic models with 1-D HEM in simulated ejector efficiency as a function of measured entrainment ratio

Fig. 3.26 displays the pressure profiles of the motive flow for all three 0-D models and the 1-D HEM model. The input parameters for the studying case are listed in Table. 3.5. The 1-D model, employing Finite Volume Method along the flow path, provides a complete pressure curve. In contrast, the 0-D thermodynamic models only calculate a few sections along the flow path.

TABLE 3.5: Boundary conditions of ejector [113]

P_m (MPa)	P_s (MPa)	T_m (°C)	T_s (°C)	$\dot{m}_s$ (kg/h)
9.2	3.6	35.3	22.4	53.3

However, for the studied case, the relative deviation between the simulated ejector outlet pressure and measured outlet pressure of three 0-D models (in the order

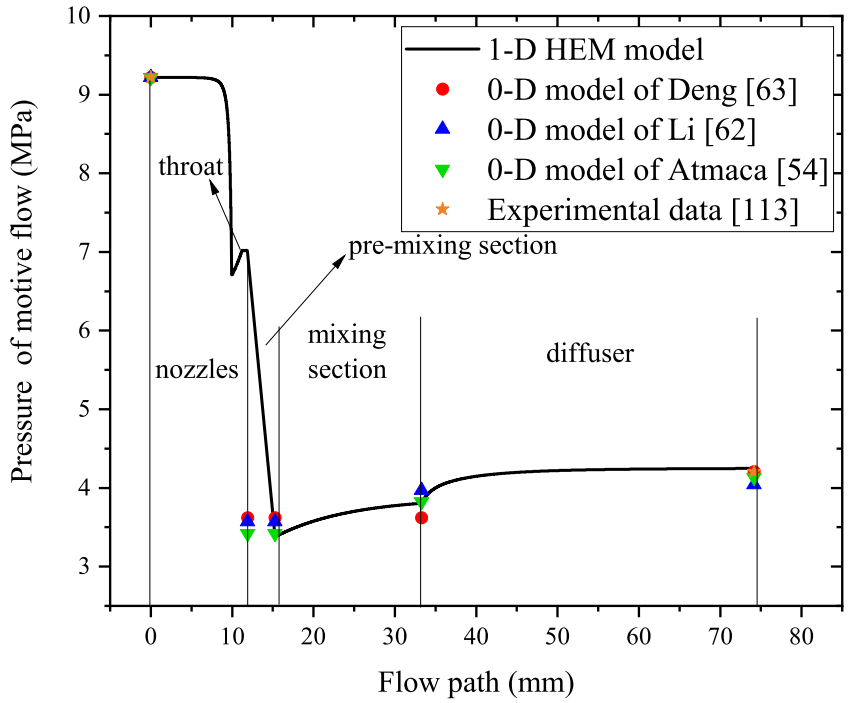

FIGURE 3.26: Pressure profiles of motive flow, with boundary conditions from Table. 3.5 and ejector geomoetry from Zhu et al. [113]

of Deng, Li, and Atmaca) are 0.13 %, 3.77 %, 1.59 %, respectively. The relative deviation of 1-D HEM is 1.13 %. Therefore, for 0-D models the accuracy of the prediction on the ejector outlet pressure is acceptable. Under certain operation conditions, it is even more accurate than 1-D HEM.

With the characteristic of quick response, 0-D models can be integrated into the ejector expansion cycle modeling. However, for the ejector design and detailed parametric analysis, it is still not able to provide enough details on the flow field inside the ejector. Moreover, taking into account the sensitivity analysis in the last chapter, the simulation accuracy of the 0-D thermodynamic models rely heavily on the proper input of isentropic efficiencies of ejector components. On the contrary, 1-D HEM uses the geometric parameters to evaluate the ejector performance, which introduces less contingency into the simulation.

3.7 Conclusion

In this chapter, a novel 1-D homogeneous equilibrium model (HEM) based on the Finite Volume Method for the entire ejector region is introduced. Given the current scarcity of 1-D models, it provides a reference and serves as an assistant tool for the study of ejectors.

Validation of the 1-D HEM utilized experimental data from the open literature [113], showcasing strong agreement between the simulated and experimental results. The relative deviations of the ejector outlet pressure and motive nozzle mass flow rate were generally below 5 % and 15 %, respectively, indicating high accuracy in the simulation results.

The established 1-D HEM serves as a valuable tool for the parametric analysis of ejectors or ejector systems within heat pump cycles. This facilitates the optimization of operational parameters and geometric design. The effect of the input temperature and pressure values of the ejector, as well as the mass flow rate of the suction flow, on the ejector performance was studied. Meticulous analysis was conducted on various geometric parameters, such as the length and diameter of the constant area mixing section, as well as the length and angle of the diffuser.

Comparison with three 0-D thermodynamic models, validated using experimental data, showcased the superior accuracy of the 1-D HEM. Additionally, the 1-D HEM demonstrated the advantage of providing more detailed profiles of thermodynamic parameters along the flow path compared to the 0-D models. The ejector efficiency calculated by the 1-D HEM is closer to real-world scenarios. While the 0-D models lack precision for ejector design, they are sufficiently accurate for system modeling with the proper input of isentropic efficiencies of ejector components.

Chapter 4

Design and prototype of an ejector expansion heat pump cycle

In this chapter, we establish an experimental test facility dedicated to investigating the performance of the ejector expansion heat pump cycle.

The test facility is designed with a two-phase ejector. The inlets and outlets of the ejector are formed by a high-pressure pump, an evaporator, and a condenser. This configuration enables precise control over both the inlet and outlet pressures of the ejector.

4.1 Description of the experimental test facility

The test facility employed in this study is illustrated schematically in Fig. 4.1. A photo of the test facility is shown in Fig. 4.2. The cycle comprises three circuits: the cooling water circuit, serving as the cold source for the condenser; the heating water circuit, functioning as the heat source for the evaporator; and the main circuit housing the refrigerant.

As depicted in Figure 4.1, the refrigerant is circuit divided into two loops: the motive flow loop and the suction flow loop, connected to the two input ports of the ejector.

In the motive flow loop, the refrigerant is condensed from the ejector outlet and flows into the main pump. The high-pressure refrigerant is then heated to saturated liquid in the electrical heater before entering the ejector at the inlet port.

Regarding the suction flow loop, the refrigerant from the condenser outlet passes through the expansion valve, where it expands to the evaporation pressure. Subsequently, it undergoes evaporation in the evaporator into saturated vapor or superheated vapor before entering the ejector.

At the ejector outlet, a condenser is used to condensate the two-phase flow from the ejector outlet into saturated or subcooled liquid. A pressure stabilizer is used to regulate the condensation pressure.

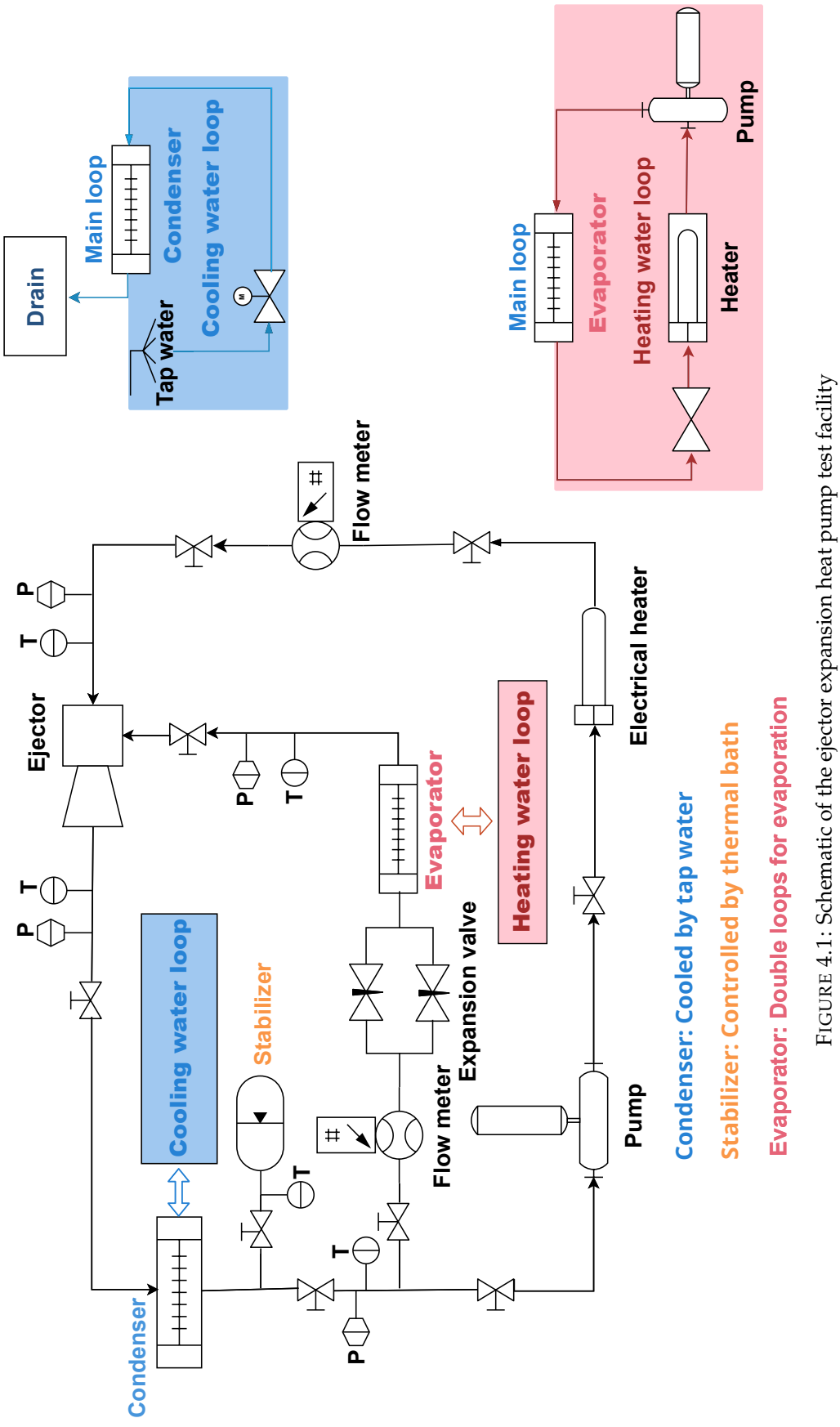

FIGURE 4.1: Schematic of the ejector expansion heat pump test facility

FIGURE 4.2: Photo of the test facility

In the established test facility, both the inlet and outlet pressures of the ejector are adjustable. The objective of the test facility is to investigate the performance of the ejector under controlled inlet and outlet conditions. By manipulating the inlet and outlet pressures of the ejector, various working modes of the ejector can be tested.

4.2 Working refrigerant

The refrigerant utilized in the test facility is R1234ze. In comparison to CO_2, R1234ze features a lower critical pressure (3.64 MPa) and a higher critical temperature (109.4 °C) . For laboratory research purposes, lower pressures require less material endurance and provide a better guarantee of system safety. Therefore, employing R1234ze as the working fluid allows the test facility to operate in the subcritical mode across a wide range of temperature applications. The key properties of R1234ze are listed in Table. 4.1.

TABLE 4.1: Properties of R1234ze

Refrigerant	Composition	Chemical formula	T_{crit} (°C)	P_{crit} (MPa)	ODP	GWP
R1234ze	HFO	$C_3F_4H_2$	109.4	3.64	0	5

4.3 Configuration of the test facility

The established ejector expansion heat pump cycle aims to investigate performance and variations in working modes under different inlet conditions. Effective operation parameters must be carefully designed for the test facility.

For the test facility, R1234ze has been selected as the working refrigerant due to the high-pressure risks associated with the CO_2 system. However, it has been observed that for two different refrigerants, they exhibit similar properties when the pressure ratio to the critical pressure is the same.

Table. 4.2 presents the viscosity ($\mu_{l,sat}$ and $\mu_{v,sat}$) and density ($\rho_{l,sat}$ and $\rho_{v,sat}$) of the saturated liquid and vapor states of both CO_2 and R1234ze at specific pressure ratios (0.31, 0.81). Analysis of the data in Table. 4.2 reveals that, when the pressure ratio to the critical pressure is the same for both CO_2 and R1234ze, the viscosity and density of their respective saturated states is similar. Considering the Reynolds Number (Eq. (3.14)), which is a function of density, velocity, viscosity, and characteristic length (diameter for the flow in the tube), for CO_2 and R1234ze, given the same tube size and velocity, they have a similar Reynolds Number (Re). Therefore, when the design of the R1234ze cycle is based on the same pressure ratio (P/P_{crit}), it can be analogies to CO_2 cycle. This approach allows for the study of ejector performance using R1234ze while drawing analogies to CO_2.

TABLE 4.2: Comparison of the properties of R1234ze and CO_2 at the same pressure ratio

P/P_{crit}	Refrigerant	P (MPa)	T_{sat} (°C)	$\mu_{l,sat}$ (μPa·s)	$\mu_{v,sat}$ (μPa·s)	$\rho_{l,sat}$ (kg/m^3)	$\rho_{v,sat}$ (kg/m^3)
0.81	R1234ze	2.96	98.82	69.02	19.46	790.12	215.18
	CO_2	6.00	21.98	62.71	18.84	751.03	210.88
0.31	R1234ze	1.13	54.94	139.26	13.75	1053.90	61.18
	CO_2	2.29	-15.00	128.29	13.47	1008.0	60.73

4.3.1 Configuration of the evaporator

The evaporation temperature is selected at -15 °C, -5 °C, and 15 °C for the CO_2 cycle, corresponding to evaporation temperatures of 54.94 °C, 66.89 °C, and 90.61 °C for R1234ze. This choice is based on the pressure relation expressed by Eq. (4.1), ensuring an identical pressure ratio between the evaporation pressure and critical pressure for both R1234ze and CO_2. The evaporation pressure for the CO_2 cycle is set at 2.29 MPa, 3.05 MPa, and 5.09 MPa, with corresponding values of 1.13 MPa, 1.50 MPa, and 2.51 MPa for R1234ze. The cooling capacity of the CO2 cycle's evaporator is established at 10 kW. The cooling capacity ($\dot{Q}cool$) of the R1234ze cycle is calculated using Eq. (4.2), where $h_{sat,v}$ and $h_{sat,l}$ represent the specific enthalpies of saturated vapor and saturated liquid at the evaporation pressure, respectively. It is

assumed that the inlet specific enthalpy of the evaporator is equal to the specific enthalpy of the saturated liquid at the evaporation pressure ($h_{sat,l}$). In real operation, however, due to pressure drop and expansion in the expansion valve before entering the evaporator, the inlet specific enthalpy of the flow is higher than the assumed value ($h_{sat,l}$). Nevertheless, as the outlet flow normally has a certain degree of superheat, this deviation can be somewhat compensated for, allowing the calculated capacity to be used for sizing the evaporator. The calculated cooling capacity ($\dot{Q}_{cool}$) of the R1234ze cycle shows slight variations with evaporation temperature, ranging between 5.2 kW and 5.22 kW.

$$\frac{P_{evap,R1234ze}}{P_{crit,R1234ze}} = \frac{P_{evap,CO_2}}{P_{crit,CO_2}} \tag{4.1}$$

$$\dot{Q}_{cool} = 10 \cdot \frac{(h_{sat,v,R1234ze} - h_{sat,l,R1234ze})}{(h_{sat,v,CO_2} - h_{sat,l,CO_2})} \tag{4.2}$$

The mass flow rate of suction flow ($\dot{m}_s$) for the R1234ze cycle can be calculated using Eq. (4.3). The calculated values vary between 133 and 204 kg/h.

$$\dot{m}_s = \dot{Q}_{cool} / (h_{sat,v} - h_{sat,l}) \tag{4.3}$$

Based on the above calculation, the evaporator employed at the ejector outlet for the test facility is the Lowara Brazed Plate Heat Exchangers, specifically the LBP400-010 model, depicted in Fig. 4.3. This cevaporator has a maximum working pressure of 30 bar and a temperature range spanning from -190 °C to 232 °C. Constructed with ten plates made of stainless steel 316L and copper brazed material, the condenser boasts a capacity of 7 kW.

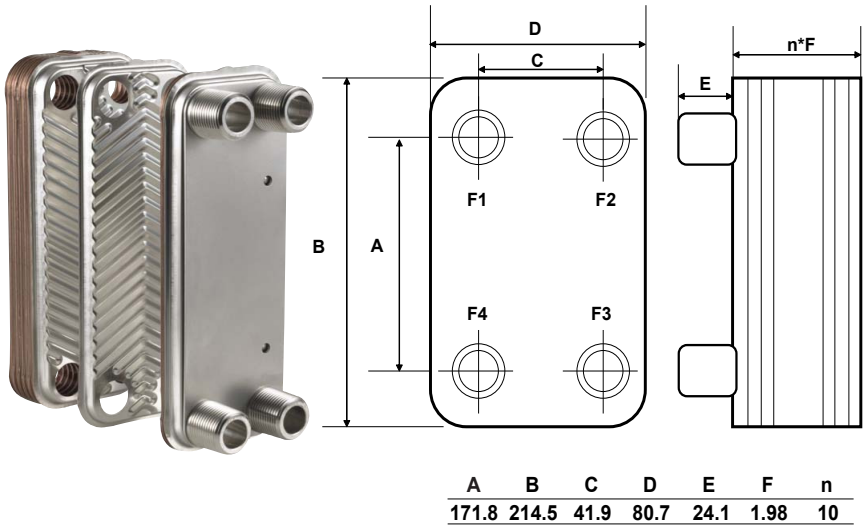

A	B	C	D	E	F	n
171.8	214.5	41.9	80.7	24.1	1.98	10

FIGURE 4.3: Schematic of the condenser at the ejector outlet (unit: mm)

For the evaporation application, the brazed plates heat exchanger will be positioned in the vertical direction. The refrigerant in liquid state enters through port F4

and exits from port F1. The hot source enters through port F2 and exits from port F3.

4.3.2 Configuration of the condenser

The condensation pressure of R1234ze cylce is designed based on the fixed pressure lift of the ejector, which means the pressure difference between the condenser and the evaporator is fixed. For the design of the test facility, two cases of 0.5 bar and 5 bar are chosen as the pressure gap.

The outlet state of the condenser is saturated liquid at the pressure that is higher than the evaporation pressure (0.5 bar and 5 bar). Then the capacity of the condenser can be calculated by Eq. (4.4). Where $\dot{m}_{mix}$ is the total mass flow rate of the motive and suction flow, and $h_{eje,out}$ is the specific enthalpy of the flow at the ejector outlet, both will be calculated in the parameters settings of the ejector.

$$\dot{Q}_{cond} = \dot{m}_{mix} \cdot (h_{eje,out} - h_{sat,cond}) \tag{4.4}$$

Based on the above calculation, the condenser at the ejector outlet for the test facility is chosen as the same model (LBP400-010) for the evaporator in the suction flow loop. The inlet port for the two-phase flow is labeled as F1, while the outlet port is labeled as F4. Cooling water is directed into port F3 and exits through port F2.

4.3.3 Configuration of the main pump

For the main pump in the motive flow loop, the inlet of the pump is saturated liquid from the outlet of the condenser. The outlet pressure of R1234ze is 2.96 MPa, corresponding to 6.00 MPa of CO_2, which is a typical high pressure (heat rejector pressure) for subcritical CO_2 heat pump cycle. The isentropic efficiency of the pump (η_{pump}) is assumed to be 0.6 for the design. And the outlet specific enthalpy h_{pump} can be calculated based on Eq. (4.5). Where h_{in} is the inlet specific enthalpy of the pump and $h_{pump,is}$ is the outlet specific enthalpy of the pump for an ideal isentropic compression.

$$\eta_{pump} = \frac{h_{pump,is} - h_{in}}{h_{pump} - h_{in}} \tag{4.5}$$

After obatainning the outlet enthalpy of the pump, the temperature and other thermodynamic parameters can be obtained by the equations of state based on the known pressure and specific enthalpy value.

The test facility is based on the assumption that the entrainment ratio (w) is 0.5, so the mass flow rate of the motive flow, which passes through the main pump is calculated by Eq. (4.6).

$$\dot{m}_m = \dot{m}_s / w \tag{4.6}$$

The pressure lift of the pump varies with the studied cases, ranging from 4.5 bar to 18 bar. And the mass flow rate varies between 266 and 408 kg/h.

Based on the above calculation, the pump in the motive flow loop for the test facility is a horizontal orientation regenerative turbine pump, specifically the T51M model in bronze fitted cast iron manufactured by MTH PUMPS, as depicted in Fig. 4.4. The pump is driven by a 7.5 hp three-phase motor with a power supply of 380V AC. It operates at a rated frequency of 50 Hz, and its rated speed is 3450 rpm (with a maximum speed of 5500 rpm). An inverter is equipped to regulate the pump's rotational speed. The working temperature range of the pump spans from -29 °C to 110 °C. The pump has a maximum pressure lift of 21 bar, and its maximum working pressure is 30 bar.

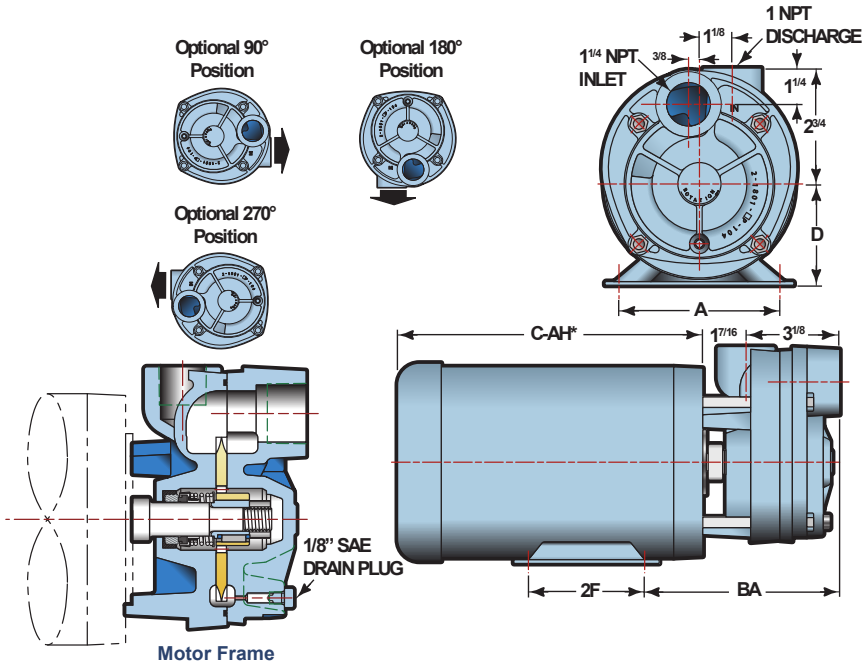

Frame	A	D	BA	2F
184TCZ	7 1/2	4 1/2	8 7/16	5 1/2

FIGURE 4.4: Schematic of the main pump in the motive flow loop (unit: inch)

4.3.4 Configuration of the main heater

For the capacity design of the main heater, the subcooled high pressure liquid from the outlet of the main pump will be heated to saturated liquid state in the main heater. The saturated temperature can be obtained using equation of state based on the pressure. The heater only works for the liquid case and no phase transition happens in the heater. The maximum working pressure of the pump should be higher than 2.96 MPa, which is the outlet pressure of the main pump. And the maximum heating load of the heater is 5.20 kW when the evaporation temperature is

54.94 °C (-15 °C analogy to the CO_2 cycle), and the pressure gap between condenser and evaporator is 0.5 bar.

Based on the above calculation, the electrical heater in the motive flow loop is an immersion heater consisting of a compact bundle of pin-shaped heating resistors provided by VULCANIC, shown in Fig. 4.5. The heater has a power rating of 5.5 kW (3 W/cm^2) and operates with a 400 V three-phase voltage. The main body is constructed of stainless steel 316L, with a maximum working pressure of 31.5 bar. The temperature range of the heater surface is between 5 and 210 °C. An integrated thermostat is employed to regulate the temperature of the heater within the range of 0 to 300 °C. The heater has a volume of 3.8 L.

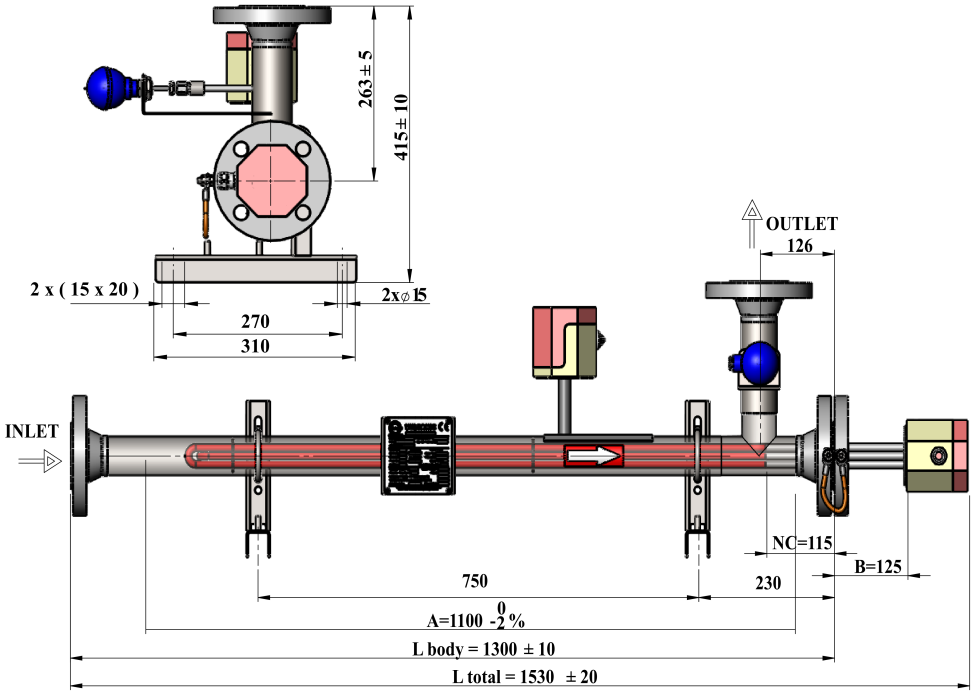

FIGURE 4.5: Schematic of the heater in the motive flow loop (unit: mm)

4.3.5 Configuration of the ejector

After the parameters setting of the inlet ports of the ejector (the inlet temperature, pressure values and mass flow rate of motive and suction flows, the ejector outlet mass flow rate ($\dot{m}_{mix}$) and specific enthalpy ($h_{eje,out}$) can be calculated based on the mass and energy conservation, respectively by Eq. (4.7) and Eq. (4.8).

$$\dot{m}_{mix} = \dot{m}_m + \dot{m}_s \tag{4.7}$$

$$(\dot{m}_m + \dot{m}_s) \cdot h_{eje,out} = \dot{m}_m \cdot h_m + \dot{m}_s \cdot h_s \tag{4.8}$$

The ejector utilized in the test facility is a product from the company Schutte & Koerting, as depicted in Fig. 4.6. Featuring a streamlined body with threaded pipe connections, the ejector is designed for versatility. The nozzle, threaded to the body, can be easily removed for cleaning or replacement. Constructed from 316L stainless steel, the ejector has a highest temperature limit of 300 °C and a pressure limit of 34 bar. Specifically designed for liquid-vapor applications, high-pressure liquid enters from the motive nozzle, while low-pressure vapor enters from the suction nozzle.

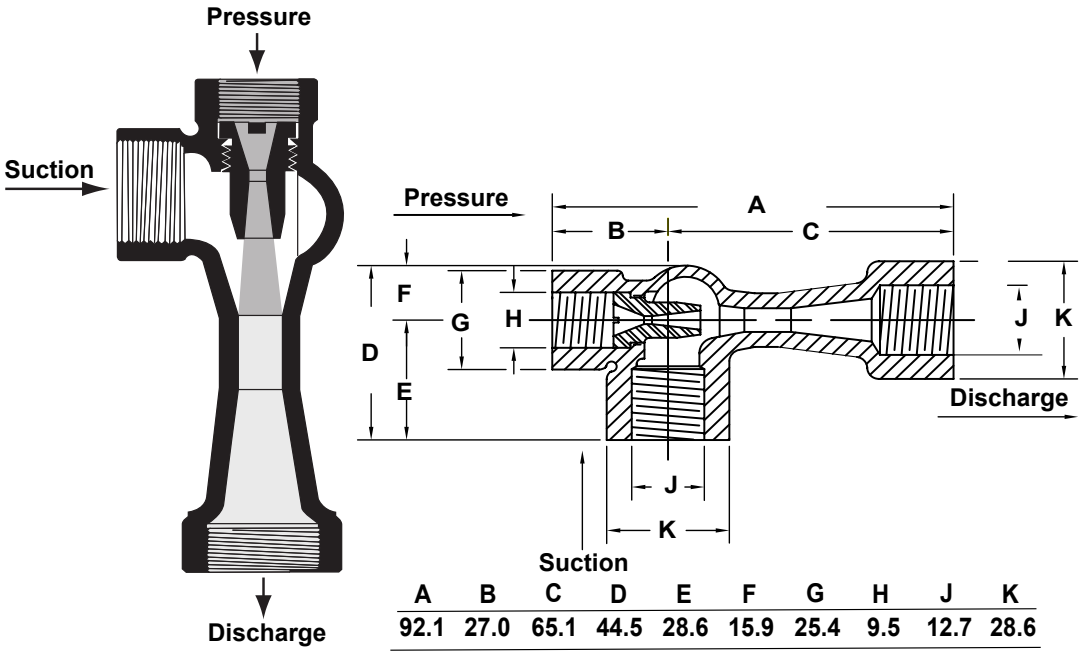

A	B	C	D	E	F	G	H	J	K
92.1	27.0	65.1	44.5	28.6	15.9	25.4	9.5	12.7	28.6

FIGURE 4.6: Schematic of the ejector (unit: mm)

Concluded from the configuration of the test facility, the operating parameters of the test facility are based on three evaporation pressures for the evaporator (11 bar, 15 bar, and 25 bar), each with optional pressure differences between the condenser outlet pressure and evaporation pressure set at 0.5 bar and 5 bar. The outlet pressure of the main pump is a fixed value of 29.6 bar. The design entrainment ratio of the ejector is 0.5, and the cooling capacity of the evaporator is approximately 5 kW for all cases. Table. 4.3 details the main operating cases for the test facility. The chosen components of the test facility match well with the parameters configuration in terms of the capacity, temperature and pressure limits.

4.4 Other components in the refrigerant circuit

The other components of the refrigerant circuit are described as follows:

4.4.1 Expansion valve in the suction flow loop

Two manually-adjusted expansion valves are installed before the evaporator to regulate the pressure difference between the suction flow pressure and the ejector outlet

TABLE 4.3: Operating parameters of the test facility in various cases

P_s (bar)	T_s (°C)	P_m (bar)	T_m (°C)	P_{cond} (bar)	T_{cond} (°C)	$\dot{m}_m$ (kg/h)	$\dot{m}_s$ (kg/h)
11.3	54.9	29.6	59.0	11.8	56.7	265.8	132.9
11.3	54.9	29.6	72.6	16.3	70.5	265.8	132.9
15.0	66.9	29.6	70.4	15.5	68.3	293.6	146.8
15.0	66.9	29.6	81.6	15.5	79.8	293.6	146.8
25.1	90.6	29.6	92.6	25.6	91.6	407.6	203.8

pressure. Two valves are employed for regulation in the event of excessive mass flow rates.

4.4.2 Stabilizer

The pressure stabilizer is employed to control the condensing pressure at the ejector outlet. It consists of a double-layer tank made of stainless steel, as shown in Fig. 4.7. The inner layer, connected to the refrigerant loop, maintains the liquid pressure within a specific range. Meanwhile, the outer layer is filled with the heat transfer fluid, and connected to a thermal bath. The thermal bath regulates the temperature of the heat transfer fluid in the outer layer of the pressure stabilizer. As the refrigerant R1234ze in the inner layer exists in a two-phase state, both the temperature and pressure are regulated in the stabilizer.

The thermal bath utilized in the test facility is a product of JULABO, model F32-ME. It operates within a working temperature range of -35 °C to 200 °C, with a precision of $\pm$0.01 °C.

4.5 The circuit of the cooling water

The water circuit is designed to condense the two-phase flow from the ejector outlet in the condenser. An open-loop water system is employed for condensation. Cooling water is sourced from the tap and then directed to the drain system. Utilizing a double-loop design and a plates brazed heat exchanger ensures there is no mixing with the refrigerant. To regulate the mass flow rate of the cooling water, an electrical valve depicted in Fig. 4.8 is employed.

4.6 The circuit of the heating water

The heating water circuit is designed to evaporate the two-phase flow following the expansion valve in the evaporator, utilizing pressured water as the heating source.

A similar immersion electrical heater from VULCANIC is employed for water heating. The heater has a maximum working pressure of 15 bar and a temperature

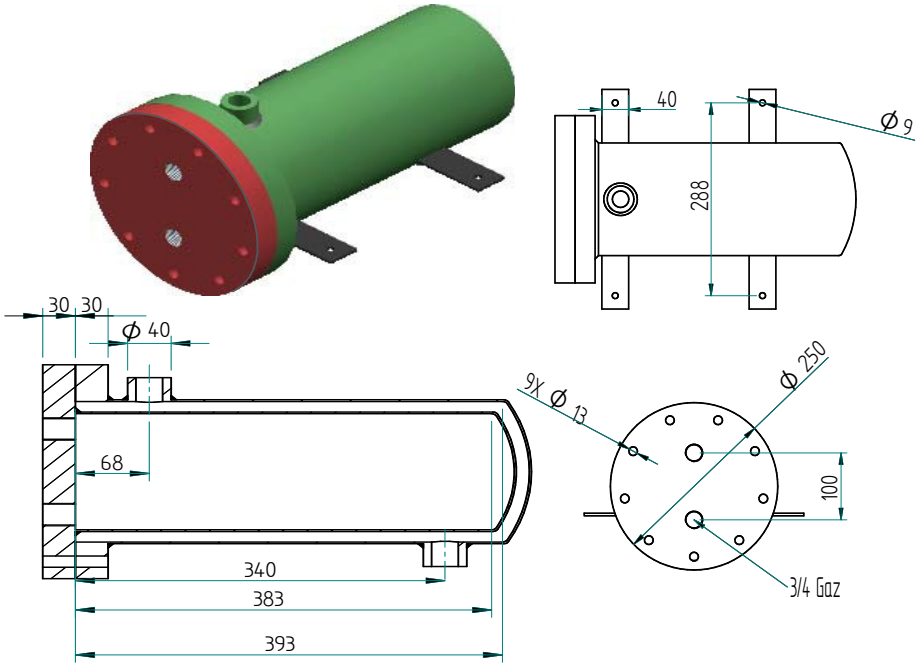

FIGURE 4.7: Schematic of the pressure stabilizer (unit:mm)

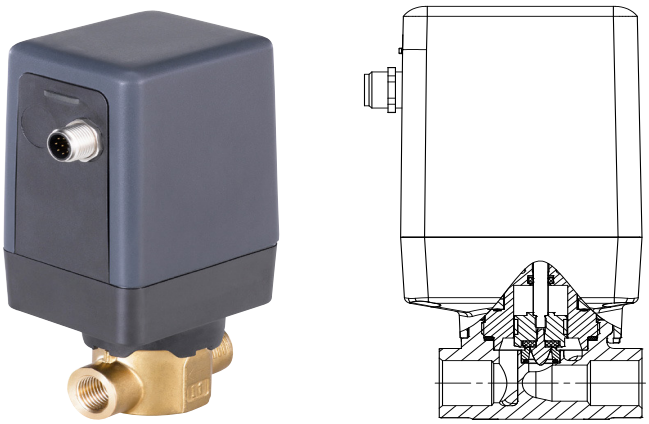

FIGURE 4.8: Schematic of the electrical valve

limit of 200 °C. It maintains a minimum mass flow rate of 2700 kg/h and a minimum volume flow rate of 2 m^3/h. The heater operates at a rated power of 5 kW, supplied by a 400 V three-phase power source.

For circulating the heating water, a similar regenerative pump from GemmeCotti is utilized. The pump has a maximum working temperature of 160 °C, a maximum pressure lift of approximately 2.5 bar, and a maximum volume flow rate of 32 m^3/h.

4.7 Measurement instruments

According to the schematic of the test bench, the measurement instruments for the cycle, including temperature and pressure sensors, as well as the mass flow meters, are detailed in Table. 4.4.

TABLE 4.4: Measurement instruments employed in the test facility

Instrument	Quantity	Range	Accuracy	Description
Tempreture sensors	5	-40 to 225 °C	±0.2 °C	Type K thermocouple
Pressure sensors	4	0 to 30 bar	±0.2 %	KELLER series 35XHTT
Mass flow meters	2	0 to 2720 kg/h	±0.15 %	MicroMotion F025S

Four absolute pressure sensors, sourced from the KELLER series 35XHTT, are strategically placed in the cycle to monitor pressures at the inlets and outlet of the ejector. Additionally, another pressure sensor of the same model is positioned at the condenser outlet to ensure the proper functioning of the pressure stabilizer.

For temperature measurements, four Type K thermocouples are installed at the inlet and outlet ports of the ejector, accompanied by an extra thermocouple at the outlet of the stabilizer.

To measure the mass flow rates of the motive and suction flows, two Coriolis mass flow meters are incorporated. Both meters operate in the liquid state with an uncertainty of ±0.15 % of the measurement value. Utilizing two transmitters, specifically the MicroMotion transmitters 1700 and 2700, the mass flow rate is displayed directly and the data is transmitted to the LabVIEW data acquisition system.

4.8 Data acquisition system

The data acquisition system is built on hardware from NI Instruments, and the control panel interface is developed using LabVIEW software. For the experimental test facility, the primary recorded data includes temperature and pressure values at the inlet and outlet ports of the ejector, temperature at the outlet of the pressure stabilizer, and mass flow rates of the motive and suction flows. Additionally, the opening of the electrical valve in the tap water loop is recorded and regulated to control the

mass flow rate of cooling water, thereby regulating the condensing pressure and temperature.

A LabVIEW interface is designed for data acquisition, system parameter monitoring, and regulation. It can display real-time information from the test facility, featuring key temperature and pressure values. Additionally, there are indicators for the electrical heater, showing whether the heater is in the on or off state.

4.9 Parameters regulations of the test facility

The inlet and outlet parameters of the ejector need to be regulated to study the ejector under different conditions.

4.9.1 Regulation of pressure and temperature of suction flow

The regulation of the evaporation pressure (P_s) is achieved by tuning the manually-adjusting expansion valve at the inlet of the evaporator. Adjusting the opening of the expansion valve allows the suction flow to reach the desired pressure.

Similarly, the regulation of the evaporation temperature (T_s) is accomplished by adjusting the electrical heater in the oil loop. By controlling the temperature of the oil entering the evaporator, the outlet temperature of the refrigerant in the main loop can be adjusted to the target temperature. Monitoring the measured temperature and pressure values of the suction flow at the evaporator outlet allows for the monitoring of the superheat degree of the suction flow.

4.9.2 Regulation of pressure and temperature of motive flow

The regulation of the high pressure of the main pump (P_m) is achieved by tuning an auxiliary inverter assembled with the main pump. The rotation speed of the pump is adjusted to attain the desired outlet pressure.

Similarly, the regulation of the temperature of the motive flow (T_m) is accomplished by adjusting the electrical heater in the motive flow loop. The outlet temperature of the heater is controlled to ensure that there is no phase change in the heater, and only liquid flows into the inlet port of the ejector.

4.9.3 Regulation of condensation temperature and pressure of ejector outlet

The regulation of the condensation pressure (P_{cond}) is managed by the pressure stabilizer, a double-layer tank where the temperature of the refrigerant is controlled by a thermal bath. The tank is sealed, and the quantity of refrigerant inside is carefully designed to prevent it from being filled with liquid or vapor-state refrigerant.

Similarly, the regulation of the condensation temperature (T_{cond}) is achieved through the tap water loop. The electrical valve is adjusted to control the mass flow rate of the

cooling water, ensuring the condensation temperature is maintained at the desired value.

4.10 Conclusion

A test facility for the subcritical ejector expansion heat pump cycle has been established to investigate the performance enhancement of ejector technology. The system is configured to allow for regulation of both the inlet and outlet pressures of the ejector.

The test facility is specifically designed for a liquid-vapor case of ejector operation, where the motive flow is high-pressure liquid, and the suction flow is low-pressure vapor. Various evaporation pressures and pressure lifts of the ejector have been designed to systematically study the impact on the ejector's performance and working mode.

The test facility is well established, however, due to the malfunction of the main pump during the pressure test, the experimental study will be conducted after the change of the main pump.

Chapter 5

Conclusions and Perspectives

Conclusions

The exploration into the realm of ejector expansion CO_2 heat pump cycles in various scales has provided a comprehensive understanding of this cutting-edge technology. The synthesis of insights from theoretical models, experimental validations, and practical observations presents a multifaceted perspective on the intricacies involved.

In Chapter 1, a comprehensive state-of-the-art review of the ejector enhanced CO_2 heat pump cycle has been conducted, elucidating the working principle, refrigerant evolution, and system configurations. The exploration has laid the foundation for understanding key achievements in this research domain.

Identified research gaps underscore the need for further exploration. Firstly, the scarcity of comparisons between different 0-D/pseudo 1-D models of ejectors calls for detailed analyses to discern the impact of model simplifications on accuracy. Additionally, the promotion of 1-D modeling, particularly using the Finite Volume Method, offers a promising compromise between modeling accuracy and computational efficiency.

While the commercialization of the CO_2 ejector expansion system marks a significant milestone, the pioneering nature of this technology necessitates more laboratory experimental validation. This validation is crucial for unraveling the complex flow patterns within the ejector and ensuring a comprehensive understanding of its behavior.

In essence, addressing these research gaps will contribute to a more robust and optimized ejector enhanced CO_2 heat pump cycle. This thesis, by shedding light on the existing knowledge and identifying areas for further exploration, aims to foster advancements in this field, ultimately contributing to the broader adoption and efficiency of this innovative technology.

The second chapter focused on 0-D thermodynamic models for ejectors. Key findings include the pivotal influence of motive nozzle efficiency and the significant

impact of compressor isentropic efficiency on overall system COP. Simplifying models by neglecting pressure variation sometimes enhanced predictive capabilities.

While proficient in estimating ejector outlet pressure and vapor quality (deviation less than 10 %), the 0-D models faced challenges in accurately forecasting ejector entrainment ratio and cycle COP (deviation reaches up to 50 %). A notable operational challenge identified was liquid imbalance during ejector expansion, contributing to simulation deviation in cycle COP.

A significant contribution is the introduction of a novel data post-processing method, effectively addressing liquid imbalance and substantially improving simulation accuracy (ejector entrainment ratio and cycle COP deviation less than 10 % in general). These insights advance our understanding of ejector-enhanced systems, providing valuable contributions to thermodynamic modeling and optimizing applications in transcritical CO_2 heat pump cycles.

In the third chapter, a novel 1-D Homogeneous Equilibrium Model (HEM) based on the Finite Volume Method is introduced for the entire ejector region, filling a gap in the scarcity of 1-D models. Validation using experimental data demonstrates high accuracy, with relative deviations below 5 % and 15 % for ejector outlet pressure and motive nozzle mass flow rate, respectively. This robust validation establishes the 1-D HEM as a reliable tool for simulating ejectors in heat pump cycles.

The 1-D HEM proves crucial for optimizing operational parameters and geometric design in ejector systems. Extensive studies on input temperature, pressure values, and suction flow mass flow rate reveal their pivotal roles in determining ejector performance. Positive correlations exist between ejector efficiency and higher inlet temperature and mass flow rate of the suction flow, while negative correlations are observed with the inlet temperature of the motive flow and the inlet pressure of the suction flow. Meticulous parametric analysis is emphasized for optimal ejector design in transcritical CO_2 heat pump systems.

A detailed analysis of geometric parameters, including the constant area mixing section's length and diameter, wall roughness, and the diffuser's length and angle, provides crucial insights. The most influential parameters are the diffuser angle and the diameter of the constant area mixing section, with the length of the mixing section also playing a substantial role. The impact of diffuser length and wall roughness on ejector performance is observed within limited extents. In summary, attaining optimal ejector design requires a comprehensive analysis of these geometric parameters.

Comparison with three 0-D thermodynamic models, validated with experimental data, highlights the superior accuracy of the 1-D HEM. Moreover, the 1-D HEM provides more detailed profiles of thermodynamic parameters along the flow path compared to the 0-D models. While acknowledging the precision of the 0-D models for system modeling, the 1-D HEM stands out as a more precise tool suitable for ejector design. In essence, the introduced 1-D HEM addresses the scarcity of 1-D

ejector modeling, offering enhanced accuracy and detailed insights, positioning it as a valuable asset for researchers and engineers engaged in ejector system optimization within heat pump cycles.

The last chapter introduces a dedicated test facility for the subcritical ejector expansion heat pump cycle, signifying a pivotal advancement in the exploration of ejector technology performance enhancement. The facility's meticulous configuration allows for precise control of both the inlet and outlet pressures of the ejector.

Specifically tailored for a liquid-vapor case of ejector operation, where the motive flow involves high-pressure liquid and the suction flow consists of low-pressure vapor, the facility is designed to accommodate various evaporation pressures and pressure lifts of the ejector. This deliberate design enables a systematic investigation into the impact on the ejector's performance and operational modes.

The establishment of this test facility serves as a crucial foundation for empirical exploration, offering the opportunity to gain practical insights into the behavior of the ejector system under diverse operating conditions. Through this comprehensive study, the chapter aims to contribute valuable knowledge to the field of ejector technology, paving the way for potential advancements and optimizations in subcritical ejector expansion heat pump cycles.

In synthesis, the collective findings contribute to advancing ejector technology within CO_2 heat pump cycles. The integration of theoretical sophistication, empirical validation, and practical applicability positions this body of work as a cornerstone for future research and industry applications. Identified research gaps not only delineate avenues for further scholarly inquiry but beckon industry practitioners to leverage these insights for the optimization and sustainability of refrigeration and heat pump systems.

This thesis represents a significant stride towards unraveling the intricacies of ejector-enhanced CO_2 heat pump cycles, steering the discourse towards increased efficiency and reliability in contemporary refrigeration technologies.

Perspectives

The perspectives of this thesis can be divided into two parts: the numerical study and the experimental study:

Numerical study

For the numerical study, few points are deserved to have a further study, both on the 0-D thermodynamic modeling and 1-D modeling of the ejector.

- Since there are all kinds of different assumptions made for the 0-D thermodynamic modeling. More 0-D thermodynamic models can be summerized and

compared to find an optimal model based on the compromise of model accuracy and model complexity.

- The accuracy of the 0-D thermodynamic models rely a lot on the input isentropic efficiencies of ejector components, a more universal correlation of the efficiencies need to be developed to reduce the inaccuracy due to the arbitrary of the input efficiencies.
- For 1-D modeling of ejector, the suction nozzle and pre-mixing section is still in 0-D. A more comprehensive model can be developed to model the two sections in 1-D.
- For 1-D Homogenous Equilibrium Model, the non-equilibrium is not included, which brings deviation for the modeling of the incipient stage of the phase transition, therefore, more research can be dedicated to improve the existing DEM and HRM, by improving the accuracy and also the versatility.
- Comparing to the CFD modeling, the 1-D modeling shows advantages on the simulation time consuming but shows disadvantages on the prediction on the shock wave and vortex inside the ejector, as well as the flow separation. To improve the 1-D modeling, these effects can be taken into account by introducing the related equations.
- For the ejector design, the optimization should be conducted for multiple parameters, a combination of the 1-D model with the optimization algorithm can be used to have a comprehensive optimization on all the geometry parameters and to find the best configuration for the given operation conditions.

Experimental study

For the experimental study, due to the malfunction of the main pump for the established test facility, the cycle can not be tested and the performance of the ejector have not be studied. Therefore, to further investigate the ejector working mode and flow field, more researchs can be conducted from the followed points:

- The test facility need to be repaired and tested under the designed working conditions to realize the steady operation of the subcritical ejector expansion heat pump cycle.
- By controlling the inlet and outlet pressure of the ejector, different working modes can be studied by changing the back pressure of the ejector and measure the entrainment ratio change. At the same time, the effect of the pressure of the motive flow on the working mode curve can also be investigated.
- The experimental results obtained can be used to validate the 0-D thermodynamic models and also the 1-D models to compare the simulation accuracy of different modeling methods.

- Different working refrigerant can be tested in the ejector expansion cycle, and the ejector pressure lift as well as the cycle COP can be compared.
- Varying the geometry of the ejector and test under the same boundary conditions, the optimal geometry configuration can be experimentally validated, and also to validate the ejector design using the 1-D modeling.
- To study in detail of the flow field in the ejector, an ejector with transparent flow path can be tested and the flow dynamics can be analyzed using the technology of high speed camera. The formation of the bubbles and the transformation of two-phase flow patterns can be observed with the high speed camera.
- The establishment of a transcritical ejector expansion heat pump cycle featuring an additional evaporator and feedback loop, as described in Chapter 2, aims to eliminate liquid imbalance between the inlet and outlet of the ejector through appropriate parameter regulations.

Appendix A

Reproduction of the ejector expansion refrigeration models

A.1 Reproduction of the model of Deng [63]

For the model of Deng [63], the model is well reproduced and the simulation results of the model are compared with the data from the original reference paper [63]. Fig. A.1 shows the entrainment ratio as a function of the inlet pressure of motive flow. And Fig. A.2 shows cycle COP as a function of the entrainment ratio of the ejector. All the input boundary conditions are listed and identical to the original reference paper by Deng et al. [63]. Where T_{sh} is the superheat degree of the suction flow. The trend of values of the simulations results match well with the data from the reference [63].

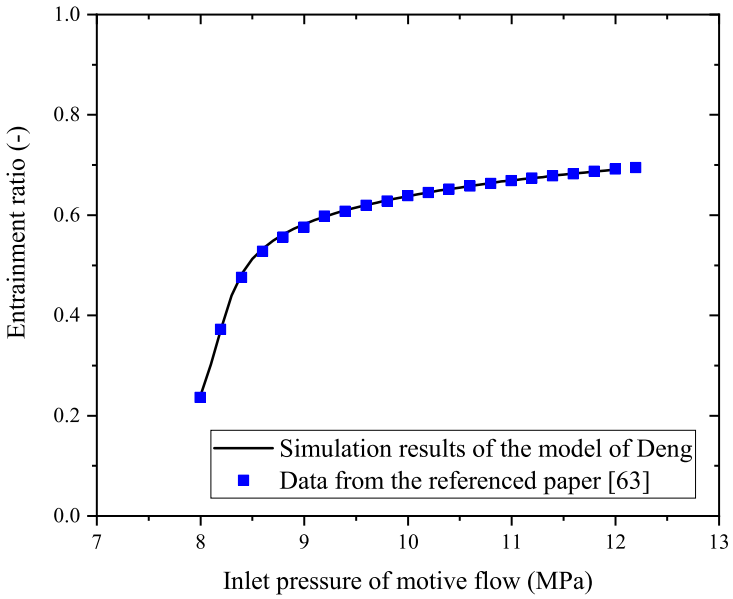

FIGURE A.1: Entrainment ratio as a function of inlet pressure of motive flow
$T_m = 36\ °C$, $T_s = 5\ °C$, $T_{sh} = 0\ °C$
$\eta_m = 0.7$, $\eta_d = 0.8$, $\eta_{comp} = 1.003 - 0.121 \cdot (P_m/P_s)$

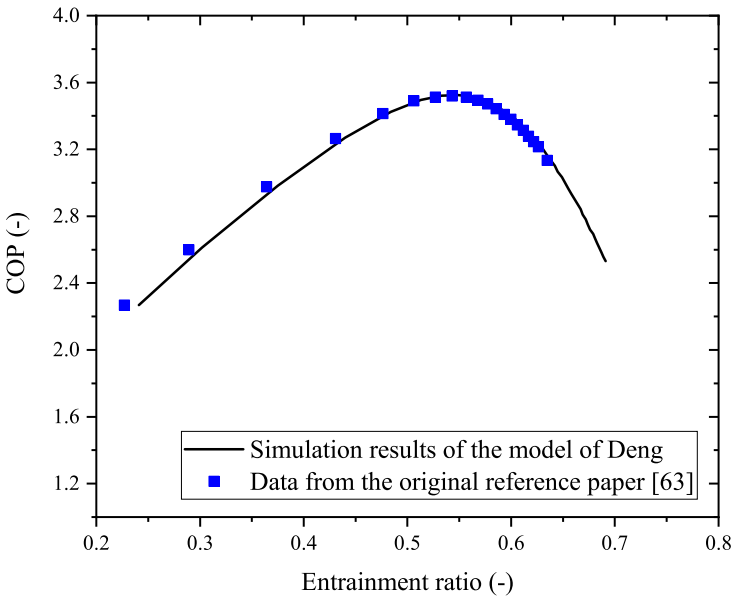

FIGURE A.2: COP as a function of entrainment ratio of the ejector
$T_m = 36\ ^\circ C$, $T_s = 5\ ^\circ C$, $T_{sh} = 0\ ^\circ C$
$\eta_m = 0.7$, $\eta_d = 0.8$, $\eta_{comp} = 1.003 - 0.121 \cdot (P_m / P_s)$

A.2 Reproduction of the model of Li [62]

For the model of Li [62], an extra evaluation parameter R (expressed by Eq. (A.1)) is introduced, which is the ratio between the COP of ejector expansion cycle ($COP_{ejector}$) and COP of basic heat pump cycle without ejector (COP_{basic}).

$$R = \frac{COP_{ejector}}{COP_{basic}} \tag{A.1}$$

Different pressure drops in the suction nozzle are studied. Fig. A.3 shows the relative performance ratio versus entrainment ratio for the cases of different pressure drop in the suction nozzle. And Fig. A.4 shows the relative performance ration change with the inlet pressure of motive flow for the cases of different entrainment ratio of the ejector. For this study, the pressure drop in the suction nozzle is fixed at 0.03 MPa. All the input boundary conditions are listed and identical to the original reference paper by Li et al. [62]. The trend of values of the simulations results match well with the data from the reference [62].

A.3 Reproduction of the model of Atmaca [54]

In the Atmaca's model [54], experimental validation was conducted using data from Ersoy and Bilir [130], as described in the original reference paper. To assess the accuracy of model reproduction, tests were performed under the same conditions as

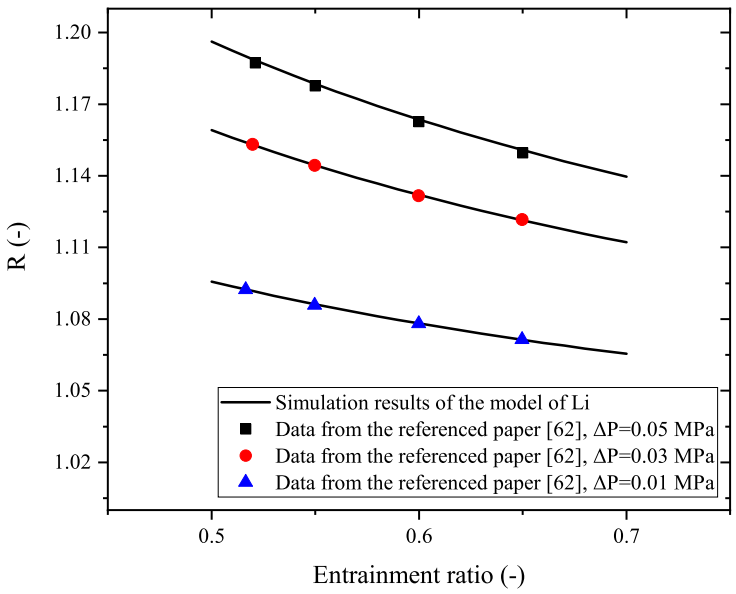

FIGURE A.3: Relative performance ratio versus entrainment ratio and pressure drop
$T_m = 40\ ^\circ C$, $T_s = 5\ ^\circ C$, $T_{sh} = 5\ ^\circ C$
$\eta_m = 0.9$, $\eta_s = 0.9$, $\eta_d = 0.8$, $\eta_{comp} = 0.75$

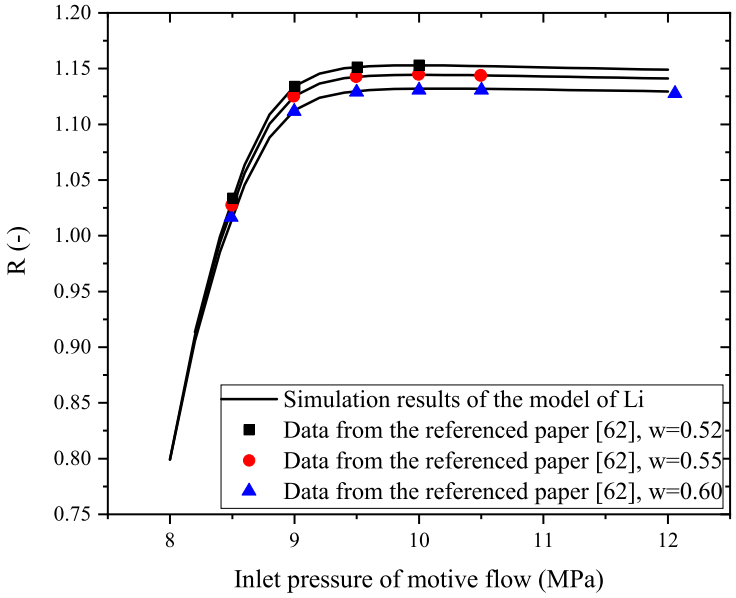

FIGURE A.4: Relative performance ratio versus inlet pressure of motive flow and entrainment ratio
$\Delta P = 0.03$ MPa, $P_m = 10$ MPa, $T_m = 40\ ^\circ C$, $T_s = 5\ ^\circ C$, $T_{sh} = 5\ ^\circ C$
$\eta_m = 0.9$, $\eta_s = 0.9$, $\eta_d = 0.8$, $\eta_{comp} = 0.75$

Ersoy and Bilir's experimental study [130]. The results are presented in Table. A.1. The error, defined as the absolute relative deviation between the simulation result and the value simulated by Atmaca from the reference [54], is 1.5 % for the entrainment ratio and 0.7 % for the ejector outlet pressure. These results indicate a convincing reproduction of the model, and the small errors observed may be attributed to differences in the used thermodynamic properties database for the refrigerant.

TABLE A.1: Comparion between simulation results of the model of Atmaca and the original data from the reference [54]

Validation Parameters	Experimental data	Numerical by Atmaca	Simulation Result	Error (%)
Entrainment ratio	0.64	0.66	0.65	1.5 %
Outlet pressure (bar)	4.21	4.60	4.63	0.7 %

Appendix B

Grid independence analyses for the 1-D HEM of ejector

In the Chapter 3's 1-D Homogeneous Equilibrium Model (HEM) of the ejector, the grid is dynamically adjusted during the modeling process. A grid independence analysis is conducted to assess its impact on simulation accuracy.

The grid is divided along the one-dimensional flow path, encompassing the motive nozzle, constant area mixing section, and the diffuser. The suction nozzle and pre-mixing section are assumed to be zero-dimensional due to the complex geometric characteristics of the suction nozzle and the abrupt change in the flow field for the pre-mixing section.

presents various grid division cases for the 1-D HEM and the key outlet parameters of the ejector. Here, dt serves as an initial input determining the minimum grid size $min(dz)$ during modeling using Cramer's rule. After the initiation of dt, the grid size dz adjusts automatically. The maximum grid size $max(dz)$, mean grid size $mean(dz)$, and the total number of nodes are also listed in Table. B.1.

From the table, it is observed that for cases where $dt = 10$, $dt = 1$, and $dt = 0.1$, the ejector outlet pressure P_{out} and ejector efficiency η_{eje} remain constant despite variations in the initial dt.

Fig. B.1 illustrates the pressure profile of the motive flow. Since the suction nozzle is considered zero-dimensional, and after mixing in the pre-mixing section, the motive flow and suction flow are assumed to have the same pressure, the pressure profile of the suction flow is not presented. The boundary conditions are listed and the ejector geometry is reffered to the ejector of Zhu et al. [113].

TABLE B.1: Grid independence analyses for the 1-D HEM of ejector

Initial dt	P_{out}	η_{eje}	min (dz)	max (dz)	mean (dz)	Number of the nodes
$dt = 100$	4.29 MPa	0.411	1.84e^{-}06 m	6.60e^{-}03 m	7.92e^{-}06 m	8965
$dt = 10$	4.29 MPa	0.407	6.08e^{-}08 m	6.63e^{-}04 m	4.96e^{-}06 m	14298
$dt = 1$	4.29 MPa	0.407	5.52e^{-}09 m	6.63e^{-}05 m	1.05e^{-}06 m	67367
$dt = 0.1$	4.29 MPa	0.407	5.46e^{-}10 m	6.63e^{-}06 m	1.19e^{-}07 m	597002

Examining Fig. B.1, a slight difference is observed when the initial dt is 10, compared to the cases $dt = 1$ and $dt = 0.1$. However, for the cases of $dt = 1$ and $dt = 0.1$, the pressure profiles of the motive flow completely overlap, suggesting that the simulation is independent of the grid.

Based on the grid independence analysis, $dt = 1$ is chosen as the initial value to determine the minimum grid size during the 1-D modeling of the ejector. For this case, the average grid size is 1.05 μm, the maximum grid size is 66.3 μm, and the total number of nodes is 67,367.

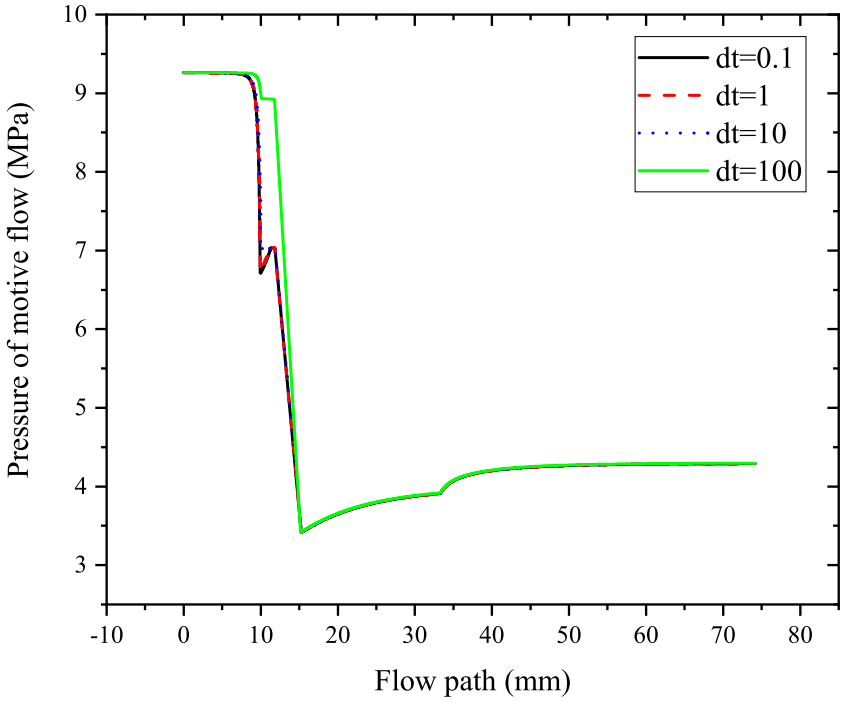

FIGURE B.1: Grid independence analyses for the 1-D HEM of ejector
$P_m = 9.3$ MPa, $T_m = 35.5\ ^\circ C$, $P_s = 3.6$ MPa, $T_s = 22.8\ ^\circ C$,
$\dot{m}_s = 46.9$ kg/h, with ejector geometry from Zhu et al. [113]

Appendix C

Key coefficients used in the 1-D HEM

The key coefficients used in the 1-D modeling of the ejector in the Chapter 3 is listed in Table. C.1.

TABLE C.1: Key coefficients used in the 1-D HEM

Parameters	Value	Description
α_{int}	5000 $W/m^2 \cdot K$	heat transfer coefficient at the interface of motive and suction flow
a_{mix}	1.329	coefficient of scale in the mixing section
a_{dif}	1.519	coefficient of scale in the diffuser section
$\varepsilon_{int,mix}$	4 μm	roughness of the interface in the mixing section
$\varepsilon_{int,dif}$	2 μm	roughness of the interface in the diffuser section
ε_w	2 μm	roughness of the wall along the flow path

Bibliography

[1] Eda Fowlks Kranakis. "The French connection: Giffard's injector and the nature of heat". In: *Technology and Culture* 23.1 (1982), pp. 3–38.

[2] Zhenying Zhang et al. "Progress in ejector-expansion vapor compression refrigeration and heat pump systems". In: *Energy Conversion and Management* 207 (2020), p. 112529.

[3] Wenxin Li et al. "An integrated predictive model of the long-term performance of ground source heat pump (GSHP) systems". In: *Energy and Buildings* 159 (2018), pp. 309–318.

[4] Brian T Austin and K Sumathy. "Transcritical carbon dioxide heat pump systems: A review". In: *Renewable and Sustainable Energy Reviews* 15.8 (2011), pp. 4013–4029.

[5] K. J. Chua, S. K. Chou, and W. M. Yang. "Advances in heat pump systems: A review". In: *Applied Energy* 87.12 (2010), pp. 3611–3624.

[6] Naeem Abas et al. "Natural and synthetic refrigerants, global warming: A review". In: *Renewable and Sustainable Energy Reviews* 90.April (2018), pp. 557–569.

[7] Arun Krishna Vuppaladadiyam et al. "Progress in the development and use of refrigerants and unintended environmental consequences". In: *Science of the Total Environment* 823 (2022), p. 153670.

[8] Kosei Takezato et al. "Heat Pump Cycle Using Refrigerant Mixtures of HFC32 and HFO1234yf". In: *Heat Transfer Engineering* 42.13-14 (2021), pp. 1097–1106.

[9] Faraz Afshari et al. "A thermodynamic comparison between heat pump and refrigeration device using several refrigerants". In: *Energy and Buildings* 168 (2018), pp. 272–283.

[10] Di Wu, Bin Hu, and R. Z. Wang. "Vapor compression heat pumps with pure Low-GWP refrigerants". In: *Renewable and Sustainable Energy Reviews* 138.April 2020 (2021).

[11] Mark O. McLinden and Marcia L. Huber. "(R)Evolution of Refrigerants". In: *Journal of Chemical and Engineering Data* 65.9 (2020), pp. 4176–4193.

[12] Man Hoe Kim, Jostein Pettersen, and Clark W. Bullard. *Fundamental process and system design issues in CO2 vapor compression systems*. Vol. 30. 2. 2004, pp. 119–174.

[13] Zhaogang Qi. "Advances on air conditioning and heat pump system in electric vehicles – A review". In: *Renewable and Sustainable Energy Reviews* 38 (2014), pp. 754–764.

[14] Yulong Song et al. "Advanced development and application of transcritical CO2 refrigeration and heat pump technology—A review". In: *Energy Reports* 8 (2022), pp. 7840–7869.

[15] Frank Bruno, Martin Belusko, and Edward Halawa. "CO2 refrigeration and heat pump systems—a comprehensive review". In: *Energies* 12.15 (2019), p. 2959.

[16] Rajib Uddin Rony et al. "Recent advances in transcritical CO2 (R744) heat pump system: A review". In: *Energies* 12.3 (2019), p. 457.

[17] Feng Cao, Yulong Song, and Mingjia Li. "Review on development of air source transcritical CO2 heat pump systems using direct-heated type and recirculating-heated type". In: *International Journal of Refrigeration* 104 (2019), pp. 455–475.

[18] Jahar Sarkar. "Review on Cycle Modifications of Transcritical CO 2 Refrigeration and Heat Pump Systems." In: *Journal of Advanced Research in Mechanical Engineering* 1.1 (2010).

[19] Yitai Ma, Zhongyan Liu, and Hua Tian. "A review of transcritical carbon dioxide heat pump and refrigeration cycles". In: *Energy* 55 (2013), pp. 156–172.

[20] Joaquim Rigola et al. "Numerical simulation and experimental validation of internal heat exchanger influence on CO2 trans-critical cycle performance". In: *International Journal of Refrigeration* 33.4 (2010), pp. 664–674.

[21] Feng Cao, Zuliang Ye, and Yikai Wang. "Experimental investigation on the influence of internal heat exchanger in a transcritical CO2 heat pump water heater". In: *Applied Thermal Engineering* 168 (2020), p. 114855.

[22] Xiang Qin et al. "A comprehensive investigation on the effect of internal heat exchanger based on a novel evaluation method in the transcritical CO2 heat pump system". In: *Renewable Energy* 178 (2021), pp. 574–586.

[23] Luca Cecchinato et al. "Thermodynamic analysis of different two-stage transcritical carbon dioxide cycles". In: *International Journal of refrigeration* 32.5 (2009), pp. 1058–1067.

[24] Honghyun Cho et al. "Performance evaluation of a two-stage CO2 cycle with gas injection in the cooling mode operation". In: *International Journal of Refrigeration* 32.1 (2009), pp. 40–46.

[25] Brian T. Austin and K. Sumathy. "Transcritical carbon dioxide heat pump systems: A review". In: *Renewable and Sustainable Energy Reviews* 15.8 (2011), pp. 4013–4029.

[26] Smith Eiamsa-ard and Pongjet Promvonge. "Review of Ranque–Hilsch effects in vortex tubes". In: *Renewable and sustainable energy reviews* 12.7 (2008), pp. 1822–1842.

[27] Ying Fu Liu, Chun Jing Geng, and Guang Ya Jin. "Vortex tube expansion transcritical CO2 heat pump cycle". In: *Applied Mechanics and Materials* 190 (2012), pp. 1340–1344.

[28] Zibing Luo et al. "Performance improvement of transcritical CO2 refrigeration cycle by integrating vortex tube expansion: Simulation and optimization". In: *Thermal Science and Engineering Progress* 45 (2023), p. 102078.

[29] A Aghagoli, M Sorin, and S Poncet. "Thermodynamics analysis of a novel transcritical CO2 vortex tube heat pump cycle". In: *Proceedings of the 27th CANCAM* 4 (2019).

[30] Ahmed Mansour et al. "Thermodynamic analysis of a transcritical CO2 heat pump integrating a vortex tube". In: *Applied Thermal Engineering* 224 (2023), p. 120076.

[31] Neeraj Agrawal and Souvik Bhattacharyya. "Non-adiabatic capillary tube flow of carbon dioxide in a transcritical heat pump cycle". In: *Energy conversion and management* 48.9 (2007), pp. 2491–2501.

[32] Kenneth B Madsen, Claus S Poulsen, and Maike Wiesenfarth. "Study of capillary tubes in a transcritical CO2 refrigeration system". In: *International Journal of Refrigeration* 28.8 (2005), pp. 1212–1218.

[33] Neeraj Agrawal and Souvik Bhattacharyya. "Optimized transcritical CO2 heat pumps: Performance comparison of capillary tubes against expansion valves". In: *International Journal of Refrigeration* 31.3 (2008), pp. 388–395.

[34] Yulong Song et al. "Experimental investigation on a capillary tube based transcritical CO2 heat pump system". In: *Applied Thermal Engineering* 112 (2017), pp. 184–189.

[35] Jun Lan Yang et al. "Exergy analysis of transcritical carbon dioxide refrigeration cycle with an expander". In: *Energy* 30.7 (2005), pp. 1162–1175.

[36] Hua Tian et al. "Study on expansion power recovery in CO2 trans-critical cycle". In: *Energy conversion and management* 51.12 (2010), pp. 2516–2522.

[37] A. Subiantoro and K. T. Ooi. "Design analysis of the novel Revolving Vane expander in a transcritical carbon dioxide refrigeration system". In: *International Journal of Refrigeration* 33.4 (2010), pp. 675–685.

[38] J. Nickl et al. "Integration of a three-stage expander into a CO2 refrigeration system". In: *International Journal of Refrigeration* 28.8 (2005), pp. 1219–1224.

[39] B. Zhang et al. "Development of a double acting free piston expander for power recovery in transcritical CO2 cycle". In: *Applied Thermal Engineering* 27.8-9 (2007), pp. 1629–1636.

[40] Hyun Jin Kim et al. "Numerical simulation on scroll expander-compressor unit for CO2 trans-critical cycles". In: *Applied Thermal Engineering* 28.13 (2008), pp. 1654–1661.

[41] Guan Haiqing, Ma Yitai, and Li Minxia. "Some design features of CO2 swing piston expander". In: *Applied Thermal Engineering* 26.2-3 (2006), pp. 237–243.

[42] Jahar Sarkar. "Ejector enhanced vapor compression refrigeration and heat pump systems - A review". In: *Renewable and Sustainable Energy Reviews* 16.9 (2012), pp. 6647–6659.

[43] Alan A. Kornhauser. "The use of an ejector in a geothermal flash system". In: *Proceedings of the Intersociety Energy Conversion Engineering Conference* 5 (1990), pp. 79–84.

[44] Jae Seung Lee, Min Soo Kim, and Mo Se Kim. "Experimental study on the improvement of CO2 air conditioning system performance using an ejector". In: *International Journal of Refrigeration* 34.7 (2011), pp. 1614–1625.

[45] Francesco Giacomelli et al. "Experimental and computational analysis of a R744 flashing ejector". In: *International Journal of Refrigeration* 107 (2019), pp. 326–343.

[46] Chen Guangming et al. "An experimental and theoretical study of a CO2 ejector". In: *International Journal of Refrigeration* 33.5 (2010), pp. 915–921.

[47] K. Ameur, Z. Aidoun, and M. Ouzzane. "Experimental performances of a two-phase R134a ejector". In: *Experimental Thermal and Fluid Science* 97.September 2017 (2018), pp. 12–20.

[48] Yinhai Zhu et al. "Experimental investigation on the performance of trans-critical CO2 ejector-expansion heat pump water heater system". In: *Energy Conversion and Management* 167.April (2018), pp. 147–155.

[49] Christian Lucas and Juergen Koehler. "Experimental investigation of the COP improvement of a refrigeration cycle by use of an ejector". In: *International Journal of Refrigeration* 35.6 (2012), pp. 1595–1603.

[50] Fang Liu, Eckhard A. Groll, and Daqing Li. "Investigation on performance of variable geometry ejectors for CO2 refrigeration cycles". In: *Energy* 45.1 (2012), pp. 829–839.

[51] Vishal Kumar, S. K. Yadav, and Shri Ram. "A comprehensive studies on constant area mixing (CAM) and constant pressure mixing (CPM) Ejectors: A review". In: *Materials Today: Proceedings* 69 (2022), pp. 513–518.

[52] Candeniz Seckin. "Parametric Analysis and Comparison of Ejector Expansion Refrigeration Cycles with Constant Area and Constant Pressure Ejectors". In: *Journal of Energy Resources Technology, Transactions of the ASME* 139.4 (2017), pp. 1–10.

[53] Kanjanapon Chunnanond and Satha Aphornratana. "Ejectors: Applications in refrigeration technology". In: *Renewable and Sustainable Energy Reviews* 8.2 (2004), pp. 129–155.

[54] Ayşe Uğurcan Atmaca, Aytunç Erek, and Orhan Ekren. "Impact of the mixing theories on the performance of ejector expansion refrigeration cycles for environmentally-friendly refrigerants". In: *International Journal of Refrigeration* 97 (2019), pp. 211–225.

[55] S. Taslimi Taleghani, M. Sorin, and S. Poncet. "Modeling of two-phase transcritical CO2 ejectors for on-design and off-design conditions". In: *International Journal of Refrigeration* 87 (2018), pp. 91–105.

[56] Lei Wang et al. "Experimental investigation on ejector performance near critical back pressure". In: *International journal of refrigeration* 80 (2017), pp. 158–168.

[57] Fenglei Li et al. "Ejector performance prediction at critical and subcritical operational modes". In: *Applied Thermal Engineering* 115 (2017), pp. 444–454.

[58] WeiXiong Chen et al. "A 1D model to predict ejector performance at critical and sub-critical operational regimes". In: *International journal of refrigeration* 36.6 (2013), pp. 1750–1761.

[59] Amel Hemidi et al. "CFD analysis of a supersonic air ejector. Part II: Relation between global operation and local flow features". In: *Applied Thermal Engineering* 29.14-15 (2009), pp. 2990–2998.

[60] Aggrey Mwesigye and Seth B Dworkin. "Performance analysis and optimization of an ejector refrigeration system using alternative working fluids under critical and subcritical operation modes". In: *Energy conversion and management* 176 (2018), pp. 209–226.

[61] Knut Emil Ringstad et al. "A detailed review on CO2 two-phase ejector flow modeling". In: *Thermal Science and Engineering Progress* 20.September (2020).

[62] Daqing Li and Eckhard A. Groll. "Transcritical CO2 refrigeration cycle with ejector-expansion device". In: *International Journal of Refrigeration* 28.5 (2005), pp. 766–773.

[63] Jian qiang Deng et al. "Particular characteristics of transcritical CO2 refrigeration cycle with an ejector". In: *Applied Thermal Engineering* 27.2-3 (2007), pp. 381–388.

[64] Khaled Ameur, Zine Aidoun, and Mohamed Ouzzane. "Modeling and numerical approach for the design and operation of two-phase ejectors". In: *Applied Thermal Engineering* 109 (2016), pp. 809–818.

[65] Min-Qiang Zeng et al. "Thermodynamic analysis of a novel multi-target temperature transcritical CO2 ejector-expansion refrigeration cycle with vapor-injection". In: *Energy* 259 (2022), p. 125016.

[66] Mojtaba Purjam, Kyaw Thu, and Takahiko Miyazaki. "Thermodynamic modeling of an improved transcritical carbon dioxide cycle with ejector: Aiming low-temperature refrigeration". In: *Applied Thermal Engineering* 188 (2021), p. 116531.

[67] Xi Liu et al. "Thermodynamic analysis of transcritical CO2 refrigeration cycle integrated with thermoelectric subcooler and ejector". In: *Energy Conversion and Management* 188 (2019), pp. 354–365.

[68] S Taslimi Taleghani et al. "Performance investigation of a two-phase transcritical CO2 ejector heat pump system". In: *Energy Conversion and Management* 185 (2019), pp. 442–454.

[69] Jahar Sarkar. "Optimization of ejector-expansion transcritical CO2 heat pump cycle". In: *Energy* 33.9 (2008), pp. 1399–1406.

[70] Tao Bai, Gang Yan, and Jianlin Yu. "Thermodynamic analyses on an ejector enhanced CO2 transcritical heat pump cycle with vapor-injection". In: *International Journal of Refrigeration* 58 (2015), pp. 22–34.

[71] Mohammed Ridha Jawad Al-Tameemi and Zhibin Yu. "Thermodynamic approach for designing the two-phase motive nozzle of the ejector for transcritical CO2 heat pump system". In: *Energy Procedia* 142 (2017), pp. 1206–1212.

[72] Lixing Zheng, Jianqiang Deng, and Zaoxiao Zhang. "Dynamic simulation of an improved transcritical CO2 ejector expansion refrigeration cycle". In: *Energy Conversion and Management* 114 (2016), pp. 278–289.

[73] Md Ezaz Ahammed, Souvik Bhattacharyya, and M Ramgopal. "Thermodynamic design and simulation of a CO2 based transcritical vapour compression refrigeration system with an ejector". In: *International journal of refrigeration* 45 (2014), pp. 177–188.

[74] Ayşe Uğurcan Atmaca, Aytunç Erek, and Orhan Ekren. "One-dimensional analysis of the convergent-divergent motive nozzle for the two-phase ejector: Effect of the operating and design parameters". In: *Applied Thermal Engineering* 181.January (2020), p. 115866.

[75] Krzysztof Banasiak and Armin Hafner. "1D Computational model of a two-phase R744 ejector for expansion work recovery". In: *International Journal of Thermal Sciences* 50.11 (2011), pp. 2235–2247.

[76] Øivind Wilhelmsen et al. "One-dimensional mathematical modeling of two-phase ejectors: Extension to mixtures and mapping of the local exergy destruction". In: *Applied Thermal Engineering* 217.7491 (2022), p. 119228.

[77] Michal Palacz et al. "Application range of the HEM approach for CO2 expansion inside two-phase ejectors for supermarket refrigeration systems". In: *International Journal of Refrigeration* 59 (2015), pp. 251–258.

[78] Wojciech Angielczyk et al. “1-D Modeling of Supersonic Carbon Dioxide Two-Phase Flow through Ejector Motive Nozzle”. In: *International Refrigeration and Air Conditioning Conference at Purdue* (2010), pp. 1–8.

[79] Wojciech Angielczyk, Yann Bartosiewicz, and Dariusz Butrymowicz. “Development of Delayed Equilibrium Model for CO2 convergent-divergent nozzle transonic flashing flow”. In: *International Journal of Multiphase Flow* 131 (2020).

[80] Krzysztof Banasiak and Armin Hafner. “Mathematical modelling of supersonic two-phase R744 flows through converging-diverging nozzles: The effects of phase transition models”. In: *Applied Thermal Engineering* 51.1-2 (2013), pp. 635–643.

[81] Ji Zhang et al. “Performance enhancement of the combined power-refrigeration cycle using a liquid-gas-gas ejector for ocean thermal energy conversion”. In: *Energy Conversion and Management* 296.September (2023), p. 117688.

[82] Christian Lucas et al. “Numerical investigation of a two-phase CO2 ejector”. In: *International Journal of Refrigeration* 43 (2014), pp. 154–166.

[83] Knut Emil Ringstad et al. “Machine learning and CFD for mapping and optimization of CO2 ejectors”. In: *Applied Thermal Engineering* 199.May (2021).

[84] Michal Palacz et al. “CFD-based shape optimisation of a CO2 two-phase ejector mixing section”. In: *Applied Thermal Engineering* 95 (2016), pp. 62–69.

[85] Yafei Li and Jianqiang Deng. “Numerical investigation on the performance of transcritical CO2 two-phase ejector with a novel non-equilibrium CFD model”. In: *Energy* 238 (2022), p. 121995.

[86] Michal Haida et al. “Numerical investigation of heat transfer in a CO2 two-phase ejector”. In: *Energy* 163 (2018), pp. 682–698.

[87] Zi Xuan Zhang et al. “Numerical investigation of the effects of inlet conditions and wall heat transfer on subcritical/transcritical CO2 nozzle performance”. In: *International Journal of Thermal Sciences* 193.December 2022 (2023), p. 108505.

[88] Michal Palacz et al. “HEM and HRM accuracy comparison for the simulation of CO2 expansion in two-phase ejectors for supermarket refrigeration systems”. In: *Applied Thermal Engineering* 115 (2017), pp. 160–169.

[89] Wojciech Angielczyk et al. “Prediction of critical mass rate of flashing carbon dioxide flow in convergent-divergent nozzle”. In: *Chemical Engineering and Processing - Process Intensification* 143.February (2019), p. 107599.

[90] Xiao Xiao Xu et al. “Experimental investigation on performance of transcritical CO2 heat pump system with ejector under optimum high-side pressure”. In: *Energy* 44.1 (2012), pp. 870–877.

[91] Yinhai Zhu et al. "Experimental investigation on the performance of transcritical CO2 ejector–expansion heat pump water heater system". In: *Energy conversion and management* 167 (2018), pp. 147–155.

[92] Yuxiang Zhang, Xinli Wei, and Xiang Qin. "Experimental study on energy, exergy, and exergoeconomic analyses of a novel compression/ejector transcritical CO2 heat pump system with dual heat sources". In: *Energy Conversion and Management* 271 (2022), p. 116343.

[93] Chen Guangming et al. "An experimental and theoretical study of a CO2 ejector". In: *International journal of refrigeration* 33.5 (2010), pp. 915–921.

[94] Huiming Zou et al. "Ejector optimization and performance analysis of electric vehicle CO2 heat pump with dual ejectors". In: *Energy* 239 (2022), p. 122452.

[95] Masafumi Nakagawa, Ariel R Marasigan, and Takanori Matsukawa. "Experimental analysis on the effect of internal heat exchanger in transcritical CO2 refrigeration cycle with two-phase ejector". In: *International Journal of Refrigeration* 34.7 (2011), pp. 1577–1586.

[96] G Boccardi et al. "Thermodynamic analysis of a multi-ejector, CO2, air-to-water heat pump system". In: *Energy Procedia* 101 (2016), pp. 846–853.

[97] Christian Lucas et al. "Experimentally validated CO2 ejector operation characteristic used in a numerical investigation of ejector cycle". In: *International journal of refrigeration* 36.3 (2013), pp. 881–891.

[98] Fang Liu, Eckhard A Groll, and Jianxing Ren. "Comprehensive experimental performance analyses of an ejector expansion transcritical CO2 system". In: *Applied Thermal Engineering* 98 (2016), pp. 1061–1069.

[99] Krzysztof Banasiak, Armin Hafner, and Trond Andresen. "Experimental and numerical investigation of the influence of the two-phase ejector geometry on the performance of the R744 heat pump". In: *International journal of Refrigeration* 35.6 (2012), pp. 1617–1625.

[100] Stefan Elbel and Pega Hrnjak. "Experimental validation of a prototype ejector designed to reduce throttling losses encountered in transcritical R744 system operation". In: *International Journal of Refrigeration* 31.3 (2008), pp. 411–422.

[101] Ali Bouzrara. "Etude expérimentale des éjecteurs: Application à la récupération de l'énergie de détente des machines frigorifiques au CO2". PhD thesis. Université de Lyon; Université de Tunis El Manar, 2018.

[102] Lixing Zheng and Jianqiang Deng. "Research on CO2 ejector component efficiencies by experiment measurement and distributed-parameter modeling". In: *Energy Conversion and Management* 142 (2017), pp. 244–256.

[103] Yinhai Zhu et al. "Flow visualization of supersonic two-phase transcritical flow of CO2 in an ejector of a refrigeration system". In: *International journal of refrigeration* 74 (2017), pp. 354–361.

[104] Michal Palacz et al. "Two-phase flow visualisation in the R744 vapour ejector for refrigeration systems". In: *Applied Thermal Engineering* 210.November 2021 (2022), p. 118322.

[105] Yafei Li et al. "Visualization of two-phase flow in primary nozzle of a transcritical CO2 ejector". In: *Energy Conversion and Management* 171 (2018), pp. 729–741.

[106] Xiang Cao et al. "Performance analysis of an ejector-assisted two-stage evaporation single-stage vapor-compression cycle". In: *Applied Thermal Engineering* 205.September 2021 (2022), p. 118005.

[107] Mortaza Yari. "Performance analysis and optimization of a new two-stage ejector-expansion transcritical CO2 refrigeration cycle". In: *International Journal of Thermal Sciences* 48.10 (2009), pp. 1997–2005.

[108] Yang He et al. "An optimal multivariable controller for transcritical CO2 refrigeration cycle with an adjustable ejector". In: *Energy Conversion and Management* 142 (2017), pp. 466–476.

[109] Jacek Smolka et al. "Performance comparison of fixed- and controllable-geometry ejectors in a CO2 refrigeration system". In: *International Journal of Refrigeration* 65 (2016), pp. 172–182.

[110] Fang Liu, Yong Li, and Eckhard A. Groll. "Performance enhancement of CO 2 air conditioner with a controllable ejector". In: *International Journal of Refrigeration* 35.6 (2012), pp. 1604–1616.

[111] Yang He et al. "A numerical contrast on the adjustable and fixed transcritical CO2 ejector using exergy flux distribution analysis". In: *Energy Conversion and Management* 196.May (2019), pp. 729–738.

[112] Philippe Haberschill et al. "Experimental study of a two-phase ejector for CO2 transcritical refrigeration system". In: *Archives of Thermodynamics* 42.4 (2021), pp. 217–246.

[113] Yinhai Zhu et al. "Comprehensive experimental study on a transcritical CO2 ejector-expansion refrigeration system". In: *Energy Conversion and Management* 151 (2017), pp. 98–106.

[114] J Köhler et al. "Experimental and theoretical study of a CO2 ejector refrigeration cycle". In: *Vortrag, VDA Winter Meeting, Saalfelden*. 2007.

[115] S. M. Liao, T. S. Zhao, and A. Jakobsen. "Correlation of optimal heat rejection pressures in transcritical carbon dioxide cycles". In: *Applied Thermal Engineering* 20.9 (2000), pp. 831–841.

[116] Yang He, Jianqiang Deng, and Zaoxiao Zhang. "Thermodynamic study on a new transcritical CO2 ejector expansion refrigeration system with two-stage evaporation and vapor feedback". In: *HVAC and R Research* 20.6 (2014), pp. 655–664.

[117] Stuart Churchill. *CEM_-_Friction-factor_equation_(1977).pdf*. 1977.

[118] M. M. Awad and Y. S. Muzychka. "Effective property models for homogeneous two-phase flows". In: *Experimental Thermal and Fluid Science* 33.1 (2008), pp. 106–113.

[119] Nikolay Ivanov Kolev. *Nikolay I. Kolev Multiphase Flow Dynamics 1*.

[120] Nikolay Ivanov Kolev. *Multiphase Flow Dynamics 2*. 2012.

[121] Huaqin Wen and Jia Yan. "Effect of mixing chamber length on ejector performance with fixed/varied area ratio under three operating conditions in refrigerated trucks". In: *Applied Thermal Engineering* 197 (2021), p. 117379.

[122] Szabolcs Varga, Armando C. Oliveira, and Bogdan Diaconu. "Influence of geometrical factors on steam ejector performance - A numerical assessment". In: *International Journal of Refrigeration* 32.7 (2009), pp. 1694–1701.

[123] M. Nakagawa et al. "Experimental investigation on the effect of mixing length on the performance of two-phase ejector for CO2 refrigeration cycle with and without heat exchanger". In: *International Journal of Refrigeration* 34.7 (2011), pp. 1604–1613.

[124] Krzysztof Banasiak, Armin Hafner, and Trond Andresen. "Experimental and numerical investigation of the influence of the two-phase ejector geometry on the performance of the R744 heat pump". In: *International Journal of Refrigeration* 35.6 (2012), pp. 1617–1625.

[125] Hongqiang Wu et al. "Numerical investigation of the influences of mixing chamber geometries on steam ejector performance". In: *Desalination* 353 (2014), pp. 15–20.

[126] Haruyuki Nishijima, Kyohei Tsuchii, and Masafumi Nakagawa. "Experimental study on the behavior of the two phase flow shock waves occurring in the ejector refrigeration cycle". In: *Mechanical Engineering Journal* 3.6 (2016), pp. 16–00255.

[127] Yinhai Zhu and Peixue Jiang. "Experimental and numerical investigation of the effect of shock wave characteristics on the ejector performance". In: *International journal of refrigeration* 40 (2014), pp. 31–42.

[128] A. Levy, M. Jelinek, and I. Borde. "Numerical study on the design parameters of a jet ejector for absorption systems". In: *Applied Energy* 72.2 (2002), pp. 467–478.

[129] Stefan Elbel. "Historical and present developments of ejector refrigeration systems with emphasis on transcritical carbon dioxide air-conditioning". In: *International Journal of Refrigeration* 34.7 (2011), pp. 1545–1561.

[130] H Kursad Ersoy and Nagihan Bilir. "The influence of ejector component efficiencies on performance of ejector expander refrigeration cycle and exergy analysis". In: *International Journal of Exergy* 7.4 (2010), pp. 425–438.

FOLIO ADMINISTRATIVE

THESE DE L'INSA LYON, MEMBRE DE L'UNIVERSITE DE LYON

NOM : YOU
(avec précision du nom de jeune fille, le cas échéant)

DATE de SOUTENANCE : 4 avril 2024

Prénoms: Cong

TITRE: Contribution to the study of ejector expansion heat pump cycle: modeling and experimental approach

NATURE : Doctorat

Numéro d'ordre : 2024ISAL0029

Ecole doctorale : MEGA de Lyon (Mécanique, Energétique, Génie civil, Acoustique)

Spécialité : Thermique Energétique

RESUME :

L'industrie du chauffage, de la ventilation, de la climatisation et de la réfrigération (CVC&R) est une contributrice notable au réchauffement climatique et à la destruction de la couche d'ozone. Pour faire face à ces préoccupations environnementales, le dioxyde de carbone (CO_2) est de plus en plus utilisé comme fluide frigorigène car il représente une alternative plus respectueuse de l'environnement. Cependant, sa basse température critique et à sa haute pression critique du CO_2 conduisent à une utilisation prédominante de ces cycles en mode transcritique, caractérisée par un rapport de pressionélevé dans le détendeur. Ce rapport de pression élevé entraîne une irréversibilité significative lors du processus de détente.
L'utilisation d'un éjecteur en remplacement des détenteurs conventionnels dansle cycle frigorifique au CO_2 transcritique implique l'accélération du fluide à haute pression à travers une tuyère convergente-divergente. Ce processus permet l'entraînement et le mélange de la vapeur basse pression provenant de l'évaporateur, conduisant à des améliorations substantielles de la récupération de pression. La diminution du travail de compression a été scientifiquement validée, conduisant à une meilleure efficacité de ces systèmes à éjection par rapport aux cycles conventionnels.
Malgré leurs avantages potentiels, les éjecteurs introduisent des complexités liées à l'écoulement diphasique et aux ondes de choc soniques. Par conséquent, la compréhension du champ d'écoulement complexe à l'intérieur de l'éjecteur est cruciale afin d'améliorer les performances des cycles frigorifiques. Des études de simulationet une étude expérimentale sont donc jugées nécessaires.
Cette thèse entreprend une investigation approfondie du cycle frigorifique avec éjecteur au CO_2 à différentes échelles. Un état de l'art en matière de frigorigènes est tout d'abord présenté. Une comparaison systématique de la technologie de l'éjecteur avec d'autres méthodes d'amélioration des performances des systèmes frigorifiques est ensuite présentée, suivie de l'introduction et de la validation de modèles thermodynamiques. Des aspects clés tels que les rendements isentropiques sont abordés, etdes techniques novatrices de post-traitement des données sont proposées.
Dans le domaine de l'exploration théorique, cette étude se plonge à l'échelle ducycle, où divers modèles thermodynamiques à zero dimension du cycle frigorifique à éjection sont examinés et validés de manière comparative à l'aide de données indépendantes. Plus précisément, pour l'éjecteur, un modèle d'équilibre homogène mono-dimensionnel pour la région de l'éjecteur est introduit, conduisant à sa conception géométrique de l'ejecteur. Ce modèle est ensuite comparé avec des modèles thermodynamiques à zéro dimension. Finalement, un banc d'essai dédié à l'étude de l'éjecteur a été developpé, fournissant des perspectives précieuses sur les performances de l'éjecteur et les modes de fonctionnement à travers des pressions d'évaporation variables.
En résumé, ce travail de recherche contribue de manière significative à la compréhension des cycles frigorifiques au CO_2, avec un accent spécifique sur la technologie de l'éjecteur. L'intégration de modèles théoriques et d'études expérimentales offre des perspectives essentielles pour optimiser la conception de l'éjecteur etles paramètres opérationnels du cycle, répondant aux besoins évolutifs de l'industrie CVC&R et promouvant des applications de réfrigération durables.

Mots-clés: Cycle frigorifique, Dioxyde de carbone, Éjecteur, Thermodynamique, Modélisation, Validation expérimentale

Laboratoire (s) de recherche : Centre de Thermique de Lyon (CETHIL UMR5008)

Directeur de thèse : Rémi Revellin

Président de jury :
Composition du jury : Catherine Colin, Brice Tremeac, Hai Trieu Phan, Rémi Revellin, Benoit Michel